
UNIVERSITY OF BIRMINGHAM

# Atomistic Simulation Studies of Storage and Ageing Behaviour of Plutonium Dioxide and Mixed Oxide Fuel

**By**

**Nathan Alan Palmer**

A thesis submitted to the University of Birmingham

for the degree of Doctor of Philosophy

The School of Chemistry

College of Engineering and Physical Sciences

The University of Birmingham

February 2019

# Abstract

Many of the fundamental aspects of the ageing of plutonium (Pu) in storage conditions are of theoretical interest and practical importance. The UK has a large Pu stockpile in interim storage at Sellafield, Cumbria. The aim of this research project was to employ atomistic simulations to study the properties and ageing behaviour of plutonium dioxide ($PuO_2$).

A range of properties of $PuO_2$ were predicted using bulk static lattice, surface and molecular dynamics simulations. These revealed that the oxygen terminated (111) is the most stable surface and that oxygen Frenkel pairs and Schottky defects are energetically favoured. Modelling of helium incorporation showed that helium trapping is effective in octahedral interstitial sites and Schottky defects, in particular on the (111) surface, with helium segregation predicted.

In addition, molecular dynamics predicted thermal properties and 1 keV cascades in $PuO_2$ varying the temperature, showing it be a thermally and radiation resilient material. Given its technological importance, mixed oxide (MOX) fuel was also modelled; with bulk lattice properties predicted varying the Pu content, showing it obeys Vegard's law. Intrinsic defects and helium incorporation was modelled in 9% Pu doped MOX fuel, of relevance to nuclear reactors.

# Preface

The research presented in this thesis was funded by the Nuclear Decommissioning Authority (NDA) as part of the Decommissioning, Immobilisation and Storage soluTIons for NuClear wasTe InVEntories (DISTINCTIVE) Consortium under the theme of '$PuO_2$ and Fuel Residues'. This research has been at numerous research conferences and events, through oral and poster presentations. In particular, a prize for the 'best and most intriguing' talk was awarded at the 7th Nuclear Waste and Decommissioning Research Forum (NWDRF) Conference (2017). The details of oral and poster presentations are listed below.

# Oral Presentations

- 7th NDA PhD Seminar, 23rd January 2019, Manchester Conference Centre.
- The School of Chemistry Postgraduate Symposium 2018, 28th-29th June 2018, University of Birmingham.
- 7th NWDRF Conference, 12th December 2017, Weetwood Hall, Leeds. Awarded for 'best and most intriguing' oral presentation.
- NDA Research Meeting, 18th October 2017, Springfield's Fuel Site, Preston.
- DISTINCTIVE Theme Two Meeting, 17th October 2017, Rheged Centre, Penrith.
- Computational Chemistry Meeting, 26th July 2017, University of Sheffield.
- DISTINCTIVE Theme Two Meeting, 14th November 2016, Rheged Centre, Penrith.

# Poster Presentations

- Final DISTINCTIVE Annual Meeting, 11th September 2018, National Railway Museum, York.
- 6th NDA PhD Seminar, 17th January 2018, Manchester Conference Centre.
- Royal Society of Chemistry Solid State Group (RSC SSG) Christmas Conference 2017, 18th-19th December 2017, University of Reading.
- 7th NWDRF Conference, 12th December 2017, Weetwood Hall, Leeds.
- DISTINCTIVE Theme Two Meeting, 17th October 2017, Rheged Centre, Penrith.
- Computational Chemistry Meeting, 26th July 2017, University of Sheffield.
- The School of Chemistry Postgraduate Symposium 2017, 29th-30th June 2017, University of Birmingham.
- Research Poster Conference 2017, 15th June 2017, University of Birmingham.
- 3rd DISTINCTIVE Annual Meeting, 5th-6th April 2017, National Railway Museum, York.
- 5th NDA PhD Seminar, 18th January 2017, Manchester Conference Centre.
- BlueBEAR Research Conference 2016, 14th December 2016, University of Birmingham.
- DISTINCTIVE Theme Two Meeting, 14th November 2016, Rheged Centre, Penrith.
- Engineering and Physical Sciences (EPS) Research Conference, 25th October 2016, University of Birmingham.
- 6th NWDRF Conference, 11th October 2016, University of Birmingham.
- Hermes Summer School 2016, 27th -31st July 2016, Cumberland Lodge, Windsor.
- Collaborative Computational Project No 5 for simulations of condensed phases (CCP5) Summer School 2016, 11th-19th July 2016, University of Lancaster.
- 2nd DISTINCTIVE Annual Meeting, 19th-20th April 2016, At-Bristol Science Centre, Bristol.

# Acknowledgements

Particular gratitude is given to the following people for their support during this PhD project:

- Dr Mark S.D. Read (School of Chemistry, University of Birmingham) – Academic Supervisor for the opportunity and for general support.
- Professor Roy L. Johnston (School of Chemistry, University of Birmingham) - 2nd Academic Supervisor for general support.
- Dr Alin M. Elena (Daresbury Laboratory) for support in molecular dynamics simulations using the DL_POLY program.
- Professor Steve C. Parker (School of Chemistry, University of Bath) for support in surface simulations using the METADISE program.
- Dr Robin Orr (National Nuclear Laboratory) and Dr Helen Steele (Sellafield Ltd.) - Industrial Supervisors for general support.

In addition, appreciation is given to:

- The NDA for the provision of a PhD studentship.
- The 'BlueBEAR' high performance computing facility at the University of Birmingham.

# Contents

# Chapter 1

# Introduction

## 1.1 Nuclear Energy in the UK

In 2017, according to the World Nuclear Association [1] approximately 11% of the world's electricity originated from nuclear energy, providing a key part of the world's energy supply mix, as shown in Figure 1.1. The production of nuclear energy for civil use has increased dramatically since its conception in the 1950s; with the USA, France and China leading producers. The UK is also a key producer of nuclear power, ranking ninth worldwide and having a net nuclear capacity of 8.9 GWe currently. The UK has fifteen operational nuclear reactors at eight sites, which contributed 21% of electricity production in 2017. Table 1.1 summarises the existing fleet of nuclear reactors.

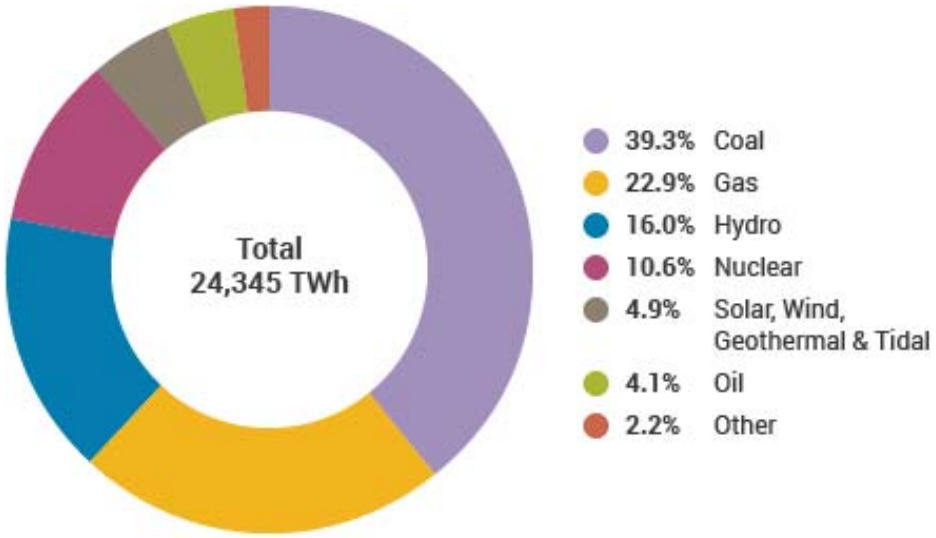


**Figure 1.1: Pie-chart of the world's electricity sources in 2017 [1].**

**Table 1.1: Nuclear reactors operating in the UK [2].**

| Power Plant | Present Capacity (MWe net) | Years of First Power | Expected Shutdown |
|---|---|---|---|
| **Dungeness B 1&2** | 2 x 520 | 1983 & 1985 | 2028 |
| **Hartlepool 1&2** | 595, 585 | 1983 & 1984 | 2024 |
| **Heysham I 1&2** | 580, 575 | 1983 & 1984 | 2024 |
| **Heysham II 1&2** | 2 x 610 | 1988 | 2030 |
| **Hinkley Point B 1&2** | 475, 470 | 1976 | 2023 |
| **Hunterston B 1&2** | 475, 485 | 1976 & 1977 | 2023 |
| **Torness 1&2** | 590, 595 | 1988 & 1989 | 2030 |
| **Sizewell B** | 1198 | 1995 | 2035 |
| **Total: 15 units** | **8883 MWe** | | |

With the exception of Sizewell B, all of the current fleet of reactors listed in Table 1.1. are Advanced Gas-cooled Reactors (AGR) designs. Sizewell B is a Pressurised Water Reactor (PWR) and the most recent power plant to be built. Most existing nuclear power plants are due to cease production by 2030. However, the UK Government remains supportive of nuclear power, which will assist in enabling it to comply to the Climate Change Act of 2008 [3]. This law aims to reduce greenhouse gas emissions by at least 80% of 1990 levels by 2050. In fact, the Government has announced a commitment to the UK nuclear industry in its 'Nuclear Sector Deal' [4] which will provide £200m of funding which includes £32m for research and development.

There are plans for new nuclear reactors in the UK [5]. Six sites have been confirmed for thirteen new nuclear reactors in the UK, which have a total capacity of 15.6 MWe by 2030. These reactors are of an enhanced design compared to the current reactors, and consist of EPRs (European Pressurised water Reactors), ABWRs (Advanced Boiling Water Reactors) and AP1000 reactors. These reactors are at various stages of planning and development. Hinkley Point C (based in Somerset), is under construction and will have two EPRs (European Pressurised water Reactor) of 3.2 GWe capacity once operational by 2026/7. However, since the end of 2018, private sector support for AP1000 reactors at Moorside in Cumbria and ABWRs at Wylfa in Wales and Oldbury, Gloucestershire have collapsed.

## 1.2 Physics and Technology of Nuclear Energy

### 1.2.1 Nuclear Fission

Nuclear energy originates from nuclear fission reactions in nuclear fuel, commonly uranium dioxide ($UO_2$). Nuclear fission involving splitting of the nucleus of an atom, releasing a large amount of energy. A schematic representation of this process is shown in Figure 1.2.

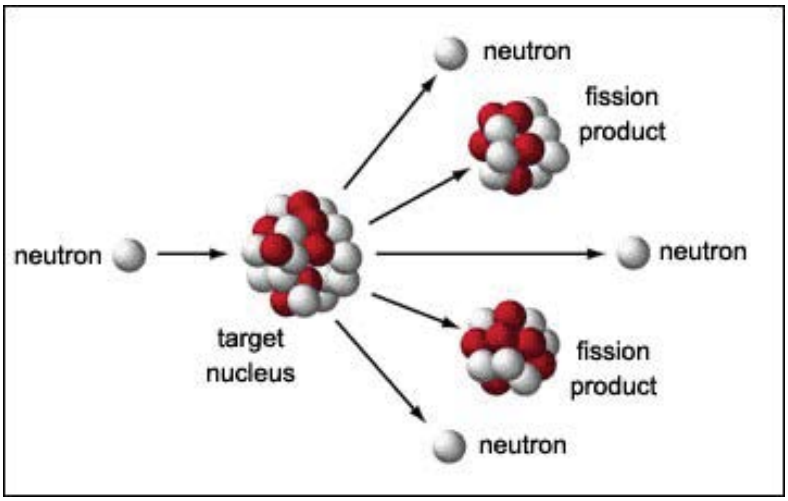


**Figure 1.2: Schematic representation of nuclear fission [6].**

As shown, nuclear fission is initiated by a neutron (typically of low energy) which is absorbed by a nucleus, which subsequently splits releasing fission fragments, and more neutrons. These neutrons go on to cause further nuclear fission reactions leading to a chain reaction process. In nuclear reactors, this chain reaction is controlled by the use of control rods or neutron absorbers. Each nuclear fission releases ~200 MeV, which is a factor of 100 million larger than the chemical energy released in combustion reactions (e.g. coal burning). Hence, due to the very high fuel energy density, nuclear power is highly energy efficient.

The large amount of energy released is demonstrated through Einstein's equation, of mass-energy equivalence. The final mass of the fission fragments and

neutrons is less than the initial mass of the fissioning nucleus. This difference in mass corresponds to the energy released in nuclear fission. This energy is released is in the form of kinetic energy of the fission products, neutrons and gamma rays (high-energy electromagnetic radiation) released. Most of this energy is converted into heat in the nuclear fuel.

The most common nuclear fuel is $UO_2$, in the form of ceramic pellets. The isotopes of an element have same number of protons (atomic number), but different numbers of neutrons and hence atomic mass numbers. Natural uranium contains two isotopes, U-235 and U-238, differing only in the number of neutrons in their nuclei. Approximately 0.7% of natural uranium (U) is U-235 and 99.3% is U-238. U-235 is a fissile isotope, meaning it fissions easily by absorbing low energy thermal neutrons.

However, U-238 is a fissionable nucleus, meaning high-energy (> 0.1 MeV) neutrons are required for fission to occur. Hence, for most nuclear reactors, the $UO_2$ is enriched to 3-5% of fissile U-235, depending on the reactor. The fission of a U-235 nucleus results in typically two fission products and two neutrons. The fission yield peaks at atomic numbers around 38 (Sr) and 54 (Xe), as shown in Figure 1.3. Fission products released are very energetic, thus unstable and rapidly undergo radioactive decay.

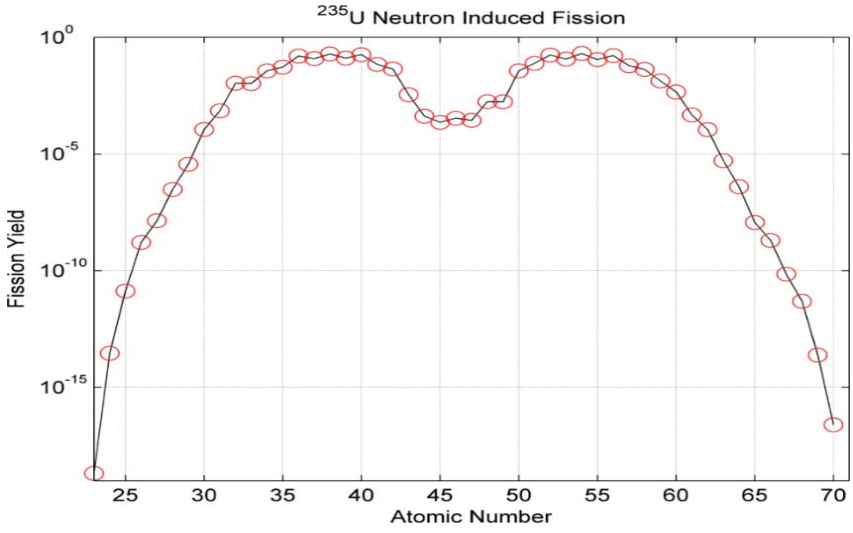


**Figure 1.3: Fission yield vs. atomic number from the neutron induced fission of U-235.**

### 1.2.2 Nuclear Reactors

The process of electricity production from nuclear fission in a reactor to electricity consumption is shown schematically in Figure 1.4.

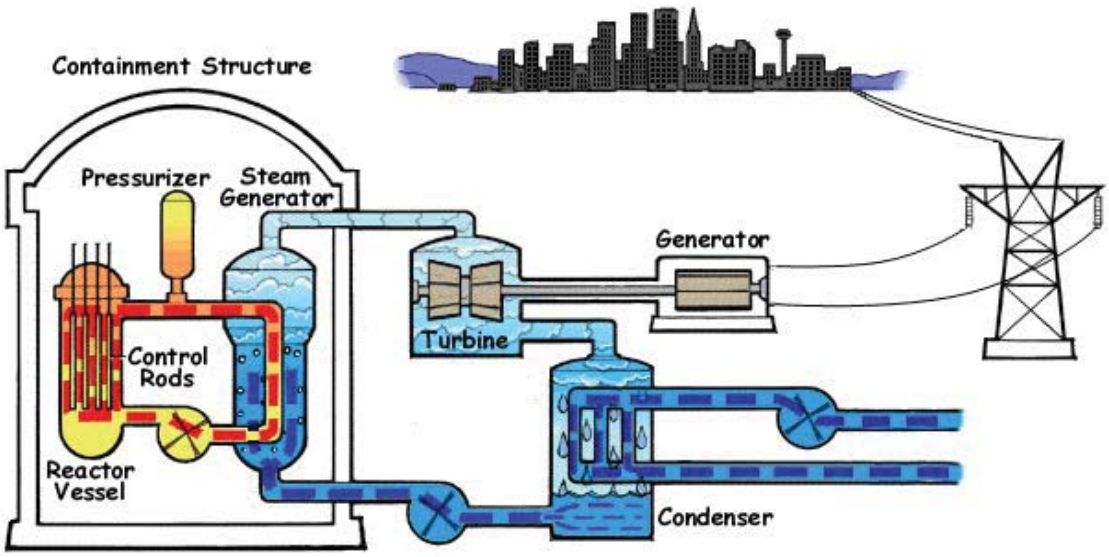


**Figure 1.4: Schematic representation of the nuclear reactor system [7].**

The UK has fourteen Advanced Gas-cooled Reactors (AGRs) and one Pressurised Water Reactor (PWR). Before these, there were Magnox reactors, which are now being decommissioned. Table 1.2 summarises the basic properties of these reactors.

**Table 1.2: Summary of properties of AGRs, PWRs and Magnox reactors.**

| Reactor Type | Fuel | Primary Coolant | Moderator | Fuel Cladding Material [2] |
|---|---|---|---|---|
| **AGR** | Enriched [1] $UO_2$ | Carbon dioxide | Graphite | Stainless steel |
| **PWR** | Enriched $UO_2$ | Pressurised light water | Pressurised light water | Zirconium alloy |
| **Magnox** | U metal | Carbon dioxide | Graphite | Magnesium, aluminium non-oxidising alloy |

**[1] Enrichment is the process of increasing the proportion of fissile U-235 in the fuel to typically 3-5%.**

**[2] This material contains the fuel to protect the fuel and prevent release of fission products.**

Nuclear fission occurs in the nuclear fuel within the core of a nuclear reactor which releases thermal energy, heating the primary coolant, which is pressurised water in PWRs and carbon dioxide in AGRs and Magnox reactors. The primary coolant transfers heat to the secondary coolant (un-pressurised water) which converts to steam in the steam generator. This steam turns the turbines and electricity is produced from generators. The electricity from the power station is then transmitted to a grid system to supply electricity to consumers. The steam is cooled in a condenser turning it back to water and supplying the secondary coolant.

There are many key components of a nuclear reactor, which are needed to ensure safe, efficient and reliable operation. The central component is the reactor core, containing the nuclear fuel in fuel rods, the primary coolant, a moderator and control rods. The primary coolant transfers heat from the core to the secondary coolant to generate steam. The moderator thermalizes the high-energy neutrons released in nuclear fission from MeV to meV levels, to ensure that nuclear fission occurs. In PWRs, pressurised light water is the primary coolant and the moderator. However, in AGRs and Magnox reactors, graphite is the moderating material.

To control or stop nuclear fission reactions, control rods (typically made of cadmium) can be inserted into the core, which effectively absorb neutrons. In PWRs, so-called 'reactor poisons' such as boron can also be inserted in the primary coolant to absorb neutrons. Finally, there is the containment, which is the structure housing the core of the nuclear reactor. It serves as an outer radiation shield and is typically made of steel reinforced concrete.

Nuclear reactors are classified by a 'generation', defining a type of reactor or groups of reactors. Figure 1.5 shows a timeline of five generations of nuclear reactors, starting with generation 1 reactors from the 1950s. In the UK, generation 1 reactors consisted of Magnox reactors. These were graphite moderated, cooled by carbon dioxide and used metallic uranium fuel. Their name is derived from the magnesium, aluminium non-oxidising alloy of the fuel cladding.

These Magnox reactors were superseded by generation 2 reactors, consisting of AGRs and PWRs, which comprise all of the UK's current fleet. Generation 3 reactors are more advanced and safer than generation 2 reactors, which include EPRs (European Pressurised-water Reactor), ABWRs (Advanced Boiling Water Reactor) and AP1000 reactors. The two EPRs being built at Hinkley Point C are generation 3 reactors, which are due to be operational in 2026/7. Generation 3+ and 4 are proposed reactors, which have the potential to utilise nuclear waste, offer passive safety, higher efficiency and lower costs. These reactors have various designs and use novel fuels and coolants. These reactors are not expected to be built and operational before 2030.

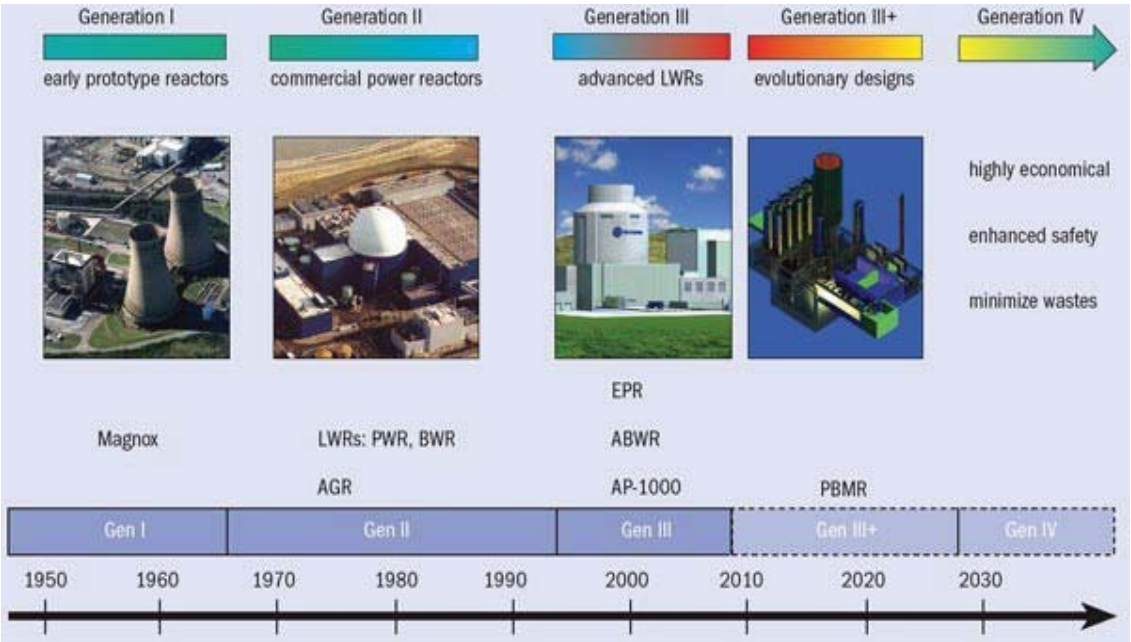


**Figure 1.5: Generations of nuclear reactors over time [7].**

## 1.3 Plutonium Background

### 1.3.1 Plutonium Production, Isotopes and Uses

There are fifteen Pu isotopes and three have been demonstrated to be useful [8]. Pu-238 is used to power spacecraft using radioisotope thermoelectric devices, which are powered from the heat generated from alpha decaying Pu. Being fissile, Pu-239 is used in nuclear weapons as sufficient amounts can cause a nuclear chain reaction. In addition, Pu-239 is a fissile component of mixed oxide (MOX) nuclear fuel, which incorporates Pu into the $UO_2$ matrix. MOX fuel currently accounts for 5% of new nuclear fuel used worldwide [9]. In addition, Pu-241 beta decays to Am-241, which is used in household smoke detectors.

Worldwide, approximately 70 tonnes of civil Pu is produced per year from spent fuel re-processing, with circa 1300 tonnes produced to date [8]. Pu is produced as a by-product of nuclear fission of U in nuclear reactors. This is because U nuclei absorb

neutrons and transmute to Pu. Pu-238 to Pu-242 isotopes are produced. Table 1.3 summarises the typical Pu isotopic content at fuel discharge in a PWR, AGR and Magnox reactor, at different mean burn-up levels.

**Table 1.3: Examples of the types of variation in Pu composition produced from different sources [8].**

| Reactor Type | Mean Fuel Burn-up [1] (MW d/t) | Percentage of Pu Isotopes at Discharge | | | | | Fissile Content [2] (%) |
|---|---|---|---|---|---|---|---|
| | | Pu-238 | Pu-239 | Pu-240 | Pu-241 | Pu-242 | |
| PWR | 33000 | 1.3 | 56.6 | 23.2 | 13.9 | 4.7 | 70.5 |
| | 43000 | 2.0 | 52.5 | 24.1 | 14.7 | 6.2 | 67.2 |
| | 53000 | 2.7 | 50.4 | 24.1 | 15.2 | 7.1 | 65.6 |
| AGR | 18000 | 0.6 | 53.7 | 30.8 | 9.9 | 5.0 | 63.6 |
| Magnox | 3000 | 0.1 | 80 | 16.9 | 2.7 | 0.3 | 82.7 |
| | 5000 | N/A | 68.5 | 25.0 | 5.3 | 1.2 | 73.8 |

**[1] Burn-up is the energy produced per unit mass of fuel initially. [2] fissile content means the fraction of the total Pu produced which is fissile, which fissions by absorption of thermal neutrons.**

As shown in Table 1.3, Pu-239 is the most abundant Pu isotope produced, followed by Pu-240, with most scarce isotope being Pu-238. All Pu isotopes are radioactive. Production of Pu-239 originates from U-238 nuclei absorbing neutrons in the nuclear fuel. In most PWRs and AGRs, 99.3% of the initial fuel is U-238. During reactor operation, U-238 nuclei absorb neutrons, which results in production of U-239. U-239 is highly unstable so beta (β) decays to Np-239, which again beta decays to Pu-239, which is relatively stable. The nuclear processes leading to Pu-239 production are summarised in Table 1.4. Beta decay is a mode of radioactive decay, whereby a nucleus emits an electron (a $\beta$ particle) and an anti-electron neutrino ($\overline{\nu_e}$) (a weakly interacting fundamental particle). To conserve charge, a neutron in the parent nucleus transmutes to a proton.

**Table 1.4: Summary of the nuclear processes generating Pu-239 from U-238 [10].**

| Nuclear Process | Nuclear Reaction | Q Value [1] (keV) |
|---|---|---|
| Neutron absorption | $U_{92}^{238} + n \rightarrow U_{92}^{239}$ | - |
| Beta decay of U-239 | $U_{92}^{239} \rightarrow Np_{93}^{239} + \beta + \overline{\nu_e}$ | 1261.5 |
| Beta decay o Np-239 | $Np_{93}^{239} \rightarrow Pu_{94}^{239} + \beta + \overline{\nu_e}$ | 722.5 |

**[1] The Q value is the energy released in a nuclear decay.**

The production of Pu-239 from U-239 is relatively fast as the half-life (time for half of the initial number of nuclei to decay) for the beta decay of U-239 is 23.45 minutes, and that of the subsequent beta decay of Np-239 is 2.356 days [10]. Being fissile, Pu-239 can absorb neutrons and fission, adding to the energy production. Table 1.5 summarises the decay properties of Pu-238 to Pu-242, of relevance to nuclear reactors.

**Table 1.5: Decay properties of Pu isotopes relevant to nuclear reactors [10].**

| Pu Isotope | Decay Mode [1] | Daughter Nucleus [2] | Q Value (MeV) | Half-life (yrs) |
|---|---|---|---|---|
| **Pu-238** | Alpha decay [3] | U-234 | 5.593 | 87.7 |
| **Pu-239** | Alpha decay | U-235 | 5.245 | 24110 |
| **Pu-240** | Alpha decay | U-236 | 5.256 | 6561 |
| **Pu-241** | Beta decay | Am-241 | 0.02078 | 14.3 |
| **Pu-242** | Alpha decay | U-238 | 4.985 | $3.73\times10^5$ |

**[1] Decay mode is the decay type of highest probability. [2] The daughter nucleus is the nucleus produced from the decay of the initial (parent) nucleus.**

The spent nuclear fuel from nuclear reactors is reprocessed to separate out the U (96%), Pu (1%) and high-level waste (3%), so that the nuclear fuel can be re-used. In the UK, this has been done at Sellafield, where there are two reprocessing facilities: the Thermal Oxide Reprocessing Plant (THORP) and the Magnox Reprocessing Plant. THORP stopped reprocessing in 2018, with the Magnox Reprocessing Plant due to close in 2020 [11].

THORP reprocessed UK and foreign oxide fuel, whilst the Magnox Reprocessing Plant reprocesses spent fuel from legacy Magnox reactors from the UK, Japan and Italy. Reprocessing of Magnox spent fuel is required due to the difficulty of safe storage, as the material corrodes in aqueous conditions. Following World War Two, reprocessing of Magnox spent fuel was also done to produce Pu as part of the UK's atomic weapons program. The combination of reprocessing for civil and military use has led to an accumulation of Pu, which is stored at Sellafield, Cumbria.

### 1.3.2 Plutonium Storage Issues in the UK

The UK owns and manages 38% of the global stockpile of civil Pu. The Pu stockpile, stored at Sellafield, is managed by the Nuclear Decommissioning Authority (NDA) on behalf of the UK Government. In 2014, there was circa 126 tonnes of Pu, which is predicted to increase to circa 140 tonnes by 2020 [12]. This is the largest amount of civil Pu stored anywhere in the world, posing numerous safety, security and cost concerns. There are various factors to consider in the safe storage of Pu. Regarding the UK, the Pu stockpile is stored at the Sellafield site as $PuO_2$ powder in steel containers. Depending on the production route and processing of the $PuO_2$, it is packaged under an argon and air mixture or pure argon. $PuO_2$ from the Magnox Reprocessing Plant are stored within intermediate polyethylene bags. $PuO_2$ from THORP are stored solely within steel containers.

Gas pressurisation is considered one of the risks to be managed during storage of sealed packages. This is as any gas pressurisation increases the risk of container rupture and release of $PuO_2$ into the store environment. The relevant gases include helium and hydrogen. The helium gas originates from the alpha decay of Pu atoms, which over many decades could become appreciable. Assessments of the risk of gas pressurisation currently conservatively assume that complete release of helium from $PuO_2$ occurs.

Hydrogen gas could be a product of radiolysis (splitting of molecules by radiation) of water and decomposition of packaging material. Due to the high flammability of hydrogen, it is important to be able to discern between any gas pressurisation originating from hydrogen and more benign gases such as helium. In addition, Am-241 is also present in the stored $PuO_2$, as it is produced from the beta decay of Pu-241, and alpha decays to Np-237, with a half-life of 432.6 years [10]**.** During the alpha decays, Am-241 nuclei also emit intense gamma rays, which pose an additional radiation hazard.

Overall, there is a need for continued safe storage of Pu at Sellafield. This requires fundamental research to underpin and optimise the storage arrangements for the long term. Computational studies can help address this issue, through atomistic simulations, which use a range of techniques to gain insight into material properties and behaviour.

### 1.3.3 Plutonium Options in the UK

The NDA, on behalf of the UK Government, have researched various options for using the Pu stockpile [12] [13]. They have shown that the preferred option of the UK Government is utilisation of Pu in nuclear fuel. Over a number of decades, the usable Pu could be used in mixed oxide (MOX) nuclear fuel, and as a component of nuclear fuel in the proposed CANDU EC6, PRISM and NuScale reactors. However, about 5% of the Pu stockpile is unsuitable for reuse [12] and would be treated as nuclear waste, requiring a robust immobilisation material to be developed and the construction of a disposal facility. The default option for Pu is the continued storage at Sellafield. However, this is only a short to medium term solution.

MOX fuel is widely used in ~40 European LWRs and is well established [9]. However, in the UK, utilisation of Pu in MOX fuel would require construction of a MOX fabrication plant and current reactors may not be suitable for MOX fuel. CANDU Energy has proposed building four 740 MWe Enhanced CANDU 6 (EC6) reactors [14] as a variant of their established CANDU (Canada Deuterium Uranium) reactors, which would use 'CANMOX' fuel and be moderated and cooled by deuterium (heavy water). In addition to the reactors, a CANMOX fuel fabrication plant would have to be built, which is predicted to take ~15 years to build. In addition, GE Hitachi has proposed building two 311 MWe Power Reactor Innovative Small Module (PRISM) reactors [15], which are modular fast reactors, which would use Pu alloy as the fuel and be cooled by molten sodium.

Furthermore, there are the Nuscale reactors [16], which are 50 MWe modular light water reactors, which could use mixed oxide (MOX) fuel, and be water cooled. Each unit would consist of up to twelve modules. Finally, there is also a generation 4 modular molten salt reactor being developed by Moltex, which would be cooled by molten salt, generating between 0.3 and 1.5 GWe. The modular reactors described have the advantages of reduced construction times and cost than conventional nuclear reactors. However, further assessments and research is required for them to be viable options for the UK Pu stockpile. It will take several years for the new reactors to be built and to start operating, with continued safe storage of Pu the default option. Hence, fundamental research is required and this thesis contributes to this through atomistic simulations. The methodology of this approach is given in the following chapter.

# Chapter 2

# Methodology

## 2.1 Introduction

Atomistic simulations provide a versatile tool in solid-state chemistry and materials science. They provide insight into the fundamental properties of materials of technological importance including catalysts [17,18,19], high temperature superconductors [20,21,22] and ionic conductors [23,24,25,26,27]. The use of simulations has grown over recent decades due to the development of supercomputers, computer codes and greater affordability. They are particularly useful in predicting properties difficult to measure experimentally and on the atomistic scale. This is particularly relevant for nuclear materials, where experiments are difficult due to their radioactivity. Hence, simulations would provide a less costly approach to understand such materials.

A multitude of fundamental aspects of nuclear materials have been studied, in particular actinide oxides, which include their defect chemistry [28,29,30], thermal properties [31,32,33], surface properties [34,35,36], and radiation damage [37,38,39,40,41]. There are a variety of techniques available, which probe different length and time scales. There are two main approaches used in computational chemistry: ab-initio methods and force-field methods. Ab-initio methods typically use Density Functional Theory (DFT), based on first-principles calculations. This approach has the benefit of being highly accurate and has been used to model actinide oxides including surface properties [42,43], defects [44,45] and thermal properties [46].

Force-field methods involve the derivation and application of empirical potentials, by fitting to experimental or ab-initio data. Hence, potentials have a domain

of validity and rely on accurate fitting data. This approach is used in this work, as it is less computationally demanding than ab-initio calculations, allowing simulations of much larger systems (1000s of atoms instead of 100s). In addition, this method can be used to model system dynamics using molecular dynamics, which is of high interest to $PuO_2$ in modelling thermal properties and radiation damage used successfully for actinide oxides [31,39,41,47]. In this chapter, an overview of the research methodology is presented, covering modelling of the bulk lattice, defects, surfaces and molecular dynamics.

## 2.2 Potential Model

### 2.2.1 Background

The foundation of atomistic simulations is the development and use of interatomic potentials, which are empirical functions of atomic positions and describe atomic interactions in a material. Empirical fitting derives the potential parameters using available experimental or theoretical data, so for a solid the potentials accurately describe the crystal structure and properties. In general, the internal energy of a solid ($U_{Solid}$) is represented as an infinite Taylor series, given by a sum over all the interactions. For a solid consisting of $N$ atoms labelled $i$, $j$, $k$, this is given by:

$$U_{Solid} = \sum_{i=1}^{N} V_i + \frac{1}{2}\sum_{i}^{N}\sum_{j}^{N} V_{ij} + \frac{1}{6}\sum_{i}^{N}\sum_{j}^{N}\sum_{k}^{N} V_{i,j,k} + \cdots \qquad \textbf{(2.01)}$$

The first sum represents the contribution from self-interactions ($V_i$), the second sum represents the pair-wise interaction ($V_{ij}$) and the third for triplet interactions ($V_{i,j,k}$) and so on. It is not possible to calculate the exact sum for a macroscopic solid. In practice, this series is truncated at second order. This approximation to the exact sum is usually valid for most solids, with parameters in the chosen terms incorporating many-body effects.

The Born model is a potential based model for interactions in ionic compounds. In this model, the solid is composed of ions treated as point charges. Two-body potentials are used which are functions of the separation between the ions, which represent either long-range or short-range interactions. The total potential between two ions ($V_{Total}$) is given by the sum of these two types of interactions:

$$V_{Total} = V_{Long-range} + V_{Short-range} \quad \textbf{(2.02)}$$

The long-range interaction between two ions $i$ and $j$, of charges $q_i$ and $q_j$ with centres separated by distance $r_{ij}$ is their electrostatic interaction, given by the Coulomb equation:

$$V_{Electrostatic}(r_{ij}) = \frac{q_i q_j}{4\pi\varepsilon_0 r_{ij}} \quad \textbf{(2.03)}$$

In ionic materials, the electrostatic interaction dominates over all interactions. There is also a short-range repulsive potential between the ions, which prevents cation-anion distances becoming too short. Typically, Buckingham, Morse or Lennard-Jones potentials are used. The Buckingham potential [48] is given by:

$$V_{Buckingham}(r_{ij}) = Ae^{\frac{-r_{ij}}{\rho}} - \frac{C}{r_{ij}^6} \quad \textbf{(2.04)}$$

The exponential term describes repulsion between the electron clouds of the ions, in accordance with the Pauli Exclusion Principle. The other term describes attraction between fluctuating dipoles, known as dispersion. $A$, $\rho$ and $C$ are empirical parameters for each ion pair interaction. Hence, the lattice energy of a solid of $N$ ions is given by the following sum:

$$U_{Solid}(r_{ij}) = \sum_i^N \sum_{j>i}^N \frac{q_i q_j}{4\pi\varepsilon_0 r_{ij}} + \sum_i^N \sum_{j>i}^N \left( Ae^{\frac{-r_{ij}}{\rho}} - \frac{C}{r_{ij}^6} \right) \quad \textbf{(2.05)}$$

Minimisation of this sum will lead to an equilibrium configuration of the solid. There are many other short-range potentials used. For example, the Morse potential for interaction between a pair of atoms is:

$$V_{Morse}(r_{ij}) = D\left(\left[1 - e^{-a(r_{ij}-r_0)}\right]^2 - 1\right) \quad \textbf{(2.06)}$$

$D$ is the bond dissociation energy given by the depth of the potential well, $r_0$ is the equilibrium separation between the atoms and $\alpha$ describes the potential shape near equilibrium. $\alpha$ is given by:

$$\alpha = \omega\sqrt{\frac{\mu}{2D}} \quad \textbf{(2.07)}$$

$\omega$ is the bond vibration frequency between the atom pair, $\mu$ is the reduced mass of the pair. $\omega$ is related to the spring force constant for the vibration ($k$) by:

$$\omega = \sqrt{\frac{k}{\mu}} \quad \textbf{(2.08)}$$

Typically, the Morse potential models covalent bonds in diatomic molecules. Another example of a short-range potential is the Lennard-Jones potential, which is typically used to describe interactions between gas atoms, given by:

$$V_{Lennard-Jones}(r_{ij}) = \left(\frac{A}{r_{ij}^{12}}\right) - \left(\frac{B}{r_{ij}^{6}}\right) \quad \textbf{(2.09)}$$

In this form, $A$ and $B$ are potential parameters. An alternative expression is:

$$V_{Lennard-Jones}(r_{ij}) = 4\epsilon\left[\left(\frac{\sigma}{r_{ij}}\right)^{12} - \left(\frac{\sigma}{r_{ij}}\right)^{6}\right] \quad \textbf{(2.10)}$$

Figure 2.10 is a graphical representation of this potential. As shown, $\epsilon$ is the depth of the potential energy minimum, occurring at the equilibrium separation $R_{min}$. $\sigma$ is the interatomic separation at which the potential is zero.

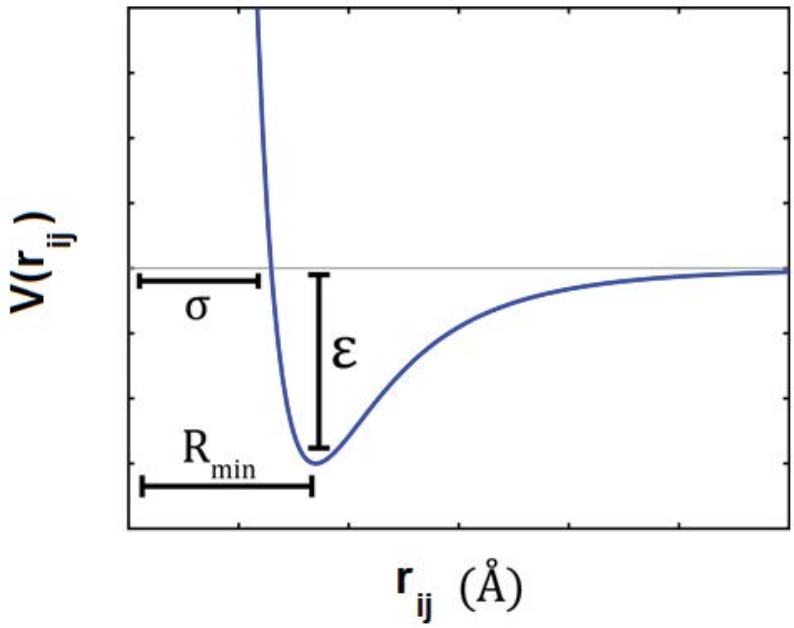


**Figure 2.10: Graphical representation of the Lennard-Jones potential [49].**

In both forms of the Lennard-Jones potential, the $\frac{1}{r_{ij}^{12}}$ term describes the repulsion between the electron clouds of the ions, as $r_{ij}$ tends to zero. The $\frac{1}{r_{ij}^{6}}$ term describes attraction between fluctuating dipoles at larger $r_{ij}$ known as dispersion.

## 2.2.2 Potential Truncation

In order for simulations to be efficient, truncation of the short-range potentials is required. This is also natural as the potentials tend to zero rapidly and are negligible at interatomic separations of ~10 Å to 20 Å, where the cut-off is typically applied. However, in general, there remains a finite value of the potential and its derivatives at the cut-off point. This leads to a discontinuity in the force at the cut-off point ($r_{cut}$).

One method to resolve this is the 'cut and shift' [50] where the potential is shifted so the potential at the cut-off is zero. However, the potential gradient and hence the force would remain finite. Hence, an additional linear term ensures the gradient is also zero at the cut-off point. In this case, the modified short-range potential is given by:

$$V_{Short-range}^{Modified}(r_{ij}) = V_{Short-range}^{Un-modified}(r_{ij}) + \alpha r_{ij} + \beta(r_{cut}) \quad \textbf{(2.11)}$$

$r_{cut}$ is the interatomic separation at the cut-off point and $\alpha$ and $\beta$ are constants to ensure the potential and its derivative are both zero at the cut-off point. However, this approach alters the entire potential, not just near the cut-off point, potentially negatively affecting calculations. Hence, it is important to ensure the cut-off is sufficiently large and the modification is suitable for the accuracy required. Furthermore, there are other methods of modifying the short-range potentials when using cut-off's. One example is tapering, where the potential is multiplied by a tapering function over a certain range of interatomic separation.

### 2.2.3 Modelling Ionic Polarisation

The electron cloud of ions distort in the presence of an electric field, which is known as ionic polarisation. In the case of ionic solids, the ions are polarised and have a fluctuating dipole moment. This causes an attraction between the ions, which is the origin of the short-range attractive term in the potentials. To incorporate polarisation in the potential model, either the shell model or partial charges are used.

To model ionic polarisation, the shell model first introduced by Dick and Overhauser [51] is widely used. In this model, an ion is represented as a core and a shell of opposite charge polarity, representing a dipole moment. In the massless shell model, the core contains all the mass of an ion, representing the nucleus and inner electrons. The massless shell surrounds the core and represents the valence electrons. The core and shell are electrostatically screened from each other so there is no electrostatic interaction and the total of the core and shell charges equals the net charge of the ion.

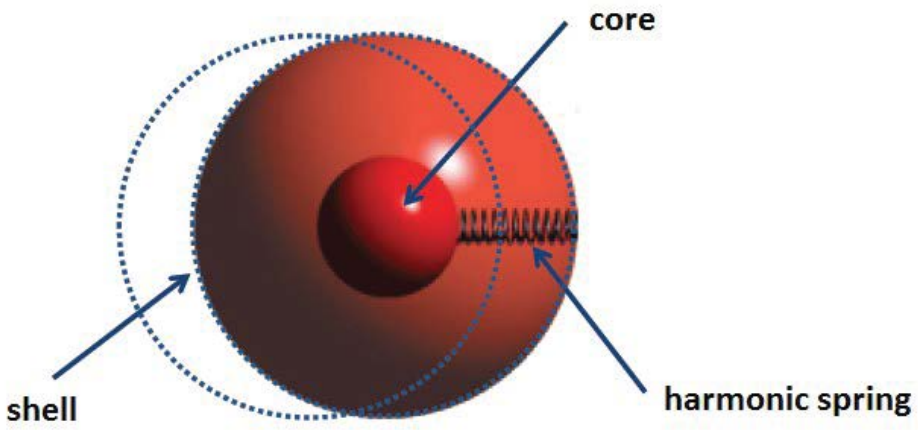


**Figure 2.11: Schematic representation of the shell model.**

The core and shell interact through an harmonic force (i.e. a spring) as shown in Figure 2.11. This corresponds to an harmonic potential between the core and shell, separated by a distance $r_{core-shell}$, which is given by:

$$V_{core-shell} = \frac{1}{2} k r_{core-shell}^2 \quad \textbf{(2.12)}$$

$k$ is the harmonic spring constant. The core and shell charges and the spring constants are empirical parameters, typically fitted to dielectric constants. The atomic polarizability ($\alpha$) in a vacuum is given by:

$$\alpha = \frac{1}{4\pi\varepsilon_0}\left(\frac{q_{shell}^2}{k}\right) \quad \textbf{(2.13)}$$

$q_{shell}$ is the shell charge. Hence, for the case of polarisable ions $i$ and $j$, the lattice energy is given by [52]:

$$U_{Solid} = \sum_i^N \sum_{j>i}^N (V_{Elec,icore,jcore} + V_{Elec,icore,jshell} + V_{Elec,ishell,jshell} + V_{Buck,ishell,jshell}) + \sum_i^N V_{core-shell,i} + \sum_j^N V_{core-shell,j} \quad \textbf{(2.14)}$$

Hence, the lattice energy incorporating the shell model is a function of various distances. For ion pairs $i$ and $j$, it is a function of their core-core distance, their core-shell distance and their shell-shell distance. It is also a function of the core-shell separation of individual ions.

An alternative implicit method to model ionic polarisation is to use partial charges. Each ion has a partial charge, which corresponds to a fraction of the oxidation state of the ion. This treats a compound as partially ionic with a degree of covalent bonding involved. This is especially important when the ions have similar electronegativity. To calculate the partial charges of the ions, Pauling's equation of ionicity ($P_{ij}$) is used [53]:

$$P_{ij} = 1 - \exp\left(\frac{-(\chi_i - \chi_j)^2}{4}\right) \quad \textbf{(2.15)}$$

$P_{ij}$ is the ionicity of the bond between atoms $i$ and $j$ and $\chi_i$ and $\chi_j$ represent the electronegativity's of the atoms. $P_{ij}$ is a number between zero and one, where zero electronegativity corresponds to a fully covalent bond and one corresponds to a fully ionic bond between the pair of atoms. In reality, most bonding falls in between these. Furthermore, due to the exponential in the equation for $P_{ij}$, the ionicity is very dependent on the difference in electronegativity of the atoms involved in bonding. For each bonding pair in a solid, the ionicity is calculated and an average value is then calculated. This parameter scales the oxidation states of ions to obtain the partial charges of the ions in the potential model.

### 2.2.4 Derivation of Potentials

It is important that the analytical form and parameterisation of the interatomic potentials is appropriate to enable reliable and accurate predictions. Derivation of potentials employs empirical fitting to available experimental or theoretical data. Typically, for crystalline solids, the fitting data is structural, mechanical and optical. In an iterative process, optimal potential parameters are determined such that there is maximal agreement of calculated and fitting data.

Typically, empirical fitting employs a least squares fitting algorithm. This involves iteratively varying the potential parameters and minimising the chi squared ($\chi^2$)

parameter. $\chi^2$ is the sum of the weighted difference squared in the fitting data ($x_{fitting}$) and the calculated data ($x_{calculated}$), given by [50]:

$$\chi^2 = \sum_i^{data} w_i (x_{fitting} - x_{calculated})_i^2 \quad \textbf{(2.16)}$$

$w_i$ is a weighting factor assigned to each data point ($i$), which depends on the importance and accuracy of the fitting data to the potential model.

## 2.3 The Electrostatic Energy

For ionic solids, the dominant component of the total energy is the electrostatic energy. Hence, in atomistic simulations, reliable and efficient calculation of this is crucial. However, this is difficult as the energy density of the electrostatic interaction increases unconditionally with distance, rather than decaying, leading to an infinite sum [50]. For three-dimensional crystal lattices, the Ewald summation method by Ewald (1921) [54,55] is used, which ensures convergence of the electrostatic energy. The summation is constrained to the natural conditions that the crystal must be charge neutral and have no net dipole moment.

In the Ewald method, the potentially infinite electrostatic sum is subjected to a Laplace transform and separated into two finite sums; in real-space ($V_{Real}$) and reciprocal space ($V_{Reciprocal}$). To obtain the real-space sum, the ions are effectively neutralised by superposition of Gaussians of opposite charge to the ions centred on the ions. For the reciprocal space sum, a second set of Gaussians equal to the charge of the ions are subsequently centred on the ions. A graphical representation of the Ewald sum in one dimension is shown in Figure 2.12.

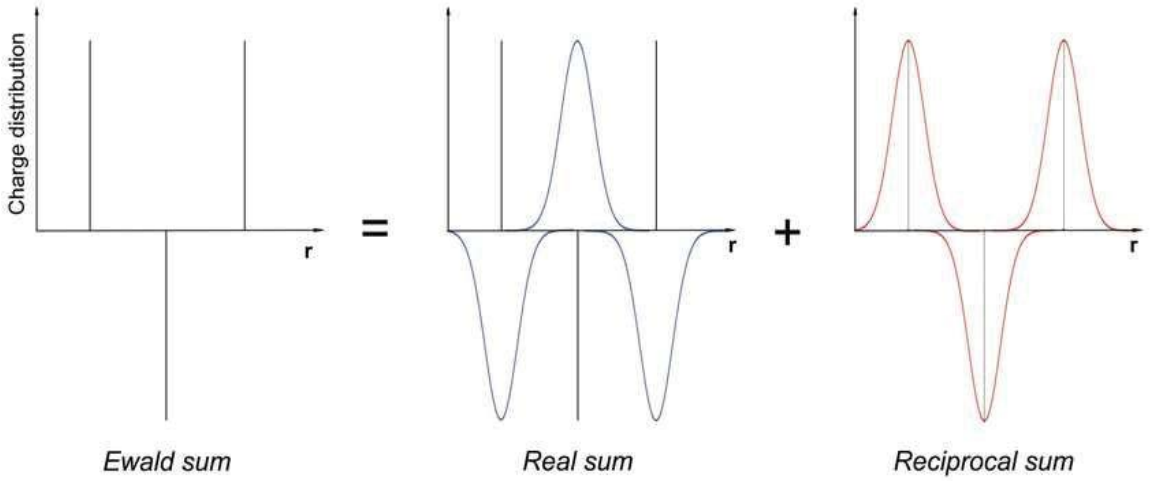


**Figure 2.12: Graphical representation of the Ewald sum [56].**

The computational expense of the Ewald sum scales with the number of ions ($N$) as $N^{3/2}$. In addition to these two contributions, there is the self-energy of the ions ($V_{Self}$), from ionic polarizability, which is included in the final sum. Hence, the total electrostatic energy of a crystal lattice is:

$$V_{Electrostatic} = V_{Real} + V_{Reciprocal} + V_{Self} \quad \textbf{(2.17)}$$

$V_{Real}$ is given by:

$$V_{Real} = \frac{1}{2}\sum_{i=1}^{N}\sum_{j=1}^{N}\frac{q_i q_j}{r_{ij}} erfc\left(\eta^{\frac{1}{2}} r_{ij}\right) \quad \textbf{(2.18)}$$

$V_{Reciprocal}$ is given by:

$$V_{Reciprocal} = \frac{1}{2}\sum_{i=1}^{N}\sum_{j=1}^{N}\sum_{G}\frac{4\pi}{V} q_i q_j \exp(iG.r_{ij})\frac{\exp\left(\frac{-G^2}{4\eta}\right)}{G^2} \quad \textbf{(2.19)}$$

$V_{Self}$ is given by:

$$V_{Self} = -\sum_{i=1}^{N} q_i^2 \left(\frac{\eta}{\pi}\right)^{\frac{1}{2}} \quad \textbf{(2.20)}$$

$q$ is the charge of an ion, $G$ is the reciprocal lattice vector, $V$ is the volume of the unit cell and $\eta$ is a constant controlling the calculations between real and reciprocal space. Calculation of the Ewald sum is constrained to cut-off radii in real and reciprocal space. These cut-off distances are chosen to for a required accuracy ($A$),

whilst minimising the number of terms to calculate. Hence, the following expressions are used:

$$\eta_{opt} = \left(\frac{Nw\pi^3}{V}\right)^{\frac{1}{3}} \quad \textbf{(2.21)}$$

$w$ is a weight parameter, representing the relative computational expense of calculations of the real and reciprocal space terms. The cut-off in real space is given by:

$$r_{max} = \left(\frac{-lnA}{\eta}\right)^{\frac{1}{2}} \quad \textbf{(2.22)}$$

The cut-off in reciprocal space is given by:

$$G_{max} = 2\eta^{\frac{1}{2}}(-lnA)^{\frac{1}{2}} \quad \textbf{(2.23)}$$

For surface modelling, the electrostatic contribution to the surface energy is calculated using the method developed by Parry [57] which is analogous to the Ewald summation, but modified for two-dimensional periodic, semi-infinite systems.

## 2.4 Energy Minimisation

### 2.4.1 Background

Structure determination in atomistic simulations requires energy minimisation of the total potential energy, or more generally the potential energy surface (PES or $\boldsymbol{V}(\boldsymbol{x})$) [58, 59], where the net forces acting in the system are zero. The PES is a multi-dimensional surface of the potential energy of a system of particles. In three dimensions, for a system consisting of $N$ particles with three degrees of freedom, the PES has $3N$ dimensions, with each atom having a position defined by three orthogonal axes; $x$, $y$ and $z$. Hence, the PES is a function of $x_1$, $x_2$……$x_{3N}$ coordinates, where $\boldsymbol{x} = (x_1, x_2 \ldots\ldots x_{3N})^{\boldsymbol{T}}$. (The superscript $T$ means transposition of the matrix, i.e. swapping of rows and columns).

Numerous search methods are available to characterise the PES to determine stationary points and hence physical properties. These points consist of minima, maxima or saddle points. The minima are of greatest interest, with the lowest or 'global' minimum corresponding to observable structures. There are minimisation methods that use the derivatives of the PES, which include the Newton-Raphson method and the conjugate gradient method. Such methods are iterative schemes to finding the minima which differ by the calculation of the search vector ($\boldsymbol{d}$) and step length ($\alpha$) at each step in the search. The search of the PES is defined in discrete steps from position $\boldsymbol{x_k}$ at step $k$ to $\boldsymbol{x_{k+1}}$ at step $k+1$ and is given by:

$$\boldsymbol{x_{k+1}} = \boldsymbol{x_k} + \alpha_k \boldsymbol{d_k} \tag{2.24}$$

$\boldsymbol{d_k}$ is the search vector at step $k$, and $\alpha_k$ is the step length. Hence, the step displacement vector ($\Delta\boldsymbol{x}$) is given by:

$$\Delta \boldsymbol{x} = \boldsymbol{x_{k+1}} - \boldsymbol{x_k} = \alpha_k \boldsymbol{d_k} \tag{2.25}$$

Two important parameters are the gradient vector ($\boldsymbol{g}$) and the Hessian matrix, ($\boldsymbol{H}$) which are calculated during the search procedure. $\boldsymbol{g}$ is the gradient of the PES given by:

$$\boldsymbol{g} = \boldsymbol{\nabla V}(\boldsymbol{x}) = \left(\frac{\partial \boldsymbol{V}}{\partial \boldsymbol{x_1}}, \frac{\partial \boldsymbol{V}}{\partial \boldsymbol{x_2}} \dots \dots \frac{\partial \boldsymbol{V}}{\partial \boldsymbol{x_{3N}}}\right)^{\boldsymbol{T}} \tag{2.26}$$

The vector $-\boldsymbol{g}$ points in the direction of the maximum rate of decrease of the potential energy towards a minimum on the PES, where $\boldsymbol{\nabla V}(\boldsymbol{x})$ is zero and thus the net force on the particles is zero. The Hessian matrix ($\boldsymbol{H}$) is the matrix of second derivatives of the PES. For a realistic PES with continuous second derivatives, then $\boldsymbol{H}$ is a real, symmetric $3N \times 3N$ matrix, given by:

$$\boldsymbol{H} = \begin{pmatrix} \frac{\partial^2 \boldsymbol{V}}{\partial \boldsymbol{x_1^2}} & \cdots & \frac{\partial^2 \boldsymbol{V}}{\partial \boldsymbol{x_1 \partial x_n}} \\ \vdots & \ddots & \vdots \\ \frac{\partial^2 \boldsymbol{V}}{\partial \boldsymbol{x_n \partial x_1}} & \cdots & \frac{\partial^2 \boldsymbol{V}}{\partial \boldsymbol{x_{3N}^2}} \end{pmatrix} \tag{2.27}$$

The process of diagonalization of $\boldsymbol{H}$ yields its eigenvectors and corresponding eigenvalues. The eigenvalues characterise stationary points on the PES,

which consist of minima, maxima or saddle points. At minima, $\boldsymbol{H}$ contains no negative eigenvalues. At maxima, $\boldsymbol{H}$ contains no positive eigenvalues. For a saddle point of order $n$, $\boldsymbol{H}$ contains $n$ negative eigenvalues corresponding to maxima in $n$ degrees of freedom. A special type of saddle point is a first order transition state, where $\boldsymbol{H}$ contains a single negative eigenvalue corresponding to a maximum in one degree of freedom.

To characterise a PES, derivative minimisation methods are used. The PES can be expressed as in vector notation as an infinite Taylor series and derivative based search methods are used to characterise it [59]. For the potential function ($\boldsymbol{V}(\boldsymbol{x})$) evaluated about an arbitrary point in configuration space labelled $a = (a_x, a_y, a_z)$ in three dimensions, the series is the following:

$$\boldsymbol{V}(\boldsymbol{x}) = \boldsymbol{V}(\boldsymbol{a}) + \boldsymbol{\nabla V}(\boldsymbol{a})^T(\boldsymbol{x}-\boldsymbol{a}) + \frac{1}{2}(\boldsymbol{x}-\boldsymbol{a})^T\boldsymbol{H}(\boldsymbol{a})(\boldsymbol{x}-\boldsymbol{a}) + \cdots \qquad \textbf{(2.28)}$$

In practice, this series is truncated so only the dominant terms are included in calculations to a required level of accuracy and efficiency. The PES is quadratic near a minimum. However, this may not be a global minimum, depending on the nature of the PES and the minimisation method used. An energy minimum is located when certain convergence criteria have been met e.g. that the maximum deviation in the gradient is less than a certain threshold.

### 2.4.2 The Conjugate Gradient Method

The conjugate gradient method [59] is a first order minimisation algorithm, as it uses only first derivatives in the minimisation process. The search vector ($\boldsymbol{d_k}$) at each step is given by:

$$\boldsymbol{d_k} = -\boldsymbol{g_k} + \frac{\boldsymbol{g_k^T}\cdot(\boldsymbol{g_k}-\boldsymbol{g_{k-1}})}{\boldsymbol{g_{k-1}^T}\cdot\boldsymbol{g_{k-1}}}\boldsymbol{d_{k-1}} \qquad \textbf{(2.29)}$$

In this method, successive gradients and search vectors are orthogonal. Calculation of $\boldsymbol{d_k}$ includes the search vector and derivative from the previous step in addition to the

current step. All this helps to ensure this method is efficient for large-scale problems, requiring a modest storage requirement. In addition, it is a useful method for locating a minimum when the initial configuration is far from an energy minimum. However, it is less efficient near a minimum, where the Newton Raphson method is more suitable.

### 2.4.3 The Newton Raphson Method

The Newton Raphson method [59] is a second order minimisation algorithm, as it uses first and second derivatives in the minimisation process. The search vector ($\boldsymbol{d_k}$) at each step is given by:

$$\boldsymbol{d_k} = -\boldsymbol{H_k}^{-1}\boldsymbol{g_k} \qquad \textbf{(2.30)}$$

$\boldsymbol{H_k}^{-1}$ is the inverse Hessian matrix calculated at step $k$ in the search. This result is derived from applying a quadratic description to the PES, where the Taylor series about a point is truncated at second order. For a quadratic function (i.e. near a minimum), this method will locate the minimum in one-step.

However, this method is less efficient when the initial configuration is far from an energy minimum, particularly for a complicated PES. Hence, in that case the conjugate-gradient method would be more appropriate. In addition, calculation of $\boldsymbol{H^{-1}}$ is computationally expensive for all but the simplest of PES, scaling with the system size as $N^3$. In addition, $\boldsymbol{H^{-1}}$ may not vary much at each step in the search, making repeated calculation potentially wasteful.

To improve efficiency of employing the Newton Raphson method, the Broyden-Fletcher-Goldfarb-Shanno (BFGS) algorithm [60] is used. In this algorithm, the exact $\boldsymbol{H^{-1}}$ is calculated initially, and is subsequently updated over a number of steps (or cycles). The exact $\boldsymbol{H^{-1}}$ is only calculated when certain criteria have been met. These include when the number of updating cycles or the energy change in a cycle exceeds certain thresholds.

### 2.4.4 Constant Pressure Energy Minimisation

GULP uses a symmetry-adapted technique of energy minimisation [50,61], using a minimum set of variables from the space group symmetry of a crystal. Structural optimisation of the unit cell is performed, which in this work occurred at constant pressure. This involves the use of the Voigt strain tensor, which scales the lattice vectors, expressed as:

$$\begin{pmatrix} 1+\varepsilon_1 & \frac{1}{2}\varepsilon_6 & \frac{1}{2}\varepsilon_5 \\ \frac{1}{2}\varepsilon_6 & 1+\varepsilon_2 & \frac{1}{2}\varepsilon_4 \\ \frac{1}{2}\varepsilon_5 & \frac{1}{2}\varepsilon_4 & 1+\varepsilon_3 \end{pmatrix} \quad \textbf{(2.31)}$$

$\varepsilon_{1-6}$ represent the six Voigt strains. Geometry optimisation of surfaces follows an analogous procedure as for the bulk, but the Voigt strain tensor is a 2×2 matrix, which scales the surface vectors.

## 2.5 Bulk Lattice Properties

Following energy minimisation of the bulk lattice, mechanical and optical properties can be calculated using the General Utility Lattice Program (GULP) developed by Julian Gale [50,61]. Mechanical properties include elastic constants and the bulk ($B$), shear ($G$) and Young's ($Y$) moduli. Optical properties include the static and high frequency dielectric constants and the refractive index. By comparison to experimental data, these predicted properties can be used to assess and derive potentials.

### 2.5.1 Mechanical Properties

Elastic constants ($C_{ij}$) represent the second derivative of the energy density of a solid with respect to strain in different directions labelled $i$ and $j$, given by:

$$C_{ij} = \frac{1}{V}\left(\frac{\partial^2 U_{Solid}}{\partial \varepsilon_i \partial \varepsilon_j}\right) \quad \textbf{(2.32)}$$

$U_{Solid}$ is the internal energy of the solid, $V$ is the system volume and $\varepsilon_i$ and $\varepsilon_j$ are the strains in directions labelled $i$ and $j$. There are six possible strain directions, thus the 6×6 elastic constant tensor. However, the number of independent elastic constants is reduced by the crystal symmetry, with a cubic crystal having only three unique elastic constants ($C_{11}, C_{12}, C_{44}$).

The mechanical moduli are calculated from the elastic constants using the Reuss, Voigt and Hill definitions [62]. In the simulations presented in this work, the Hill definition was used, which is the average of the other two. The moduli are important parameters characterising the hardness of a material. In terms of the resulting strain, the bulk modulus measures the response to applied isotropic pressure, the shear modulus that to shear stress and the Young's modulus that to uniaxial stress. For solids, typically, the moduli are of the order of 100 GPa ($10^{11}$ GPa). The compressibility is the inverse of the bulk modulus. The Poisson's ratio ($\nu$) is the ratio of orthogonal strains in response to uniaxial stress.

### 2.5.2 Optical Properties

Static and high frequency dielectric constants are calculated, which measure the optical response of a solid to an applied electromagnetic field. In the static case, both atomic nuclei and electrons are able to respond to the field, both contributing to the dielectric constant. However, in the high frequency case, only electrons are able

to respond to the field, due to the much larger mass of the nuclei. These dielectric constants are represented by a 3×3 dielectric constant tensor; which for the static case is given by:

$$\boldsymbol{\varepsilon}^{\mathbf{0}}_{\boldsymbol{\alpha\beta}} = \boldsymbol{\delta}_{\boldsymbol{\alpha\beta}} + \frac{4\pi}{V}(\boldsymbol{q}\boldsymbol{D}^{-\mathbf{1}}_{\boldsymbol{\alpha\beta}}\boldsymbol{q}) \quad \textbf{(2.33)}$$

$\boldsymbol{D}_{\boldsymbol{\alpha\beta}}$ is the positional second derivative matrix of the particles, $\boldsymbol{q}$ is a vector of charges and $V$ is the system volume. When the shell model is used for the ions, $\boldsymbol{\varepsilon}^{\mathbf{0}}_{\boldsymbol{\alpha\beta}}$ includes both the cores and the shells. This formulation is identical for the high frequency dielectric constant tensor ($\boldsymbol{\varepsilon}^{\infty}_{\boldsymbol{\alpha\beta}}$), except only the shells are used, which represent electrons. The refractive index ($n$) of a material is the square root of the dielectric constant ($\varepsilon$):

$$n = \sqrt{\varepsilon} \quad \textbf{(2.34)}$$

## 2.6 Modelling Lattice Defects

### 2.6.1 Background

All solids at a finite temperature will contain defects, which are either intrinsic or extrinsic defects [52]. Intrinsic defects are in thermodynamic equilibrium with the solid, which contain atoms or vacancies of the material. Extrinsic defects are externally added to the solid e.g. dopants in semiconductors and non-stoichiometric compounds. All solids in equilibrium at a finite temperature will contain intrinsic defects, explained by thermodynamics [52]. Thermodynamically, this can be quantified through the change in the Gibbs free energy of the solid ($\Delta G$) at constant temperature ($T$) and pressure ($P$), with respect to defect formation:

$$\Delta G = \Delta H - T\Delta S \quad \textbf{(2.35)}$$

$\Delta H$ is the change in enthalpy and $\Delta S$ is the change in configurational entropy with respect to defect formation. Hence, the total Gibbs free energy ($G$) of the solid is:

$$G = G_0 + \Delta H - T\Delta S \quad \textbf{(2.36)}$$

$G_0$ is the Gibbs free energy of the 'pure' solid. Figure 2.13 shows the variation in $G$, $\Delta H$ and $T\Delta S$ with defect concentration ($n_d$).

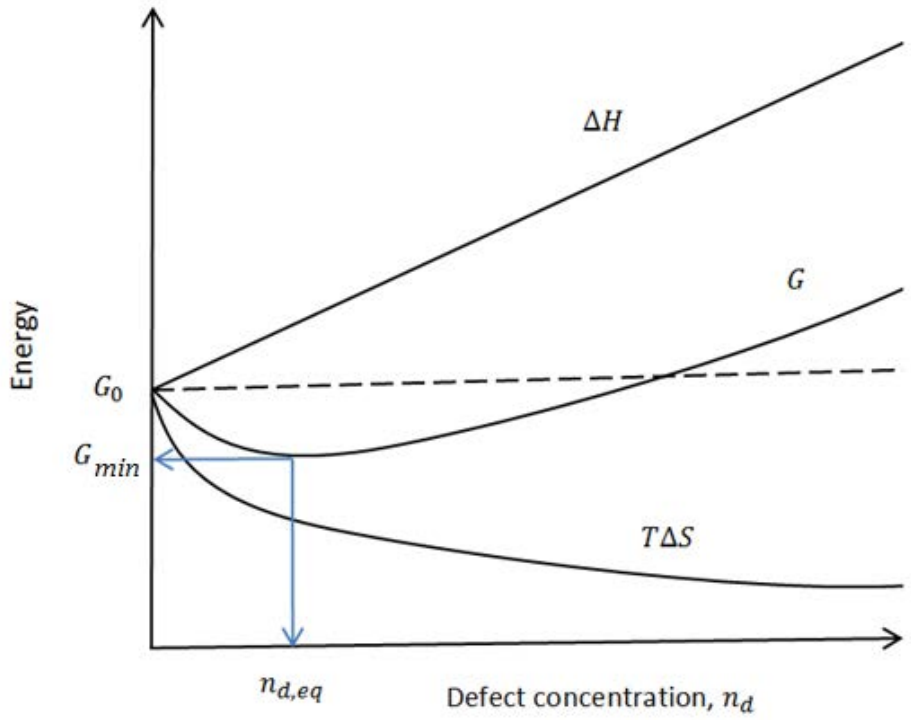


**Figure 2.13: Graph of the variation of $G$, $\Delta H$ and $T\Delta S$ as a function of defect concentration ($n_d$) for a solid.**

$\Delta H$ is usually endothermic (positive) and approximately constant with temperature and increases linearly with defect concentration ($n_d$). The change in configurational entropy ($\Delta S$) depends on the level of disorder in the solid, and is given by the Boltzmann equation for a disordered system:

$$\Delta S = k_B ln W \quad \textbf{(2.37)}$$

$k_B$ is the Boltzmann constant and $W$ is the number of ways of randomly distributing defects in available sites in the solid. However, the $T\Delta S$ term decreases (i.e. becomes more negative) with increasing defect concentration, making $\Delta G$ exothermic (negative) and defect formation spontaneous. Hence, at thermal equilibrium there is a minimum in $G$ ($G_{min}$) at an equilibrium defect concentration ($n_{d,eq}$), calculated from:

$$\left(\frac{\partial \Delta G}{\partial n_d}\right)_T = 0 \quad \textbf{(2.38)}$$

There are different types of intrinsic and extrinsic defects that can occur in solids, consisting of point defects and bound defects. These defects are summarised in Tables 2.1 and 2.2. Note there may be combinations of bound defects and point defects not included in the tables.

**Table 2.1: Summary of point defects in solids.**

| Point Defect | Description |
|---|---|
| **Vacancy** | An atom removed from the solid. |
| **Interstitial** | An atom in an interstitial site of the lattice. |
| **Antisite** | An atom occupying a site of a different atom in the material. |
| **Substitution** | An extrinsic atom occupying a crystallographic atomic site. |

**Table 2.2: Summary of bound defects in solids.**

| Bound Defect | Description |
|---|---|
| **Frenkel pair** | A displaced interstitial leaving a vacancy. |
| **Schottky** | A defect cluster of vacancies that constitutes one stoichiometric unit of the material. |

## 2.6.2 The Mott-Littleton Method

To calculate defect energies, the Mott-Littleton method [63] is widely used, and is embedded in GULP [50]. This method involves partitioning the crystal lattice in two spherical regions centred on the defect (or defect configuration); region 1 and region 2, as shown in Figure 2.14.

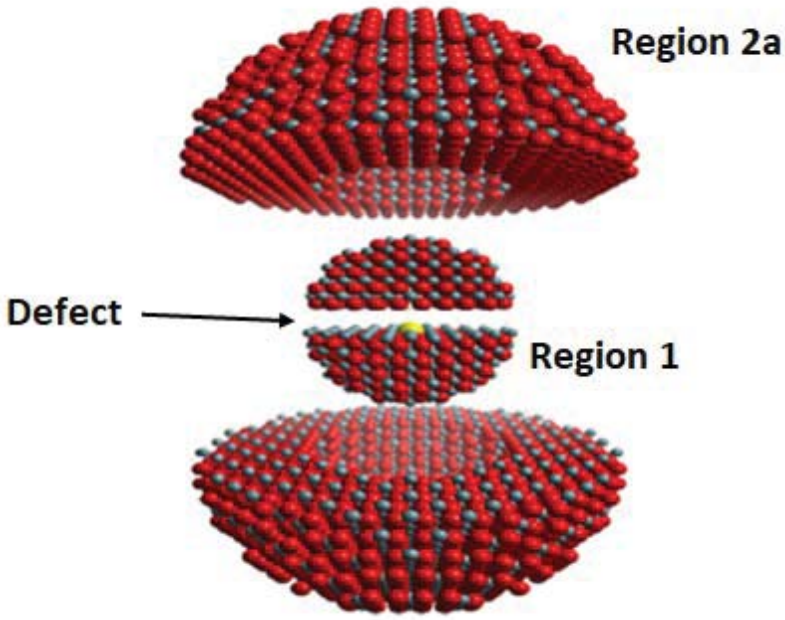


**Figure 2.14: Schematic representation of the Mott-Littleton method for modelling a bulk defect.**

The ions in these two regions are relaxed in response to the defect until their energy is minimised. Region 1 is the inner spherical region and is relaxed explicitly. Region 2 is composed of region 2a and 2b and is a classical dielectric continuum. Region 2a surrounds region 1 and region 2b extends beyond region 2a to infinity (in theory).

Region 1 is most perturbed by the defect, which is relaxed explicitly with all relevant interactions considered, until there is no net force acting on the ions. Typically, region 1 has a radius of ~1-2 nm, containing several hundred ions. Region 2 is less strongly perturbed by the defect and treated as a polarised insulating material, with contribution per ion to the bulk polarisation ($\boldsymbol{P}$) given by [52] :

$$\boldsymbol{P} = \left(1 - \frac{1}{\varepsilon_r \varepsilon_0}\right)\left(\frac{q}{4\pi \boldsymbol{r}}\right) \qquad \textbf{(2.39)}$$

$\varepsilon_r$ is the relative permittivity of the material, $q$ is the charge of the defect and $\boldsymbol{r}$ is the displacement vector of an ion. Ions in region 2 behave harmonically as a function of their displacements.

Region 2a ensures continuity between regions 1 and 2b. Typically, region 2a has a radius of ~3nm containing several thousand ions. Ions in region 2b are relaxed with only the long-range electrostatic interaction due to the charge of the defect. Hence, the radius of region 2a is greater than that of region 1 by at least the short-range potential cut-off distance. In addition, the sizes of regions 1 and 2a are determined by ensuring the defect energy is fully converged with respect to the relative region sizes. In this work, the region radii from Read et al. (2014) [64] were used. This corresponds to a region 1 radius of 14 Å and a region 2a radius of 28 Å. Regions 1 and 2a comprise of ~1600 and ~12,000 ions respectively.

Calculation of the defect formation energy ($E_D^F$) [50] is based on calculation of the defective lattice energy ($E_{Total}^{Defect}(\boldsymbol{x},\boldsymbol{y})$), which is the sum of the lattice energies of regions 1, 2a and 2b, given by:

$$E_{Total}^{Defected}(\boldsymbol{x},\boldsymbol{y}) = \boldsymbol{E_1}(\boldsymbol{x}) + \boldsymbol{E_{2a}}(\boldsymbol{x},\boldsymbol{y}) + \boldsymbol{E_{2b}}(\boldsymbol{y}) \quad \textbf{(2.40)}$$

$E_1$ is the energy of region 1, associated with the ionic displacements of coordinate vector $\boldsymbol{x}$. Similarly, $E_{2b}$ is the energy of region 2b, associated with the ionic displacements of coordinate vector $\boldsymbol{y}$. $E_{2a}$ is the energy of region 2a associated with ionic displacements of coordinate vectors $\boldsymbol{x}$ and $\boldsymbol{y}$. As the displacements in region 2b are relatively small, the harmonic approximation is valid. Hence, the energy of region 2b is given by:

$$E_{2b}(\boldsymbol{y}) = \frac{1}{2}\boldsymbol{y^T H_{2b} y} \quad \textbf{(2.41)}$$

$\boldsymbol{H_{2b}}$ is the Hessian matrix for region 2b. Assuming the ions in region 2 are in equilibrium, then:

$$\left(\frac{\partial E_{Total}^{Defected}(\boldsymbol{x},\boldsymbol{y})}{\partial \boldsymbol{y}}\right)_{\boldsymbol{x}} = \left(\frac{\partial E_{2a}(\boldsymbol{x},\boldsymbol{y})}{\partial \boldsymbol{y}}\right)_{\boldsymbol{x}} + \boldsymbol{H_{2b}}\boldsymbol{y} = 0 \quad \textbf{(2.42)}$$

Substitution of equation (2.35) into equation (2.33) gives the defective lattice energy as:

$$E_{Total}^{Defected}(\boldsymbol{x},\boldsymbol{y}) = E_1(\boldsymbol{x}) + E_{2a}(\boldsymbol{x},\boldsymbol{y}) - \frac{1}{2}\left(\frac{\partial E_{2a}(\boldsymbol{x},\boldsymbol{y})}{\partial \boldsymbol{y}}\right)_{\boldsymbol{x}} \boldsymbol{y} \quad \textbf{(2.43)}$$

Clearly, by only considering explicitly the ions in region 1 and region 2a, and not in region 2b, the defect calculation is more efficient. The defect formation energy ($E_D^F$) is given by the difference in the defected and pure lattice energies:

$$E_D^F = \mathrm{E}_{Total}^{Defected}(\boldsymbol{x},\boldsymbol{y}) - \mathrm{E}_{Total}^{Pure}(\boldsymbol{x},\boldsymbol{y}) \quad \textbf{(2.44)}$$

### 2.6.3 The Supercell Method

The supercell method is an alternative approach to modelling defects to the Mott-Littleton method. In this method, a supercell (grown from the unit cell) is generated and energy minimised to determine the optimal geometry. To calculate defect energies, a defect is inserted in the centre of the supercell, which is subsequently energy minimised. The defect formation energy is calculated as the difference in the internal energies of the defective and pure supercells.

To ensure the defect energy is converged, the supercell needs to be of a sufficient size. Hence, convergence testing is required by analysing the defect energy as a function of supercell size. The converged defect energy should agree with the value from using the Mott-Littleton method for a bulk defect calculation. A benefit of using the supercell method is that one can investigate concentration effects by varying the size of the supercell or the number of defects incorporated. However, in practice, the Mott-Littleton method may be more efficient, depending on the region sizes required.

## 2.7 Modelling Surfaces

### 2.7.1 Types of Surfaces

Simulations of surfaces predict a range of surface properties including surface energy, structure and morphology. There are three types of surfaces, which have a net charge, $Q$ and dipole moment, $\mu$ [50,65]. Type 1 surfaces consist of layers of coplanar anions and cations and, therefore, have zero charge and zero dipole moment. Typically, type 1 surfaces are the lowest energy and stable surfaces, and are most likely to be observed.

Type 2 surfaces consist of layers where the ions are not coplanar, but certain surfaces can be cleaved from the bulk which are non-polar (have no dipole moment), but may have a charge. To obtain a zero dipole, the surface is reconstructed. Finally, type 3 surfaces consist of alternating layers of anions and cations. These surfaces are polar (have a dipole moment) and have a charge. Hence, type 3 surfaces are relatively high energy, unstable surfaces and are unlikely to be observed. The structures of these three types of surface are shown in Figure 2.15.

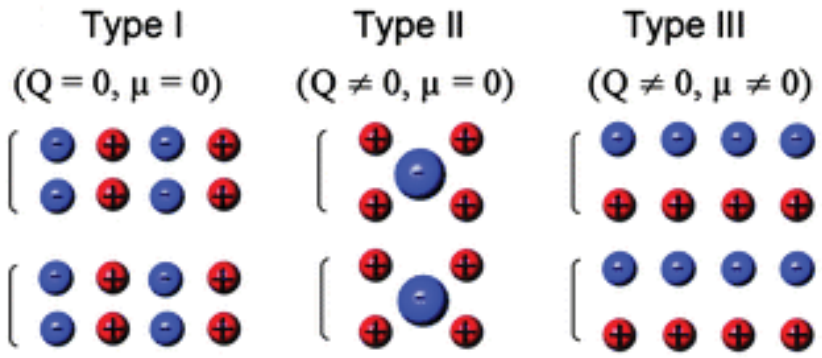


**Figure 2.15: Schematic diagrams of the three types of surfaces [66].**

### 2.7.2 Modelling Pure Surfaces

All surface simulations presented in this work use the Minimum Energy Techniques Applied to Dislocations, Interface and Surface Energies (METADISE) program developed by Watson et al. (1996) [67]. A crystallographic surface is represented by Miller indices $(h, k, l)$ and identified as a plane in the crystallographic unit cell of a crystal. To model a particular surface, the unit cell of the crystal is cleaved and then it is replicated periodically in two dimensions.

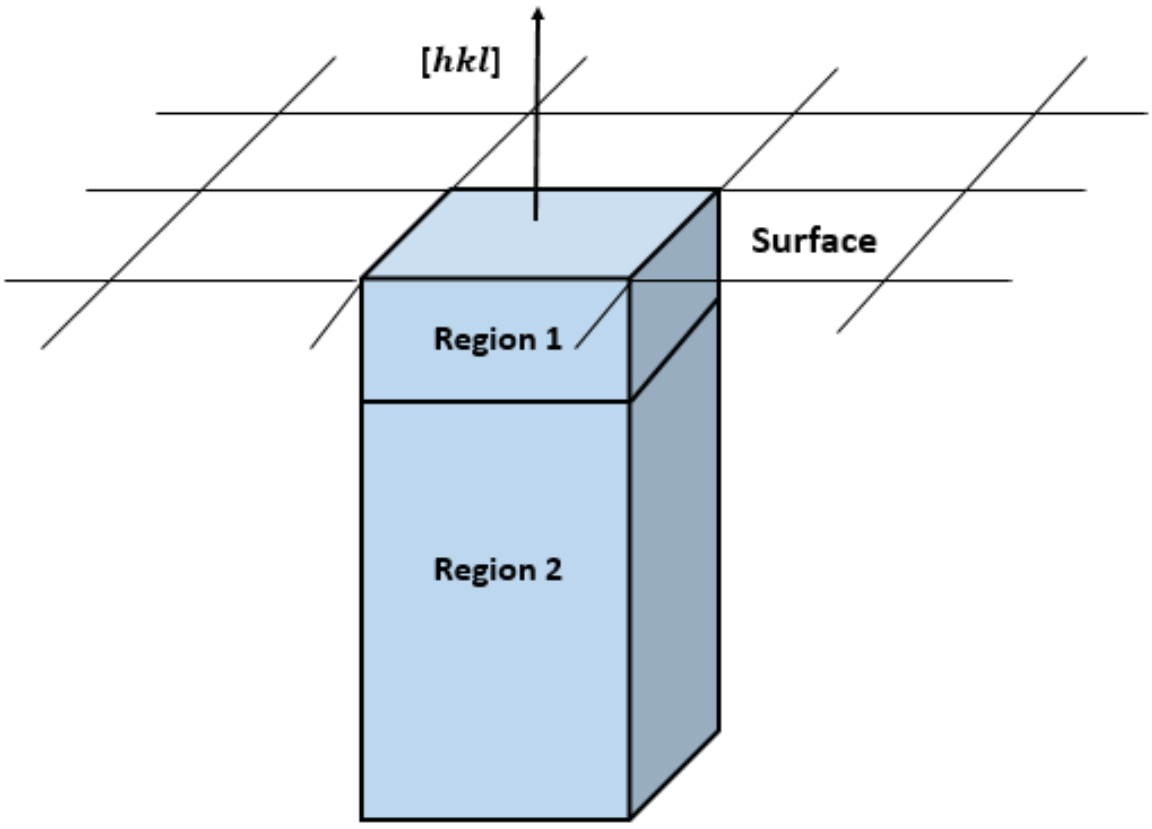


**Figure 2.16: Schematic representation of a surface.**

Figure 2.16 shows a simple representation of a surface. Region 1 represents the surface layers, with region 2 representing the bulk lattice. These regions consist of stacks of planes parallel to the surface. The total energy of the crystal is the sum of the lattice energies of the two regions given by [67]:

$$E_{Total} = E_1 + E_2 \quad \textbf{(2.45)}$$

An alternative expression includes the boundary interaction energy between the two regions, $E_{12}$ and $E_{21}$, given by:

$$E_{Total} = E_{11} + E_{12} + E_{22} + E_{21} \quad \textbf{(2.46)}$$

where $E_{12} = E_{21}$ and $E_{11}$ (or $E_{Surface}$) represents the energy of the ions in region 1, and $E_{22}$ (or $E_{Bulk}$) represents the energy of ions in region 2.

As region 2 represents the bulk crystal below a particular surface, $E_{22}$ is independent of the surface modelled and is constant. Energy minimisation of the surface is applied only to region 1, to obtain the relaxed surface energy and geometry optimised surface. The electrostatic contribution to the surface energy is calculated using the method developed by Parry [57] which is analogous to the Ewald summation, but is modified for two-dimensional periodic, semi-infinite systems. The depths of regions 1 and 2 are determined by ensuring the surface energy is fully converged with respect to the relative region sizes. In the simulations presented, the ratio of the depths of regions 1 to region 2 is 1:4.

### 2.7.3 Surface Energies

The specific surface energy ($\gamma$) is defined as the energy per unit area required to cleave a surface from the bulk crystal and is a measure of surface stability. The specific surface energy is calculated using the following equation [67]:

$$\gamma = \frac{E_{Surface} - \frac{1}{2}E_{Bulk}}{A} \quad \textbf{(2.47)}$$

$E_{Surface}$ is the surface energy of region 1 and $E_{Bulk}$ is the energy of region 2 and $A$ is the surface area. The factor of a half is due to the fact there are twice as many ions in region 2 compared to region 1. The surface energy is calculated as either the relaxed energy ($E_{Surf}^{Rel}$) or unrelaxed energy ($E_{Surf}^{Unrel}$), the former corresponding to the energy minimised surface.

There are two values calculated for the unrelaxed surface energy based on different interpretations by Hartman and Gibbs. Hartman (1989) [68] stated that the unrelaxed surface energy is calculated by considering two separate slices of the crystal for a surface. The slice energy is the chemical energy released when converting vapour to a crystal surface slice [69]. For a fixed number of sub-slices in each slice, the unrelaxed surface energy is the sum of their energies, which is divided by the surface area to obtain the specific (unrelaxed) surface energy.

Gibbs defined the (unrelaxed) surface energy as the 'surface excess' per unit area of surface. The surface excess is the difference in the energies of the ions at the surface relative to their energy in the bulk. An additional parameter of a surface is the attachment energy ($E_{Surf}^{Attach}$). The attachment energy is the chemical energy released when an additional slice of the $d$ spacing (interplanar spacing of identical planes) of the crystal is added onto the crystal surface from infinity [69].

### 2.7.4 Modelling Defective Surfaces

Simulations of defective surfaces involve calculation of surface defect energies and structural properties. This is performed using the CHAOS code [70] embedded in the METADISE program. This employs the Mott-Littleton method applicable to surfaces, thus adopting a two-region approach [71]. This is shown schematically in Figure 2.17, which depicts the CHAOS regions 1 and 2a centred on a defect, within region 1 of the surface.

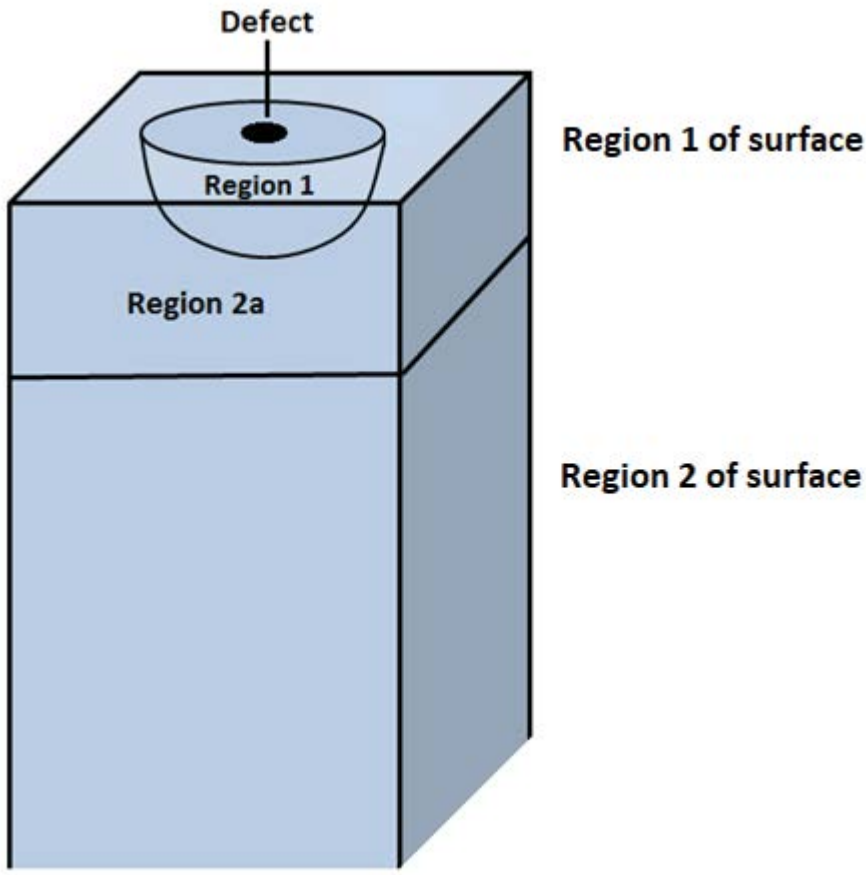


**Figure 2.17: Schematic representation of modelling a surface defect.**

For deeper surface defects, these regions would become more spherical, becoming spherical for a bulk defect. Typically, convergence testing of the defect energy is performed to determine the optimal region 1 and 2a radii. In the simulations presented, the region 1 radius is 9 Å and the region 2a radius is 35 Å.

To model a defect, initially the relaxed pure surface is modelled and then a defect is added in region 1 of the surface in the centre of the hemispheres. Subsequently, the surface is relaxed in response to the defect, with region 1 explicitly relaxed following the Mott- Littleton procedure. The defect formation energy is calculated as the difference in lattice energies of the defective and pure surfaces. In general, for charged defects, this energy is corrected due to a spurious electrostatic potential created from the surface relaxation.

### 2.7.5 Crystal Morphology

The crystal morphology describes the topology of a crystal of importance to crystals in equilibrium and crystal growth. From surface simulations, the surface energies calculated were used to predict the crystal equilibrium morphology, allowing comparison to experimental data. This is achieved through a Wulff construction [72, 71], which states that that the equilibrium crystal shape is obtained when there is minimal total surface energy for a fixed volume, such that:

$$\gamma_{Total} = \sum_i \gamma_i A_i = C_{min,const\,Vol} \quad \textbf{(2.48)}$$

$\gamma_i$ is the specific surface energy and $A_i$ is the area of the $i^{th}$ crystallographic face. In the Wulff construction, a normal vector ($\boldsymbol{h_i}$) to the corresponding surface is drawn from the crystallite centre for all relevant surfaces. The magnitude of this vector is proportional to the surface energy, such that:

$$h_i = \lambda \gamma_i \quad \textbf{(2.49)}$$

$\lambda$ is a constant of proportionality. Subsequently, tangents to these vectors are made and the inner envelope of these gives the equilibrium crystal shape. However, this approach does not consider kinetic factors such as growth rate, and is limited to growth of small crystals. To predict the crystal growth morphology, the same method is followed, but using the modulus of the surface attachment energies instead

of the surface energies. This ensures surfaces with the least exothermic attachment energies dominate the growth morphology. This considers kinetic factors as those surfaces with the highest rate of growth are least expressed in the crystal growth morphology.

## 2.8 Molecular Dynamics

### 2.8.1 Background

In order to model a system of thousands of interacting particles, the PES can become complicated so approximations are made and special methods are used. Molecular dynamics is one such method [73], which predicts time-averaged system properties, based on classical mechanics. Fundamentally, system properties at a given time ($t$) will depend on the positions ($\boldsymbol{r}$) and momenta ($\boldsymbol{p}$) of the system's particles. These particles, which are atoms or molecules, interact through forces and have an acceleration in accordance with Newton's second law, given by:

$$\boldsymbol{F} = \frac{d\boldsymbol{p}}{dt} \tag{2.50}$$

$\boldsymbol{F}$ is the net force acting on a particle of mass $m$. The derivative is the rate of change of the particles linear momentum, equal to its acceleration. Hence, over time, the particles will follow a trajectory in a $6N$ dimensional phase space, with $3N$ positional components and $3N$ momentum components. The force is the negative derivative of the potential ($V$) with respect to position, given by:

$$\boldsymbol{F} = -\frac{\partial \boldsymbol{V}}{\partial \boldsymbol{r}} \tag{2.51}$$

The forces experienced by the particles cause movement and each particle has an equation of motion. Molecular dynamics involves numerical integration over time of the particles equations of motion and, hence, prediction of the particles

trajectories in phase space. From this, system time-averaged properties are calculated. Calculations are split up into time steps ($\Delta t$) which are between ~1 and 10 femto ($10^{-15}$) seconds. Typically, the time scales for molecular dynamics simulations are between ~10 and 1000 pico ($10^{-12}$) seconds and the length scales are between ~1 and 10 nano ($10^{-9}$) metres. For a given property $A$, the expectation (average) value ($< A >$) from a simulation of $M$ time steps is given by [55]:

$$< A > = \frac{1}{M} \sum_{i=1}^{M} A(\boldsymbol{p^N}, \boldsymbol{r^N}) \quad \textbf{(2.52)}$$

This approximates the true time average from statistical mechanics or experiments, as only part of the phase space is explored in a simulation. The true time average from an experiment is:

$$< A > = \lim_{t \to \infty} \frac{1}{t} \int_{t=0}^{\infty} A(\boldsymbol{p^N}, \boldsymbol{r^N}) \; dt \quad \textbf{(2.53)}$$

Typically, the system is equilibrated to reach the desired temperature for example, and this is followed by a production phase, from which average properties are obtained.

## 2.8.2 Ensembles

In statistical mechanics, an ensemble represents a collection of particles in a given macrostate with an associated probability. There are four commonly used ensembles in molecular dynamics, depending on what macrostate the system is in. For a given ensemble, certain physical quantities are fixed and others vary over time. In statistical mechanics, the expectation value of a given property is given by [55]:

$$< A > = \iint \boldsymbol{dp^N dr^N} A(\boldsymbol{p^N}, \boldsymbol{r^N}) \rho(\boldsymbol{p^N}, \boldsymbol{r^N}) \quad \textbf{(2.54)}$$

This integral is over all $6N$ dimensions of phase space. $\rho(\boldsymbol{p^N}, \boldsymbol{r^N})$ is the probability density of the ensemble, which is the probability per unit volume that the ensemble is in a given macrostate. Providing this integral covers all the possible configurations of the ensemble, and then the ensemble average is equal to the time

average of the property, which is the ergodic hypothesis. Depending on the ensemble, at equilibrium, a thermodynamic property will be minimised or maximised. Table 2.3 summarises the properties of these ensembles.

**Table 2.3: Summary of properties of ensembles used in molecular dynamics [55].**

| Ensemble | Fixed Quantities | At Equilibrium |
|---|---|---|
| **Micro-canonical ($NVE$)** | Particle number ($N$), volume ($V$), energy ($E$) | Maximise entropy ($S$) |
| **Canonical ($NVT$)** | Particle number ($N$), volume ($V$), temperature ($T$) | Minimise Helmholtz free energy ($F$) |
| **Isothermal-isobaric ($NPT$)** | Particle number ($N$), pressure ($P$), temperature ($T$) | Minimise Gibbs free energy ($G$) |
| **Grand canonical ($\mu VT$)** | Chemical potential (μ), volume ($V$), temperature ($T$) | Maximise product ($PV$) |

In simulations, approximations are made to calculate the ensemble or time averages of a given property. In practice, sampling of the possible configurations in phase space is performed to estimate the average. In a molecular dynamics simulation, there are replications of an ensemble made and the system evolves over time, with ensemble averages calculated. Only the micro-canonical ($NVE$) and isothermal-isobaric ensemble ($NPT$) ensembles were used in the simulations presented.

In the micro-canonical ensemble ($NVE$) ensemble, the particle number ($N$), system volume, ($V$) and energy ($E$) are constant, but other properties including system temperature and pressure vary over time. Molecular dynamics simulations using this ensemble generate particle trajectories of constant energy. Hence, the systems total energy, or Hamiltonian ($\mathcal{H}$) is conserved, which is given by the sum of the systems kinetic energy ($E_{K.E.}$) and potential energy ($E_{P.E.}$):

$$\mathcal{H}(t, \boldsymbol{r^N}, \boldsymbol{p^N}) = E_{K.E.}(t, \boldsymbol{p^N}) + E_{P.E.}(t, \boldsymbol{r^N}) \quad \textbf{(2.55)}$$

The kinetic energy is dependent on the momenta of the particles ($\boldsymbol{p}^N$). The potential energy is dependent on the positions of the particles ($\boldsymbol{r}^N$). As the system evolves over time, there is exchange of potential energy and kinetic energy, with the total energy conserved.

In the isothermal-isobaric ($NPT$) ensemble, the particle number ($N$), system pressure ($P$) and system temperature ($T$) are constant, but other properties including system volume and energy vary over time. However, to maintain constant pressure and temperature, special procedures are performed throughout the simulations. This is particularly important during equilibration of the system to achieve the target temperature and pressure. In this ensemble, the Gibbs free energy ($G$) is conserved.

### 2.8.3 Periodic Boundary Conditions

Molecular dynamics aims to calculate system properties that are representative of a macroscopic sample, and so is comparable to experiments. It achieves this by using periodic boundary conditions (PBC) [55], whereby the simulation cell is replicated periodically in three dimensions to represent the bulk system. The simulation cell of the system can be four different shapes; a cube, a truncated octahedron, a hexagonal prism or a rhombic dodecahedron. The choice of shape will depend on the geometry of the system.

PBC in three dimensions for a cubic system is shown in Figure 2.18. Using PBC, the particles in the central simulation cell are conserved. Hence, when particles move outside the simulation cell (the blue spheres), identical 'images' reappear in the simulation cell. However, one has to ensure particles do not interact with their images, by ensuring the simulation cell size is at least twice the cut-off of the short-range potentials.

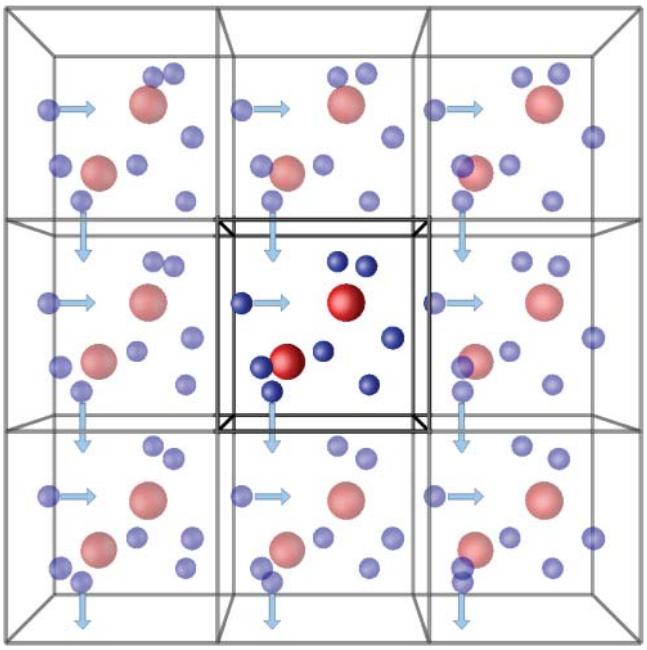

**Figure 2.18: Schematic representation of PBC in three dimensions [74].**

### 2.8.4 Integration Algorithm

Molecular dynamics involves evolving a system of particles under the influence of potentials which means their motions are coupled. It is not possible for particle trajectories to be calculated analytically, so their equations of motion are numerically integrated over time using an integration algorithm. A finite difference method is employed [73], where the calculations are split into time intervals.

At a given time $t$, calculation of the net force on a particle allows calculation of its acceleration, using Newton's second Law. The acceleration is fixed over the time step ($\Delta t$). Knowing the position and velocity at time $t$, combined with the acceleration, allows the velocities and positions at time step $t + \Delta t$ to be calculated. This process is repeated at subsequent time steps to construct trajectories of the particles. In a similar way, this method works backwards in time as well, making the method time-

reversible. There are different types of integration algorithms, and choice will depend on considerations of computational efficiency and accuracy.

A commonly used integration algorithm is the velocity Verlet algorithm [75]**.** To calculate the particles positions and velocities from time $t$ to $t + \Delta t$, the calculation is performed in three stages. The first stage requires the particles position ($\boldsymbol{r}$), velocity ($\boldsymbol{v}$), and force, ($\boldsymbol{F}$) at time $t$. The velocity at time $t + \frac{\Delta t}{2}$ is calculated using the particles velocity and acceleration ($\boldsymbol{a}$) at time $t$ given by the equation:

$$\boldsymbol{v}\left(t + \frac{\Delta t}{2}\right) = \boldsymbol{v}(t) + \boldsymbol{a}(t)\frac{\Delta t}{2} \quad \textbf{(2.56)}$$

Hence, the particles position is calculated using $\boldsymbol{v}\left(t + \frac{\Delta t}{2}\right)$:

$$\boldsymbol{r}(t + \Delta t) = \boldsymbol{r}(t) + \boldsymbol{v}\left(t + \frac{\Delta t}{2}\right)\Delta t \quad \textbf{(2.57)}$$

In the second stage, recalculation of the forces and hence acceleration is performed at time $t + \Delta t$ due to the change in particles positions. Finally, in the third stage, the velocity at time $t + \Delta t$ is:

$$\boldsymbol{v}(t + \Delta t) = \boldsymbol{v}\left(t + \frac{\Delta t}{2}\right) + \boldsymbol{a}(t + \Delta t)\frac{\Delta t}{2} \quad \textbf{(2.58)}$$

## 2.8.5 Incorporation of Shells

To incorporate the shells of polarisable ions in molecular dynamics, there are essentially two main approaches used. One is the 'dynamical' or 'adiabatic shell model' [76], where the shells of an ion species are assigned a mass. This allows a dynamical description of the shells, which would obey Newton's laws. The core-shell frequency ( $\nu_{core-shell}$) is given by:

$$\nu_{core-shell} = \frac{1}{2\pi}\left(\frac{k_2}{x(1-x)m}\right)^{1/2} \quad \textbf{(2.59)}$$

$x$ is the fraction of the atomic mass ($m$) assigned to the shells and $k_2$ is the core-shell harmonic spring constant. $x(1-x)m$ is the reduced mass of the core-shell unit. $x$ is determined by ensuring that $\nu_{core-shell}$ is at least a factor of three larger than the rigid-ion vibrational frequency in the bulk lattice. This ensures there is minimal exchange of kinetic energy between the core-shell units and the surrounding bulk lattice (hence 'adiabatic').

The alternative approach is the 'relaxed shell model' [77] , where the shells have zero mass, and hence do not follow Newton's equations. The shells respond instantaneously to the cores, such that the net force on the shells is zero. In practice, the shell configurations are relaxed (energy minimised) at each time-step in a simulation, by use of the conjugate gradient method. In this work, this particular approach was used in DL_POLY when core-shell potentials were implemented. However, incorporation of shells in molecular dynamics increases the computational expense considerably compared to using rigid-ions, which are more commonly used.

### 2.8.6 System Pressure and Temperature

The viral ($W$) equation is used to calculate the pressure of a system in molecular dynamics [55]. The virial is the expectation (average) value of the scalar product of the force acting on the particles and their position. The virial theorem states that for a system of $N$ particles in equilibrium at temperature $T$, the virial is conserved according to the following equation:

$$W = \langle \sum_1^N \boldsymbol{F}.\boldsymbol{r} \rangle = -3Nk_BT \qquad \textbf{(2.60)}$$

$\boldsymbol{F}$ is the force acting on a particle and $\boldsymbol{r}$ is the positon of the particle, with the angled brackets indicating the expectation value. The virial is composed of two parts, and assuming pairwise interactions, is given by:

$$W = -3PV + \sum_i^N \sum_{j>i}^N F_{ij}.r_{ij} = -3Nk_BT \qquad \textbf{(2.61)}$$

$P$ is the instantaneous pressure of the system, $V$ is the volume and $F_{ij}$ is the force acting between two particles $i$ and $j$, separated by distance $r_{ij}$. Rearranging this equation gives the system pressure as:

$$P = \frac{1}{V}[Nk_BT - \frac{1}{3}W] \quad \textbf{(2.62)}$$

Hence:

$$P = \frac{2E_{K.E.} - W}{3V} \quad \textbf{(2.63)}$$

During a molecular dynamics simulation, the forces are routinely calculated and the virial and the instantaneous pressure of the system are calculated. In constant pressure simulations, the pressure is controlled by a barostat used in a number of different algorithms.

The system temperature is directly calculated from the kinetic energy of the system [55]. The instantaneous temperature at a given time $t$ ($T(t, \boldsymbol{p^N})$) is calculated from the kinetic energy using the equipartition theorem:

$$T(t, \boldsymbol{p^N}) = \frac{2}{k_B f} E_{K.E.}(t, \boldsymbol{p^N}) \quad \textbf{(2.64)}$$

$k_B$ is the Boltzmann constant and $f$ is the number of degrees of freedom of the system. For an unconstrained three dimensional, periodic system of $N$ particles, $f = 3N - 3$. Three degrees of freedom are subtracted to ensure the system has zero net linear momentum. Typically, during equilibration, the particle velocities are scaled repeatedly after a number of time steps. The velocities calculated are scaled by a scaling factor ($s$) defined by the ratio of target temperature ($T_{target}$) to the calculated temperature, ($T_{calculated}$) at time $t$:

$$s = \frac{T_{target}}{T_{calculated}} \quad \textbf{(2.65)}$$

Hence the kinetic energy of the system during equilibration is given by:

$$E_{K.E.}(t, \boldsymbol{p^N}) = \frac{1}{2}\sum_{i=1}^{N} m_i s v_i^2 \quad \textbf{(2.66)}$$

During equilibration, the velocities are scaled repeatedly after a number of time-steps. In fixed temperature simulations, a thermostat controls the temperature, using one of a number of different algorithms.

To maintain a constant temperature, the system is coupled to a heat bath, allowing energy exchange, which is controlled by a thermostat and the velocities of the particles are scaled. To maintain constant pressure, the system volume is varied, which is controlled by a barostat. There are special algorithms used in molecular dynamics to maintain constant temperature and pressure. In such algorithms, the equations of motion of the particles are modified depending on various parameters.

These parameters include properties of the system e.g. kinetic energy and properties of the thermostat and barostat. In the work presented, the Nose-Hoover algorithm [78] is used for the isothermal-isobaric ensemble. An important parameter is the relaxation times of the thermostat and barostat used, which are typically between ~0.5 and 2 ps. These are characteristic times for the temperature and pressure fluctuations during a simulation. Having modified the particles equations of motion, the changes are then implemented in a velocity integration algorithm to evolve the system.

### 2.8.7 The Radial Distribution Function

From molecular dynamics simulations, the radial (or pair) distribution function ($g(r)$) can be determined for the system for solids, liquids and gases. This parameter gives structural information on the atomic scale. It gives the relative probability of finding two particles separated by a distance between $r$ and $r + dr$ in the system [55], as shown in Figure 2.19.

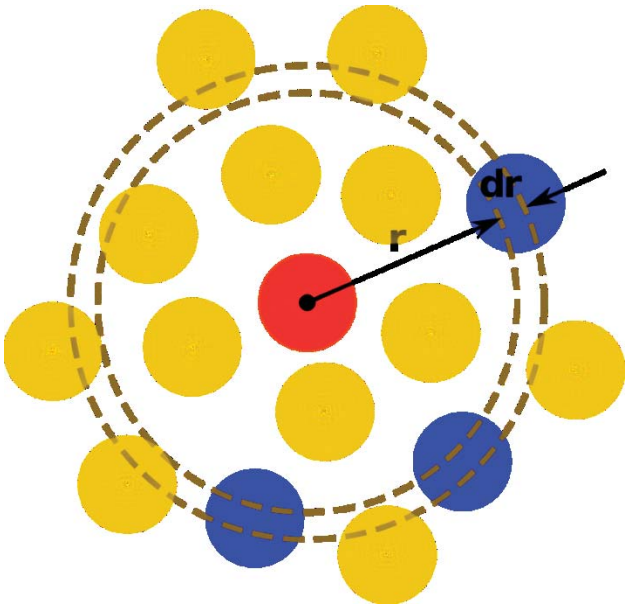


**Figure 2.19: Diagram showing a spherical shell of particles for calculation of $g(r)$[79].**

For a spherical shell of radius $r$ and width $dr$ centred on a given particle, the number of particles in the shell is given approximately by:

$$N_{Shell} \approx 4\pi\rho r^2 dr \qquad \textbf{(2.64)}$$

$\rho$ is the number density of particles in the shell. $g(r)$ is then calculated as the ratio of $N_{Shell}$ to the number in the case of an ideal gas (where $g(r)$ is unity for $r$ greater than zero). Calculations of $g(r)$ are used to obtain structural and dynamical information about the system. The peaks of $g(r)$ spectra correspond to peaks in a diffraction pattern, with the area beneath each peak equal to the number of neighbouring particles. Furthermore, the widths of the peaks reflect dynamical properties of the system.

Furthermore, $g(r)$ spectra are related to neutron and x-ray diffraction data by a Fourier transform, enabling comparison to experimental data. $g(r)$ spectra are characteristic of the state of matter of a material. For crystalline solids, they consist of many relatively narrow peaks, whereas for liquids or amorphous solids, there are fewer broader and shorter peaks, due to the greater system disorder and reduced density. For liquids or amorphous solids, as $r$ increases, $g(r)$ tends to unity, which indicates no long-range order in the system. For gases, $g(r)$ is approximately unity for all $r$ (except near zero), due to the random particle distribution. For all states of matter,

$g(r)$ tends to zero as $r$ tends to zero due to electron-electron repulsion between atoms.

The calculation of $g(r)$ is performed throughout a molecular dynamics simulation to obtain a time averaged value. Sampling is performed at regular time intervals over a range of $r$, with the number of particles at different distances (per bin) recorded in a histogram. The accuracy of the calculated $g(r)$ will depend on the frequency of system sampling and the length of the simulation.

# Chapter 3

# $PuO_2$ Potentials and Defects

## 3.1 Literature Review

There has been a broad range of research based on computational modelling of nuclear fuels such as uranium dioxide ($UO_2$) and mixed oxide (MOX) fuel. Fewer studies have been reported for $PuO_2$. However, research on this important compound has been growing over the last decade, as there is a greater need from the nuclear industry. In particular, in the UK, there is a need to understand ageing phenomena relevant to long-term storage. Hence, computational techniques provide a useful tool to explore the detailed atomistic behaviour to compliment experimental studies, utilising affordable computing power. This is particularly relevant to nuclear materials due to their radiotoxicity.

Many important computational studies on $PuO_2$ use interatomic potentials. These studies, based on atomistic simulations, have focussed on understanding $PuO_2$ on an atomistic scale, to enhance fundamental understanding. Read et al. (2014) [64] derived potentials to predict bulk lattice and defect properties of $PuO_2$. Oxygen Frenkel pairs and Schottky defects were shown to be the most energetically favourable types of intrinsic defects.

Other studies have used molecular dynamics. Mingjie et al. (2012) [80] and Arima et al. (2005) [81] predicted thermal properties of $PuO_2$. These included heat capacity, thermal expansion coefficient and thermal conductivity typically over a large temperature range from 300 K to the melting point. Simulations of radiation damage in

nuclear materials are a key area of research. In the case of $PuO_2$, there is spontaneous alpha decay of Pu nuclei, causing lattice damage through the alpha particle and the recoil atoms. To our knowledge, none of these radiation damage simulations have been performed on $PuO_2$, rather on $UO_2$. For example, Martin et al. has modelled the effect of temperature [41] and cascade energy [82] on the radiation damage.

For a 10 keV cascade, Martin et al. (2015) [41] modelled over a temperature range of 700-1800 K, and they predict the maximum damage level accommodated decreases with temperature, explained by complex temperature effects on defect clustering mechanisms. Martin et al. (2011) [82] modelled cascades over an energy range of 1-80 keV at 300 K and 700 K predicting a linear dependence of the damage level on the cascade energy, in agreement with the Norgett, Robinson and Torrens (NRT) atom displacement model [83].

Devanathan et al. (2009) [84] did extensive radiation damage modelling for 1 keV U recoils in $UO_2$ using five different potentials for $UO_2$. They highlighted the potentially drastic effects of the chosen potentials on the simulation results. However, this is expected to some extent as the potentials will have been derived differently, predicting different properties with variable accuracy. In addition to $UO_2$, radiation damage modelling has been performed on other materials related to $PuO_2$. These include Pu metal [85,**86**] and other fluorite structured oxides including ceria ($CeO_2$) [87] and yttria stabilised zirconia (YSZ) [88]. Generally, studies show that fluorite structured oxides are robust to radiation, as defect annihilation is very efficient.

## 3.2 Crystallographic Structure

Plutonium dioxide ($PuO_2$) is a binary ionic oxide that is readily formed by spontaneous oxidisation of plutonium (Pu) metal in air, amongst various other chemical routes. The most stable state in such conditions corresponds to the tetravalent (4+) oxidation state of Pu ions. In this case, $PuO_2$ adopts the fluorite structure with space

group $Fm\bar{3}m$ (number 225) [89] . This structure consists of a cubic close packed array of Pu ions with oxygen ions occupying tetrahedral sites in the lattice. Hence, the structure is an interpenetrating array of Pu and oxygen sub-lattices. Figure 3.1 shows the observed unit cell of pure $PuO_2$. $PuO_2$ has a lattice constant ($a_0$) of 5.398 Å and a density of 11.65 $gcm^{-3}$ [89].

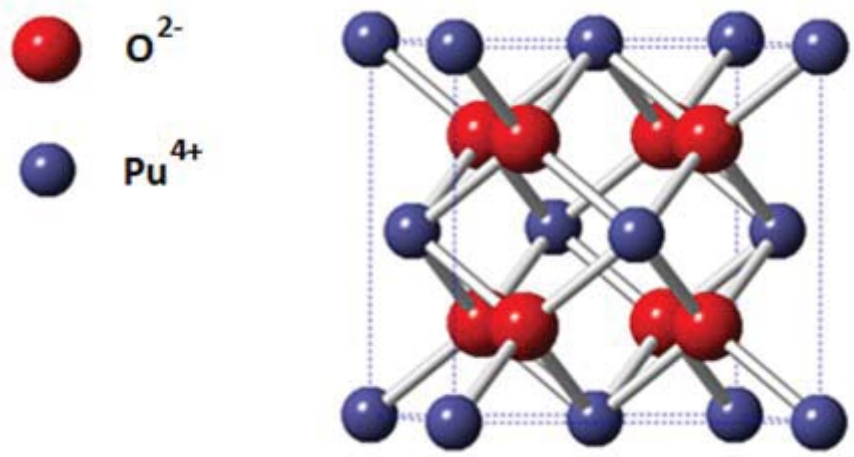


**Figure 3.1: The observed unit cell of fluorite structured $PuO_2$.**

As shown in the unit cell, the Pu ions arrange in a face centred cubic containing the oxygen ions which form an inner cube. The Pu ions have eight-fold coordination, whilst the oxygen ions have four-fold coordination. There are four Pu ions and eight oxygen ions per unit cell. Being the most stable state of Pu oxide of relevance to storage, atomistic simulations of $PuO_2$ will be performed, requiring suitable interatomic potentials. These will need to be evaluated to accurately predict bulk lattice properties and to model intrinsic defects. This information can be used to predict properties not used in the potential derivation and the preferred types of defects.

## 3.3 Evaluation of Potentials

There is a range of published potentials available for $PuO_2$, in particular relating to static lattice and molecular dynamics simulations. In this work, for static lattice simulations, a single potential set was chosen. Six published potentials were selected and evaluated using static lattice simulations using the General Utility Lattice Program (GULP) developed by Julian Gale [50,61]. Structural, mechanical and optical properties were calculated and then compared to reported data from the literature.

The potentials considered were classified as either fully ionic models (FIMs) or partially ionic models (PIMs). In FIMs, the Pu and oxygen ions are assumed to have a charge corresponding to the formal oxidation state of the ions. In this work, the oxidations states were 4+ for the Pu ions and 2- for oxygen ions. The bonding between ions is assumed to be fully ionic in character, with ionic polarisation incorporated using the shell model.

In PIMs, the Pu and oxygen ions are assumed to have only a fraction of the charge corresponding to their formal oxidation state. The bonding between the ions is assumed to be partially ionic in character with some degree of covalent type bonding. This model is a way of incorporating ionic polarisation, instead of using the shell model; this is termed a 'rigid-ion' model. There were four FIMs and two PIMs evaluated. After evaluation of these potentials, the most appropriate potential was chosen for further simulations of $PuO_2$.

### 3.3.1 Fully Ionic Models

There were three FIMs evaluated. Two of these use the shell model, with the potentials of Arima et al. (2005) [81] and Dwivedi et al. (1990) [90] being a rigid-ion model. These potentials consist of Buckingham potentials, with parameters summarised in Tables 3.10 to 3.12.

**Table 3.10: Parameters of the potentials of Read et al. (2014) [64] and Jackson et al. (1986) [91].**

| Ion Pair | Short-range Parameters | | | | Shell Model Parameters | | |
|---|---|---|---|---|---|---|---|
| | $A$ (eV) | $\rho$ (Å) | $C$ (eV Å$^6$) | | Ion | $q_{shell}$ ($e$ $C$) | $k$ (eV Å$^{-2}$) |
| Pu- O[a] | 1116.3317 | 0.3926 | 0.00 | | $Pu^{4+}$ | 6.54 | 206.77 |
| O-O[b] | 11272.6 | 0.1363 | 134.0 | | $O^{2-}$ | -4.40 | 296.2 |
| | $r_{min}$ (Å) | $cut_1$(Å) | $r_{mini}$ (Å) | $cut_2$ (Å) | $cut_{core-shell}$ (Å) | | |
| | 0.00 | 1.20 | 2.10 | 2.60 | | | |
| | $r_{max}$ (Å) | | | | 0.60 | | |
| | 15.0 | | | | | | |

a- Read et al. (2014) [64], b- Jackson et al. (1986) [91], Buckingham four-range potential.

**Table 3.11: Parameters of the potentials of Arima et al. (2005) [81] and Dwivedi et al. (1990) [90].**

| Ion Pair | Short-range Parameters | | | |
|---|---|---|---|---|
| | $A$ (eV) | $\rho$ (Å) | $C$ (eV Å$^6$) | $r_{max}$ (Å) |
| Pu- O[a] | 1129.687 | 0.383 | 0.0 | 15.0 |
| O-O[b] | 22759.564 | 0.149 | 27.89 | |

a- Arima et al. (2005) [81] , b- Dwivedi et al. (1990) [90].

**Table 3.12: Parameters of the potentials of Arima et al. (2005) [81], Meis et al. (1998) [92] and Catlow (1977) [93].**

| Ion Pair | Short-range Parameters | | | | Shell Model Parameters | | | |
|---|---|---|---|---|---|---|---|---|
| | $A$ (eV) | $\rho$ (Å) | $C$ (eV Å$^6$) | $r_{max}$ (Å) | Ion | $q_{shell}$ ($e$ $C$) | $k$ (eV Å$^{-2}$) | $cut_{core-shell}$ (Å) |
| Pu- O[a] | 1129.7 | 0.383 | 0.0 | 10.0 | $Pu^{4+}$ | - | - | - |
| O-O | 22764.0[b] | 0.149[b] | 31.984[c] | 12.0[c] | $O_c^{2-}$ | -2.86 | 52.308 | 0.90 |

a- Arima et al. (2005) [81], b- Catlow (1977) [93], c- Meis et al. (1998) [92].

### 3.3.2 Partially Ionic Models

There were three PIMs evaluated. These are rigid-ion models, which use partial charges. The parameters of these potentials are summarised in Tables 3.13-3.15. These potentials consist of Buckingham and Morse potentials. The potentials of Uchida et al. (2014) [94] potentials use both and assume partial charges of 56.5% of the formal charges. The analytical form is:

$$V(r_{ij}) = \frac{z_i z_j e^2}{4\pi\varepsilon_0 r_{ij}} + A\,exp\left(-\frac{r_{ij}}{\rho}\right) - \frac{C}{r_{ij}^6} + D\left(\left[1 - e^{-a(r_{ij}-r_0)}\right]^2 - 1\right) \qquad \textbf{(3.1)}$$

$z_i e\ C$ and $z_j e\ C$ are the partial charges of the ions $i$ and $j$ separated by a distance $r_{ij}$. The short-range potentials consist of both Buckingham and Morse potentials. $A$, $\rho$ and $C$ are parameters of the Buckingham potential. Regarding the Morse potential, $D$ is the dissociation energy associated with an ion pair, $\alpha$ is a factor describing the shape of the potential and $r_0$ is the anion-cation bond length. The short-range potential parameters for this potential are summarised in Table 3.13. The potentials of Arima et al. (2005) [81] and Inaba et al. (1999) [95] assume partial charges of 67.5% of the formal charge. The Buckingham potential parameters are summarised in Table 3.14.

**Table 3.13: Short-range parameters of the potentials of Uchida et al. (2014) [94].**

| Ion Pair | Short-range Parameters | | | | | | |
|---|---|---|---|---|---|---|---|
| | $A$ (eV) | $\rho$ (Å) | $C$ (eV Å$^6$) | $D$ (eV) | $\alpha$ (Å$^{-1}$) | $r_0$ (Å) | $r_{max}$ (Å) |
| **Pu-O** | 56167.3 | 0.2517 | 0.00998 | 0.186 | 2.0 | 2.37 | 15.0 |
| **O-O** | 483083.6 | 0.1783 | 93.508 | - | - | - | |

**Table 3.14: Parameters of the potentials of Arima et al. (2005) [81] and Inaba et al. (1999) [95].**

| Ion Pair | Short-range Parameters | | | |
|---|---|---|---|---|
| | $A$ (eV) | $\rho$ (Å) | $C$ (eVÅ$^6$) | $r_{max}$ (Å) |
| **Pu-O[a]** | 57425.1843 | 0.1985 | 0.0 | 15.0 |
| **O-O[b]** | 979.0570 | 0.332 | 17.3556 | |
| **Pu-Pu[a]** | $2.804598231\times10^{14}$ | 0.065 | 0.0 | |

**a- Arima et al. (2005) [81], b- Inaba et al. (1999) [95].**

Finally, there are the Yamada et al. (2000) [96] and Kawamura (1992) [97] potentials. In these potentials, the charge of the oxygen ion is -1.2$e$ $C$ and for Pu it is +2.4$e$ $C$. As with the Uchida et al. (2014) potentials, these have the same form as in equation 3.1. The short-range potential parameters are summarised in Table 3.15.

**Table 3.15: Short-range potential parameters of the Yamada et al. (2000) [96] and Kawamura (1992) [97] potentials.**

| Ion Pair | Short-range Parameters | | | | | | |
|---|---|---|---|---|---|---|---|
| | $A$ (eV) | $\rho$ (Å) | $C$ (eV Å$^6$) | $D$ (eV) | $\alpha$ (Å$^{-1}$) | $r_0$ (Å) | $r_{max}$ (Å) |
| **Pu-O[a]** | 514248.864 | 0.24 | 0.0 | 13.0 | 1.56 | 2.339 | 15.0 |
| **O-O[b]** | 226344.0217 | 0.32 | 400.0 | - | - | - | |

**a- Yamada et al. (2000) [96], b- Kawamura (1992) [97].**

### 3.3.3 Structural, Mechanical and Optical Properties

Using the FIMs and PIMs, structural, mechanical and optical properties of $PuO_2$ were calculated. For the FIMs, these predictions and reported data are summarised in Tables 3.16 to 3.18. For the PIMs, they are summarised in Tables 3.19 to 3.21.

**Table 3.16: FIMs predictions of lattice parameter ($a_0$) and elastic constants of $PuO_2$ with reported data.**

| Potentials | $a_{0,calc}$ (Å) | $a_{0,exp}$ (Å) | Elastic Constants (GPa) | | | | | |
|---|---|---|---|---|---|---|---|---|
| | | | $C_{11,calc}$ | $C_{11,lit}$ | $C_{12,calc}$ | $C_{12,lit}$ | $C_{44,calc}$ | $C_{44,lit}$ |
| **Read and Jackson et al.** | 5.39819 | 5.39819[a] | 408.6 | 424.3[b], 430.6[c] | 130.2 | 111.7[b], 128.4[c] | 67.3 | 69.2[b], 67.3[c] |
| **Arima and Dwivedi et al.** | 5.38084 | | 503.6 | | 106.1 | | 98.7 | |
| **Arima, Meis and Catlow et al.** | 5.37537 | | 502.0 | | 107.5 | | 53.6 | |

a- Belin et al. (2004) [89], exp, $PuO_2$, b- Cooper et al. (2014) [33] , potentials, $PuO_2$, c- Meis et al. (1998) [92], potentials, $PuO_2$.

**Table 3.17: FIMs predictions of the bulk, Young's and shear moduli of $PuO_2$ with reported data.**

| Potentials | Moduli (GPa) | | | |
|---|---|---|---|---|
| | Bulk, $B_{calc}$ | Bulk, $B_{lit}$ | Young's, $Y_{calc}$ | Shear, $G_{calc}$ |
| Read and Jackson et al. | 223.0 | 215.9[a], 178.0[b] | 345.6 | 90.4 |
| Arima and Dwivedi et al. | 238.6 | | 466.7 | 131.1 |
| Arima, Meis and Catlow et al. | 239.0 | | 464.1 | 111.0 |

a- Cooper et al. (2014) [33], potentials, $PuO_2$, b- Idiri et al. (2004) [98], exp, $PuO_2$.

**Table 3.18: Other FIMs predictions of properties of $PuO_2$ with reported data.**

| Potentials | Compressibility ($GPa^{-1}$) | Poisson Ratio, $\nu$ | Dielectric Constants | | | |
|---|---|---|---|---|---|---|
| | | | $\varepsilon_{0,calc}$ | $\varepsilon_{0,lit}$ | $\varepsilon_{\infty,calc}$ | $\varepsilon_{\infty,exp}$ |
| **Read and Jackson et al.** | 0.00448 | 0.242 | 15.92 | 19.27[a] | 3.23 | 3.0[b] |
| **Arima and Dwivedi et al.** | 0.00419 | 0.174 | 11.45 | | - | |
| **Arima, Meis and Catlow et al.** | 0.00418 | 0.176 | 14.55 | | 2.78 | |

**a- Meis et al. (1998) [92], potentials, $PuO_2$, b- Haire (2000) [99], exp, $PuO_2$.**

**Table 3.19: PIMs predictions of lattice parameter ( $a_0$) and elastic constants of $PuO_2$ with reported data.**

| Potentials | $a_{0,calc}$ (Å) | $a_{0,exp}$ (Å) | Elastic Constants (GPa) | | | | | |
|---|---|---|---|---|---|---|---|---|
| | | | $C_{11,calc}$ | $C_{11,lit}$ | $C_{12,calc}$ | $C_{12,lit}$ | $C_{44,calc}$ | $C_{44,lit}$ |
| **Uchida et al.** | 6.95295 | 5.39819[a] | 103.7 | 424.3, 430.6[c] | 55.5 | 111.7[b] | 33.7 | 69.2[b], 67.3[c] |
| **Arima and Inaba et al.** | 5.38011 | | 467.1 | | 117.0 | | 109.0 | |
| **Yamada and Kawamura et al.** | 6.93450 | | 1930.6 | | -199.4 | 128.4[c] | -223.0 | |

a- Belin et al. (2004) [89], exp, $PuO_2$, b- Cooper et al. (2014) [100], potentials, $PuO_2$, c- Meis et al. (1998) [92], potentials, $PuO_2$.

**Table 3.20: PIMs predictions of the bulk, Young's and shear moduli of $PuO_2$ with reported data.**

| Potentials | Moduli (GPa) | | | |
|---|---|---|---|---|
| | Bulk, $B_{calc}$ | Bulk, $B_{lit}$ | Young's, $Y_{calc}$ | Shear, $G_{calc}$ |
| Uchida et al. | 71.6 | 215.9[a], 178.0[b] | 65.0 | 29.5 |
| Arima and Inaba et al. | 233.7 | | 420.2 | 131.9 |
| Yamada and Kawamura et al. | 510.6 | | 1884.7 | -69.8 |

a- Cooper et al. (2014) [100], potentials, $PuO_2$, b- Idiri et al. (2004) [98], exp, $PuO_2$.

**Table 3.21: Other PIMs predictions of properties of $PuO_2$ with reported data.**

| Potentials | Compressibility ($GPa^{-1}$) | Poisson Ratio, $\nu$ | Dielectric Constants | | | |
|---|---|---|---|---|---|---|
| | | | $\varepsilon_{0,calc}$ | $\varepsilon_{0,lit}$ | $\varepsilon_{\infty,calc}$ | $\varepsilon_{\infty,exp}$ |
| **Uchida et al.** | 0.0140 | 0.349 | 2.27 | 19.27[a] | - | 3.0[b] |
| **Arima and Inaba et al.** | 0.00428 | 0.200 | 3.34 | | - | |
| **Yamada and Kawamura et al.** | 0.00196 | -0.115 | -0.77 | | - | |

**a-Meis et al. (1998) [92], potentials, $PuO_2$, b- Haire (2000) [99], exp, $PuO_2$.**

## Analysis and Discussion

Having obtained a range of predicted properties of $PuO_2$, one can then compare the accuracy of the different potentials used to decide which set to proceed with. Static lattice simulations using the GULP code predicted a range of properties and some were used in the derivation of the potentials used. In assessing the potentials, only properties with reported data will be used. The % deviation of a calculated value ($x_{calc}$) to a reference value ($x_{ref}$) of a property is given by the following equation:

$$\Delta\% = \frac{x_{calc} - x_{ref}}{x_{ref}} \times 100\% \quad \textbf{(3.2)}$$

## Lattice Parameter

How accurate the potentials replicate the structure of $PuO_2$ is an important aspect of their evaluation. The experimental value of the lattice parameter ($a_0$) of fluorite structured $PuO_2$ is 5.39819 Å. The % deviations for the FIMs and PIMs are summarised in Table 3.22.

**Table 3.22: Selected potentials deviations for the lattice parameter of $PuO_2$.**

| FIM | $\Delta\%$ $(a_0)$ | PIM | $\Delta\%$ $(a_0)$ |
|---|---|---|---|
| **Read and Jackson et al.** | 0.00 | **Uchida et al.** | 28.80 |
| **Arima and Dwivedi et al.** | -0.32 | **Arima and Inaba et al.** | -0.34 |
| **Arima, Meis and Catlow et al.** | -0.42 | **Yamada and Kawamura et al.** | 28.46 |

From the calculated deviations for the lattice parameter for all the potentials, the Read and Jackson et al. potentials are the most accurate, with zero deviation. In addition, generally the FIMs performed much better than the PIMs, with the Uchida et al. and Yamada and Kawamura et al. potentials very inaccurate, overestimating the lattice parameter by ~30%. These two potentials assign similar

charges to the ions, ~50% to 60% of the full oxidation state charges. This would mean the electrostatic interactions would be considerably reduced. Hence, the overestimation of the lattice parameter would be due to the reduced electrostatic attraction between the Pu and oxygen ions. However, the Arima and Inaba et al. potentials gave quite an accurate lattice constant underestimating by only 0.34% compared to experiment. Unlike the other two PIMs, they do not use the Morse potential for the Pu-O short-range interaction, and use a Buckingham potential with partial charges of 67.5% of the formal charges.

Excluding the least accurate two potentials, all of the others underestimate the experimental lattice constant, predicting a slightly contracted unit cell. From this analysis, the number of potentials to be evaluated was reduced to four. An important point in the evaluation of the potentials is the GULP code used, which is based on static lattice (0K) simulations, so only the potential energy is considered. Hence, obviously those potentials that used GULP in their derivation would perform better here. It is known that this is at least the case for the Read and Jackson et al. and parts of the Arima, Meis and Catlow et al. potentials, which both perform well.

## Mechanical Properties

Having analysed the calculations of the lattice constant of $PuO_2$, this reduced the number of potentials to be evaluated to four (one PIM and three FIMs). In addition to structural predictions, the accuracy of predicted mechanical properties is also of importance. Of particular relevance are the three elastic constants of $PuO_2$ ($C_{11}, C_{12}, C_{44}$) and the bulk modulus for which there is reported data. There is only one reported experimental value on the bulk modulus of $PuO_2$, the other reported data from potential-based calculations. With the PIMs, the predictions for all three potentials are presented although only the Arima and Inaba et al. potentials are considered for future use.

For calculations of the elastic constants, the Read and Jackson et al. potentials are the most accurate when comparing to reported data. In fact, for $C_{44}$, the potential agrees exactly with the reference value to 1 d.p. For the bulk modulus, the predictions agree relatively well with the reported data. All of the potential predictions overestimate the experimental value considerably (by 10s of GPa), with the Read and Jackson et al. potentials most accurate. Regarding the PIMs, it is clear that only the Arima and Inaba et al. potentials give the best agreement to the literature for all the mechanical properties, with the Yamada and Kawamura et al. set particularly inaccurate (yielding negative values).

## Optical Properties

GULP readily calculates dielectric constants at zero frequency ($\varepsilon_0$) and at very high frequency ($\varepsilon_\infty$) using the potentials. As shown by the results, the potentials incorporating the shell model are much more accurate than those that use cores only. These shell based potentials are able to predict both dielectric constants, not only $\varepsilon_0$. In addition, the PIMs fail to calculate $\varepsilon_0$ accurately for $PuO_2$, underestimating the experimental value significantly. The two most appropriate FIMs are the Read and Jackson et al. potentials and the Arima, Meis and Catlow et al. potentials, with the % deviations given in Table 3.23.

**Table 3.23: Selected potentials deviations for dielectric constants of $PuO_2$.**

| FIMs | $\Delta\%$ **($\boldsymbol{\varepsilon_0}$)** | $\Delta\%$ **($\boldsymbol{\varepsilon_\infty}$)** |
|---|---|---|
| **Read and Jackson et al.** | -17.39 | 7.52 |
| **Arima, Meis and Catlow et al.** | -24.48 | -7.48 |

As shown in Table 3.23, the deviation from the reference data for both sets of potentials are very similar for $\varepsilon_\infty$. However, the Read and Jackson et al. potentials predicts a closer value for $\varepsilon_0$ than the Arima, Meis and Catlow et al. potentials by ~7%. Hence, overall, the Read and Jackson et al. potential are more accurate at predicting these optical properties.

### 3.3.4 Selected $PuO_2$ Potentials

Overall, the potentials of Read and Jackson et al. were the most accurate, predicting a range of $PuO_2$ properties very well. This can be explained as the potentials were fitted to data using GULP and the method of fitting has been successfully used by Read et al. for other fluorite structured oxides including uranium dioxide ($UO_2$) [30] and ceria ($CeO_2$) [101]. The potentials of Read and Jackson et al. are shown in Figures 3.2 to 3.5. A potential problem occurs when using Buckingham potentials with a finite dispersion term (i.e. $C \neq 0$). This is as the Buckingham potential has an unphysical maximum as $r_{ij} \to 0$ and then diverges towards negative infinity. This would imply unphysical attraction of the ions, as there would no electrostatic repulsion. However, this is normally neglected as many potentials are used for modelling equilibrium conditions and so do not probe small interatomic separations.

In this work, this problem is overcome as the Read and Jackson et al. potentials have no dispersion term (i.e. $C = 0$) for the Pu-O potential. For the O-O potential, it is a 'Buckingham four-range' potential, shown in Figure 3.3. This potential consists of splining polynomial functions between the repulsive and attractive components of the Buckingham potential. With the addition to the repulsive Coulomb potential, the total O-O potential is repulsive. The total Pu-O potential has a minimum at -53.07 eV at an ionic separation of 1.7 Å. The Pu-Pu potential is a purely repulsive Coulomb potential.

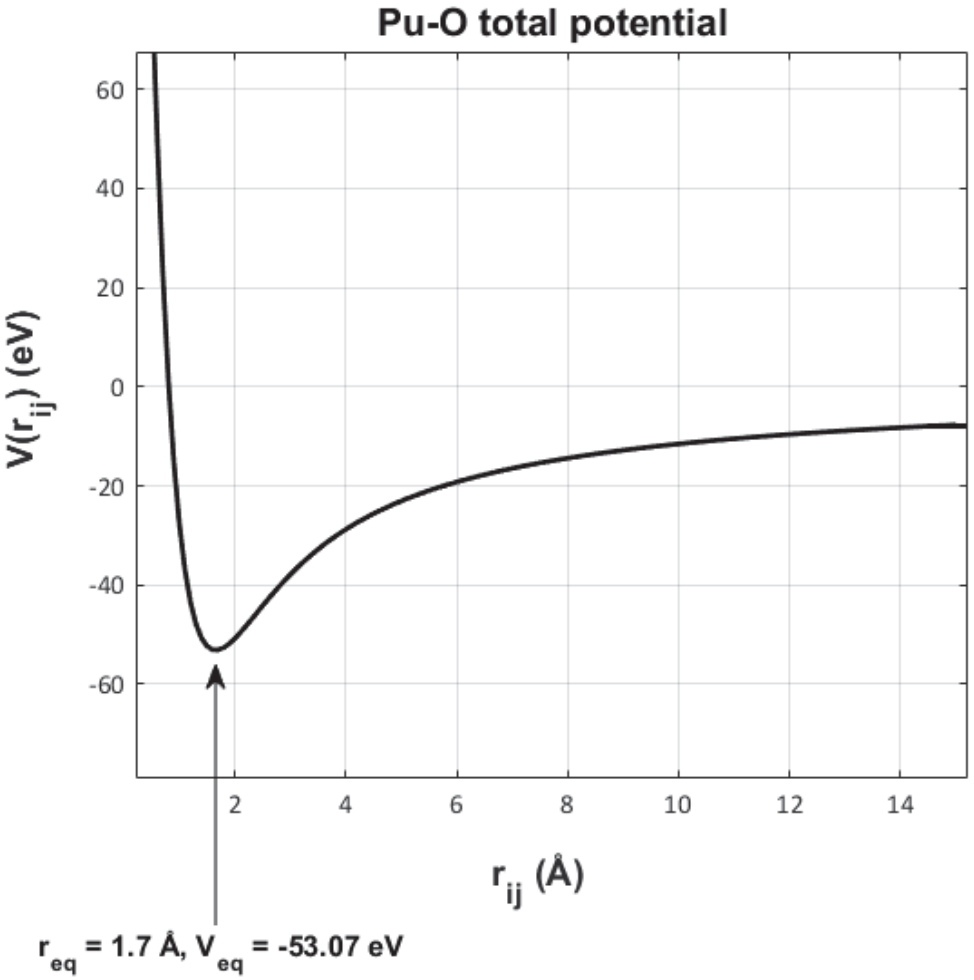


**Figure 3.2: Graph of the total Pu-O potential of Read et al. (2014) [64].**

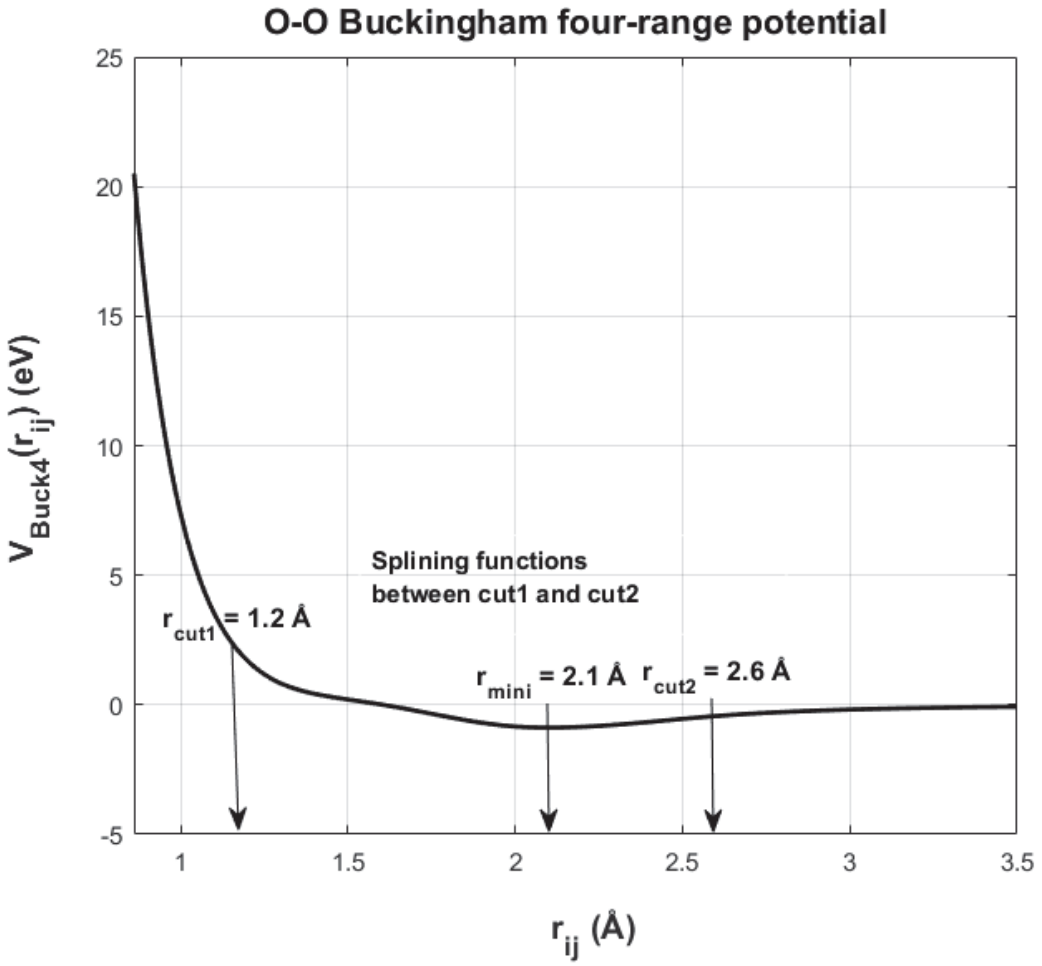


**Figure 3.3: Graph of the O-O Buckingham four-range potential of Jackson et al. (1986) [91].**

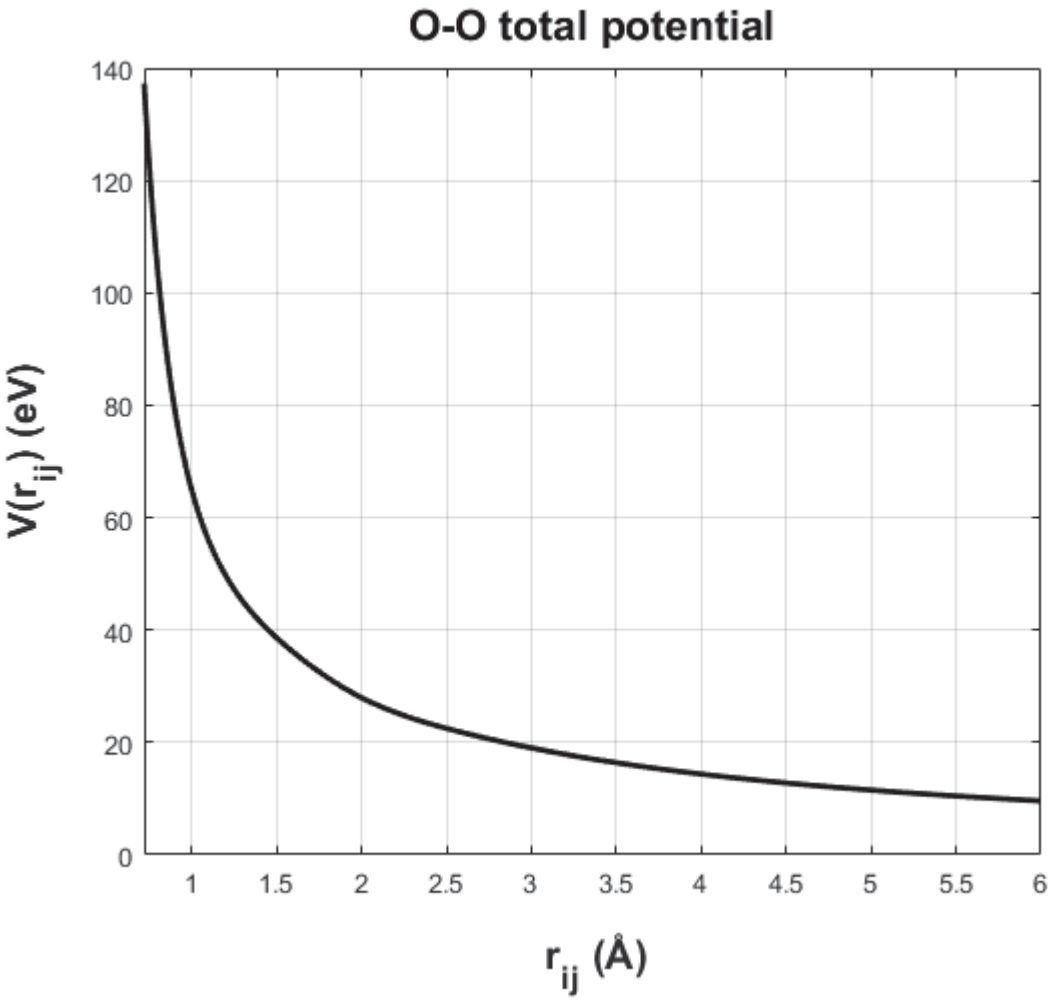


**Figure 3.4: Graph of the total O-O potential.**

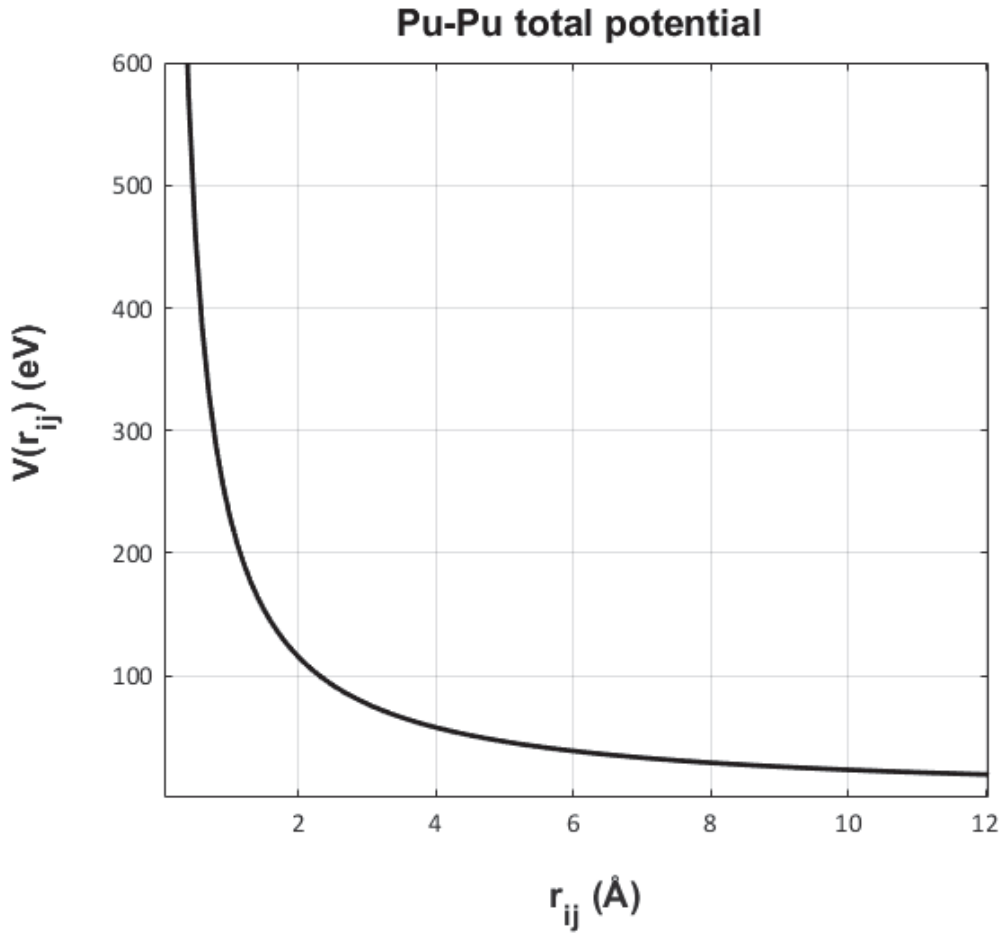


**Figure 3.5 : Graph of the total Pu-Pu potential.**

## 3.4 Intrinsic Defects

Having determined that the Read and Jackson et al. potentials are the most accurate potentials out of those considered, the next stage was to simulate intrinsic defects in $PuO_2$. This would determine which types of intrinsic defects are energetically preferred. The defects modelled were point defects (vacancies, interstitial atoms) and bound defects (Frenkel pairs and Schottky defects). The Mott-Littleton method was used to calculate defect formation energies ($E_D^F$) which is approximately the change in enthalpy $\Delta H$. In addition, for bound defects, their binding energy ($E_D^B$) was also calculated as the difference in energy of the bound defect energy to that of the

constituent point defects at 'infinite dilution'. All calculated energies were compared to available reference data from the literature. In this work, all defect simulations presented used the Mott-Littleton method with a region 1 radius of 14 Å and a region 2a radius of 28 Å from Read et al. (2014) [64], which ensured suitable defect energy convergence. Regions 1 and 2a comprise of ~1600 and ~12,000 ions respectively.

### 3.4.1 Kröger-Vink Notation

To describe defects in solids, the Kröger-Vink notation [102] is widely used. In this notation, a vacancy is indicated by the symbol $V_X$ with $X$ the element symbol of the atom removed. Interstitial atoms are indicated by the symbol $X_i$. For an atom $X$ substituted at a position normally occupied by atom $Y$, its symbol is $X_Y$. Regarding the charges of the defects, the effective charge ($q_e$) is indicated which is defined as the charge of the defect with respect to the charge of an equivalent site in the pure crystal given by [103]:

$$q_e = Z_d - Z_s \quad \textbf{(3.3)}$$

$Z_d$ is the real charge on the defect and $Z_s$ is the real charge on that site in the pure crystal. To describe the effective charges in the notation, superscripts are used, with / representing a unit of effective negative charge and ■ representing a unit of effective positive charge. A superscript of $X$ indicates zero effective charge.

### 3.4.2 Point Defects

Table 3.24 summarises the calculated point defect formation energies for oxygen and Pu vacancies and interstitials. The fractional positions of the defects within the crystallographic unit cell are also given.

**Table 3.24: Point defect formation energies ($E_D^F$) for $PuO_2$.**

| Point Defect | Fractional Position | Calculated $E_D^F$ (eV) |
|---|---|---|
| **Oxygen vacancy, $V_O^{\blacksquare\blacksquare}$** | (0.25, 0.25, 0.25) | 17.08 |
| **Oxygen interstitial, $O_i^{//}$** | (0.50, 0.50, 0.50) | -11.76 |
| **Pu vacancy, $V_{Pu}^{////}$** | (0.0, 0.0, 0.0) | 80.04 |
| **Pu interstitial, $Pu_i^{\blacksquare\blacksquare\blacksquare\blacksquare}$** | (0.50, 0.50, 0.50) | -59.99 |

### 3.4.3 Frenkel Pairs

The defect formation reaction for an oxygen Frenkel pair (OFP) is given by:

$$O_O^X \rightleftharpoons \{V_O^{\blacksquare\blacksquare} + O_i^{//}\} \quad \textbf{(3.4)}$$

The curly brackets indicate the Frenkel pair is a bound defect.

The defect formation reaction for a Pu Frenkel pair (PuFP) is given by:

$$Pu_{Pu}^X \rightleftharpoons \{V_{Pu}^{////} + Pu_i^{\blacksquare\blacksquare\blacksquare\blacksquare}\} \quad \textbf{(3.5)}$$

There were three OFPs modelled, and their positional information and formation and binding energies are summarised in Table 3.25. The oxygen interstitial was fixed at an octahedral site of fractional position (0.50, 0.50, 0.50), with the position of the oxygen vacancy varied as shown in Table 3.25. The '$OFP_1$' and '$OFP_2$' defects are equivalent, except that the fractional $y$ coordinate is 0.25 for '$OFP_1$' but -0.25 for '$OFP_2$'. '$OFP_3$' is different to the other two Frenkel pairs in terms of the oxygen vacancy position. The closest possible configuration of an oxygen vacancy and interstitial results in their combination when the lattice is relaxed. However, this is not the case for the PuFPs, as the Pu vacancy and interstitial are sufficiently separated.

**Table 3.25: Frenkel pair configuration and formation ($E_D^F$) and binding energies ($E_D^B$).**

| Frenkel Pair | Defect Configuration | Calculated $E_D^F$ (eV) | Calculated $E_D^B$ (eV) | Reported $E_D^F$ (eV) |
|---|---|---|---|---|
| **$OFP_1$** | Oxygen vacancy (-0.25, 0.25, -0.25), oxygen interstitial (0.50, 0.50, 0.50) | 4.25 | -1.08 | 3.48[a], 5.02[b], 4.65[c], 5.3[d] 2.72-2.92[e] |
| **$OFP_2$** | Oxygen vacancy (-0.25, -0.25, -0.25), oxygen interstitial (0.50, 0.50, 0.50) | 4.14 | -1.19 | |
| **$OFP_3$** | Oxygen vacancy (0.25, -0.25, 0.25), oxygen interstitial (0.50, 0.50, 0.50) | 3.65 | -1.68 | |
| **PuFP** | Pu vacancy (0.0, 0.0, 0.0), Pu interstitial (0.50, 0.50, 0.50) | 15.74 | -4.32 | 15.19[a], 12.07[b], 16.84[c], 14.1[d] |

**a- Lu et al. (2015) [44], ab-initio, $PuO_2$, b- Cooper et al. (2014) [33], potentials, $PuO_2$, c- Terentyev (2007) [104], potentials, $PuO_2$, d- Freyss et al. (2006) [105], ab-initio, $PuO_2$, e- Murch et al. (1987) [106], exp, $UO_2$.**

## Analysis and Discussion

Of the three Frenkel pairs modelled, '$OFP_1$' and '$OFP_2$' have very similar formation and binding energies, with only ~0.1 eV energy difference. This is expected, as they are essentially equivalent configurations, differing only in the sign of the $y$ coordinate of the oxygen vacancy. '$OFP_3$' has the lowest formation energy of 3.65 eV and, hence, the largest binding energy. The oxygen vacancy and interstitial are closer together that lowers the defect energy given they have opposite charges and attract.

The calculated values compare particularly well with values from Cooper et al. and Terentyev. They are rather higher than the experimental range by Murch et al. but this is due to the elevated temperatures in the diffusion experiments performed on $UO_2$. Regarding the PuFP, the formation energy of 15.74 eV is a factor of ~4 larger than that of the OFPs. This reflects the much larger energy required to displace a heavy Pu ion to form a stable Frenkel pair.

### 3.4.4 Schottky Defects

The defect formation reaction for a Schottky defect is given by:

$$Pu_{Pu}^{X} + 2O_{O}^{X} \rightleftharpoons \{V_{Pu}^{////} + 2V_{O}^{\blacksquare\blacksquare}\} + PuO_{2\,(surface)} \qquad \textbf{(3.6)}$$

$PuO_{2\,(surface)}$ is the lattice energy for a $PuO_2$ formula unit, which is -103.58 eV. This is added to the defect formation energy calculated, thus there is consideration that atoms are removed from the bulk lattice to the surface. There were three Schottky defects modelled, with their calculated formation and binding energies summarised in Table 3.26. The two oxygen vacancies were distinguished as '$O_1$' and '$O_2$'. The positions of the '$O_2$' and Pu vacancies are fixed as shown in Table 3.26. '$Schottky_1$'and '$Schottky_2$' defects are equivalent except that the fractional $y$ coordinate of the '$O_1$' vacancy is -0.25 for '$Schottky_1$' but is 0.25 for '$Schottky_2$'. '$Schottky_3$' is different to the other two Schottky defects in terms of the '$O_1$' vacancy position.

**Table 3.26: Schottky defect positions and formation ($E_D^F$) and binding energies ($E_D^B$).**

| Schottky Defect | Defect Configuration | Calculated $E_D^F$ (eV) | Calculated $E_D^B$ (eV) | Reported $E_D^F$ (eV) |
|---|---|---|---|---|
| **$Schottky_1$** | $O_1$ vacancy (-0.25, -0.25, -0.25), $O_2$ vacancy (0.25, 0.25, 0.25), Pu vacancy (0.0, 0.0, 0.0) | 5.79 | -4.84 | 7.51[a], 5.09[b], 7.38[c] |
| **$Schottky_2$** | $O_1$ vacancy (-0.25, 0.25, -0.25), $O_2$ vacancy (0.25, 0.25, 0.25), Pu vacancy (0.0, 0.0, 0.0) | 5.78 | -4.84 | |
| **$Schottky_3$** | $O_1$ vacancy (0.25, 0.25, -0.25), $O_2$ vacancy (0.25, 0.25, 0.25), Pu vacancy (0.0, 0.0, 0.0) | 6.32 | -4.31 | |

**a- Lu et al. (2015) [44], ab-initio, $PuO_2$, b- Cooper et al. (2014) [100], potentials, $PuO_2$, c- Terentyev (2007) [104], potentials, $PuO_2$.**

### Analysis and Discussion

Of the three Schottky defects, '$Schottky_1$' and '$Schottky_2$' have virtually the same formation and binding energies. This is expected as they are essentially equivalent configurations differing only in the $y$ coordinate of the '$O_1$' vacancy. '$Schottky_3$' has the largest formation energy of 6.32 eV and hence the least binding energy. This is due to the to the configuration being less energetically favourable. Compared to '$Schottky_1$' and '$Schottky_2$', '$Schottky_3$' is a more confined vacancy cluster with the two oxygen vacancies closer, increasing their repulsion and the defect energy.

The calculated values compare particularly well with reported computational data falling within the range of values. The Schottky defect formation energies are ~1.5- 2.7 eV greater than that of the OFPs, showing that OFPs in particular are the energetically preferred forms of intrinsic defects in $PuO_2$. This finding is reported in modelling studies of other fluorite-structured oxides including $CeO_2$ [101] and $UO_2$ [30].

## 3.5 Summary

In summary, six published $PuO_2$ potentials were evaluated and the Read and Jackson et al. potentials were the most accurate for static lattice simulations. They were used to simulate defective $PuO_2$, with intrinsic defects modelled using the Mott-Littleton method. These defects included point defects and bound defects of Frenkel pairs and Schottky defects. Where applicable, defects formation and binding energies were calculated which agreed well with reported data. Regarding the bound defects, the defect energies are very sensitive to the defect configuration. Those defects where there is minimal Coulomb repulsion and maximal Coulomb attraction between constituent point defects are energetically preferred. OFPs and Schottky defects (especially OFPs) have the lowest formation energies, showing these are the energetically preferred forms of intrinsic defects in $PuO_2$.

# Chapter 4

# Properties of $PuO_2$ Surfaces

## 4.1 Literature Review

Through atomistic simulations, there can be detailed predictions of surface structure, reactivity and stability. Generally, these predictions are relatively difficult to obtain in experiments, so simulations are a viable alternative. Understanding the surface chemistry of nuclear materials such as $UO_2$ and $PuO_2$ is necessary to underpin and optimise nuclear fuel manufacture, operation, and long-term storage arrangements. The latter is relevant to the $PuO_2$ stockpile, where the complex ageing behaviour in storage is not well understood.

There are currently only a few published computational surface studies of $PuO_2$ or related fluorite structured oxides. These studies have focussed on the low index surfaces; the (100), (110) and (111) surfaces. The studies cover modelling gaseous adsorption (including $H_2$ Yu et al. (2016) [107] and $CO_2$ Yu et al. (2014) [108] on $PuO_2$), hydroxylation (Jomard et al. (2014) [42] for $PuO_2$, R*á*k et al. (2013) [43] for $UO_2$, $NpO_2$, $PuO_2$, Tan et al. (2005) [109] for $UO_2$, $PuO_2$) and the thermodynamic and chemical stability (Sun et al. (2012) [110] and Jomard et al. (2011) [111] for $PuO_2$). There is agreement in the literature that the order of stability for the dry, lowest index $PuO_2$ (or other ionic fluorite structured binary oxides) surfaces follows (111) $>$ (110) $>$ (100), but with full hydroxylation, this order of stability is reversed [43,109].

Hence, the (111) surface dominates the equilibrium crystal morphology of dry $PuO_2$, whilst the (100) surface dominates that of fully hydroxylated

$PuO_2$. Indeed, studies of $UO_2$ surfaces have shown this is the case, with the (111) surface dominating the equilibrium crystal morphology [112, 113] leading to octahedral shaped crystallites. Abramowski et al. (1999) [112] used five different potentials for $UO_2$ and they all confirmed that and predicted that the growth morphology of $UO_2$ is a truncated octahedron, with (200) facets at the corners.

Boyarchenkov et al. (2012) [114] used molecular dynamics to model surfaces of isolated nanocrystals of $UO_2$. These were very long simulations of ~1000ns, that predicted the shape of the nanocrystal at equilibrium to be a truncated octahedron, but with (100) facets at the corners. This is in agreement with single crystal experiments by Castell et al. (2003) [115] for $UO_2$, where the crystals were cleaved to reveal microscopic voids using electron microscopy. However, Boyarchenkov et al. (2012) [114] stated that the theoretically predicted morphology may not always agree with experimental observations, as the crystal morphology will depend on crystal purity and crystal growth conditions.

For $UO_2$, Williams et al. (2015) [35] explored a range of surfaces and modelled grain boundaries and oxygen diffusion at elevated temperatures. They found the (111), (221) and (331) surfaces are the most stable surfaces, which correspond to highest coordination of surface U ions. In addition, oxygen diffusion was enhanced near grain boundaries, which depends on the local structure and temperature.

Ceria ($CeO_2$) is a surrogate material for $PuO_2$. As for plutonium, the ceria ion is stable in either the 4+ or the 3+ oxidation state and $CeO_2$ is isostructural with $PuO_2$. Numerous computational surface studies have been performed focussing on various aspects of the low index surfaces; the (100), (110) and (111) surfaces. These have been both potential based (Baudin et al. (2000) [116], Conesa et al. (1995)[117] ) and ab-initio (Branda et al. (2008)[118], Skorodumova et al. (2004)[119]). In addition, the surfaces of $Ce_2O_3$ were investigated by Branda et al. (2008) and Conesa et al. (1995), who showed they are stabilised by oxygen vacancies.

Given the limited number of surface studies on $PuO_2$, simulations will be of high value. This chapter presents simulations of a range of pure surfaces of pure

$PuO_2$, predicting structure and energetics. Following that, results of defective lowest index surfaces are also presented. Such information will be useful to predict morphology, surface defect properties and defect segregation behaviour of $PuO_2$.

## 4.2 Energies of Pure Surfaces

The Minimised Energy Techniques Applied to Dislocations, Interfaces and Surfaces Energies (METADISE) program [67] was used to model a range of pure, non-polar (zero dipole) $PuO_2$ surfaces. The potentials of Read et al. (2014) [64] and Jackson et al. (1986) [91] (abbreviated Read et al. (2014)) were transferred from modelling the bulk lattice to surfaces. In analogy to Williams et al. (2015) [35] (abbreviated Williams et al.) for $UO_2$, the $\{n10\}$, $\{n11\}$ and $\{nn1\}$ surfaces were modelled where $n$ = 1, 2, 3. To ensure energy convergence, the depth of region two was four times that of region one. The calculated and reported unrelaxed and relaxed surface energies is summarised in Table 4.1. Appendix A gives the energies for other zero dipole, higher index surfaces of pure $PuO_2$. These include the $\{n10\}$, $\{n11\}$ and $\{nn1\}$ sets where $n$ = 4, 5, 6,7,8,9 and other novel surfaces. The percentage relaxation ($\%\Delta E_{Surf}$) is given by:

$$\%\Delta E_{Surf} = \frac{E_{Surf}^{Rel} - \bar{E}_{Surf}^{Unrel}}{\bar{E}_{Surf}^{Unrel}} \times 100\% \quad \textbf{(4.1)}$$

**Table 4.1: Surface energies and associated areas of pure $PuO_2$ surfaces.**

| Surface | Area (Å$^2$) | $E^{Unrel}_{Surf,Hartman}$ (Jm$^{-2}$) | $E^{Unrel}_{Surf,Gibbs}$ (Jm$^{-2}$) | $\overline{E}^{Unrel}_{Surf}$ (Jm$^{-2}$) | $E^{Rel}_{Surf}$ (Jm$^{-2}$) | $\%\Delta E_{Surf}$ |
|---|---|---|---|---|---|---|
| **(100)** | 29.14 | 6.28 | 6.31 | 6.30 | 2.44 | -61.21 |
| **(110)** | 41.21 | 3.27 | 3.36 | 3.32, 3.148[a] | 2.07, 1.539[a] | -37.50 |
| **(111)** | 50.47 | 1.63 | 1.67 | 1.65, 1.479[a] | 1.32, 1.069[a], 1.33[b] | -19.70 |
| **(210)** | 65.16 | 12.66 | 10.13 | 11.40 | 3.02, 3.35[b] | -73.48 |
| **(211)** | 71.38 | 8.21 | 6.56 | 7.38 | 2.30 | -68.90 |
| **(221)** | 87.42 | 11.03 | 8.33 | 9.68 | 1.63, 1.65[b] | -83.21 |
| **(310)** | 92.15 | 20.31 | 16.25 | 18.28 | 3.09, 3.30[b] | -83.09 |
| **(311)** | 96.65 | 10.44 | 7.46 | 8.95 | 2.62, 2.94[b] | -70.68 |
| **(331)** | 127.02 | 2.30 | 2.91 | 2.61 | 1.74, 1.76[b] | -33.36 |

**a- Tasker (1979) [113], potentials, $UO_2$, b- Williams et al. (2015) [35], potentials, $UO_2$.**

## Analysis and Discussion

The simulation results are commensurate with the literature findings that for the lowest index surfaces of $PuO_2$, the (111) surface is the most stable surface, followed by the (110) surface then the (100) surface. In terms of relaxed surface energies ( $E_{Surf}^{Rel}$), and hence stability, the energetically preferred surfaces are the (111), (221) and (331) surfaces, decreasing in stability with increasing $n$. Therefore, the (111) surface would dominate the equilibrium morphology of $PuO_2$, leading to octahedral crystallites, in agreement with the literature.

Excluding the (100) surface, the least stable surface is the (310) surface followed by the (210) surface. Hence, the simulations predicted that the $\{nn1\}$ set of surfaces are most energetically stable, with generally the $\{n10\}$ set the least stable. Both sets of surfaces become less stable for larger $n$. The difference in the relaxed and unrelaxed surface energies ($\Delta E_{Surf}$) vary considerably depending on the surface.

Generally, these results are in good agreement with reported data for $UO_2$ from Williams et al. and Tasker (1979) [113] (abbreviated Tasker). The small deviations are due to the difference in compound and hence the potentials used. Tasker only modelled the (110) and (111) surfaces. Taskers' results are within 0.3 $Jm^{-2}$ less than that obtained (except 0.53 $Jm^{-2}$ for the relaxed (110) surface). In contrast, data of $E_{Surf}^{Rel}$ from Williams et al. are larger from the results in the range 0.01-0.32 $Jm^{-2}$ for the (111) and (311) surfaces respectively, but the general trends for surface stabilities agree.

## 4.3 Structure of Pure Surfaces

A key aspect for understanding the surfaces is their structure. One can compare the unrelaxed to the relaxed structures, hence, predicting the effects of relaxation on the structure of the surface (specifically region 1 in the modelling). Structural analysis was performed for the (100), (110) and (111) surfaces and the other stable (221) and (331) surfaces.

### 4.3.1 The (100) Surface

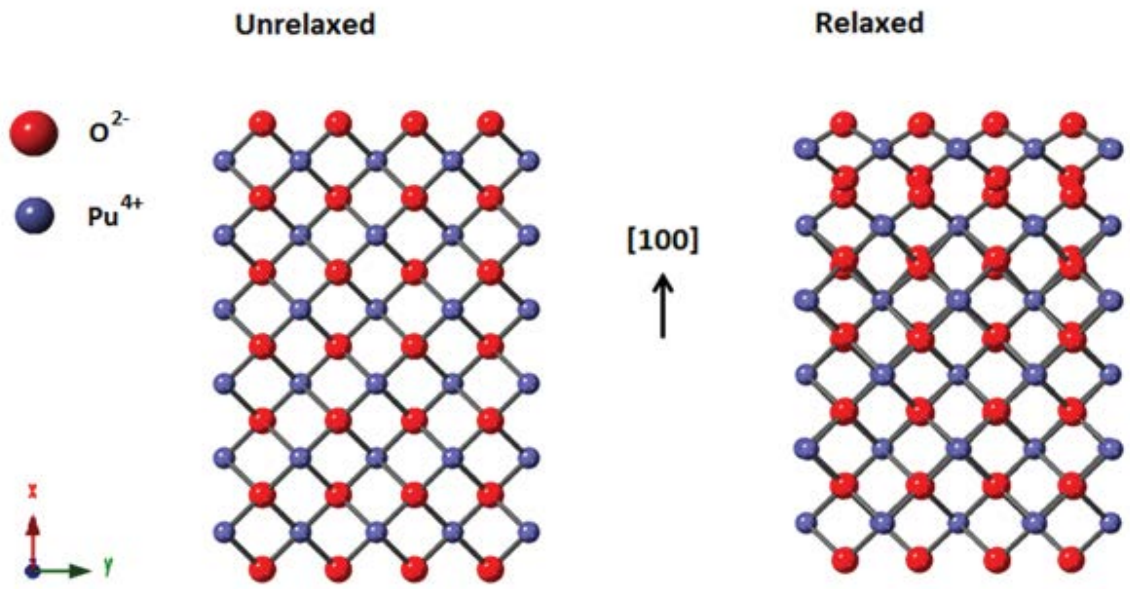


**Figure 4.1: Side-views of the unrelaxed and relaxed (100) surface.**

The structure of the (100) surface is shown in Figure 4.1 and was predicted to be the least stable surface. It is a Tasker type three surface, consisting of alternating charged layers of oxygen and Pu ions. Technically, cleavage of the (100) surface can lead to a charged oxygen or Pu terminated surface, which would be polar, although the oxygen terminated one is preferred. Hence, pure (100) surfaces as

described would not exist as simple terminations of the bulk material. A charge compensation mechanism is needed to stabilise the surface. In the modelling, the dipole of this surface was quenched by removal of 50% of the surface oxygen ions from region 1 to region 2. The effect of the relaxation of the surface is clear from Figure 4.1. The second layer of oxygen ions is rumpled. However, the oxygen ions deeper in the surface are relatively bulk-like and less distorted.

Tasker (1979) suggested that the surface could also be stabilised by defects including steps and ledges on the surface**.** Indeed, faceting has been observed in experiments of LEED (Low Energy Electron Diffraction) on $UO_2$ [120]**.** Potential based studies by Tan et al. (2005) [109] suggested that oxygen vacancies could stabilise the surface with the presence of facetted 'trenches'. They also found that for $PuO_2$ and $UO_2$ the (100) surface is stabilised by hydroxylation of the surface. In fact, for full hydroxylation, it is more stable than the (110) and (100) surfaces, in agreement with ab-initio calculations by R$\acute{a}$k et al. (2013) [43] for $PuO_2$.

### 4.3.2 The (110) Surface

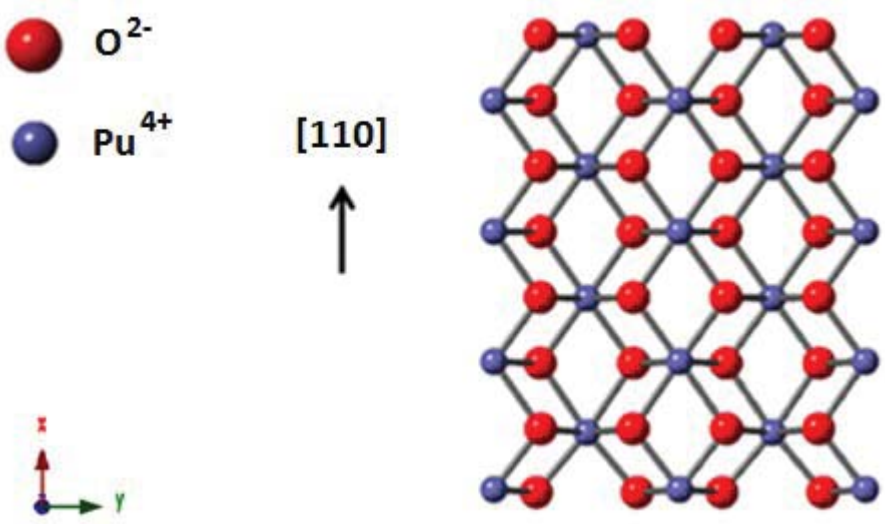


**Figure 4.2: Side-view of the relaxed (110) surface.**

The structure of the relaxed (110) surface is shown in Figure 4.2. It is a Tasker type one surface consisting of alternating stoichiometric layers of oxygen and Pu ions. It has a stability intermediate of the (100) and (111) surfaces of the low index surfaces. Overall, upon surface relaxation, there was predicted to be only a marginal surface ion contraction of the oxygen ions. Ionic separations in the top surface layers vary slightly for the relaxed surface. As expected, deeper into the surface region, the more bulk-like the structure becomes.

For the top layer, upon relaxation, the O-Pu separation reduces from 2.34 Å in the unrelaxed case to 2.27 Å. The horizontal O-O separation for the relaxed surface is either 2.93 Å or 2.47 Å, with there being non-uniform expansion and contraction. Before relaxation, this was constant and intermediate at 2.70 Å. For the first two layers, there is vertical contraction as the O-O separation reduces from 2.70 Å to 2.66 Å. Although the horizontal Pu-Pu separation remains constant, the vertical separation reduces from 3.82 Å to 3.72 Å. Hence, there are relatively large changes for

the top layer(s). This vertical contraction is in agreement with Tasker who also predicted surface rumpling.

### 4.3.3 The (111) Surface

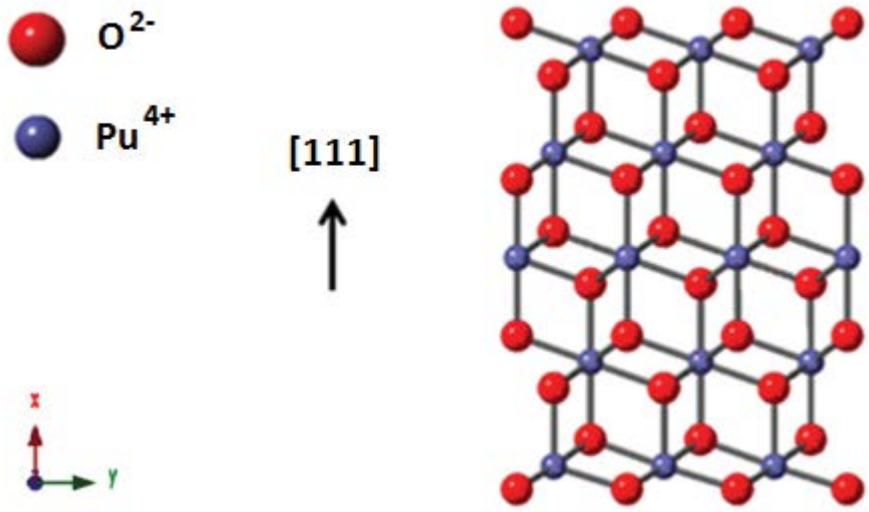


**Figure 4.3: Side-view of the relaxed (111) surface.**

The structure of the relaxed (111) surface is shown in Figure 4.3 and is the most stable surface, which is the case for other binary fluorite structured oxides including $CeO_2$ ,$ThO_2$ and $UO_2$. This surface is a Tasker type two non-polar surface consisting of alternating layers of oxygen and Pu ions. Technically, cleavage of the (111) surface can lead to an oxygen or Pu terminated surface, which would be polar [111]. A charge compensation mechanism would be needed to eliminate this. However, the oxygen-terminated surface is more stable, due to the high coordination number of surface Pu ions of seven, similar to the bulk value of eight. For the top layer, the O-Pu separation reduces from 2.34 Å to 2.31 Å, a small contraction. However, the O-O and Pu-Pu separations are unchanged, at 3.82 Å.

Using the calculated relaxed surface energies, one can predict the equilibrium growth morphology by a Wulff construction [72]. For $PuO_2$, this was shown to be octahedral as shown in Figure 4.4. Being the lowest energy surface, the (111) surface dominates the morphology, giving an octahedral shaped crystallite. This is in agreement with modelling studies for $UO_2$ [112-114] and single crystal experiments on $UO_2$ [115].

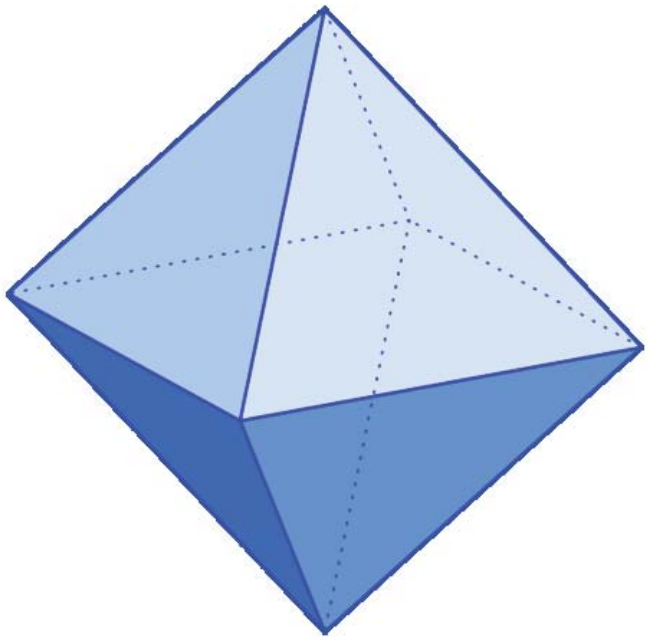

**Figure 4.4: Wulff construction of the equilibrium morphology of $PuO_2$ [121].**

### 4.3.4 The (221) Surface

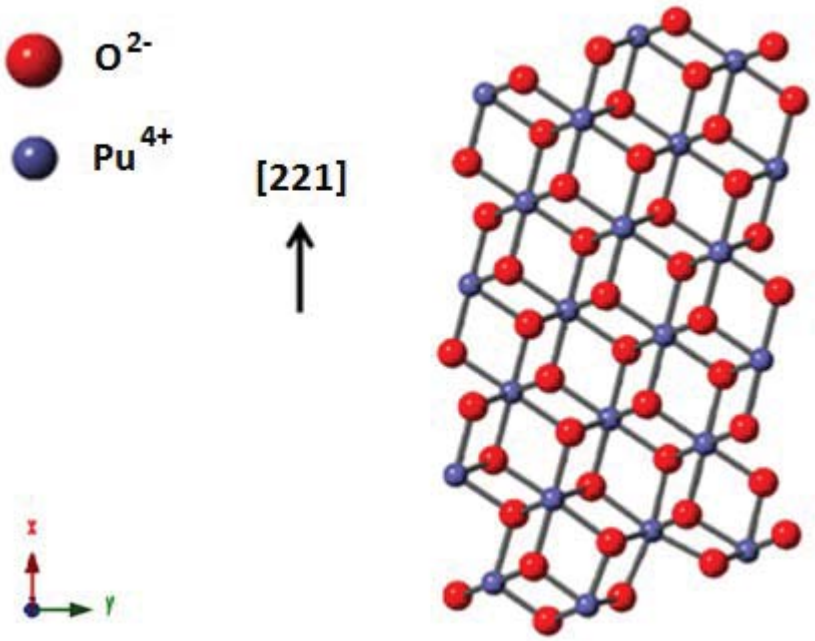


**Figure 4.5: Side-view of the relaxed (221) surface.**

The structure of the relaxed (221) surface is shown in Figure 4.5 and was predicted to be second most stable surface, in agreement with Williams et al. for $UO_2$. Williams et al. explained this is due to the high coordination numbers of surface U ions of 6, 7 and 8, as for $PuO_2$. The surface is a faceted Tasker type two surface. The O-Pu separation for the unrelaxed surface is 2.34 Å. However, for the relaxed surface, this varies from 2.18 Å to 2.41 Å, showing there was moderate contraction and expansion upon structural relaxation.

### 4.3.5 The (331) Surface

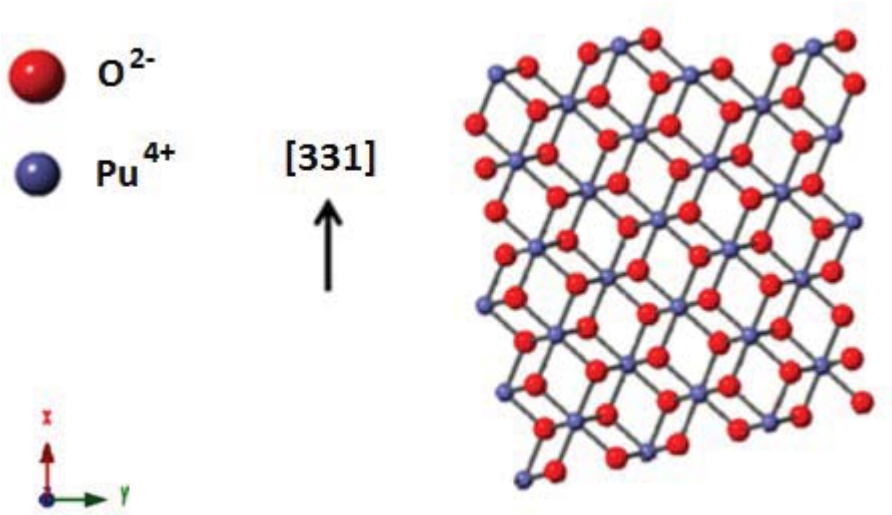


**Figure 4.6: Side-view of the relaxed (331) surface.**

The structure of the relaxed (331) surface is shown in Figure 4.6 and was predicted to be the third most stable surface, in agreement with Williams et al. for $UO_2$. It is a facetted Tasker type two surface consisting of coplanar oxygen and Pu ions. Williams et al. explained that the high stability of this surface is due to the high coordination numbers of surface U ions of 6, 7 and 8, as for $PuO_2$. The unrelaxed surface has fixed O-Pu separations of 2.34 Å. However, for the top layer of the relaxed surface, this separation varies from 2.19 Å to 4.46 Å, showing there was considerable contraction and expansion upon structural relaxation.

## 4.4 Attachment Energies and $d$ Spacing's

The calculated attachment energies ($E_{Surf}^{Attach}$) and $d$ spacing's of the PuO2 surfaces modelled are given in Table 4.2.

**Table 4.2: Attachment energies ($E_{Surf}^{Attach}$ per $PuO_2$) and $d$ spacing's of pure $PuO_2$ surfaces.**

| Surface | $E_{Surf}^{Attach}$ per $PuO_2$ (eV) | Calculated and Experimental [a] $d$ Spacing [1] (Å) | % $\Delta$ ($\times 10^{-2}$) |
|---|---|---|---|
| **(100)** | -2.86 | 5.3981, 5.3960 | 3.93 |
| **(110)** | -2.10 | 3.8170, 3.8155 | 4.06 |
| **(111)** | -1.28 | 3.1166, 3.1154 | 3.87 |
| **(210)** | -12.87 | 2.4141, 2.4132 | 3.97 |
| **(211)** | -9.14 | 2.2038, 2.2029 | 3.74 |
| **(221)** | -15.05 | 1.7994, 1.7987 | 3.87 |
| **(310)** | -29.20 | 1.7070, 1.7064 | 3.73 |
| **(311)** | -15.74 | 1.6276, 1.6270 | 3.65 |
| **(331)** | -4.57 | 1.2384, 1.2379 | 4.15 |

**a- Belin et al. (2004) [89], experimental, $PuO_2$. [1] The $d$ spacing of a surface plane is its repeat distance within the bulk crystal, parallel to the surface normal.**

## Analysis and Discussion

These calculated $d$ spacing's agree very well with the crystallographic data, to within 0.05%, showing the suitability of the potentials for modelling surfaces of $PuO_2$. Attachment energies are used to predict the growth morphology of a crystal, with those surfaces with the least exothermic values dominating. From the results, the lowest index surfaces i.e. the (100), (110) and (111) have the least exothermic attachment energies, with the other surfaces (apart from the (331) surface) having energies several eV more exothermic.

The most stable, (111) surface has the least exothermic attachment energy of -1.28 eV/$PuO_2$, and hence would dominate the growth morphology of $PuO_2$, leading to the formation of octahedral crystallites, as for the equilibrium morphology. Appendix A summarises the calculated attachment energies and $d$ spacing's for other non-polar, higher index surfaces of pure $PuO_2$. These include the $\{n10\}$, $\{n11\}$ and $\{nn1\}$ sets where $n$ = 4, 5, 6, 7, 8, 9 and other novel surfaces.

## 4.5 Defective $PuO_2$ Surfaces

### 4.5.1 Simulation Details

To model realistic surfaces, defects need to be considered. Focusing on the lowest index surfaces of $PuO_2$; the (100), (110) and (111) surfaces, intrinsic defects were incorporated. These include point defects (interstitials and vacancies) and bound defects (Frenkel pairs and Schottky defects). The formation and segregation energies of these defects were calculated. Surface defects can be modelled in METADISE either using the Mott-Littleton method using the embedded CHAOS code [70] or as part of a conventional surface simulation. The latter approach involves insertion of a defect in region 1 of a surface, which gives rise to concentration effects.

Regarding the Mott-Littleton approach, in order to determine suitable region 1 and 2a radii, convergence testing of the defect energy is required, ensuring region 1 and 2a are contained within region 1 of the surface. In this work, this was done by modelling a Schottky defect in the (111) surface, yielding appropriate region 1 and 2a radii of 9 Å and 35 Å respectively. Appendix B gives more convergence testing data. All surface defects were positioned in region 1 of the surface. The segregation energy of a surface defect is defined as the difference in the defect formation energy at the surface to that in the bulk lattice, given by:

$$E_D^{Seg} = E_{D,Surf}^{F,Reg1} - E_{D,Bulk}^{F} \quad \textbf{(4.2)}$$

The segregation energy is a measure of defect stability at the surface compared with the bulk. If the segregation energy is exothermic (i.e. negative), there would be an energetic preference for the defect to form on the surface compared to within the bulk lattice. Modelling charged defects on a surface can lead to a shift in the defect energy due to the electrostatic potential. Hence, the defect energies were normalized by addition of an energy correction term ($E_{Corr}$) such that:

$$E_{D,Surf}^{F,Corr} = E_{D,Surf}^{F,Reg1} + E_{Corr} \quad \textbf{(4.3)}$$

The energy correction term is the difference in the bulk lattice defect energy ($E^F_{D,Bulk}$) to the defect energy in region 2 of the surface ($E^{F,Reg2}_{D,Surf}$) given by:

$$E_{Corr} = E^F_{D,Bulk} - E^{F,Reg2}_{D,Surf} \quad \textbf{(4.4)}$$

In this work, the energy correction was only applied to point defects on the surfaces, owing to their net charge. For comparison, the calculated bulk intrinsic defect formation energies of $PuO_2$ are summarised in Table 4.3.

**Table 4.3: Calculated bulk intrinsic defect formation energies ($E^F_{D,Bulk}$) of $PuO_2$.**

| Defect | $E^F_{D,Bulk}$ (eV) |
|---|---|
| **Oxygen vacancy, $V_O^{\blacksquare\blacksquare}$** | 17.08 |
| **Oxygen interstitial, $O_i^{//}$** | -11.76 |
| **Pu vacancy, $V_{Pu}^{////}$** | 80.04 |
| **Pu interstitial, $Pu_i^{\blacksquare\blacksquare\blacksquare\blacksquare}$** | -59.99 |
| **OFP** | 3.65 |
| **PuFP** | 15.74 |
| **Schottky defect** | 5.78 |

## 4.5.2 Point Defects

The calculated point defect formation and segregation energies for the low index $PuO_2$ surfaces are summarised in Tables 4.4 to 4.6. The defect depth is the distance from the top of the surface to the centre of the defect configuration.

**Table 4.4: Calculated point defect formation and segregation energies for the (100) surface.**

| Point Defect | Defect Depth (Å) | $E^{F}_{D,Surf}$ (eV) | $E^{F,Corr}_{D,Surf}$ (eV) | $E^{Seg}_{D}$ (eV) |
|---|---|---|---|---|
| Oxygen vacancy, $V_O^{\blacksquare\blacksquare}$ | 0.37 | 38.28 | 16.51 | -0.57 |
| Oxygen interstitial, $O_i^{//}$ | - | - | - | - |
| Pu vacancy, $V_{Pu}^{////}$ | 1.23 | 39.28 | 82.04 | 2.00 |
| Pu interstitial, $Pu_i^{\blacksquare\blacksquare\blacksquare\blacksquare}$ | - | - | - | - |

**Table 4.5: Calculated point defect formation and segregation energies for the (110) surface.**

| Point Defect | Defect Depth (Å) | $E^{F}_{D,Surf}$ (eV) | $E^{F,Corr}_{D,Surf}$ (eV) | $E^{Seg}_{D}$ (eV) |
|---|---|---|---|---|
| Oxygen vacancy, $V_O^{\blacksquare\blacksquare}$ | 0.07 | 17.94 | 16.00 | -1.08 |
| Oxygen interstitial, $O_i^{//}$ | 0.98 | -14.21 | -12.48 | -0.73 |
| Pu vacancy, $V_{Pu}^{////}$ | 0.17 | 77.32 | 80.55 | 0.51 |
| Pu interstitial, $Pu_i^{\blacksquare\blacksquare\blacksquare\blacksquare}$ | 0.98 | -60.84 | -71.42 | -11.44 |

**Table 4.6: Calculated point defect formation and segregation energies for the (111) surface.**

| Point Defect | Defect Depth (Å) | $E^{F}_{D,Surf}$ (eV) | $E^{F,Corr}_{D,Surf}$ (eV) | $E^{Seg}_{D}$ (eV) |
|---|---|---|---|---|
| Oxygen vacancy, $V_O^{\blacksquare\blacksquare}$ | 0.10 | 26.52 | 17.49 | 0.41 |
| Oxygen interstitial, $O_i^{//}$ | 0.83 | -19.13 | -13.28 | -1.53 |
| Pu vacancy, $V_{Pu}^{////}$ | 0.78 | 65.16 | 82.55 | 2.51 |
| Pu interstitial, $Pu_i^{\blacksquare\blacksquare\blacksquare\blacksquare}$ | 0.83 | -43.94 | -69.89 | -9.90 |

## Analysis and Discussion

Point defects are unlikely to occur alone on stoichiometric $PuO_2$ surfaces, owing to their charge, which would de-stabilize the surfaces. Clearly, interstitials are not feasible on the (100) surface, although vacancies are. This is because the surface is initially highly strained and additional ions increase the strain and instability of the surface. Regarding oxygen vacancies, the (110) surface is predicted to be the preferred surface, having the smallest formation energy and most exothermic segregation energy, although these energies differ by only ~0.5 eV to those of the (100) surface. In contrast, Pu vacancies are more likely to form in the bulk lattice than on these surfaces.

Vacancies are not favoured on the (111) surface, with an endothermic segregation energy, which is understandable due to its large stability. The energies of interstitials are similar for the (110) and (111) surfaces, which both have similar exothermic segregation energies differing between ~0.8- 1.5 eV, and is an order of magnitude larger for the Pu interstitial than for the oxygen interstitial. This suggests that these surfaces are more likely to grow by addition of more oxygen and Pu ions, which would be exhibited in the growth morphology of $PuO_2$.

### 4.5.3 Frenkel Pairs and Schottky Defects

The calculated defect formation and segregation energies of Frenkel pairs and Schottky defects for the low index $PuO_2$ surfaces are listed in Tables 4.7 to 4.9.

**Table 4.7: Calculated bound defect formation and segregation energies for the (100) surface.**

| Bound Defect | Defect Depth (Å) | $E_{D,Surf}^{F,Reg1}$ (eV) | $E_D^{Seg}$ (eV) |
|---|---|---|---|
| **OFP** | - | - | - |
| **PuFP** | - | - | - |
| **Schottky** | 0.66 | 1.55 | -4.24 |

**Table 4.8: Calculated bound defect formation and segregation energies for the (110) surface.**

| Bound Defect | Defect Depth (Å) | $E_{D,Surf}^{F,Reg1}$ (eV) | $E_D^{Seg}$ (eV) |
|---|---|---|---|
| **OFP** | 2.27 | 4.72 | 1.08 |
| **PuFP** | 6.29 | 18.44 | 2.70 |
| **Schottky** | 0.10 | 2.19 | -3.59 |

**Table 4.9: Calculated bound defect formation and segregation energies for the (111) surface.**

| Bound Defect | Defect Depth (Å) | $E_{D,Surf}^{F,Reg1}$ (eV) | $E_D^{Seg}$ (eV) |
|---|---|---|---|
| **OFP** | 5.89 | 4.66 | 1.01 |
| **PuFP** | 6.24 | 20.87 | 5.13 |
| **Schottky** | 0.33 | 4.76 | -1.02 |

## Analysis and Discussion

For the (100) surface, only oxygen vacancies are energetically favourable. Frenkel pairs and Schottky defects were simulated on the (110) and (111) surfaces. Regarding Frenkel pairs, the segregation energies are all endothermic, thus are more likely to form in the bulk lattice. This is especially the case for the Pu, rather than oxygen Frenkel pairs, as those energies are a factor of ~2.5 and ~5 greater for the (110) and (111) surfaces respectively.

In contrast, the segregation energies of Schottky defects are all exothermic for all three surfaces. Schottky defect segregation is preferred on the (100) and (110) surfaces, where the segregation energies differ by only ~0.7 eV, and least so on the (111) surface, which has ~2.6 eV smaller energy comapred to the (110) surface . This trend reflects the order of stability of these surfaces, with the least stable (100) surface the one most stabilised by Schottky defects. Overall, in stoichiometric $PuO_2$, where the (111) surface is dominant, it is predicted that Schottky defects are likely to segregate to surfaces, whilst oxygen Frenkel pairs remain in the bulk lattice.

## 4.6 Summary

Overall, a range of pure and defective surfaces of $PuO_2$ were successfully simulated. In particular, surface and attachment energies and $d$ spacing's of pure surfaces were calculated, and compared to reported data. The suitability of the potentials to model surfaces is shown by the excellent agreement of the calculated $d$ spacing's with experiment and the good agreement of energies to the literature on $UO_2$. The most stable surface was predicted to be the (111) surface ($E_{Surf}^{Rel}$= 1.32 $Jm^{-2}$), which is oxygen terminated. The (221) and (331) surfaces were the next most stable surfaces respectively, followed by the (110) surface. However, the (111) surface dominates the equilibrium morphology of $PuO_2$, which is octahedral.

Intrinsic defects were simulated on the (100), (110) and (111) surfaces, with defect formation and segregation energies calculated. The (100) surface was predicted to be the least stable surface, but is stabilised by Schottky defects and oxygen vacancies. Generally, the (111) and (110) surfaces were predicted to have similar defect properties. In particular, segregation of interstitials and Schottky defects from the bulk lattice to these surfaces is shown to be energetically favourable. In contrast, Frenkel pairs were unstable on the surfaces compared with the bulk lattice.

# Chapter 5

# Helium Behaviour in $PuO_2$

## 5.1 Literature Review

Safe and effective management of spent nuclear fuel demands intensive research to understand ageing behaviour of relevance to long-term storage. Spent nuclear fuel consists of a range of radioactive fission products, which decay along alpha decay chains, including Pu-238, Pu-239, Cm-242, Cm-244 and Am-241 [122]. This results in helium gas accumulation in the materials with a yield of at least four times larger than the fission products xenon (Xe) or krypton (Kr) [123]. Helium has a relatively low solubility in ceramic materials such as $UO_2$ and $PuO_2$ of ~0.5 to 1 wt. %, leading to bubble formation [124]. These bubbles accumulate at grain boundaries, leading to a loss of grain cohesion and possibly rapid release of the helium. This is of concern for safe management of stored $PuO_2$ due to the risk of gas pressurisation of storage cans.

It has been reported that helium gas has led to deterioration in the mechanical integrity of the materials. Ronchi et al. (2004) [123] reported the dramatic embrittlement of $PuO_2$ pellets stored in nitrogen for forty years, which was attributed to helium release. Such disintegration increases the surface area of the material, increasing the risk of water contact and radioactivity release. In addition, helium is relevant to mixed oxide (MOX) fuel, which contains both alpha decaying U and Pu isotopes. It is expected that after ~10, 000 years of storage in a repository, the concentrations of helium could reach up to ~0.7 at. % in $UO_2$ and ~4.0 at. % in MOX fuel [125].

Due to the importance of the role of helium in nuclear materials, many experimental studies have been performed since the 1960s and computational

studies since the early 1990s. Most of the computational studies have focussed on helium behaviour in $UO_2$ at different levels of radiation damage and temperatures. Of particular interest is the most stable location of the helium atoms in the $UO_2$ and $PuO_2$. There is no general agreement on the preferred helium location, which include octahedral interstitial sites, vacancies and Schottky defects.

The preferred helium trapping sites are determined by calculation of helium incorporation and solution energies. Tian et al. (2013) [126], Freyss et al. (2006) [105] calculated helium solution energies in $PuO_2$ and Crocombette (2002)[127] for $UO_2$. The solution energy, according to the point defect model of Matzke [128] and Lidiard [129], depends on the stoichiometry and temperature. This model indicates that for the stoichiometric case, the octahedral interstitial sites (OISs) are preferred, with oxygen vacancies preferred for the hypo-stoichiometric case and U or Pu vacancies preferred for hyper-stoichiometric case.

Helium migration and diffusion mechanisms have also been investigated. Dabrowski et al. (2014) [130] performed ab-initio calculations of helium migration in pure and defective $UO_2$. They predicted that the octahedral interstitial sites are the most stable helium sites in pure $UO_2$, even at advanced temperatures. They also showed the migration energy barriers are reduced by an order of magnitude for a vacancy assisted migration, rather than direct migration from interstitial to neighbouring interstitial sites.

A multitude of molecular dynamics studies have investigated helium behaviour in uranium dioxide ($UO_2$). Govers et al. (2009) [131] modelled helium diffusion in $UO_{2+-x}$ over temperatures 1000 K to 3000 K. They predicted helium diffusion coefficients and activation energies, which revealed two diffusion regimes for $UO_2$. One is an oxygen vacancy assisted mechanism in $UO_{2-x}$ at lower temperatures; the other is an intrinsic migration mechanism between interstitial sites, which dominates at higher temperatures in stoichiometric $UO_2$.

Furthermore, Lee et al. (2015) [47] investigated the effects of nano pores and helium bubbles on the thermal conductivity of single $UO_2$ crystals. They

predicted nano pores, in particular those filled with helium decrease the thermal conductivity, with the helium atoms acting as phonon scattering centres. Parfitt et al. (2008) [132] investigated the phenomenon of helium resolution in $UO_2$. This is where helium atoms are returned to the bulk lattice from helium bubbles through interactions with displacement cascades from an atomic recoil in an alpha decay. They predicted thermal and ballistic recoil contributions to the helium resolution, which increases with helium bubble pressure.

In summary, there is a multitude of published computational studies on helium behaviour on nuclear materials, with many focussed on $UO_2$. Many of these studies are applicable to in-reactor conditions at advanced temperatures and pressures, not fully applicable to long-term storage scenarios. Evidently, more research is required to address this, which is particularly important for stored $PuO_2$. Hence, the focus of this chapter is atomistic simulations of helium behaviour in $PuO_2$. In particular, helium incorporation was modelled in the pure and defective material, with appropriate energies calculated for not only the bulk lattice but also for the (111) surface. From this, the most stable trapping sites can be determined, which is the origin of the finite solubility of helium in $PuO_2$.

## 5.2 Helium Incorporation

### 5.2.1. Introduction

Static lattice simulations were performed to investigate helium incorporation in OISs, vacancies and Schottky defects in $PuO_2$. This was to predict the favourability of helium trapping in different sites, which is the origin of the finite solubility of helium in $PuO_2$. Using GULP [50,61], the Mott-Littleton method [63] was used to calculate the incorporation energies of helium atoms in the various sites ($E_{He}^{Incorp}$). This was calculated as the difference in the defect formation energies for the configuration of

trapped ($E^F_{He,trapped}$) to untrapped helium ($E^F_{He,untrapped}$), divided by the number of helium atoms ($N_{He}$), given by:

$$E^{Incorp}_{He} = \frac{1}{N_{He}}[E^F_{He,trapped} - E^F_{He,untrapped}] \quad \textbf{(5.1)}$$

For a single helium atom in an OIS, the defect energy is equivalent to the incorporation energy. In the untrapped configuration, the helium atom(s) were positioned in neighbouring OIS(s) to the trapping defect. Hence, the incorporation energy is a measure of energetic preference of the helium in a defect over an OIS. An analogous method was used to calculate the transition state energies for short migration paths of helium to the defects.

The Lennard-Jones potentials of Grimes et al. (1990) [133] were used for helium interactions in $PuO_2$, which incorporates the shell model. Originally, these potentials were derived for $UO_2$ from ab-initio calculations, but were assumed suitable for $PuO_2$ in this work. In addition, the potentials of Read et al. (2014) [64] and Jackson et al. (1986) [91] (abbreviated Read et al.) were used for modelling the $PuO_2$ lattice, which is a fully ionic model incorporating the shell model. In all of these simulations, the Mott-Littleton region radii were 14 Å and 28 Å for regions 1 and 2a respectively.

## 5.2.2 Helium Potentials

The parameters of the Lennard-Jones potentials of Grimes et al. (1990) [133] are summarised in Table 5.1. In addition, graphs of the helium-based potentials are shown in Figures 5.1 to 5.3. The He-He interaction is very weak, with the minimum energies ~17 and ~30 times larger for the He-O and He-Pu pairs respectively, which are comparable to the thermal energy at room temperature.

**Table 5.1: Parameters of potentials of Grimes et al. (1990) [133].**

| Interacting Pair | Short-range Parameters | | Shell Model Parameters | | |
|---|---|---|---|---|---|
| | $A_{ij}$ (eV Å$^{-12}$) | $B_{ij}$ (eV Å$^{-6}$) | Ion | $q_{shell}$ (e $C$) | $k$ (eV Å$^{-2}$) |
| He-He | 69.3559 | 0.493712 | | | |
| He-O | 2247.836 | 11.762 | $Pu^{4+}$ | 6.54 | 206.77 |
| He-Pu[1] | 500.425 | 7.366 | $O^{2-}$ | -4.40 | 296.2 |
| | $r_{max}$ (Å) | | He | -1.00 | 72.70 |
| | 15.0 | | $cut_{core-shell}$ (Å) | | |
| | | | 0.60 | | |

[1] The He-Pu potential is set equal to the He-U potential from Grimes et al. (1990) [133].

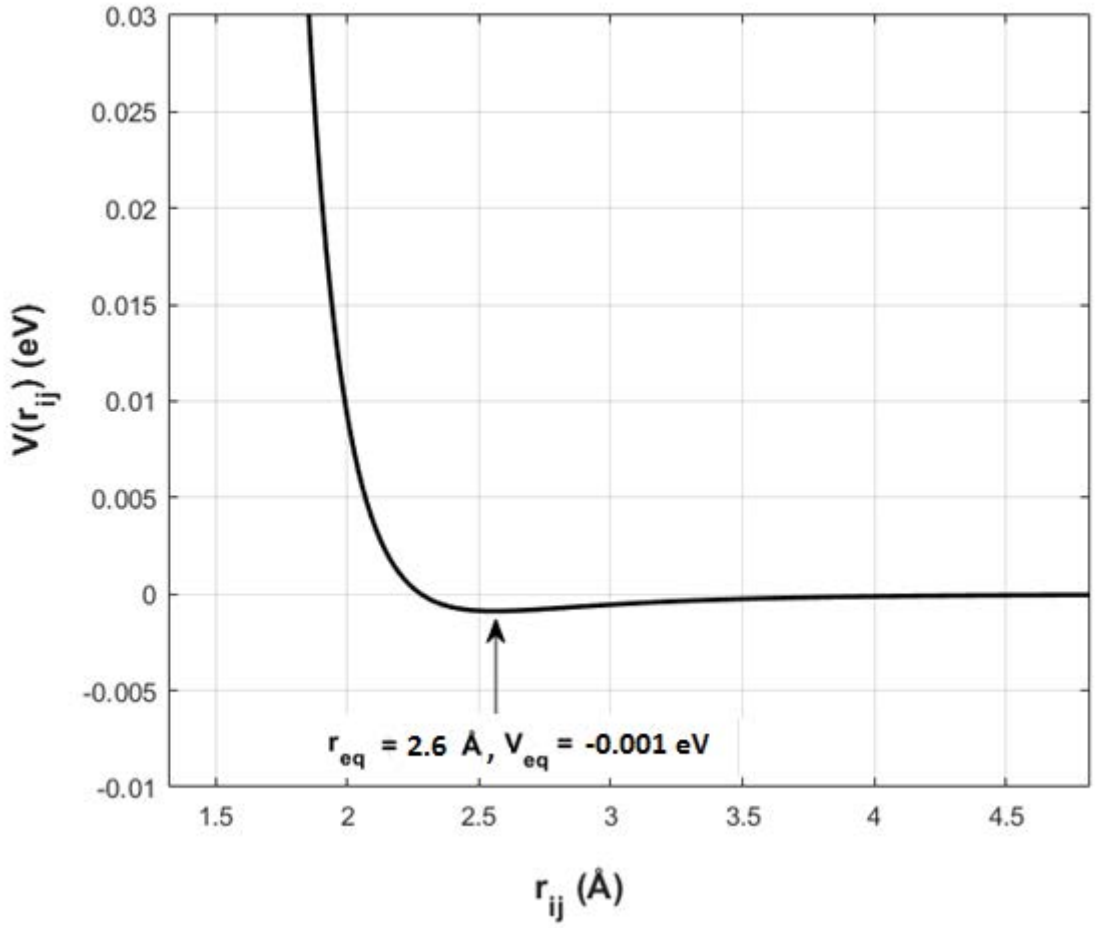


**Figure 5.1: Graph of the He-He potential of Grimes et al. (1990).**

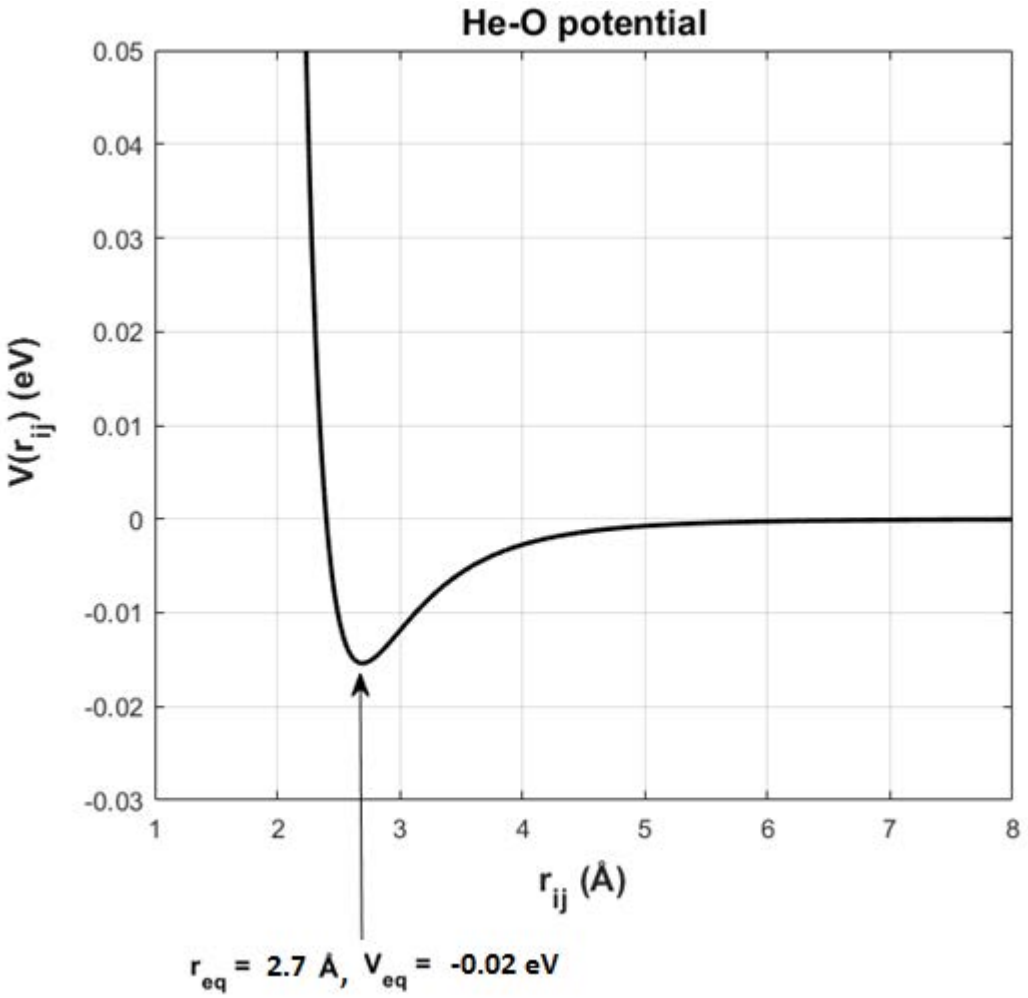


**Figure 5.2: Graph of the He-O potential of Grimes et al. (1990).**

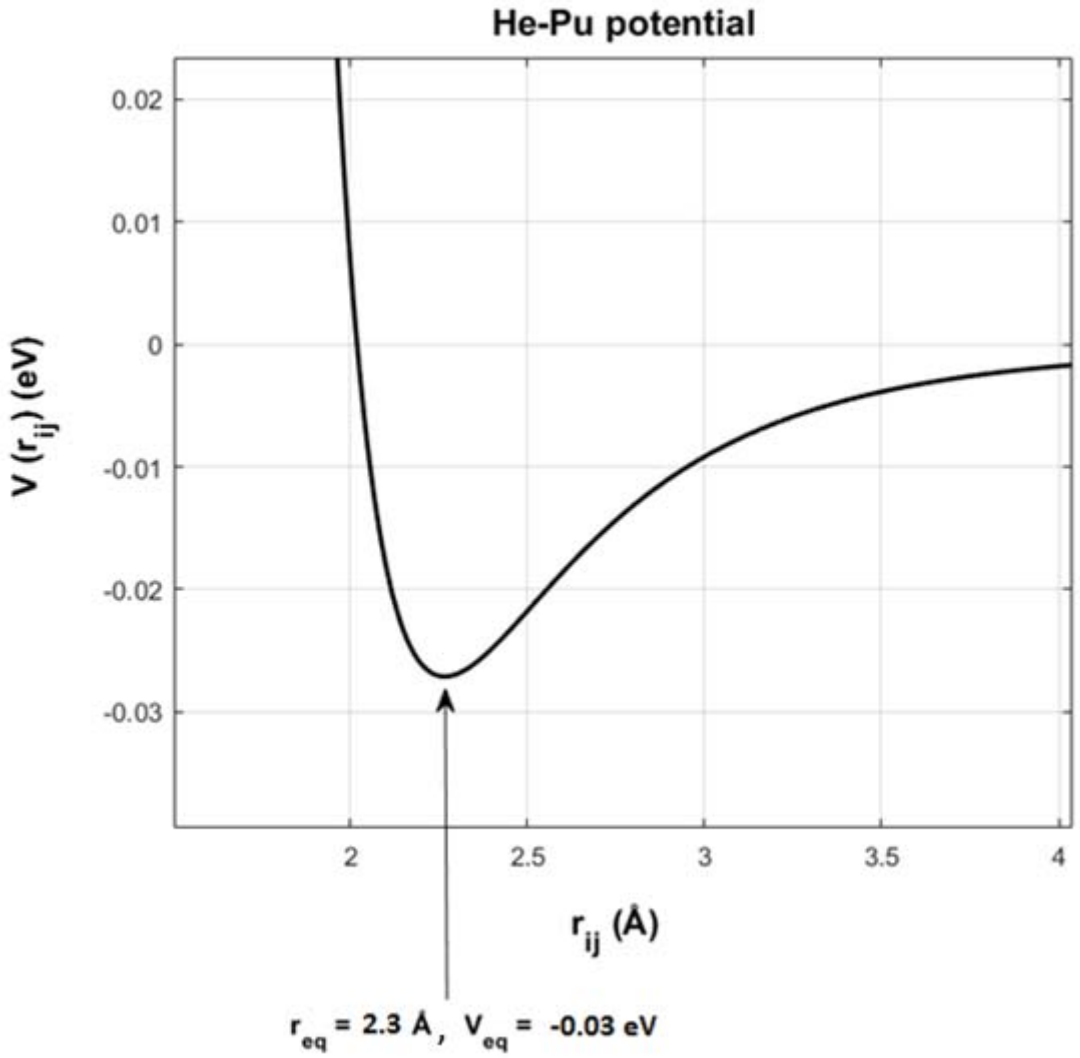


**Figure 5.3: Graph of the He-Pu potential of Grimes et al. (1990) (He-U in paper).**

### 5.2.3 Helium in Pure $PuO_2$

Firstly, helium incorporation energies in OISs were calculated. To investigate helium clustering, up to three helium atoms were positioned in a single OIS and binding energies per helium atom ($E_{He}^{B}$) calculated as the difference in the defect formation energy of the cluster of helium atoms ($E_{He,cluster}^{F}$) to that of individual separated helium atoms in OISs ($N_{He}E_{He}^{F}$), divided by the number of helium atoms ($n_{He}$), given by:

$$E_{He}^{B} = \frac{E_{D,cluster}^{F} - N_{He}E_{He}^{F}}{N_{He}} \quad \textbf{(5.2)}$$

For a single helium atom in an OIS, the binding energy is equivalent to the incorporation energy. The calculated and reported helium defect formation and binding energies are summarised in Table 5.2.

**Table 5.2: Defect formation ($E_D^F$) and binding energies ($E_{He}^B$) of helium atom(s) trapped in a single OIS in $PuO_2$.**

| Number of Helium Atoms in OIS | Calculated $E_D^F$ (eV) | Calculated $E_{He}^B$ (eV) | Reported $E_D^F$ (eV) |
|---|---|---|---|
| **1** | -0.07 | 0.0 | 2.73[a], 0.45[b], 1.02[c], -0.1[d], 0.4[e], -0.1[e*], 1.3[f], -0.1[g] |
| **2** | 1.68 | 0.91 | - |
| **3** | 3.18 | 1.13 | - |

**a-Tian et al. (2013) [126], ab-initio, $PuO_2$, b- Yakub et al. (2010) [134], potentials, $UO_{2+x}$, c- Gryaznov et al. (2010) [135], ab-initio, $PuO_2$, d- Govers et al. (2009) [131], potentials, $UO_2$, e- Freyss et al. (2006) [105], ab-initio, $PuO_2$, e*- Freyss et al. (2006) [105], ab-initio, $UO_2$, f- Crocombette (2002) [127], ab-initio, $UO_2$,**

**g- Grimes et al. (1990) [133], potentials, $UO_2$.**

## Analysis and Discussion

The defect formation and binding energies of the helium atom(s) in an OIS indicate that clustering is not energetically favourable. However, insertion of one helium atom is energetically favourable, although only weakly with a small exothermic incorporation energy of -0.07 eV, which corresponds to a temperature of about 540 K. Hence, below this temperature this trapping process would be effective.

The predicted incorporation energy from this work is in good agreement with three studies that predicted a value of -0.1 eV [131,105,133]. Addition of more helium atoms was predicted to be endothermic, with the helium clusters having much larger endothermic binding energies. In fact, for four helium atoms in an OIS the configuration was unstable as there was no energy minimum found. This would seem to contradict the observed clustering of helium atoms in $PuO_2$ [123] and $UO_2$ [124,136]. However, this phenomenon is strongly dependent on the temperature and the presence of defects in the material.

### 5.2.4 Helium in Defective $PuO_2$

Following simulations of helium trapping in pure $PuO_2$, simulations of helium entrapment in defective $PuO_2$ were performed. The trapping sites considered were oxygen and Pu vacancies and a Schottky defect. The helium untrapped and trapped defect configurations and corresponding defect formation energies are summarised in Table 5.3. The calculated and reported helium incorporation energies are summarised in Table 5.4.

**Table 5.3: Trapped and untrapped helium configurations and defect formation energies ($E_D^F$) in $PuO_2$.**

| Trapping Helium Defect | Helium Untrapped Configuration | Calculated $E_D^F$ (eV) | Helium Trapped Configuration | Calculated $E_D^F$ (eV) |
|---|---|---|---|---|
| **Oxygen vacancy, $V_O^{\blacksquare\blacksquare}$** | He (0.50, 0.50, 0.50), oxygen vacancy (0.25, 0.25, 0.25) | 17.45 | He in oxygen vacancy (0.25, 0.25, 0.25) | 16.90 |
| **Pu vacancy, $V_{Pu}^{////}$** | He (0.50, 0.50, 0.50), Pu vacancy (0.0, 0.0, 0.0) | 80.08 | He in Pu vacancy (0.0, 0.0, 0.0) | 79.84 |
| **Schottky** | $He_1$ (0.50, 0.0, 0.0), $He_2$ (0.50, 0.50, 0.50), $He_3$ (-0.50, -0.50, -0.50), Pu vacancy (0.0, 0.0, 0.0), $O_1$ vacancy (0.25, 0.25, 0.25), $O_2$ vacancy (-0.25, -0.25, -0.25) | 5.52 | $He_1$ in Pu vacancy (0.0, 0.0, 0.0), $He_2$ in $O_1$ vacancy (0.25, 0.25, 0.25), $He_3$ in $O_2$ vacancy (-0.25, -0.25, -0.25) | 5.00 |

**Table 5.4: Helium incorporation energies ($E_{He}^{Incorp}$) in defective $PuO_2$.**

| Trapping Helium Defect | Calculated $E_{He}^{Incorp}$ (eV) | Reported $E_{He}^{Incorp}$ (eV) |
|---|---|---|
| **Oxygen vacancy, $V_O^{\blacksquare\blacksquare}$** | -0.55 | 0.34[a] , -0.19 to -0.09[b], -0.5[c], 1.7[d], -0.23[e] |
| **Pu vacancy, $V_{Pu}^{////}$** | -0.24 | 0.36[a], -0.2 to 0.18[b], 0.7[c], 0.1[d] ,-0.2[e] |
| **Schottky** | -0.17 | 0.49[a] |

**a- Tian et al. (2013) [126], ab-initio, $PuO_2$, b- Govers et al. (2009) [131], potentials, $UO_2$, c- Freyss et al. (2006) [105], ab-initio, $PuO_2$, d- Crocombette (2002) [127], ab-initio, $UO_2$, e- Grimes et al. (1990) [133], potentials, $UO_2$.**

## Analysis and Discussion

The helium incorporation energies in the various defect sites give a measure of which trapping sites are preferred. Clearly, the oxygen vacancy was predicted to be the most energetically favoured trapping site, followed by the Pu vacancy, which has under half as much incorporation energy. This is as the oxygen vacancy provides a larger free volume than the Pu vacancy due to the difference in crystal radii. $O^{2-}$ ions have a crystal radius of 1.38 Å but $Pu^{4+}$ ions it is 1.14 Å [137].

Finally, helium incorporation in the Schottky defect was exothermic, and for stoichiometric $PuO_2$, this would be the preferred trapping defect, possibly forming a helium bubble nucleation centre. This is as the Schottky defect provides a large localised free volume for the helium atoms. Figure 5.4 shows the configuration of three helium atoms trapped in a Schottky defect.

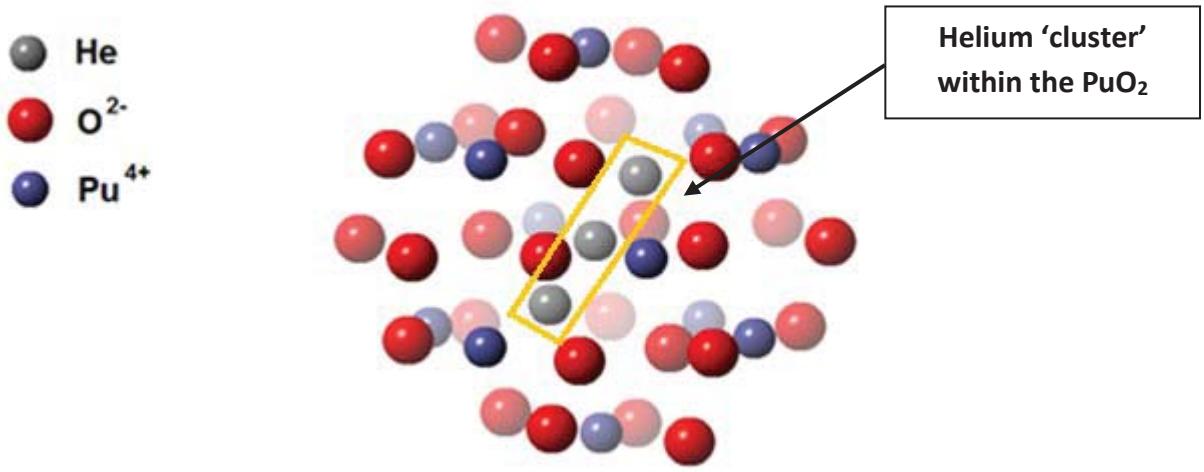


**Figure 5.4: Configuration of helium atoms (grey) trapped in a Schottky defect.**

### 5.2.5 Helium Migration

Thus far, the simulations of helium trapping had only considered the initial and final states of the helium atom(s) involved, from an OIS to a nearby vacancy. Hence, it has not considered the migration pathway of the helium atom(s). In reality, the least energetic pathways would be preferred. For the scenarios considered, a helium atom migrated very small distances (~1 Å) from an OIS to the nearest vacancies possible. For cases that involved trapping in oxygen vacancies, the helium atom started in a nearby OIS, so it is very probable that the helium atom would simply 'jump' to the vacancy.

However, for cases that involved trapping in Pu vacancies, the helium atom would have to pass between oxygen atoms in the oxygen sub-lattice of $PuO_2$ before occupying a Pu vacancy. This migration would cause localised strain in the lattice. The migration path would be characterised by a transition state with an associated 'energy barrier' or activation energy ($E_{Act}$). The helium atoms would need to have sufficient kinetic energy to overcome this barrier. This would occur with a

transition state probability ($Pr_{TS}$) proportional to the corresponding Boltzmann factor, given by:

$$Pr_{TS} \propto e^{-\frac{E_{Act}}{k_B T}} \quad \textbf{(5.3)}$$

Determination of the transition state position and the associated activation energy is important to determine favoured migration mechanisms. These parameters were calculated for helium migration from an OIS to a Pu vacancy and to another OIS. The transition state position was assumed to be centred between two adjacent oxygen ions. The initial, transition state and final defect configurations and corresponding defect formation energies are summarised in Table 5.5. The calculated and reported helium migration activation energies are summarised in Table 5.6.

**Table 5.5: Helium migration defect formation energies ($E_D^F$) in $PuO_2$.**

| Trapping Helium Defect | Helium Untrapped configuration | Calculated $E_D^F$ (eV) | Transition State Configuration | Helium Trapped Configuration | Calculated $E_D^F$ (eV) |
|---|---|---|---|---|---|
| **Pu vacancy, $V_{Pu}^{////}$** | He (0.50, 0.50, 0.50), Pu vacancy (0.0, 0.0, 0.0) | 80.08 | He (0.50, 0.25, 0.25), Pu vacancy (0.0, 0.0, 0.0) | He in Pu vacancy (0.0, 0.0, 0.0) | 79.84 |
| **OIS** | He (0.50, 0.50, 0.50) | -0.07 | He (0.50, 0.25, 0.25) | He (0.50, 0.0, 0.0) | -0.07 |

**Table 5.6: Helium migration activation energies ($E_{Act}$) in $PuO_2$.**

| Helium Transition Site | Calculated $E_{Act}$ (eV) | Reported $E_{Act}$ (eV) |
|---|---|---|
| **Pu vacancy, $V_{Pu}^{////}$** | 4.18 | 1.9[a], 4.15[b], 2.56[c], 2.26-3.5[d], 1.36-1.75[e], 0.56- 0.65[e*], 1.73-1.99[f], 3.04[f*], 1.93[g], 3.8[h] |
| **OIS** | 3.51 | |

**a-Talip et al. (2014) [138], exp, 750-2200°C, $Pu^{238}$ doped $UO_2$, b- Dabrowski et al. (2014) [130], ab-initio, $UO_2$, c- Yakub et al. (2010) [134], potentials, $UO_{2+x}$, d- Govers et al. (2009) [131], potentials, $UO_2$, e- Roudil et al. (2008) [139], exp, 100-300°C, natural U oxides, e*- Roudil et al. (2008) [139], exp, 300-1000°C, natural U oxides, f- Ronchi et al. (2004) [123], exp, up to 2100°C, f*- Ronchi et al. (2004) [123], exp, up to 2100°C for high burn up nuclear fuel, g- Trocellier et al. (2003) [124], exp, 300-1000°C, $UO_2$), h- Grimes et al. (1990) [133], potentials, $UO_2$.**

## Analysis and Discussion

The results show that short migration pathways have relatively large migration energy barriers of a few eV. The helium atoms would need to acquire at least the activation energy to overcome such a barrier. For helium atom migration between OISs in pure $PuO_2$, there is zero energy difference between the initial and final configurations, indicating helium atoms would remain in the OIS.

Reported theoretical data of the activation energy, including from this works, tend to overestimate compared to experimental data. The closest agreement to the calculated value of 3.51 eV is 3.04 eV from experiments of Ronchi et al. (2004) [123] in highly irradiated nuclear fuel. However, many theoretical studies have shown vacancy assisted helium migration pathways significantly lower the activation energies, which would be in closer agreement with other experimental data.

## 5.3 Helium on the (111) Surface

The (111) surface dominates the equilibrium morphology of $PuO_2$, being the lowest energy surface. Hence, following construction of the pure (111) surface, simulations of helium incorporation on the pure and defective surface were performed. Helium atoms were positioned in randomly located trapping sites within region 1 of the surface, at a 'defect depth'. This is the distance from the top of the surface to the centre of the defect configuration.

Helium incorporation energies were calculated as for the bulk, which are summarised in Table 5.7. In addition, the transition state energy was calculated as 3.45 eV when a helium atom was positioned between two adjacent oxygen ions, at a depth of 10.13 Å, which is very similar to the bulk value of 3.51 eV. This is due to the comparable structure of the (111) surface to that of the bulk lattice.

**Table 5.7: Helium incorporation energies ($E_{He}^{Incorp}$) in the pure and defective (111) $PuO_2$ surface.**

| Helium Trapping Site | Defect Depth (Å) | | Calculated $E_{He,Surf}^{Incorp}$ (eV) | Calculated $E_{He,Bulk}^{Incorp}$ (eV) |
|---|---|---|---|---|
| | Untrapped | Trapped | | |
| **OIS** | 21.04 | | -0.07 | -0.07 |
| **Oxygen vacancy, $V_O^{\blacksquare\blacksquare}$** | 5.89 | 0.10 | -3.97 | -0.55 |
| **Pu vacancy, $V_{Pu}^{////}$** | 6.24 | 0.78 | -3.69 | -0.24 |
| **Schottky defect** | 5.75 | 0.33 | -1.59 | -0.17 |

### Analysis and Discussion

For helium incorporation in the pure (111) surface, there is no energetic favourability in OISs compared to in the bulk lattice, both having the same incorporation energy of -0.07 eV. This is due to the structure of the surface being very similar to the bulk lattice, which also explains the comparable transition state energy for the surface to the bulk lattice.

However, the calculated helium incorporation energies for individual vacancies and Schottky defects are approximately an order of magnitude more exothermic for the surface than in the bulk lattice of around -1 eV. Hence, helium atoms would prefer to be trapped in surface vacancies and Schottky defects rather than those in the bulk lattice. For stoichiometric $PuO_2$, Schottky defects are the most favourable type of intrinsic defect, with negative segregation energies for the (111) surface. Hence, helium segregation (and possible release) is predicted to defective surfaces.

## 5.4 Summary

In summary, static lattice simulations were performed to investigate helium incorporation in pure and defective $PuO_2$. OISs, lattice vacancies and Schottky defects were the helium trapping sites modelled. Incorporation energies were calculated, which showed that a single helium atom insertion in an OIS in $PuO_2$ is weakly exothermic, but addition of more helium atoms is endothermic. Occupation of a helium atom in an oxygen vacancy is preferred over a Pu vacancy, due to the larger free volume available. However, in stoichiometric $PuO_2$, it was predicted that OISs and Schottky defects are the energetically preferred trapping sites, possibly forming effective helium bubble nucleation centres.

In addition, short migration pathways of a helium atom were modelled, consisting of helium migration from an OIS to a Pu vacancy or another OIS. In particular, the activation energies of migration associated with the transition state were predicted which were a few eV. These are appreciable sized energies and would present a limiting factor for helium migration in $PuO_2$. However, the presence of vacancies and thermal effects would likely reduce the activation energies significantly.

Helium incorporation in the pure and defective (111) surface was also modelled as for the bulk lattice. It was calculated there is the same incorporation energy within OISs of the pure (111) surface compared to the bulk lattice of -0.07 eV. However, helium trapping in individual vacancies and Schottky defects was shown to be an order of magnitude more exothermic for the surface than that of the bulk lattice, contributing to helium segregation to the surface.

# Chapter 6

# Thermal Properties of $PuO_2$

## 6.1 Literature Review

Understanding of the thermal properties of nuclear materials is important due to the high temperate gradients experienced both in reactor and storage conditions. The temperature gradients in reactor fuel can be very large, in excess of 2000 K, which is partly due to the relatively low thermal conductivity of the actinide oxide fuel [140]. This, in addition to the high radiation fields of the reactor core, can lead to fuel restructuring affecting the thermomechanical properties. These properties include thermal expansion coefficients, heat capacity and thermal conductivity. Prediction of these properties is also important to understand the 'pellet-cladding interaction' (PCI) in nuclear reactors [141] which would affect the durability and performance of the fuel in terms of heat transfer to the primary coolant.

A number of actinide oxides adopt the fluorite structure; $UO_2$, $PuO_2$, $ThO_2$ etc. At sufficiently high temperatures, they can become super ionic conductors. This is known as the 'Bredig' or λ transition [142] , and is reported to occur at ~80% of the melting temperature, and is characterised by peaks in the heat capacity, thermal linear expansion coefficient and a rapid disordering of the oxygen sub-lattice [141] . In storage conditions, many nuclear materials, including $PuO_2$, are self-heating due to the alpha decay of the nuclei of actinide atoms. This can lead to relatively large temperature gradients in the material, affecting thermomechanical properties. Understanding of these effects is needed to help underpin effective management of stored nuclear material in the long term.

Despite the importance thermal properties of nuclear materials, experimental efforts are hindered by their radiotoxicity, and hence difficulty in making reliable measurements. Atomistic simulations, in particular molecular dynamics, have provided a useful method to predict thermal properties of nuclear materials. Molecular dynamics is well suited to modelling systems in thermal equilibrium, with the system in an ensemble representing the macrostate of the system, with certain thermodynamic quantities conserved. This enables ensemble averages at a given temperature and pressure to be calculated, including thermal properties.

Many of the molecular dynamics studies relating to $PuO_2$, have focussed on prediction of thermal properties of mixed oxide (MOX) fuel and $UO_2$. Matsumoto et al. (2015) [140] performed non-equilibrium molecular dynamics on $UO_2$, $PuO_2$ and MOX fuel with 20 at. % Pu content ($U_{0.8}Pu_{0.2}O_2$ ) to predict the thermal conductivity over a temperature gradient, over 300 K to 2000 K. Their predictions of the thermal conductivity as a function of temperature were in good agreement with the literature. They predicted that the thermal conductivity was slightly smaller for MOX fuel than $UO_2$ or $PuO_2$, due to the phonon-lattice interactions, with plutonium atoms acting as phonon scattering centres.

Cooper et al. (2015) [143] used molecular dynamics to predict thermophysical properties and oxygen transport in the mixed oxide $U_xPu_{1-x}O_2$, over 300 K to 3200 K. In the temperature range of 2200 K to 2900 K, they predicted different 'superionic' transition temperatures for different MOX solid solutions. They showed that the Bredig peak in the heat capacity decreased with increasing plutonium content, which was predicted for $PuO_2$ at 2300 K, in contrast to other studies in not predicting a peak for $PuO_2$. They also predicted reduced oxygen defect formation enthalpies in MOX solid solutions than $UO_2$ or $PuO_2$. At high temperatures, there was a large increase in oxygen diffusivity, characterised by increased oxygen sub-lattice disorder.

In addition, Cooper at al. (2014) [33] developed robust many-body potentials to model thermomechanical properties of a range of fluorite structured actinide oxides. These included (Am, Ce, Cm, Np, Th, Pu, U)$O_2$. In their novel approach,

they incorporated a many body embedded atom model (EAM) in their potentials, which include other two-body potentials (Coulomb, Buckingham, and Morse). They fitted their potentials to basic structural and mechanical properties available at room temperature, with the EAM enabling reproduction of Cauchy's violation for the elastic constants ($C_{12} \neq C_{44}$) observed for fluorite-structured materials. Using molecular dynamics, they illustrated the accuracy of using their potentials to predict a range of thermomechanical properties from 300 K to 3000 K, to within ~10% of experimental data. In particular, their work predicted an accurate melting temperature of $UO_2$ of between 3000 K and 3100 K, which is in good agreement to the experimental value of 3150 K [144]. In addition, they noted that as the potentials accurately modelled the oxides at high temperatures, they would also be suitable for modelling high-energy damage cascades.

Clearly, the accuracy and reliability of atomistic simulations rely on the empirical potentials on which they are based. Potentials are derived using empirical fitting procedures to basic data of the material, with a domain of validity and applicability. However, they can also be assessed in terms of how well they predict properties not used in the fitting. Balboa et al. (2017) [32] chose five rigid-ion potentials and assessed them based on their prediction of thermomechanical properties of MOX solid solutions, from 300 K to the melting temperature over the full range of plutonium content.

From extensive testing based on molecular dynamics, they concluded the Potashnikov et al. (2011) [145] and Cooper et al. (2014) potentials were the most accurate. The Cooper et al. set was considered most suitable for prediction of thermomechanical properties, which predicted ductile like behaviour during crack propagation. This was closely followed by the Potashnikov et al. potentials, which accurately predicted brittle like behaviour at low temperatures. Their work illustrated the strong dependence on the potentials used, as the Yamada et al. (2000) [96] set predicted an unrealistic phase transition of $PuO_2$ around 1800 K and the Tiwary et al. (2011) [146] potentials were only suitable for static lattice simulations.

Kurosaki et al. (2001) [141] and Yamada et al. (2000) did very similar molecular dynamics simulations to predict physicochemical properties of $UO_2$, $PuO_2$ and MOX fuel with 20 at.% Pu content ($U_{0.8}Pu_{0.2}O_2$). They varied temperatures over 300 K to 2500 K and to calculate compressibility, the external pressure was varied from 0.1 MPa to 1.5 MPa in thermal equilibrium conditions. They predicted the Bredig transition for $UO_2$ at temperature 2350 °C, with super ionic behaviour predicted at 2500 K, near the 2610 K observed [147] which is in agreement with neutron scattering experiments [148] . This phenomenon was also predicted for the MOX solid solution at a similar temperature, but not for $PuO_2$, even at 2500 K (94% the melting temperature), which is in agreement with experiments. However, for $PuO_2$, it is possible the Bredig transition occurs even closer to the melting temperature. This is in contrast to molecular dynamics simulations by Cooper et al. (2015) who predicted a Bredig transition temperature of 2300 K for $PuO_2$, which is ~80% of the melting temperature.

Arima et al. (2005) [81] performed molecular dynamics simulations of $UO_2$ and $PuO_2$ to predict thermal properties. They employed a partially ionic model (PIM) over a temperature range of 300 K to 2000 K. They accurately predicted the thermal expansion and their predicted thermal conductivity agreed with experimental data above 500 K. They underestimated the experimental constant pressure heat capacity, and more so for $PuO_2$. They explained this is due to the Schottky defect, small polaron and Frenkel defect contributions to the heat capacity, which are sensitive to temperature and the complex 5f electron behaviour of $PuO_2$.

Mingjie et al. (2012) [80] performed molecular dynamics which predicted thermal properties of $PuO_2$ over 300 K to 3000 K. Using the potentials by Arima et al. (2005) they predicted these properties accurately, and determined empirical fitted equations of the lattice constant and constant pressure heat capacity as a function of temperature. They showed the sensitivity of the predicted melting temperature to the modelling method. By heating a solid supercell of $PuO_2$ and predicting density variation, this ‘one-phase simulation’ (OPS), significantly overestimated the experimental melting temperature of $PuO_2$.

However, a 'two-phase simulation' (TPS) increased accuracy. It involved a simulation cell consisting of solid and liquid phases, which were equilibrated at different temperatures. From the density results, they predicted a much more accurate melting temperature of 3320±10 K, which is close to the experimental value obtained by De Bruycker et al. (2010) [149]. The TPS approach was also used by Cooper et al. (2014), who accurately predicted the melting temperature of $UO_2$.

Overall, there have been a number of molecular dynamics based studies investigating the thermal properties of actinide oxides and MOX fuel, typically over a large temperature range, from room temperature to the melting point. The simulation results have been shown to be sensitive to the potentials used, each having their own domain of validity. In addition, it appears from the literature, there has been more computational studies on $UO_2$ and MOX fuel, given their technological importance as nuclear fuels.

There have been relatively few studies of thermal properties of $PuO_2$, despite the importance to storage and in-reactor scenarios. This chapter focusses on molecular dynamics simulations predicting a range of thermal properties of $PuO_2$ from 300 K to 3000 K. Covering this large range of temperature allows prediction of the temperature dependence of $PuO_2$ applicable to a range of applications.

## 6.2 Simulation Details

Molecular dynamics simulations were performed using DL_POLY programme [150] to predict a range of thermal properties of $PuO_2$ over a large temperature range. The aim of this was to understand $PuO_2$ and also to assess the accuracy of two $PuO_2$ potentials. These potentials included the Read et al. (2014) [64] and Jackson et al. (1986) [91] (abbreviated Read et al.) set and Arima et al. (2005) and Inaba et al. (1999) [95] (abbreviated Arima et al.) set. The prior set is a fully-ionic model (FIM)

incorporating the shell model, whilst the latter is a partially ionic model (PIM) using ion cores with a charge of 67.5% of the oxidation state.

To assess the potentials, the simulation results were compared to available experimental data. This is necessary to decide which potentials to use for further molecular dynamics simulations of radiation damage. The results included predictions of the temperature dependence of the lattice parameter ($a_0$), thermal linear expansion coefficient ($\alpha_T$), enthalpy ($H$), constant pressure heat capacity ($C_P$) and radial distribution function (RDF or $g(r)$) data.

Regarding the Arima et al. potentials, there are minima for the total Pu-O potential and for the short-range O-O potential. Due to the energy scales of the graphs to view the potential forms, these are not visible. For the Pu-O potential, the minimum is -23.83 eV and at an ionic separation of 1.98 Å. For the short-range O-O Buckingham potential, it is -0.001 eV at ionic separaton of 4.71 Å. However, with the addition of the O-O repulsive Coulomb potential, the total O-O potential has no minimum, and diverges as the ionic sparation tends to zero, due to the finite dispersion term. However, this is not the case for the Pu-O and Pu-Pu potentials as there is no dispersion term, and the total Pu-Pu potential is repulsive.

The molecular dynamics simulations performed were based on equilibration of the simulation cell at different temperatures at constant pressure in the Nose Hoover isothermal isobaric (NPT) ensemble. For the Read et al. potentials, the temperature range was 300 K to 2000 K and for the Arima et al. potentials, it was 298 K to 3000 K. The simulations were performed on a cubic 6 × 6 × 6 $PuO_2$ supercell, consisting of 2592 ions (864 Pu ions and 1728 oxygen ions). Three-dimensional periodic boundary conditions (PBCs) were applied to replicate an effectively infinite crystal.

Furthermore, the time step used in the simulations was one femto-second (1 fs), with data acquired every 10 time steps. The external pressure applied to the supercell was fixed at atmospheric pressure (1 atm). During equilibration, there was rescaling of the ions velocities every 50 time steps for the supercell to reach the desired temperature. To control the temperature and pressure, a thermostat and a barostat

were used with relaxation times of 0.5 ps and 0.1 ps respectively. The production phase followed the equilibration phase, from which ensemble averages were obtained. The length of the equilibration phase varied depending on the temperature, from 30 ps to 400 ps. The length of the production phase was twice that of the equilibration phase, with no velocity rescaling involved.

## 6.3 Thermal Linear Expansion

The calculated and experimental data of the lattice parameter ($a_0$) as a function of temperature is shown in Figure 6.1. From this, the thermal linear expansion coefficient ($\alpha_T$) was calculated from the partial derivative of the lattice parameter with respect to temperature at constant pressure, given by:

$$\alpha_T = \frac{1}{a_{0,298K}}\left(\frac{\partial a_0(T)}{\partial T}\right)_P \quad \textbf{(6.1)}$$

Hence, $\alpha_T$ gives the fractional change in the lattice parameter per unit increase in temperature. The calculated and experimental data of $\alpha_T$ as a function of temperature is shown in Figure 6.2. Experimental data for thermal expansion of $PuO_2$ is from Yamashita et al. (1997) [151] , from high temperature x-ray diffraction experiments from 298 K to 1300 K. Table 6.1 gives the calculated and reported experimental data of $\alpha_T$ at 298 K and 1200 K.

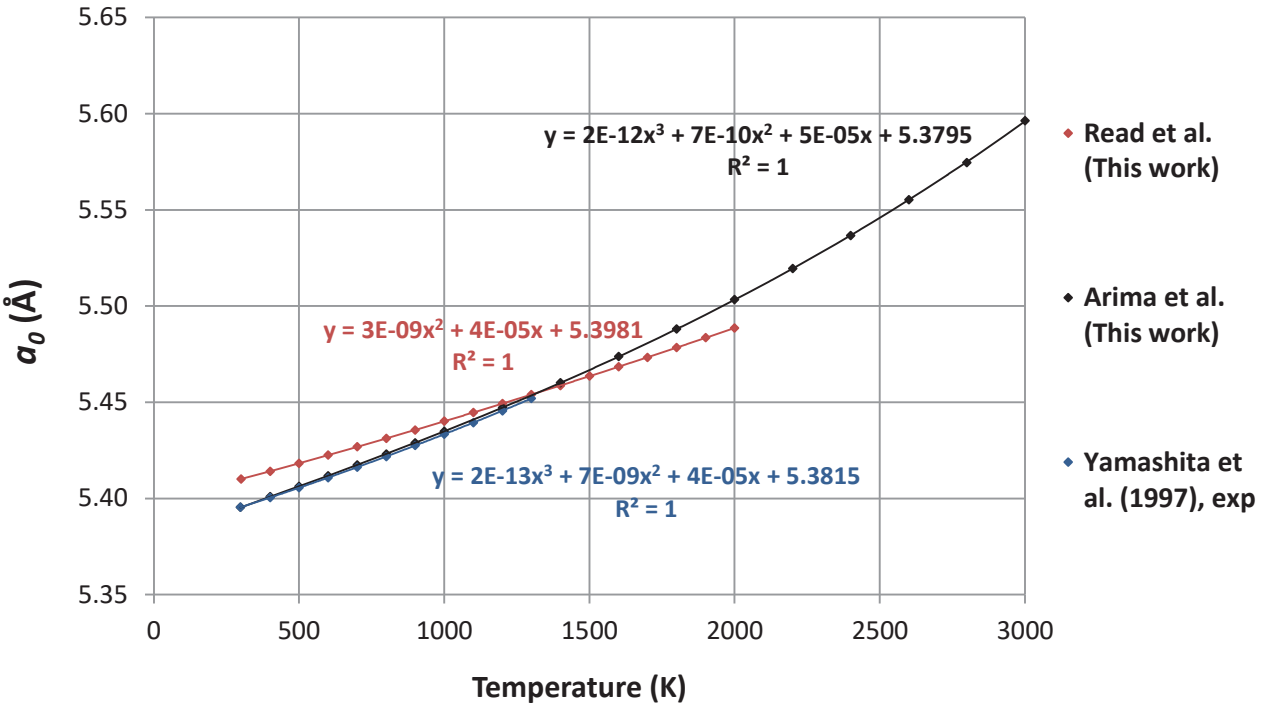


**Figure 6.1: Variation of the lattice parameter ($a_0$) of $PuO_2$ as a function of temperature.**

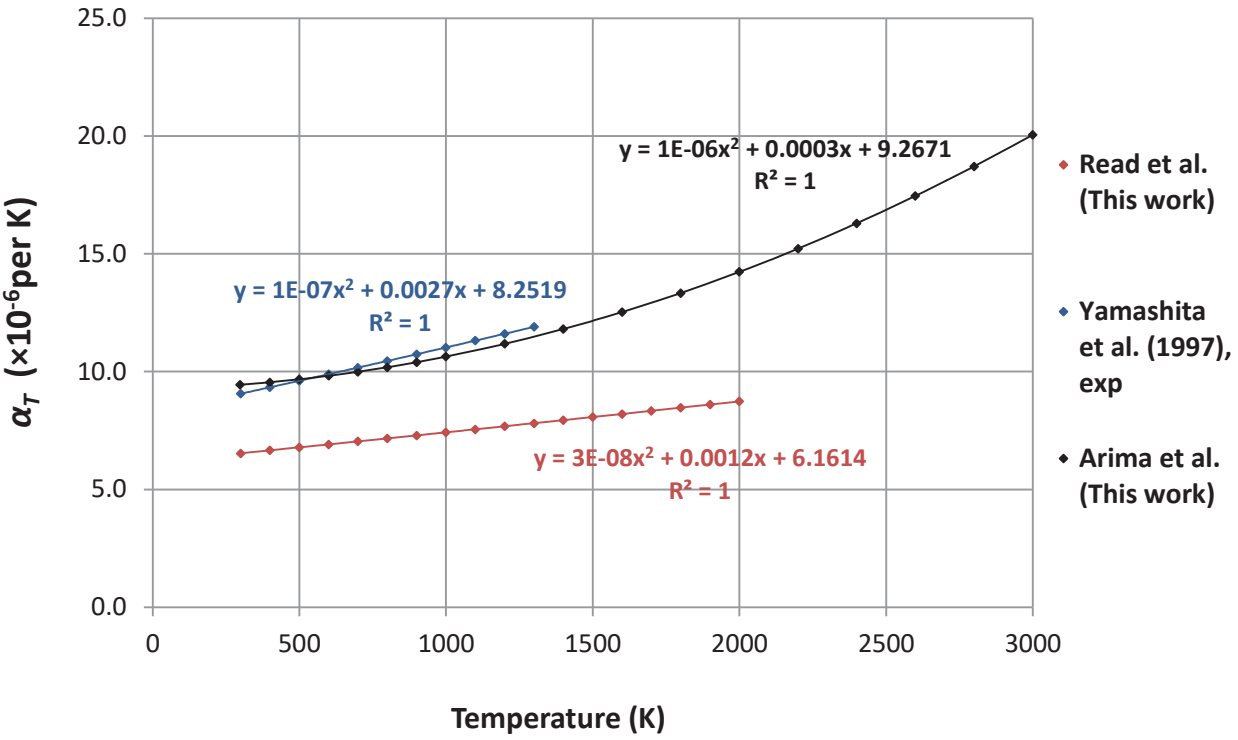


**Figure 6.2: Variation of $\alpha_T$ of $PuO_2$ as a function of temperature.**

**Table 6.1: Calculated and experimental $\alpha_T$ of $PuO_2$ at 298 K and 1200 K.**

| $\alpha_T$ at 298 K ($\times 10^{-6}$ per K) | | | $\alpha_T$ at 1200 K ($\times 10^{-6}$ per K) | | |
|---|---|---|---|---|---|
| Calculated | | Experimental | Calculated | | Experimental |
| Read et al. (This work) | Arima et al. (This work) | | Read et al. (This work) | Arima et al. (This work) | |
| 6.66 | 9.44 | 9.04[a], 8.84[b], 8.1[c], 8.4[d*], 8.71[e] | 7.81 | 11.18 | 11.61[a], 12.27[b], 12.0[c] 12.14[e] |

a- Yamashita et al. (1997) [151], b-Taylor (1984) [152], c- Touloukian et al. (1977) [153], d*- Marples (1976) [154] at 300K, e- Fahey et al. (1974) [155].

## Analysis and Discussion

The simulation results for thermal expansion show the sensitivity of the results to the potentials used. Overall, it is clear the Arima et al. potentials produce more accurate results than those of Read et al. From the calculation variation of $\alpha_T$, the Read et al. potentials underestimate the experimental data by over 20% from 300 K to 2000 K. In addition, the calculated lattice parameter overestimates up to 1300K and underestimates above this temperature.

However, the variation is less than ~0.5%. In contrast, the Arima et al. potentials perform better, agreeing almost exactly with experimental data for variation of the lattice parameter with temperature. The calculated variation in $\alpha_T$ is not as good, but acceptable, with the deviation from experiments less than ~10%. The Arima et al. potentials predict a change in the lattice parameter by only ~0.2 Å (or ~4%) over a 2700 K temperature range. This shows that $PuO_2$ is a thermally robust material, making it useful as a component of nuclear fuel.

The differing simulation results are due to the differences in the two potentials used. It was expected the Read et al. potentials would not perform well for this modelling, as they were fitted to data of one phase of $PuO_2$ at room temperature using static lattice calculations, so are unable to accurately predict thermal expansion behaviour. However, the Arima et al. potentials were fitted to experimental data on the thermal expansion of $CeO_2$, so it was expected to perform well in this modelling. Therefore, the Read et al. potentials were neglected in further molecular dynamics simulations of $PuO_2$.

## 6.4 Enthalpy and Constant Pressure Heat Capacity

Using the Arima et al. potentials, further molecular dynamics simulations were performed to calculate the enthalpy ($H$) and constant pressure heat capacity ($C_P$) of $PuO_2$. The temperature was varied from 298 K to 3000 K, with the external pressure 1 atm. The enthalpy ($H$) of a system in equilibrium at a constant pressure ($P$) and temperature ($T$) is given by:

$$H = U + PV \quad \textbf{(6.2)}$$

$U$ is the internal energy of the system, $P$ is the external pressure and $V$ is the volume. The amount of heat absorbed or released from the system is equal to the enthalpy, with the $PV$ term the amount of work done by the system against its environment. The calculated and experimental enthalpy as a function of temperature is shown in Figure 6.3. This was calculated as the difference in enthalpy per formula unit at temperature $T$ ($H(T)$) to that at 300 K ($H_{300K}$). Experimental data is from Oetting et al. (1982) [156] and Fink (1982) [157] .

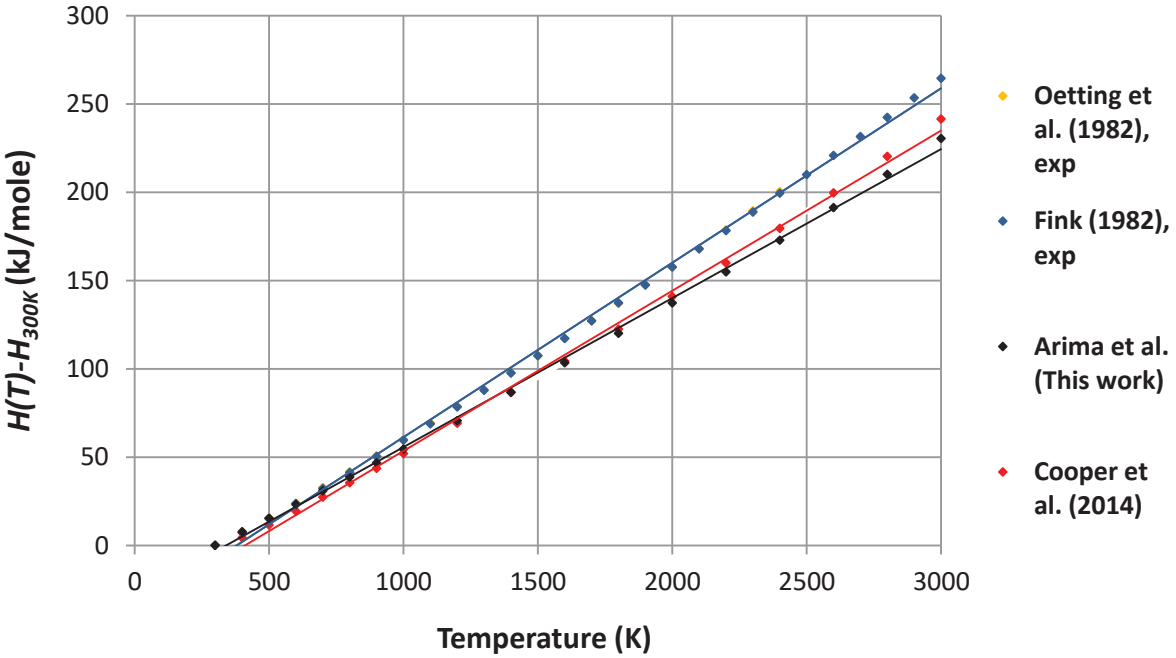


**Figure 6.3: Results of the variation of the enthalpy ($H$) of $PuO_2$ as a function of temperature.**

The constant pressure heat capacity ($C_P$) is the partial derivative of the enthalpy with respect to temperature, given by:

$$C_P = \left(\frac{\partial H}{\partial T}\right)_P \qquad (6.3)$$

$C_P$ is a measure of the amount of heat energy required to raise the temperature of a system in equilibrium by 1 K, at constant pressure. The calculated and experimental heat capacity as a function of temperature is shown in Figure 6.4. All of the data were fitted to functions that are of an appropriate form and obtain $R^2$ values closest to unity.

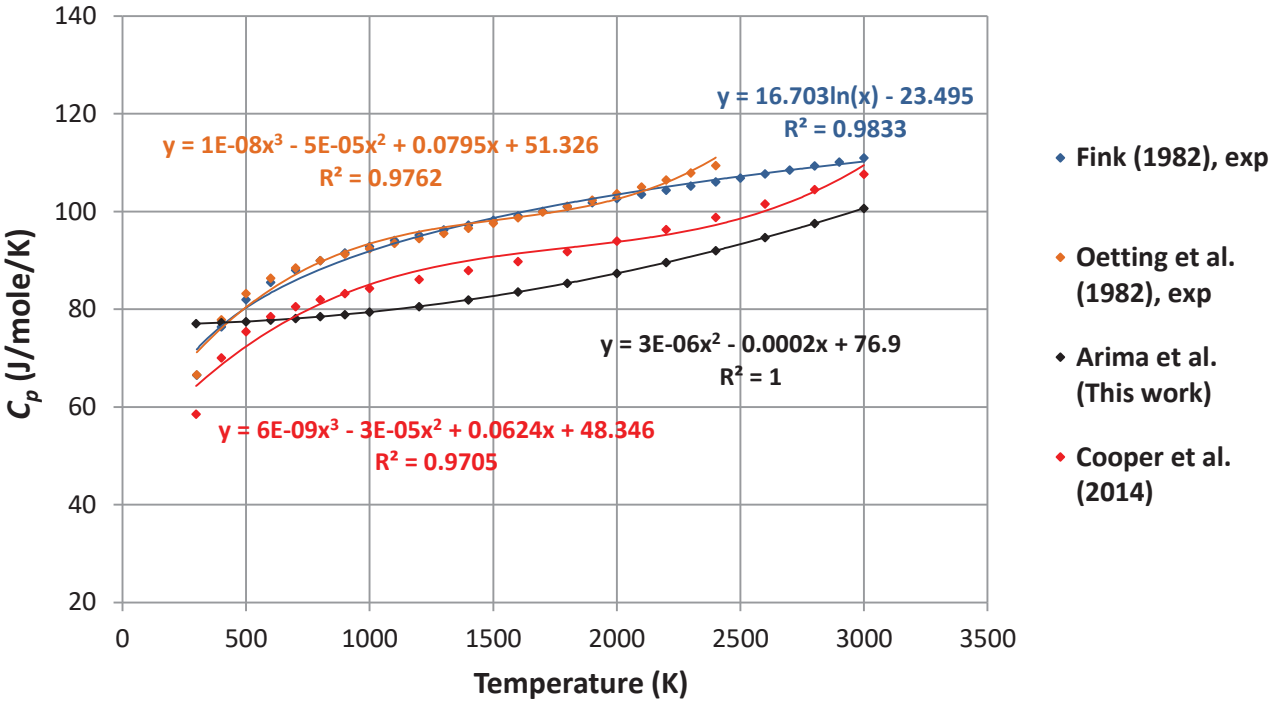


**Figure 6.4: Results of the variation of constant pressure heat capacity ($C_P$) of $PuO_2$ as a function of temperature.**

## Analysis and Discussion

$C_P$ is relatively large for $PuO_2$, showing a large amount of thermal energy is needed to raise the temperature. Although the Arima et al. potentials give a correct order of magnitude for $C_P$, the results underestimate the experimental data by ~10% to 20% and were fitted to a quadratic function. However, this quadratic dependence on temperature is not fully accurate as $C_P$ would tend to a large finite value as the temperature tends to zero, and does not show the expected curvature.

The Cooper et al. (2014) [100] potentials give improved agreement and their results fitted to a cubic, but also underestimate the experimental data. Although both of these potentials are PIMs, the Cooper et al. potentials incorporate many-body effects by using an embedded atom method, which could explain the better agreement with experimental data. In addition, Arima et al. reported that the contribution to $C_P$ by Schottky defects could be important for $PuO_2$.

## 6.5 Radial Distribution Function Spectra

From a molecular dynamics simulation, the radial (or pair) distribution function ($g(r)$) can be determined for the system of particles, be it a solid, liquid or gas. This parameter gives information on the structure and dynamics of the material on the atomic scale. It gives the relative probability of finding two particles separated by a radial distance between $r$ to $r + dr$ in the system. $g(r)$ is related to neutron and x-ray diffraction data by a Fourier transform, with the peaks of $g(r)$ spectra corresponding to peaks in the diffraction pattern. There is a $g(r)$ spectrum for each type of atomic pair in the system.

In the simulations presented, the $g(r)$ spectra for $PuO_2$ were determined at different temperatures over 298 K to 3000 K. This could be compared to experimental data or be used to predict the diffraction patterns of $PuO_2$ at different temperatures. Temperatures of 298 K, 600 K, 1000 K and 3000 K were considered. For $PuO_2$, there is the Pu-Pu, O-Pu and O-O ion pairs. In the simulations, the $g(r)$ data was collected every 10 time steps, each of 1 fs and the bin size for data collection was 0.01 Å for $r$ from zero Å to 15 Å inclusive. Figures 6.5 to 6.7 show the calculated $g(r)$ spectra for the ion pairs at different temperatures.

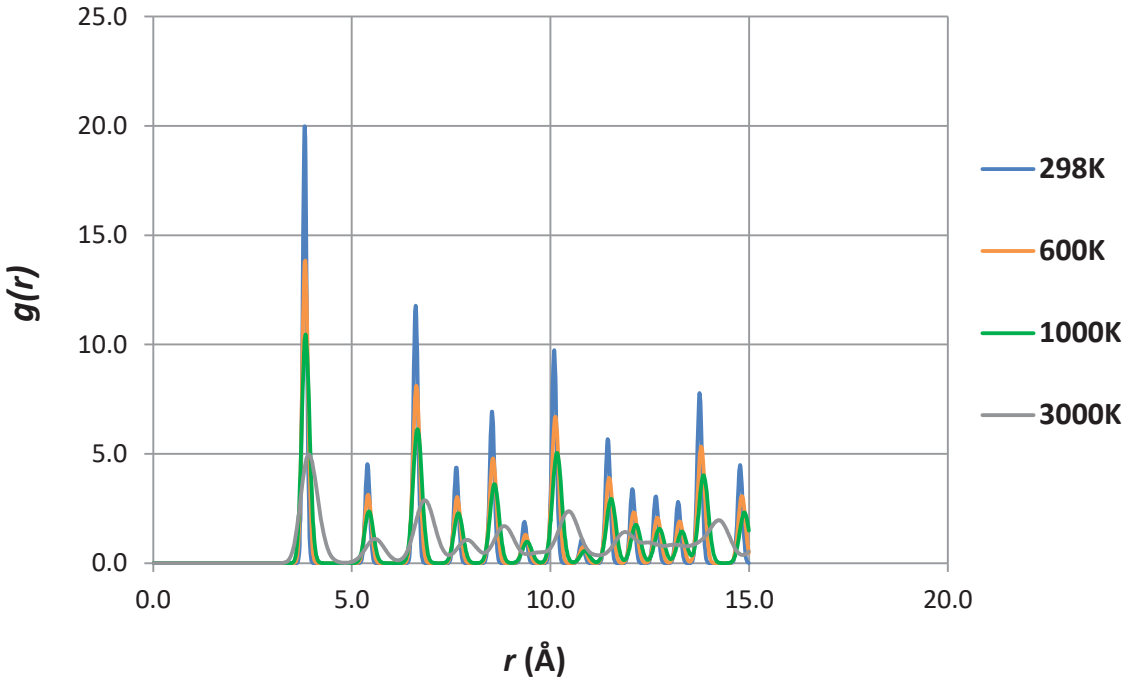


**Figure 6.5: $g(r)$ spectra for Pu-Pu pairs in pure $PuO_2$ at different temperatures.**

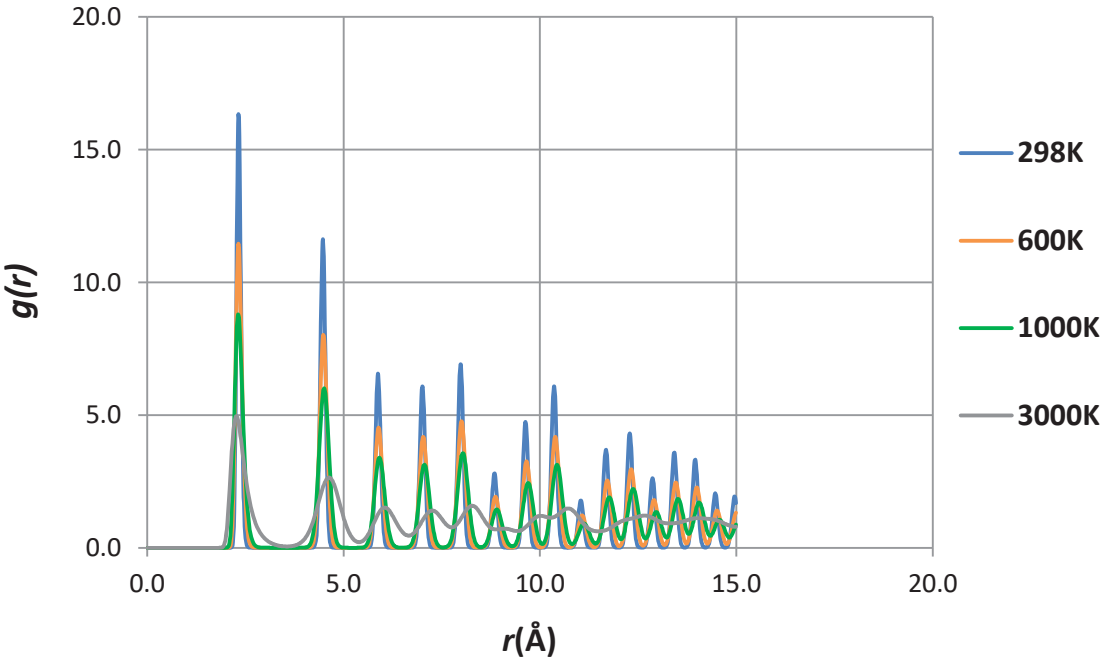


**Figure 6.6: $g(r)$ spectra for Pu-O pairs in pure $PuO_2$ at different temperatures.**

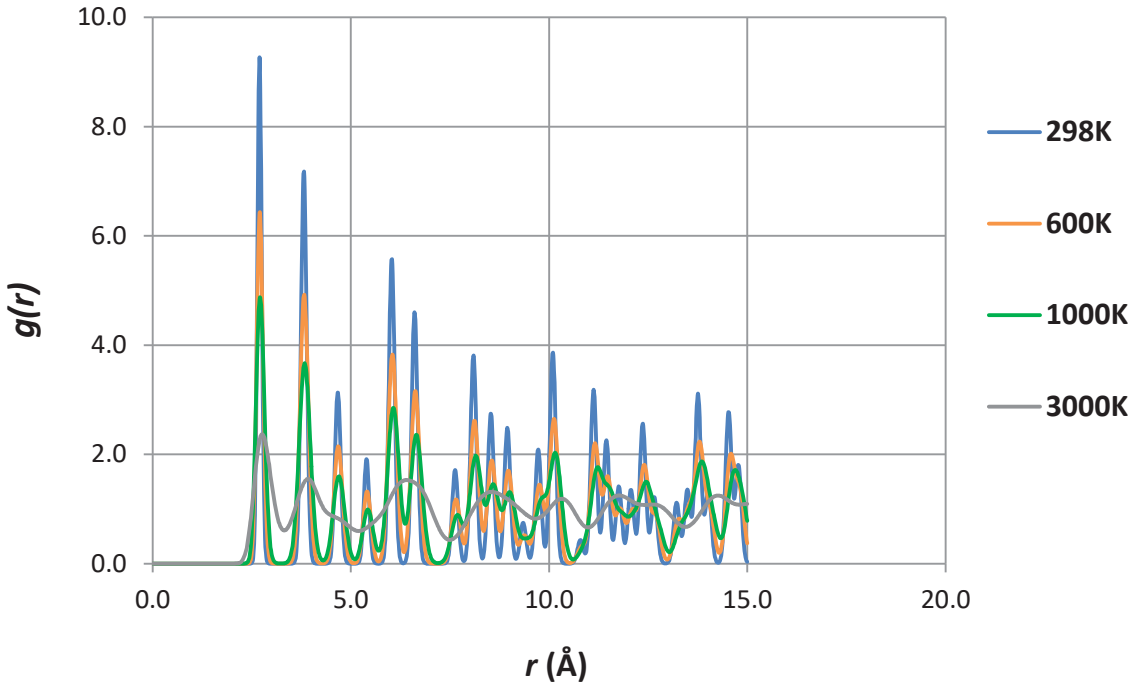


**Figure 6.7: $g(r)$ spectra for O-O pairs in pure $PuO_2$ at different temperatures.**

## Analysis and Discussion

The $g(r)$ spectra show the temperature dependence on the local structure of $PuO_2$. At 298 K, all three of the spectra for each pair shows clear, narrow peaks of fluorite structured $PuO_2$. As the temperature increases, the peak heights decrease and they broaden. This is due to the greater oscillatory motion of the ions and the reduction in the system density with increasing temperature. Hence, the probability of finding neighbouring atoms is randomised and reduced, explaining the peak broadening and the disappearance of some minor peaks with increasing temperature.

Furthermore, the $g(r)$ spectra illustrate the thermal resistance of $PuO_2$ with most of the peaks retained even at 1000 K, thus crystallinity and long-range order was preserved. In addition to the peak height reduction and broadening with increasing temperature, the peaks also shift slightly to larger $r$. This effect appears larger

for the Pu-Pu and Pu-O ion pairs, and is due to the relatively small thermal expansion of the $PuO_2$ lattice, which the Arima et al. potentials accurately predicted.

## 6.6 Summary

Overall, molecular dynamics simulations were performed to predict thermal expansion, enthalpy, constant pressure heat capacity and pair distribution functions of $PuO_2$ as a function of temperature from 298 K to 3000 K. This allowed assessment of the Read et al. and Arima et al. potentials incorporating temperature, by comparing to available experimental data. The Read et al. potentials were shown to be unsuitable for molecular dynamics simulations. For example, it underestimated thermal expansion of $PuO_2$ by over 20% over 300 K to 2000 K. However, this was expected as those potentials were not fitted to thermal expansion data, as oppose to the Arima et al. potentials. Indeed, the Arima et al. potentials performed much better overall, agreeing well with thermal expansion experimental data.

However, these potentials performed less well for predictions of the enthalpy and constant pressure heat capacity, underestimating the latter by ~10% to 20%. These deviations were probably due to the contributions of Schottky defects and multi-body effects that were not explicitly incorporated. The molecular dynamics simulations also produced $g(r)$ spectra of $PuO_2$ at temperatures 298 K, 600 K, 1000 K and 3000 K, which could be compared to experimental diffraction data. $PuO_2$ was shown to be a thermally robust material, with very small thermal expansion and preserved crystallinity evident from room temperature to close to the melting point. However, only thermal equilibrium situations of pure $PuO_2$ have been modelled, with radiation damage not incorporated. Radiation damage in $PuO_2$, originating from the alpha decay of Pu nuclei, will be the focus of the next chapter.

# Chapter 7

# 1 keV Cascades in $PuO_2$

## 7.1 Literature Review

Radiation damage in solids refers to the damage caused to the structure due to radiation, which can originate internally or externally. Radiation can take many forms including alpha decay, beta decay and gamma emission. All of these are relevant to nuclear materials, which are self-radioactive. Isotopes of the actinides including U and Pu undergo spontaneous alpha decay, in which a high-energy alpha particle (a helium nucleus) is emitted from the parent nucleus, which recoils to conserve momentum. The alpha particles have energies of a few MeV and the recoil atom energy is in the range 10-100 keV.

Particles with energies of MeV-GeV dissipate most of their energy through electron collisons, whereas those with energies of 10s of keV dissipate most of their energy through nuclear-based ballistic collisions. In ballistic collisions, the recoil atom causes most structural damage to the material, typically displacing ~1000 atoms per alpha decay [158]. This is because the recoil atom is much larger and heavier than the alpha particle with a much smaller range of ~10 nm compared to ~10 µm for the alpha particle [158]. Pu nuclei undergo alpha decay, emitting an alpha particle of energy ~5 MeV and a U daughter nucleus of energy ~86 keV. Many of the Pu isotopes relevant to storage are long-lived, with Pu-238 having the shortest half-life of 87.7 years [10]. The ease at which atoms are displaced will depend on their bonding and mass. This is quantified through the concept of 'displacement energy', which is the minimum energy needed to displace an atom to create a stable Frenkel pair.

The first atom the recoil atom hits is called the 'primary knock on atom' (PKA) which hits further atoms causing a displacement cascade in the material. After the initial impact of the PKA, there is a 'ballistic phase' which lasts a few pico seconds, which consists of a 'thermal spike' (at tenths of 1ps) where the local temperature is so high it induces local melting and long-range migration of energetic atoms. After this phase, there is a 'thermal phase', where the excess kinetic energy of the system is dissipated as it returns to thermal equilibrium, lasting tens of pico seconds. The displacement cascades consist of many Frenkel pairs, which peak during the ballistic phase. As the material has thermal energy, these may combine and disappear but some may remain causing structural modification to the material. This could affect macroscopic mechanical properties.

Fundamental understanding of the radiation damage is required to underpin safe and effective management of nuclear materials as fuel in a reactor or in storage forms. In light of its importance, the research in this area is considerable. Atomistic simulations have provided a useful tool partly as experiments are difficult due to the radiotoxicity of nuclear materials. They have also revealed information on length and time scales inaccessible to some experiments. This is particularly relevant to radiation damage simulations, where there is interest in the very early stages of the damage on the sub-pico second timescale. In addition, the energies involved in simulations are relevant, with recoil energies being in the range 10 keV to 100 keV, losing energy through ballistic collisions. The growth in computer power over recent years has facilitated computational studies of radiation damage, as the high-energy events require large simulation supercells.

There have been a multitude of computational studies on radiation damage over the last decade. Many nuclear materials of technological importance are binary fluorite structured oxides, which include $UO_2$, $AmO_2$, $PuO_2$, $ThO_2$ etc. It is known that these oxides are particularly robust to radiation damage making them useful as nuclear fuels [159]. However, it is not fully understood why this is the case in terms of the mechanisms involved in radiation damage on the atomic scale. Hence,

many atomistic simulations have been reported, in particular on $UO_2$. Typically, these consisted of molecular dynamics simulations to study the evolution of the radiation damage on the pico-second to nano-second time scales and nm length scales.

Essentially, there are two approaches to the modelling: one is to project a PKA in the simulation supercell in the NVE ensemble, the other is to artificially create defects to simulate the damage. In the first approach, typically, the PKA energy and direction are varied. In the second approach, the concentrations and types of defects are varied. In addition, the effect of system temperature is also investigated. In these potential based simulations, the conventional short-range potential is augmented by a Universal Ziegler-Biersack- Littmark (ZBL) [160] which is splined on to the short-range part at short interatomic distances. This is a screened Coulombic potential between nuclei, which is needed to accurately model high-energy ballistic collisions between ions.

Using molecular dynamics, Martin et al. (2015) [41] investigated the effect of the bulk temperature on the radiation damage in $UO_2$ from 700 K to 1800 K. For a 10 keV PKA, they showed the maximum radiation damage accommodated decreased with temperature. Although they predicted most Frenkel pairs would recombine, ~10% of each type remained on the timescales of the simulations. These eventually formed vacancy and interstitial clusters at the end of the simulations. In addition, the formation of these clusters was sensitive to temperature, with the so-called 'vacancy sweeping' mechanism less efficient at high temperatures (above 1000 K), hindering vacancy cluster formation and growth. In contrast, the so-called 'loop punching' mechanism was more efficient at high temperatures, promoting interstitial cluster formation and growth.

In another molecular dynamics study, Martin et al. (2014) [161] varied the energy of the PKA from 0.2 keV to 20 keV at 700 K and 1400 K. They showed that the number of defects is proportional to the PKA energy, in agreement with the Kinchen-Pease model (1955)[162]. They showed most of the defects annihilated after 20 ps, but some remained. In addition, they showed that the temperature had little effect

on the damage, which was linearly dependent on the PKA energy. Their earlier study [82] varied the PKA energy of from 1 keV to 80 keV at 300 K and 700 K. Sub-cascades and overlaps are more frequent at higher energy. The thermal spike resulted in a void at the centre of the displacement cascade, surrounded by interstitial clusters.

Aidhy et al. (2015) [88] modelled radiation damage in cubic zirconia ($ZrO_2$) and yttria (Yr) stabilised cubic $ZrO_2$ (YSZ) using molecular dynamics. YSZ adopts the fluorite structure and has been used as a surrogate to $UO_2$ and $PuO_2$. They introduced 100 Frenkel pairs per sub lattice in a 16 × 16 × 16 supercell at 1500 K for both $ZrO_2$ and YSZ. They evolved the systems over 60 ps, which revealed interstitial and vacancy clustering in $ZrO_2$. However, in YSZ, the $Y^{3+}$ ion doping introduces oxygen vacancies, which lead to much less Zr clustering. This is due to the reduced migration energy barriers in vacancy-assisted migration of Zr ions, increasing their diffusion.

In addition, Aidhy et al. (2011) [87] did molecular dynamics simulations on $CeO_2$ and $UO_2$. $CeO_2$ adopts the fluorite structure and has been used as a surrogate to $PuO_2$. They introduced 50 Frenkel pairs per sub-lattice in a 10 × 10 × 10 supercell at temperatures up to 1000 K. They evolved the system over 1 ns, revealing vacancy and interstitial clustering. However, there were differences in the type of defect clusters formed in the two compounds, which depended strongly on temperature.

In $CeO_2$, even at 300 K, charged cubo-octahedral clusters were formed in $CeO_2$ as the oxygen ions were mobile. This occured in $UO_2$ only at much higher temperatures, around 1000 K. In $CeO_2$ at 1000 K, both the Ce and oxygen ions were mobile, which led to the formation of Schottky defects and dislocation loops. The dislocation loops were characterised by an extra plane in the [111] direction. This was primarily due to the much lower mobility of the heavy U ions compared to the much lighter Ce ions. Hence, this study indicated the importance of cation diffusivity to defect clustering in defected fluorite structured oxides.

Other computational studies focussed on other aspects of the radiation damage. Tian et al. (2011) [163] performed molecular dynamics simulations of 10 keV U recoils in $UO_2$ introduced in four directions at 300 K. Their results showed that the

different directions had very little effect on the damage. These 10 ps simulations showed that an order of magnitude more oxygen atoms were displaced than U atoms, with oxygen atoms much more mobile. Furthermore, they showed most Frenkel pairs recombined, with a small fraction remaining at the end of the simulations. Although fractionally more oxygen Frenkel pairs recombined, about twice as many remained at the end of the simulation than U Frenkel pairs, reflecting the stoichiometry. This was because the oxygen ions are more easily displaced than U ions, even though they are more susceptible to recombine and restore the crystalline structure.

Finally, a computational study by Devanathan et al. (2009) [84] investigated the effect of potentials used in molecular dynamics simulations of radiation damage in $UO_2$. They used five published rigid ion potentials, which were typically fit to various equilibrium data and had different analytical forms. The simulations consisted of 1 keV PKA recoils over 15 ps. Many of the potentials gave results that agreed that $UO_2$ is a highly radiation tolerant material, with less than 10% of displaced atoms remaining as Frenkel pairs or defect clusters at the end of the simulations. However, the study highlighted the sensitivity of the simulation results on the potentials. The average displacement energy varied by about a factor of three and there were dramatic variations predicted in the spatial distribution and types of defects produced.

In summary, there has been a range of reported computational studies of radiation damage in $UO_2$ and surrogates, with relatively few on $PuO_2$. Pu isotopes of importance to stored $PuO_2$ undergo alpha decay. Hence, in long-term storage conditions, the self-irradiation dose could be significant, effecting material properties. This means understanding of the fundamental aspects of radiation damage in $PuO_2$ is needed for safe and effective management for long-term storage. One way to address this is use of molecular dynamics, which is the focus of this chapter. In particular, modelling of 1 keV cascades in $PuO_2$ will be presented, analysing the temperature and defect evolution in the material.

## 7.2 Simulation Details

Molecular dynamics simulations were performed to model 1 keV cascades in $PuO_2$ at 298 K and 700 K. Consequently, the Arima et al. (2005) [81] and Inaba et al. (1999) [95] (abbreviated Arima et al.) potentials were modified in order to accurately model the high-energy collisions between the ions. The Universal Ziegler-Biersack- Littmark (ZBL) [164] pair potential was used, which is a short-range repulsive exponential function. It is a function of interatomic separation and the charges of the ions, acting at sub-Å separations.

For each ion pair, the ZBL potential is connected to the lower energy Buckingham potentials by a spline function, which is a parameterised exponential fifth order polynomial function. The parameters of the spline function are determined by boundary conditions of the transition region. These conditions are that the total potential (electrostatic and Buckingham potentials) and their first and second derivatives are continuous at the boundaries of the transition region. These conditions ensure energy and momentum conservation at the boundary points. It is also important to ensure the total potential and its derivative (i.e. the force) is smooth over the transition region.

ZBL potentials were added to the O-Pu and O-O Arima et al. potentials, but not to the Pu-Pu ion pair as for this pair it is a purely electrostatic potential. Hence, the spline function was used and splining parameters were calculated for the O-Pu and O-O ion pairs. For both of these pairs, the ZBL potentials acted at a separation of less than 1 Å. The transition region acted over the range 1 Å to 2 Å, which ensured the total potentials and derivatives were sufficiently smooth. The accuracy of the modified potentials was assessed by equilibrating a $6 \times 6 \times 6$ $PuO_2$ supercell at 298 K and results comparing to those using the un-modified potentials. There was no significant difference in the simulation results, which showed the modified potentials were suitable for further simulations.

The simulations of 1 keV cascades used a cubic 12 × 12 × 12 $PuO_2$ supercell, which consisted of 20736 ions (6912 Pu ions and 13824 oxygen ions). Periodic boundary conditions (PBCs) were used to replicate an effectively infinite crystal. The time step used in the simulations was 1 femto second (1 fs), with data acquired every 10 time steps. Firstly, the supercell was equilibrated to a desired temperature (either 298 K or 700 K) over 100 ps (using a time step of 1 fs) in the Nose Hoover isothermal isobaric (NPT) ensemble. The external pressure applied to the supercell was fixed at 1 atm.

Furthermore, rescaling of ion velocities was performed for the first 50 ps and done every 50 time steps for the supercell to reach the desired temperature. In addition, a thermostat and a barostat were used with relaxation times of 0.5 ps and 0.1 ps respectively. Following the equilibration phase, there was the cascade phase in the micro canonical (NVE) ensemble over 50 ps, with no velocity rescaling. The cascade was initiated by projection of a 1 keV Pu projectile (simulating the primary knock-on atom (PKA)) from the centre of the supercell in the [111] direction. Following the cascade phase, there was another equilibration phase identical to the initial equilibration phase to restore the supercell to thermal equilibrium.

From these simulations, there was a range of data collected relating to the cascade events at temperatures 298 K and 700 K. Of particular interest is the lattice damage evolution in terms of defects and the temperature variation over time. After projection of the Pu PKA, there is the 'ballistic phase', lasting a few pico seconds, which consists of a 'thermal spike' where the temperature peaks and there is long-range migration of ions. Focussing on initial temperatures of 298 K and 700 K, the effect of temperature will be analysed during the ballistic phase. To obtain detailed structural information, the pair distribution functions were calculated; using data collected every 10 time steps and a bin size of 0.01 Å over a radius from zero to 15 Å inclusive.

## 7.3 Temperature Evolution

### 7.3.1 Behaviour at 298 K

Prior to the cascade simulation, the 12 × 12 × 12 $PuO_2$ supercell was equilibrated to a temperature of 298 K. Then in the NVE ensemble, the 1 keV Pu PKA was projected from the centre of the supercell (at t = 0.01 ps). The kinetic energy of the system increased by an amount equal to the energy of the projectile of 1 keV. Figures 7.10 and 7.11 show the temperature variation over time at the beginning of the cascade phase.

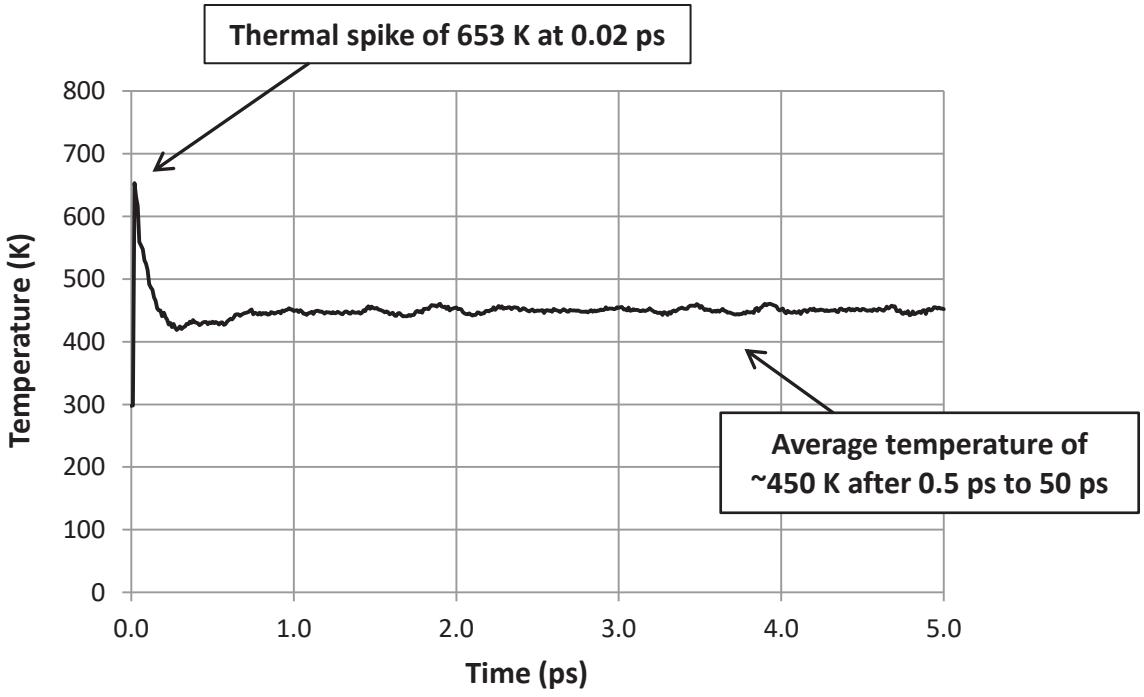


**Figure 7.10: Graph of the variation of system temperature over time during the first 5 ps of the cascade phase.**

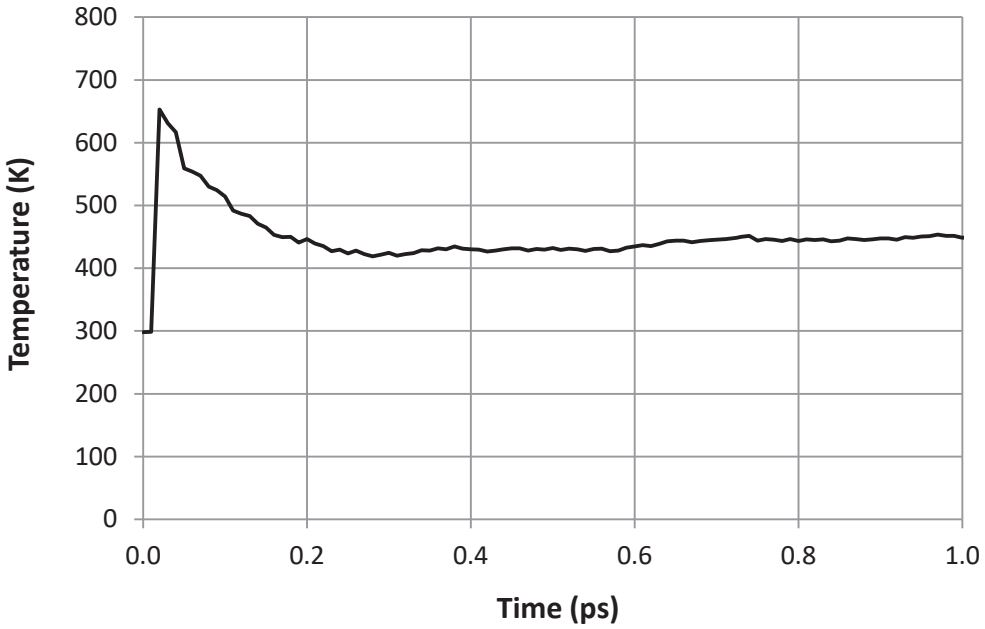


**Figure 7.11: Graph of the variation of the system temperature over time during the first 1 ps of the cascade phase.**

## Analysis and Discussion

The graphs show that there was a 'thermal spike' shown by the very rapid rise in the system temperature to 653 K which then decayed to an average of ~450 K for the rest of the cascade phase, an increase of 51% on the initial temperature of 298 K. The temperature peaked at 653 K at 0.02 ps which is 0.01 ps after the 1 keV cascade was initiated, an increase of 119% on the initial temperature. This shows the system responded very rapidly to the high-energy PKA.

In fact, after 0.28 ps, the system temperature decreased to a minimum of 419 K before rising again to an average of ~450 K after 0.5 ps. The decrease in the temperature was due to the exchange of kinetic energy with potential energy of the system. Following the cascade phase, there was another equilibration phase of 100 ps, identical to the initial equilibration. The first 50 ps of this phase involved rescaling of the ions velocities every 50 time steps. The temperature was restored to an average of ~300 K after 0.4 ps. Figures 7.12 and 7.13 show the large variations of the system

temperature during the first 0.2 ps of this equilibration phase, due to rapid velocity rescaling.

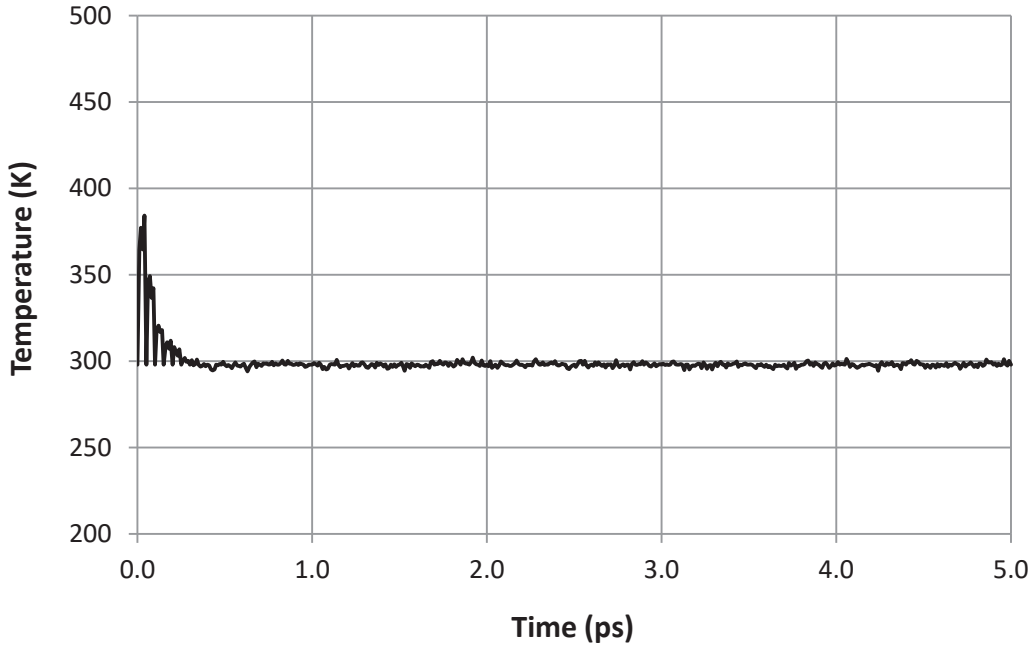


**Figure 7.12: Graph of the variation of system temperature over time during the first 5 ps of the post-cascade equilibration.**

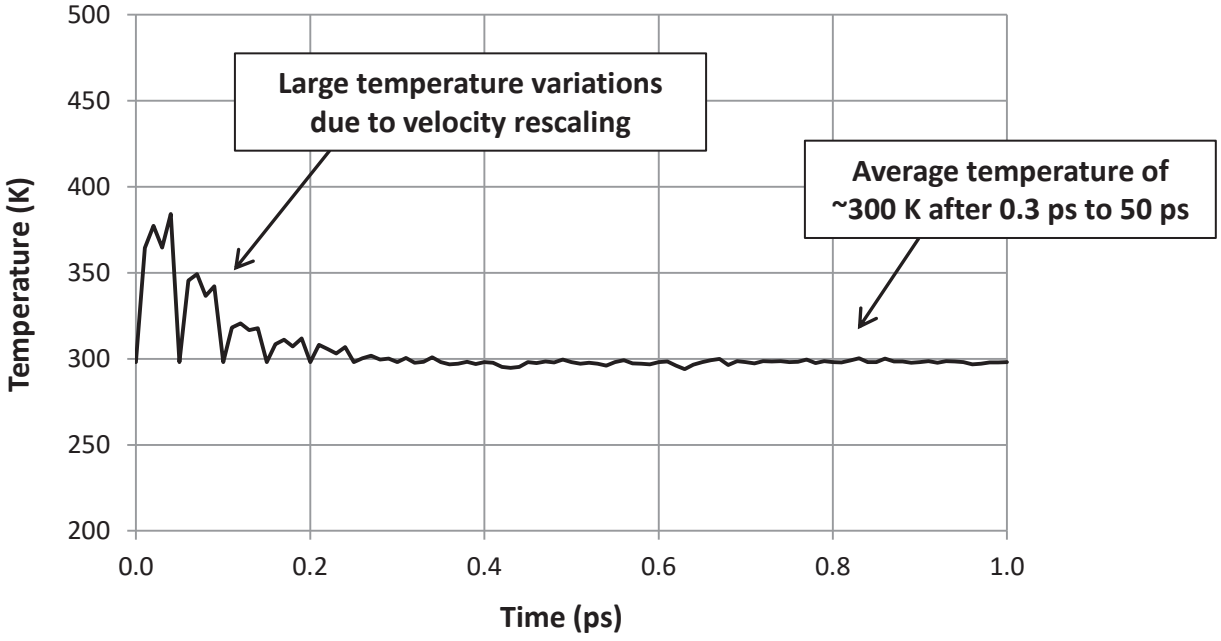


**Figure 7.13: Graph of the variation of system temperature over time during the first 1 ps of the post-cascade equilibration.**

## Analysis and Discussion

From Figures 7.12 and 7.13, the effect of the velocity rescaling is clear as the system temperature fluctuated significantly up to 0.2 ps. After 0.3 ps, the system temperature stabilised to an average of ~300 K. Overall, the temperature results show that the system temperature increased from 298 K to 653 K after 0.01 ps from the initiation of the cascade in the 'thermal spike' followed by a decrease in the system temperature to an average of ~450 K. It was only when the system was equilibrated again that the system temperature decreased to an average of ~300 K, which occurred within 1 ps after the cascade phase.

### 7.3.2 Behaviour at 700 K

The same simulations were performed at a system temperature of 700 K. Figures 7.14 and 7.15 show the temperature variation over time at the beginning of the cascade phase.

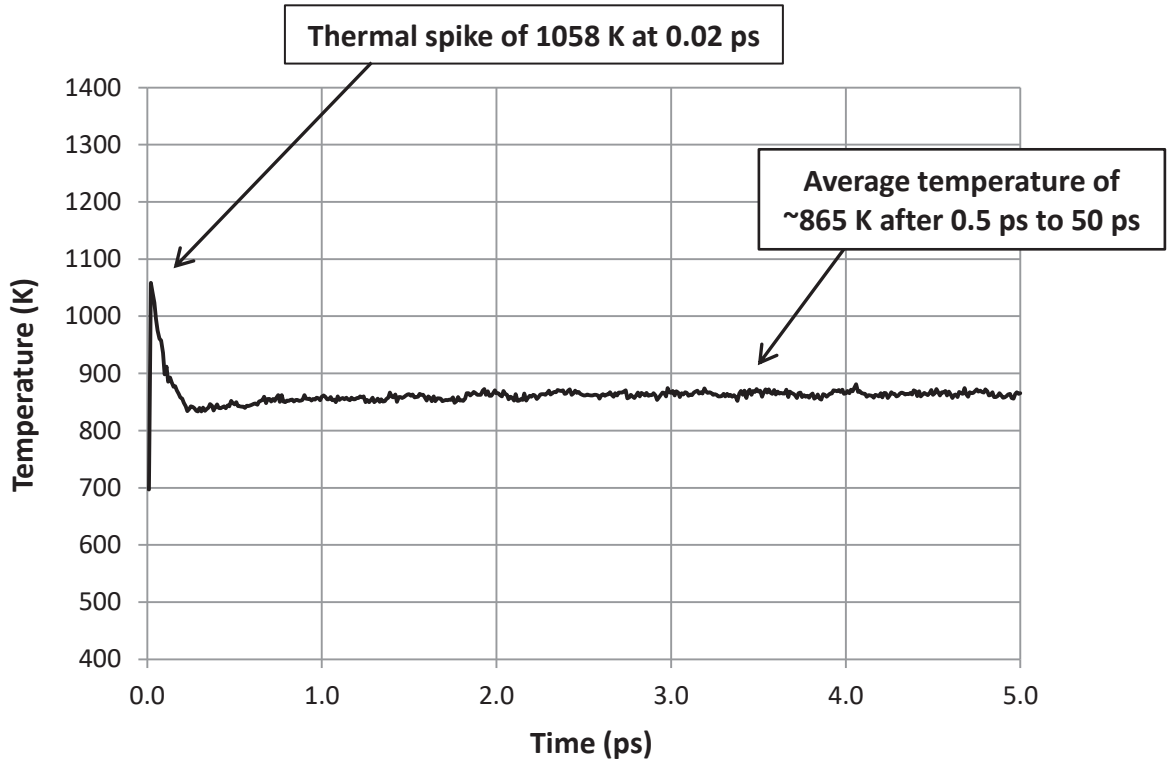


**Figure 7.14: Graph of the variation of system temperature over time during the first 5 ps of the cascade phase.**

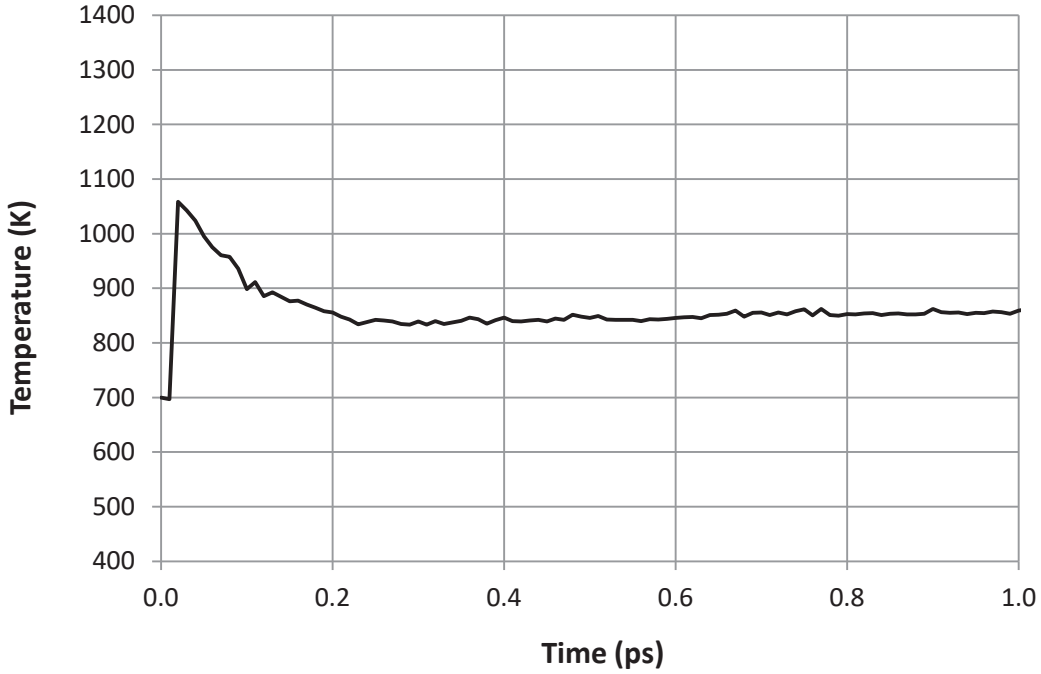


**Figure 7.15: Graph of the variation of the system temperature over time during the first 1 ps of the cascade phase.**

## Analysis and Discussion

The graphs show that there was a 'thermal spike', corresponding to a very rapid rise in the system temperature to 1058 K which then decreased to an average of 865 K for the rest of the cascade phase, an increase of 24% on the initial temperature of 700 K. The temperature peaked at 1058 K at 0.02 ps which is 0.01 ps after the 1 keV cascade was initiated, an increase of 51% on the initial temperature. This shows the system responded very rapidly to the high-energy PKA.

In fact, after 0.29 ps, the system temperature decreased to a minimum of 834 K before rising again to an average of ~865 K after 0.5 ps. The decrease in the temperature was due to the exchange of kinetic energy with potential energy of the system. Following the cascade phase, there was another equilibration phase of 100 ps, identical to the initial equilibration. The temperature was restored to an average of ~700 K after 0.3 ps. Figures 7.16 and 7.17 show the large variations of the system

temperature during the first 0.2 ps of this equilibration phase, due to rapid velocity rescaling.

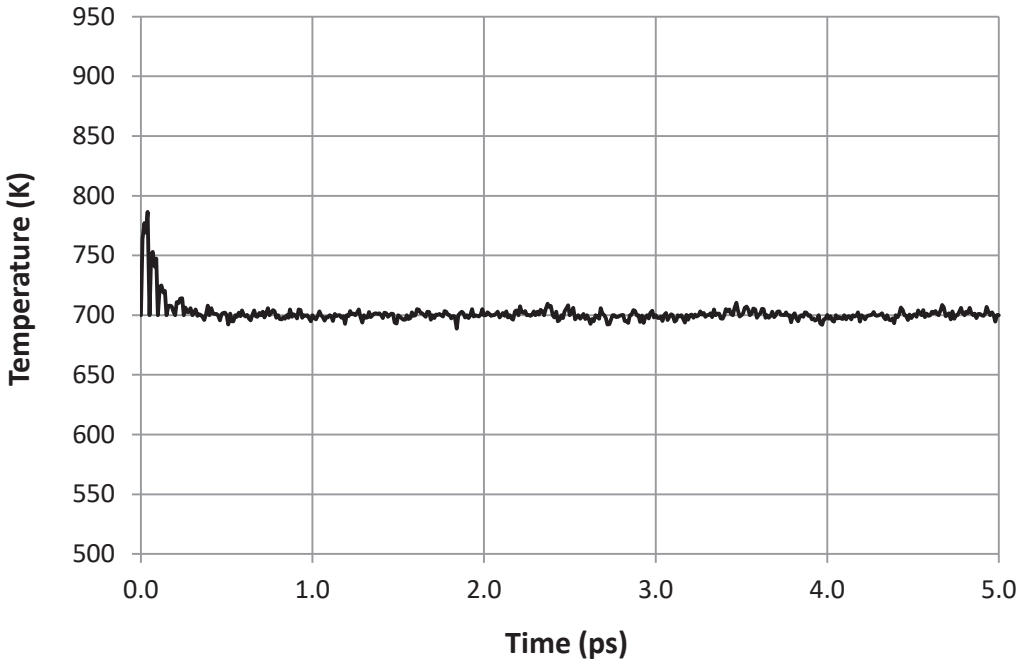


**Figure 7.16: Graph of the variation of system temperature over time during the first 5 ps of the post-cascade equilibration.**

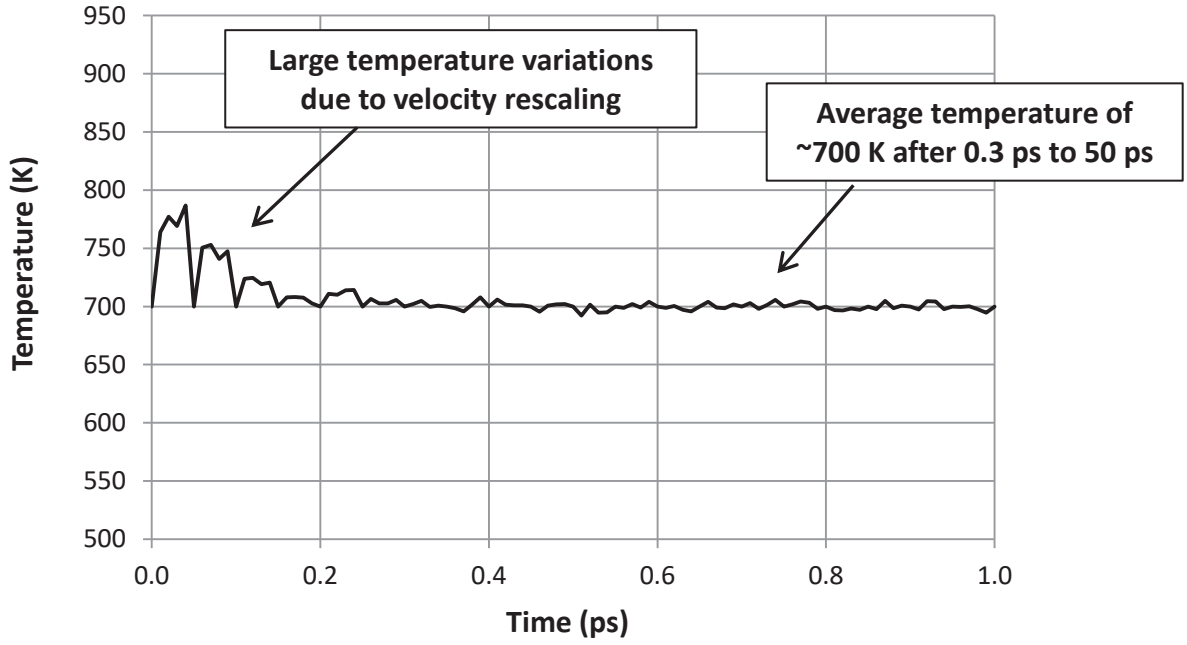


**Figure 7.17: Graph of the variation of system temperature over time during the first 1ps of the post-cascade equilibration.**

## Analysis and Discussion

From Figure 7.17, the effect of the velocity rescaling is clear as the system temperature fluctuated significantly up to 0.2 ps. After 0.3 ps, the system temperature stabilised to an average of ~700 K. Overall, the temperature results show that the system temperature increased from 700 K to 1085 K after 0.01 ps from the initiation of the cascade in the 'thermal spike' followed by a decrease in the system temperature to an average of ~865 K. It was only when the system was equilibrated again that the system temperature decreased to an average of ~700 K, which occurred within 1 ps after the cascade phase.

Hence, the time dependence of the temperature variation for the cascade and post cascade equilibrium was essentially the same for the two temperatures of 298 K and 700 K. However, there were some key differences in the temperature variation for the two temperatures during the cascade phase. In particular, the relative increase in the system temperatures from the initial temperature to the

peak temperature and to the average temperature was very different. The increase was about a factor of two larger for the 298 K case than that of the 700 K case.

## 7.4 Defect Evolution

### 7.4.1 Behaviour at 298 K

From the cascade simulations, there was a large amount of data accumulated on the defect evolution during the cascade phase and afterwards in the post-cascade equilibration. Types of defects include oxygen and Pu vacancies, interstitials and Frenkel pairs. An interstitial was classed as a defect if an ion was displaced from a crystalline site by a minimum distance of 1 Å. Defect data was collected every ten time steps. The number of Frenkel pairs was calculated as half the number of interstitials or vacancies for each ion type. The defect data presented was from the cascade phase for the damage peak, at the end of the cascade phase and at the end of the post-cascade equilibration. Focussing on the simulations initially at 298 K, regarding the cascade phase, the defect evolution is shown in Figures 7.18 and 7.19. Table 7.1 summarises the defect data.

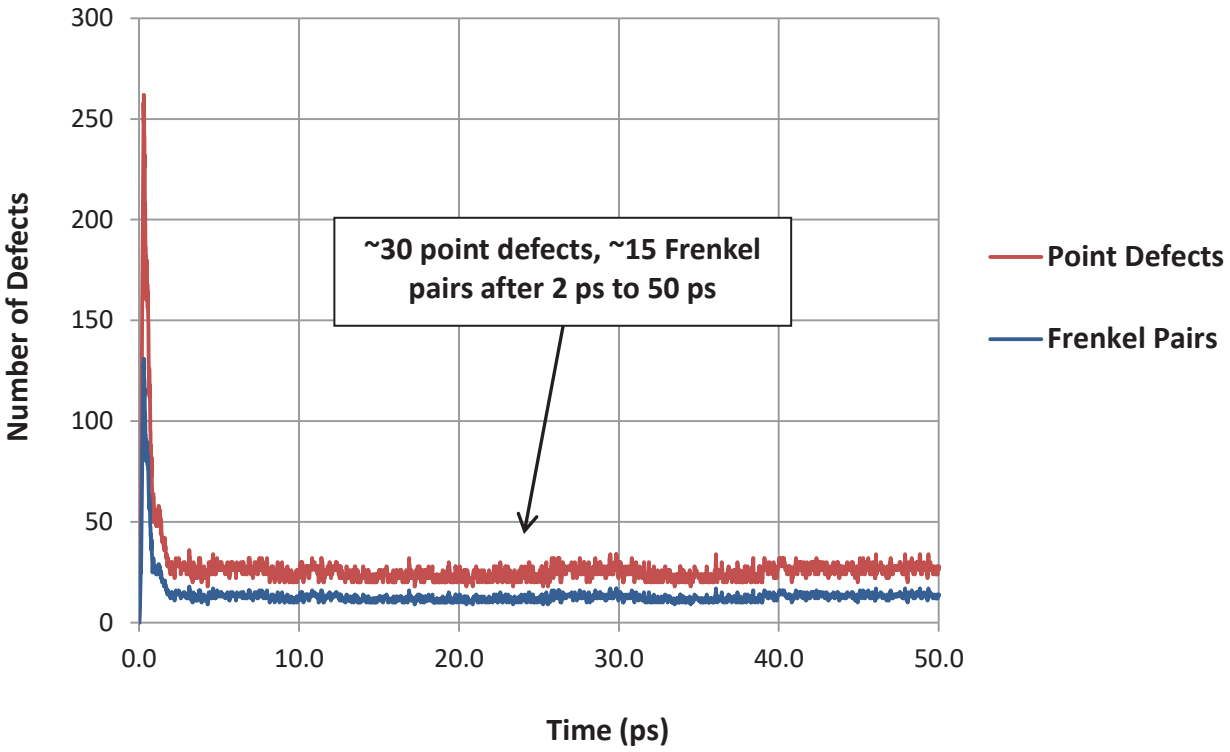


**Figure 7.18: Number of defects over time during the cascade phase.**

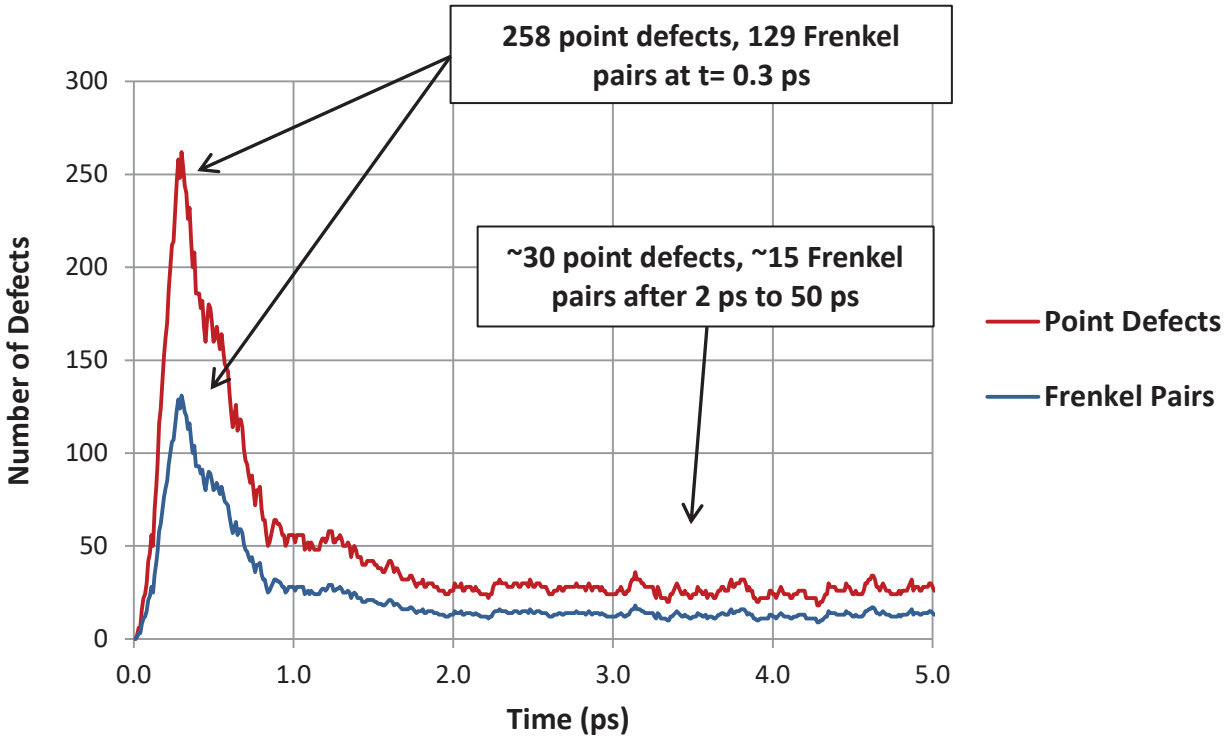


**Figure 7.19: Number of defects over time during the first 5 ps of the cascade phase.**

**Table 7.1: Summary of defect data from 298 K, 1 keV cascade simulations.**

| Number of Defects | | Defect Peak, t= 0.3 ps | End of Cascade Phase, t = 50 ps | End of Post-Cascade Equilibration, t= 150 ps |
|---|---|---|---|---|
| **Point Defects** | | 258 | 28 | 30 |
| **Frenkel Pairs** | **Oxygen** | 103 | 11 | 12 |
| | **Pu** | 26 | 3 | 3 |
| | **Total** | 129 | 14 | 15 |
| | **Ratio O:Pu** | 3.96 | 3.67 | 4.00 |

## Analysis and Discussion

The defect data for an initial temperature of 298 K show that $PuO_2$ is a robust material, with a rapid damage recovery to the 1 keV cascade. The number of Frenkel pairs peaked at 129, 0.3 ps after the initiation of the cascade and the thermal spike. This was due to the time taken for the damage to accumulate in the lattice. The number of Frenkel pairs reduced rapidly to an average of ~25 after 1 ps and to ~15 after 2 ps, when it stabilised for the remainder of the cascade phase.

During the post-cascade equilibration, the number of Frenkel pairs did not change very much, with 15 Frenkel pairs remaining at the end, as average temperature was decreased from ~450 K back to ~300 K. This shows that these defects that were created from the cascade remained in the structure on the timescale of the simulations. This could have been due to the relatively large distances between the vacancies and interstitials and their low diffusion. Throughout the simulations, the ratio of oxygen to Pu defects was approximately 4, due to lower displacement energy of the oxygen ions compared to Pu ions.

### 7.4.2 Behaviour at 700 K

Focussing on the simulations initially at 700 K, regarding the cascade phase, the defect evolution is shown in Figures 7.20 and 7.21. Table 7.2 summarises the defect data.

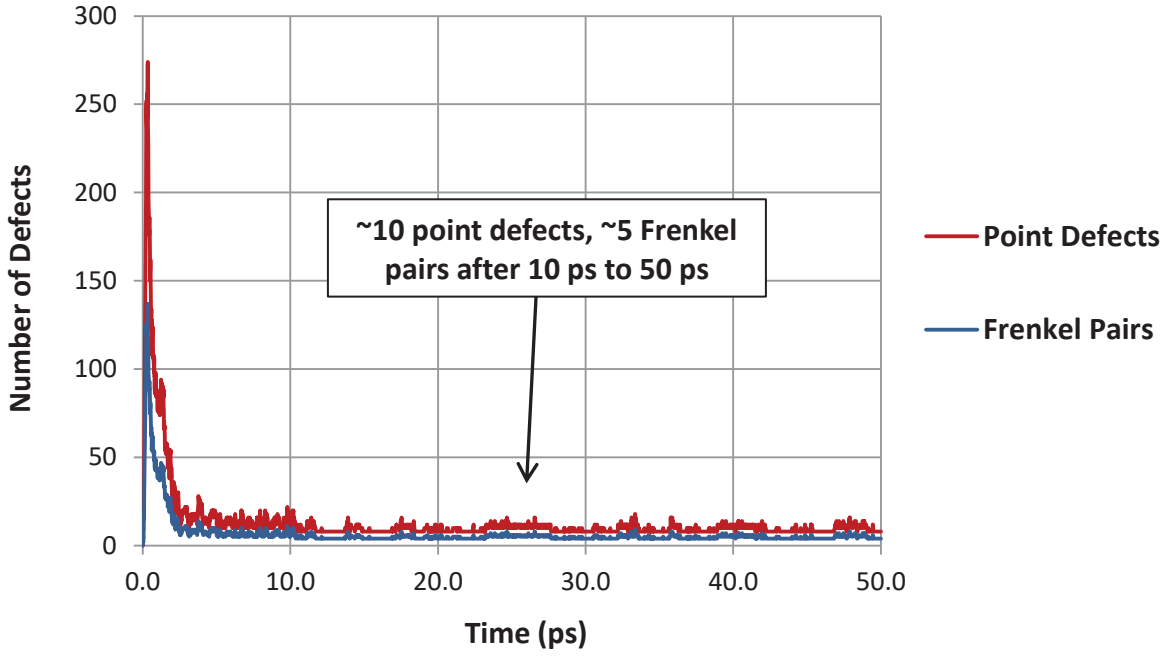


**Figure 7.20: Number of defects over time during the cascade phase.**

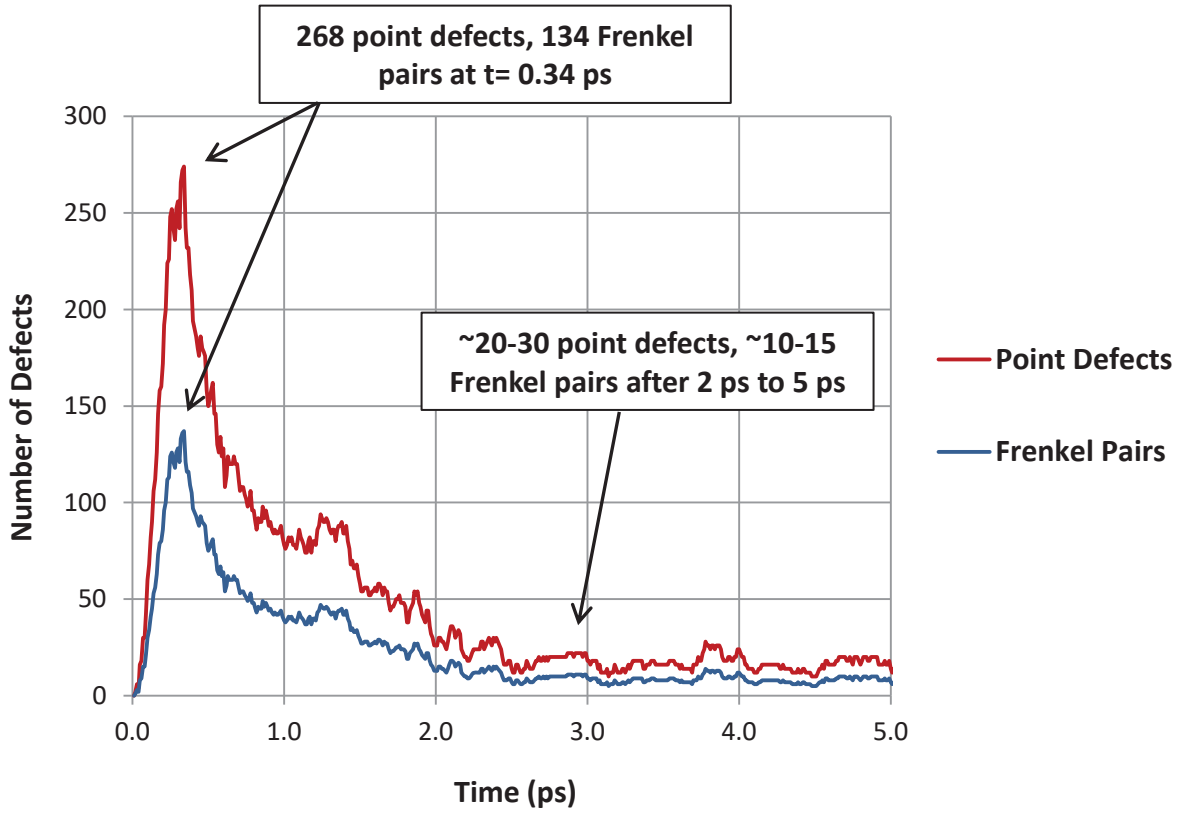


**Figure 7. 21: Number of defects over time during the first 5 ps of the cascade phase.**

**Table 7.2: Summary of defect data from 700 K, 1 keV cascade simulations.**

| Number of Defects | | Defect Peak, t= 0.34 ps | End of Cascade Phase, t = 50 ps | End of Post-Cascade Equilibration, t= 150 ps |
|---|---|---|---|---|
| **Point Defects** | | 268 | 8 | 12 |
| **Frenkel Pairs** | **Oxygen** | 109 | 2 | 4 |
| | **Pu** | 25 | 2 | 2 |
| | **Total** | 134 | 4 | 6 |
| | **Ratio O:Pu** | 4.36 | 1.00 | 2.00 |

## Analysis and Discussion

The defect data for an initial temperature of 700 K shows that $PuO_2$ is a robust material, with a rapid damage recovery to the 1 keV cascade, which was enhanced at the higher temperature. The number of Frenkel pairs peaked at 134, 0.34 ps after the initiation of the cascade and the thermal spike. This was due to the time taken for the damage to accumulate in the lattice. The number of Frenkel pairs showed a downward trend throughout the cascade phase, in contrast to the 298 K case, where it stabilised after 2 ps, due to the greater kinetic energy of the system and hence ionic diffusion, allowing more Frenkel pairs to be annihilated over time. The peak in defects occurred at 0.34 ps, where the peak number of Frenkel pairs was 134, about 4% more than for the 298 K case.

The number of Frenkel pairs decreased rapidly to an average of ~40 after 1 ps, and to ~15 after 2 ps. The number continued to decrease but more gradually to ~5 Frenkel pairs after 10 ps, a decrease of 67% from those at 2 ps. The number stabilises after 10ps, with 4 Frenkel pairs at the end of the cascade phase, two of each type. This is much lower than the 14 Frenkel pairs at the end of the cascade phase for the 298 K case. This shows that the damage recovery is more effective at higher temperatures, with defect annihilation more efficient. This could have been due the greater diffusion compared to that at lower temperatures, allowing more Frenkel pairs to be annihilated.

During the post-cascade equilibration, the number of Frenkel pairs hardly changed, with 6 Frenkel pairs remaining at the end, as the average temperature was lowered from ~865 K back to ~700 K. This could have been due to the relatively large distance between the few vacancies and interstitials and their low diffusion. Nevertheless, the final number of Frenkel pairs is much less than the 15 Frenkel pairs that remained for the 298 K case, again showing damage recovery was more effective at 700 K. Throughout the simulations, the ratio of oxygen to plutonium defects varied between 1 and 4.

## 7.5 Radial Distribution Function Spectra

In addition to temperature and defect data from the 1 keV cascade simulations, the radial (or pair) distribution functions ($g(r)$) were also calculated. In the simulations, the $g(r)$ data was collected every 10 time steps (10 fs) and the bin size for data collection was 0.01 Å over a radius from zero to 15 Å inclusive.

### 7.5.1 Spectra at 298 K

Figures 7.22 to 7.24 show the $g(r)$ spectra for the Pu-Pu, Pu-O and O-O pairs at the end of the cascade phase (after 50ps), with the initial temperature at 298 K. The graphs show that the peak heights of $g(r)$ were less than compared to the pure system at 298 K. This is due to the higher average temperature after the cascade of 450 K and due to the presence of 14 Frenkel pairs, which increases the structural disorder. Nevertheless, many peaks are still present following the cascade phase, showing that the lattice remained crystalline following the 1 keV cascade.

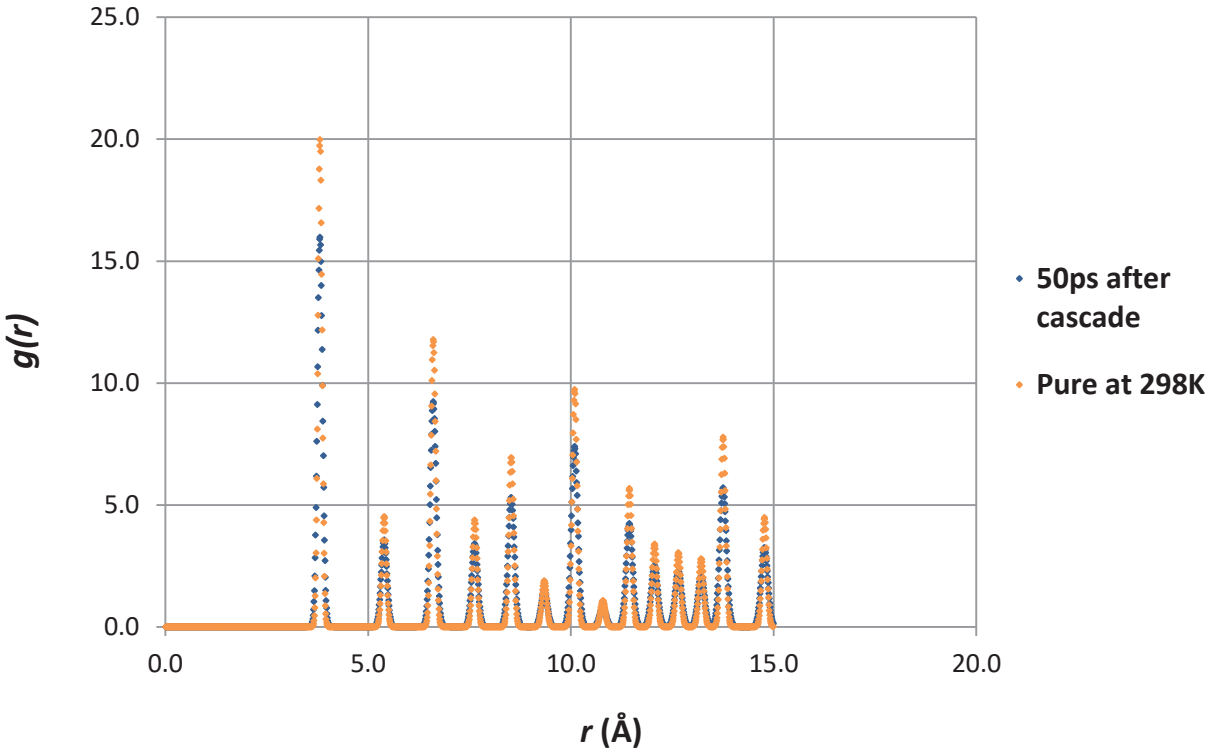


**Figure 7.22: $g(r)$ spectra for Pu-Pu pairs in pure $PuO_2$ at 298 K and after 50 ps of the 1 keV cascade.**

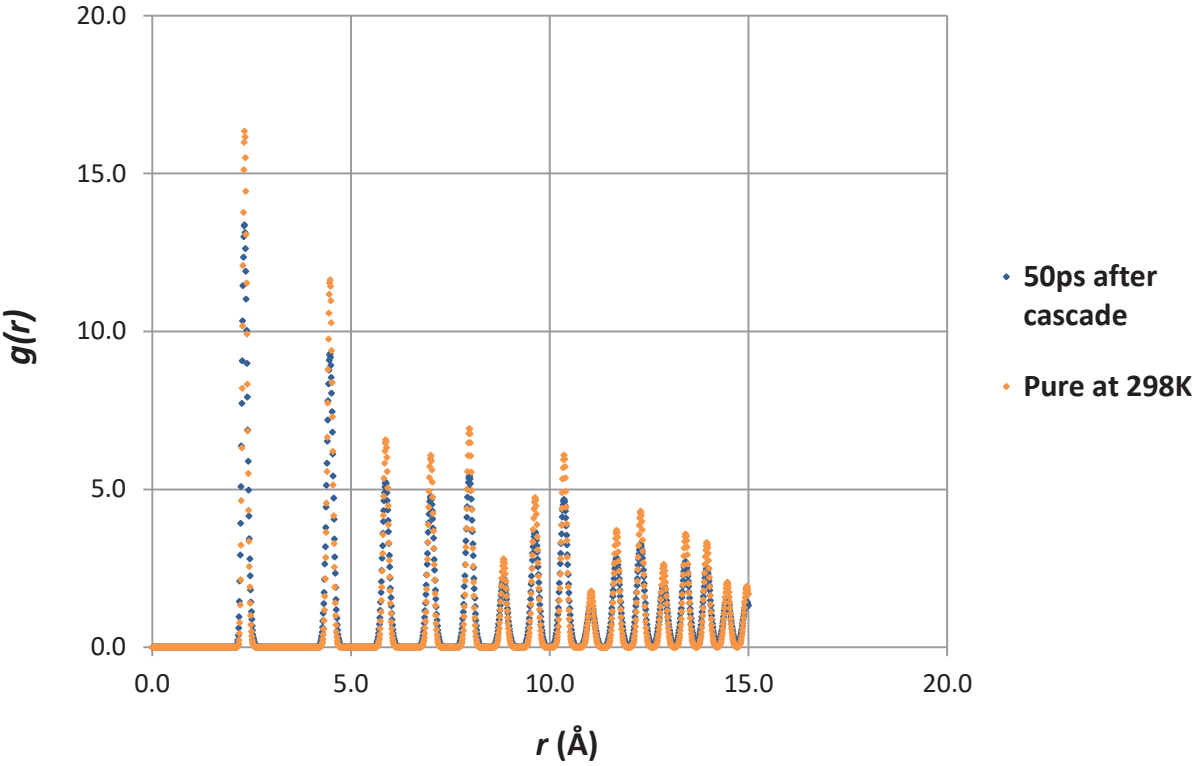


**Figure 7.23: $g(r)$ spectra for Pu-O pairs in pure $PuO_2$ at 298 K and after 50 ps of the 1 keV cascade.**

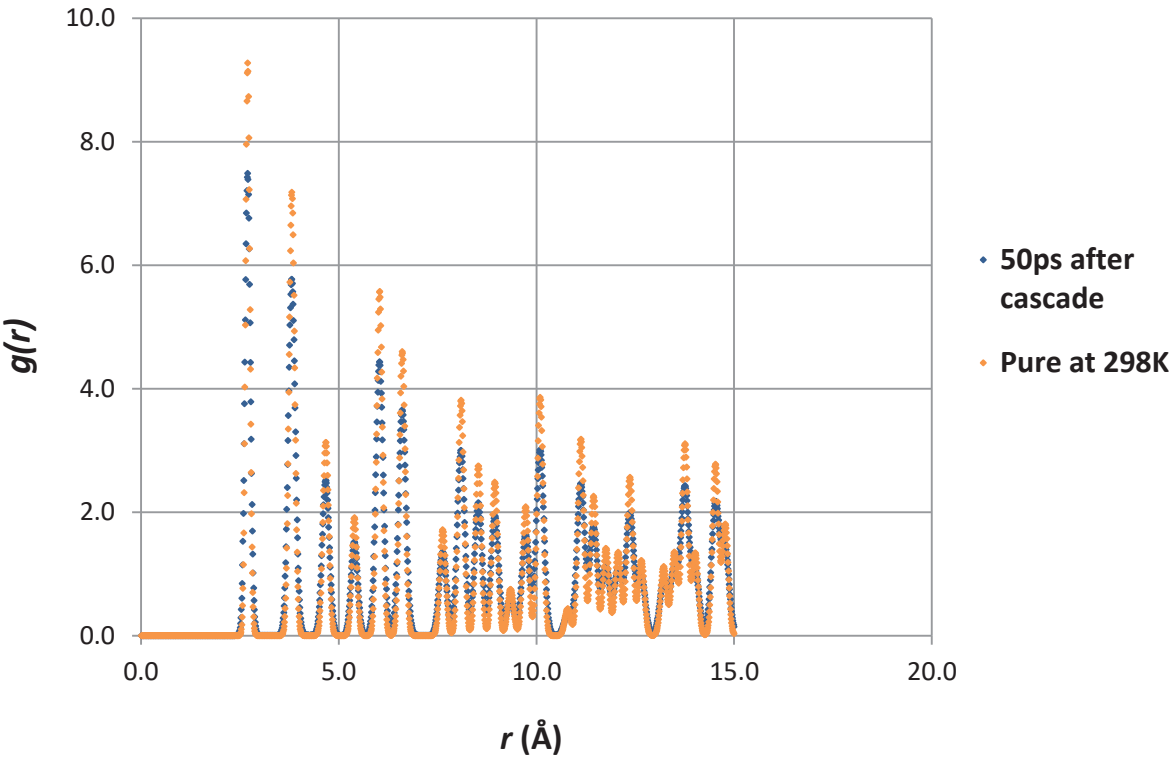


**Figure 7.24: $g(r)$ spectra for O-O pairs in pure $PuO_2$ at 298 K and after 50 ps of the 1 keV cascade.**

### 7.5.2 Spectra at 700 K

Figures 7.25 to 7.27 show the $g(r)$ spectra for the Pu-Pu, Pu-O and O-O pairs for pure $PuO_2$ and for at the end of the cascade phase after 50 ps, with the initial temperature at 700 K. The graphs show that the peak heights of $g(r)$ decreased for the case after the cascade, compared to the pure system at 700 K. This is due to the higher average temperature after the cascade of ~865 K and due to the presence of 4 Frenkel pairs, increasing the structural disorder.

However, the peak heights decreased slightly less than the case at 298 K due to two reasons. One reason is that the relative increase in the temperature after the cascade was 24% on the initial temperature of 700 K, whereas for the 298 K case, the temperature increased 51% on the initial temperature of 298 K. The other reason is the many more defects present after the cascade for the 298 K case than for

the 700 K case- 14 Frenkel pairs compared to 4 respectively. As for the 298 K case, many peaks are still present following the cascade phase, showing that the lattice remained crystalline following the 1 keV cascade.

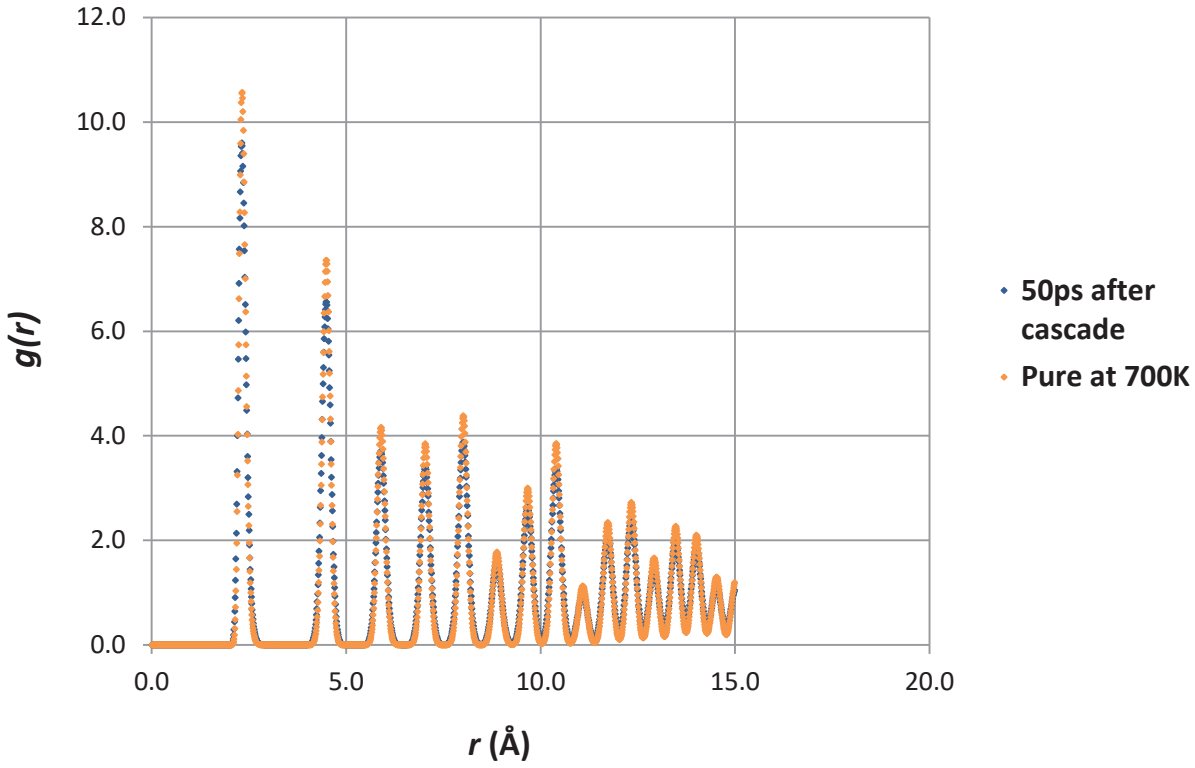


**Figure 7.25: $g(r)$ spectra for Pu-Pu pairs in pure $PuO_2$ at 700 K and after 50 ps of the 1 keV cascade.**

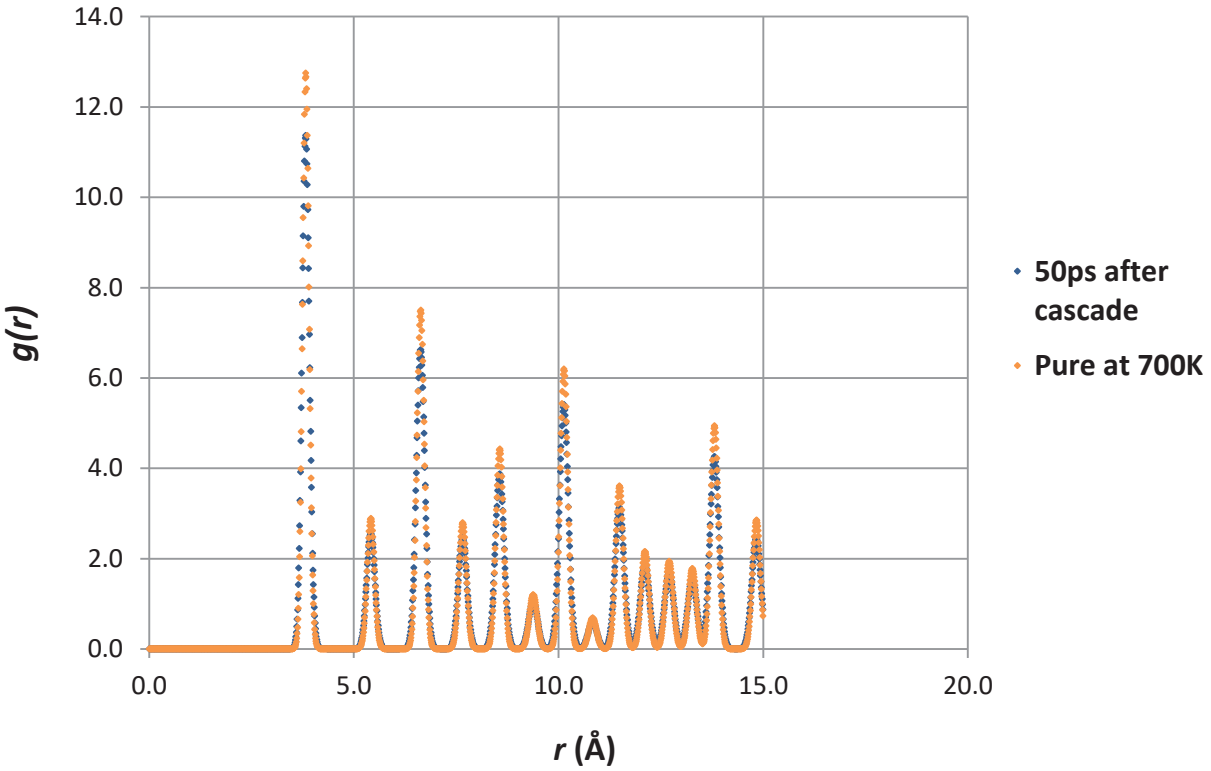


**Figure 7.26: $g(r)$ spectra for Pu-O pairs in pure $PuO_2$ at 700 K and after 50 ps of the 1 keV cascade.**

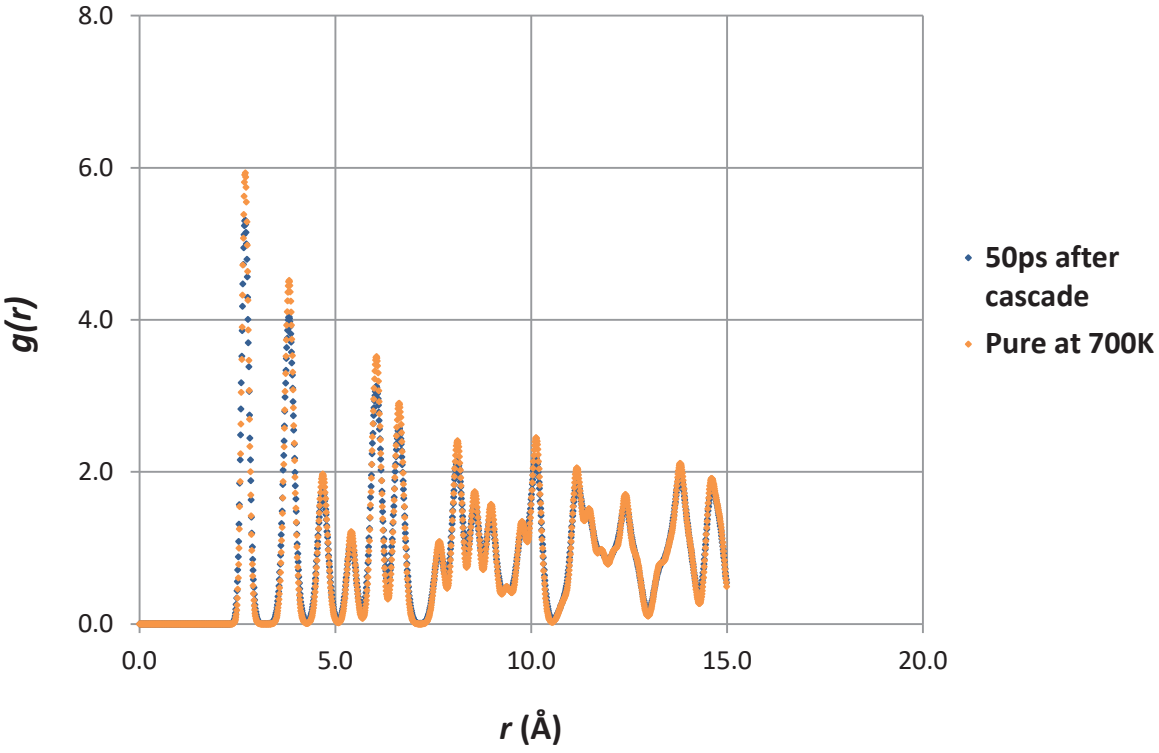


**Figure 7.27: $g(r)$ spectra for O-O pairs in pure $PuO_2$ at 700 K and after 50 ps of the 1 keV cascade.**

## 7.6 Summary

Molecular dynamics simulations were performed to model 1 keV cascades in a 12 × 12 × 12 $PuO_2$ supercell at 298 K and 700 K. To model ballistic collisions, the Arima et al. potentials were connected to ZBL potentials through splining. The simulation results showed that $PuO_2$ is a radiation tolerant material, in accordance with high-energy implantation experiments of other fluorite-structured oxides**.** This was expected due to the low cascade energy of 1 keV. However, experiments have shown such oxides remained crystalline even when irradiated with 940 MeV Pb ions for cubic $ZrO_2$ [165] and 944 MeV Pb ions in $UO_2$ and YSZ [159]. Such high energies cover the electron energy loss regime of the ions, inaccessible to molecular dynamics.

From the simulation results, the number of Frenkel pairs decreased rapidly within tenths of a pico second after the peak damage independent of temperature. The 'thermal spike' occurred immediately after the start of the cascade, where the temperature peaked and then decreased as the excess energy was absorbed by the system. This increased the average temperature to over 100 K above the initial temperature within a few ps. Regarding temperature effects, it was shown from the results that the number of defects after 50 ps following the cascade was a factor of ~3 larger for the initial temperature of 298 K than for 700 K. This indicated that the radiation tolerance of $PuO_2$ increases with increasing temperature. This is in agreement with Martin et al. (2015) [41] molecular dynamics simulations of 10 keV cascades in $UO_2$ at 700 K and 1800 K.

# Chapter 8

# Properties of Mixed Oxide Fuel

## 8.1 Literature Review

Mixed oxide (MOX) nuclear fuel is a solid solution of $UO_2$ and $PuO_2$ and is widely used as fuel in nuclear reactors. Worldwide, as of 2018, it accounts for 5% of new nuclear fuel used [9]. MOX fuel is a relatively new nuclear fuel, having been first manufactured for commercial use in the 1980s. As of 2018, over thirty reactors in Europe use MOX fuel. In the UK, Pu use in MOX fuel is a key option for the Pu stockpile. Various proposed reactors could use the MOX fuel e.g. the Candu EC6 reactors, which would use 2% Pu content in their 'CANMOX' fuel [14].

In principle, the use of MOX fuel is an economical way of re-using nuclear fuel. Most light water reactors have their fuel discharged about every three years, and the U and Pu in the spent fuel is extracted when processed and can be used to manufacture MOX fuel. From processing, ~96% is U, ~3% is high-level waste and ~1% of fuel discharged is Pu, allowing ~97% of the fuel to be recycled [11]. For fissile content, the Pu extracted can be used in MOX fuel, mitigating the need for fuel enrichment. On average, commercial MOX consists of ~9.5% Pu content. Of the extracted Pu, ~7 to 11% is mixed with $UO_2$, which in fissile terms is equivalent to $UO_2$ enriched with ~4.5% of U-235 [9].

Helium accumulation is also relevant to MOX fuel, which contains both U and Pu isotopes which alpha decay. It is expected that after 10,000

years of storage in a repository, the concentrations of helium could reach up to 0.7 at. % in $UO_2$ and 4 at. % in MOX fuel [125]. With the growth of MOX fuel in new reactors, helium ingrowth would be a growing concern, particularly for spent MOX fuel in storage. Due to the relevance of MOX fuel to the nuclear industry, there have been numerous experimental and computational studies. As with other nuclear materials, experiments are more difficult due to the radioactivity of MOX fuel.

Beauvy (1992) [166] investigated the non-ideality of MOX fuel relative to a solid solution, with varying oxygen stoichiometry and Pu content for the compound $(U_{1-y}Pu_y)O_{2\pm x}$. This is assessed by comparing to an ideal solid solution, which is characterised by following Vegard's Law (1921) [167]. Vegard's Law is an empirical relation that the lattice parameter(s) of a solid solution composed of two isostructural components will be a weighted average of the two lattice parameter(s) of these two components [103]. This is applicable to MOX fuel, as both $UO_2$ and $PuO_2$ adopt the fluorite structure with cations in the tetravalent oxidation state. When only the Pu content is varied, Beauvy (1992) [166] showed by x-ray diffraction that, overall, MOX fuel follows Vegard's Law with the lattice parameter linear above ~5% Pu content. However, this is very sensitive to the stoichiometry, with the oxygen deficient, hypo-stoichiometric phase shown not to be an ideal solid solution.

In contrast, Kato et al. (2009) [168] studied self-radiation damage in MOX fuel, due to the alpha decay of Pu and U nuclei. Aged MOX pellets and powders were used, which contained ~19% to 49% Pu content. They showed the lattice parameter of the MOX fuel matrix saturated at 0.29%. The samples were annealed at high temperatures to study gas release and defect recovery. They proposed three recovery stages at different temperature ranges, associated with different defect annihilation mechanisms.

There have been many computational studies on MOX fuel, which have investigated different content, stoichiometry's and temperatures. Balboa et al. (2017) [32] performed molecular dynamics simulations on MOX fuel using five different potentials. They predicted a range of thermomechanical properties over a large

temperature range and Pu content range. Although the results varied with the potentials used, they showed that MOX fuel is a solid solution up to 2000 K, in agreement with experiments by Nichenko et al. (2013) [169] and Popov et al. (2000) [170] also performed molecular dynamics simulations to investigate the thermal conductivity of MOX fuel.

The calculated thermal conductivity decreased with increasing Pu content, due to the Pu atoms acting as phonon scattering centres. In contrast, molecular dynamics simulations by Arima et al. (2008) [171] showed that the thermal conductivity was not affected by the Pu content for stoichiometric fuel, but rather depended on the temperature and oxygen defects. Other molecular dynamics studies have simulated MOX fuel with a specific Pu content, typically in the range 20% to 30%. Terentyev (2007) [104] simulated MOX fuel with 30% Pu content, and investigated thermal properties and oxygen diffusion. They showed that generally the MOX fuel properties were intermediate to that of pure $UO_2$ and $PuO_2$. Interestingly, they observed a 'strong interaction' between point defects and Pu atoms, affecting diffusion of point defects.

Kurosaki et al. (2001) [141] and Yamada et al. (2000) [96] focussed on 20% Pu content and their simulation results for a range of thermal properties agreed well with Terentyev (2007), partly because as they used the same potentials. Ma et al. (2014) [172] performed molecular dynamics simulations on MOX fuel with 25% Pu content, which showed oxygen defects had a large effect on thermal properties. They predicted a very small effect of the Pu when oxygen vacancies are present.

In summary, there has been a range of computational and experimental studies of MOX fuel. Further understanding of properties and ageing behaviour of MOX fuel is needed for storage and in-reactor applications. This chapter will present atomistic simulations of MOX fuel to predict bulk lattice properties varying the Pu content. Furthermore, there will be a focus on 9% Pu doped MOX fuel, which is typical for reactors, including modelling of intrinsic defects and helium incorporation of relevance to ageing behaviour.

## 8.2 Simulation Details

Static lattice simulations of MOX fuel were performed using the General Utility Lattice Program (GULP) [50,61], and the Pu concentration was varied in the solid solution of formula $Pu_xU_{1-x}O_2$. Structural, mechanical properties and defect and solution energies of Pu were calculated. The potentials of Read et al. (2010, 2014) [30,64] and Jackson et al. (1986) [91] (abbreviated Read et al.) were used for $UO_2$ and $PuO_2$. Both potential sets, which are FIMs, employ the O-O Buckingham-four range potential and the shell model. The potential parameters for $PuO_2$ and $UO_2$ are summarised in Table 8.1 and Table 8.2.

**Table 8.1: Parameters of the potentials of Read et al. (2014) [64] and Jackson et al. (1986) [91] for $PuO_2$.**

<table>
<tr><th>Ion Pair</th><th colspan="4">Short-range Parameters</th><th colspan="3">Shell Model Parameters</th></tr>
<tr><td></td><td colspan="2">$A$ (eV)</td><td>$\rho$ (Å)</td><td>$C$ (eV Å$^6$)</td><td>Ion</td><td>$q_{shell}$ ($e$ $C$)</td><td>$k$ (eV Å$^{-2}$)</td></tr>
<tr><td>Pu- O[a]</td><td colspan="2">1116.3317</td><td>0.3926</td><td>0.00</td><td>$Pu^{4+}$</td><td>6.54</td><td>206.77</td></tr>
<tr><td rowspan="3">O-O[b]</td><td colspan="2">11272.6</td><td>0.1363</td><td>134.0</td><td>$O^{2-}$</td><td>-4.40</td><td>296.2</td></tr>
<tr><td>$r_{min}$ (Å)</td><td>$cut_1$(Å)</td><td>$r_{mini}$ (Å)</td><td>$cut_2$ (Å)</td><td colspan="3" rowspan="2">$cut_{core-shell}$ (Å)</td></tr>
<tr><td>0.00</td><td>1.20</td><td>2.10</td><td>2.60</td></tr>
<tr><td rowspan="2"></td><td colspan="4">$r_{max}$ (Å)</td><td colspan="3" rowspan="2">0.60</td></tr>
<tr><td colspan="4">15.0</td></tr>
</table>

**a- Read et al. (2014) [64], b- Jackson et al. (1986) [91], Buckingham four-range potential.**

**Table 8.2: Parameters of the potentials of Read et al. (2010) [30] and Jackson et al. (1986) [91] for $UO_2$.**

<table>
<tr><th>Ion Pair</th><th colspan="4">Short-range Parameters</th><th colspan="3">Shell Model Parameters</th></tr>
<tr><td></td><td>$A$ (eV)</td><td colspan="2">$\rho$ (Å)</td><td>$C$ (eV Å$^6$)</td><td>Ion</td><td>$q_{shell}$ ($e$ $C$)</td><td>$k$ (eV Å$^{-2}$)</td></tr>
<tr><td>U- O[a]</td><td>1027.5967</td><td colspan="2">0.402616</td><td>0.00</td><td>$U^{4+}$</td><td>6.54</td><td>110.75343</td></tr>
<tr><td rowspan="3">O-O[b]</td><td>11272.6</td><td colspan="2">0.1363</td><td>134.0</td><td>$O^{2-}$</td><td>-4.40</td><td>296.2</td></tr>
<tr><td>$r_{min}$ (Å)</td><td>$cut_1$(Å)</td><td>$r_{mini}$ (Å)</td><td>$cut_2$ (Å)</td><td colspan="3" rowspan="2">$cut_{core-shell}$ (Å)</td></tr>
<tr><td>0.00</td><td>1.20</td><td>2.10</td><td>2.60</td></tr>
<tr><td rowspan="2"></td><td colspan="4">$r_{max}$ (Å)</td><td colspan="3" rowspan="2">0.60</td></tr>
<tr><td colspan="4">15.0</td></tr>
</table>

**a- Read et al. (2010) [30], b- Jackson et al. (1986) [91], Buckingham four-range potential.**

Two methods were employed to simulate MOX fuel: the 'mean-field' and 'supercell' methods. In the mean-field method, the cations were assigned an occupancy factor ($x$) where $0 \leq x \leq 1$, which was varied depending on the Pu content. Hence, the cations had a mixed U and Pu character, with all interactions scaled by the appropriate occupancy factor. In the supercell method, a supercell of $UO_2$ was doped by substitution of U ions with Pu ions. The Pu content was varied, which was quantified by the fraction of U ions replaced by Pu ions in the $UO_2$ supercell, equivalent to $x$.

Note that although real MOX fuel has a fixed concentration of Pu of ~10%, the name is retained when varying the Pu content over the full range. Figure 8.1 illustrates the two methods for the MOX fuel unit cell with a 25% Pu content ($Pu_{0.25}U_{0.75}O_2$). Both methods were used to calculate structural and mechanical properties. However, only the supercell method was used to calculate defect energies and solution energies.

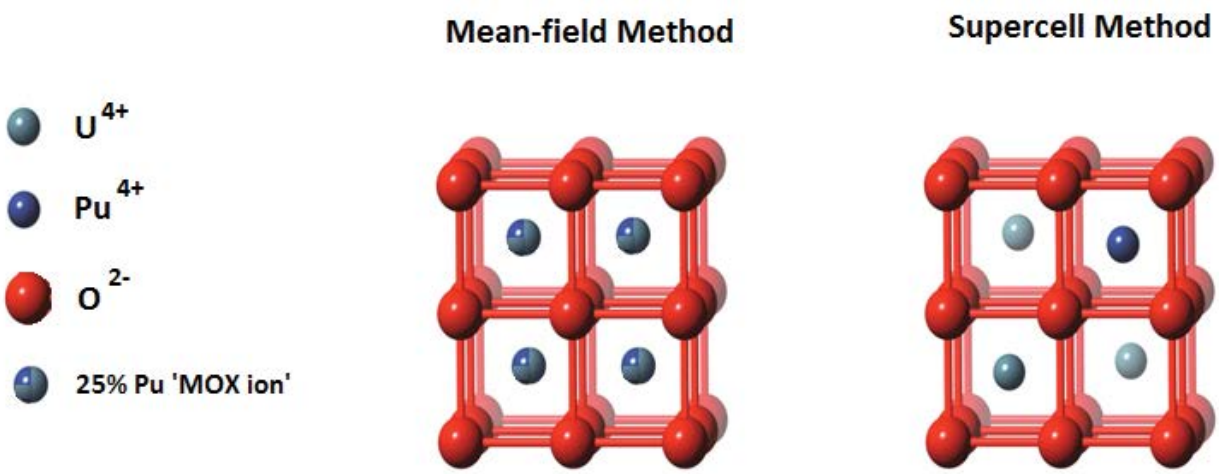


**Figure 8.1: Schematics of the mean-field and supercell methods for modelling 25% Pu MOX fuel.**

In the supercell method, a 2 × 2 × 2 $UO_2$ supercell (64 oxygen ions and 32 U ions) was substitutionally doped with Pu ions. The doping was random, ensuring a homogeneous Pu distribution in the supercell. Energy minimisation was then performed on this supercell and a range of properties calculated. The Pu concentrations modelled were 3.125%, 6.25%, 12.5%, 25% and 50%. In the mean-field simulations, the

occupancy factor ($x$) of the cations was varied from 0 to 0.9 in intervals of 0.1, and also 0.05 to 0.09 in intervals of 0.01 as this is a range of relevance to commercial MOX fuel.

## 8.3 Plutonium Doping Energies

To predict the solubility of Pu in MOX fuel as a solid solution, the defect formation and solution energies were calculated using the supercell method. The energies were calculated as a function of Pu concentration. For a given Pu concentration ($x$), the defect formation energy was calculated as the difference in the lattice energy of the supercells with and without the Pu defects, expressed per defect given by:

$$E_{Pu}^{F} = 32x\left[E_{Lattice}^{Defected} - E_{Lattice}^{Pure}\right]_{Supercell} \quad \textbf{(8.1)}$$

The Pu solution energy was calculated using the following equation:

$$E_{Sol}^{Pu} = E_{Pu}^{F} + \left[E_{PuO2}^{Pure} - E_{UO2}^{Pure}\right]_{Formula} \quad \textbf{(8.2)}$$

Hence, the solution energy is the defect formation energy in addition to the difference in lattice energies (per formula unit) for the parent phases. Table 8.2 summarises the defect formation and solution energies for substitution of a Pu ion in $UO_2$ and for a U ion in $PuO_2$. The variation in these energies with Pu content are shown in Figures 8.2 and 8.3.

**Table 8.3: Summary of calculated defect formation energies ($E_D^F$) and solution energies ($E_{Sol}$) for Pu ion substitution in $UO_2$ and U ion substitution in $PuO_2$.**

| Defect | $E_D^F$ (eV) | $E_{Sol}$ (eV) |
|---|---|---|
| $Pu_U^X$ | -1.57 | -3.17 |
| $U_{Pu}^X$ | 1.61 | 3.21 |

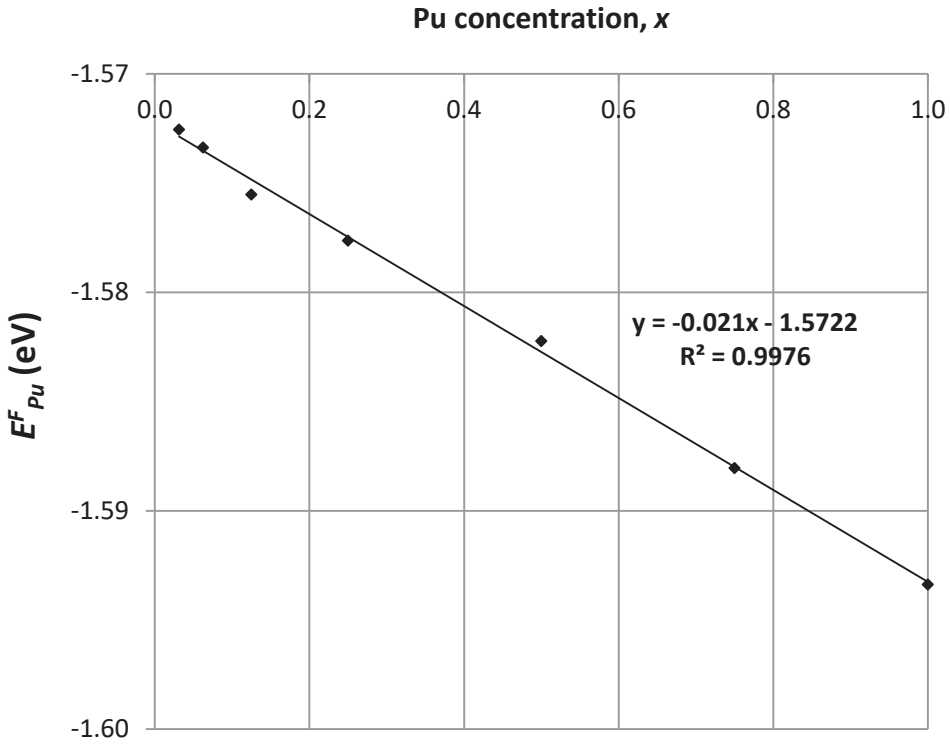


**Figure 8.2: Graph of the Pu defect formation energy ($E_{Pu}^{F}$) in MOX fuel as a function of Pu concentration ($x$).**

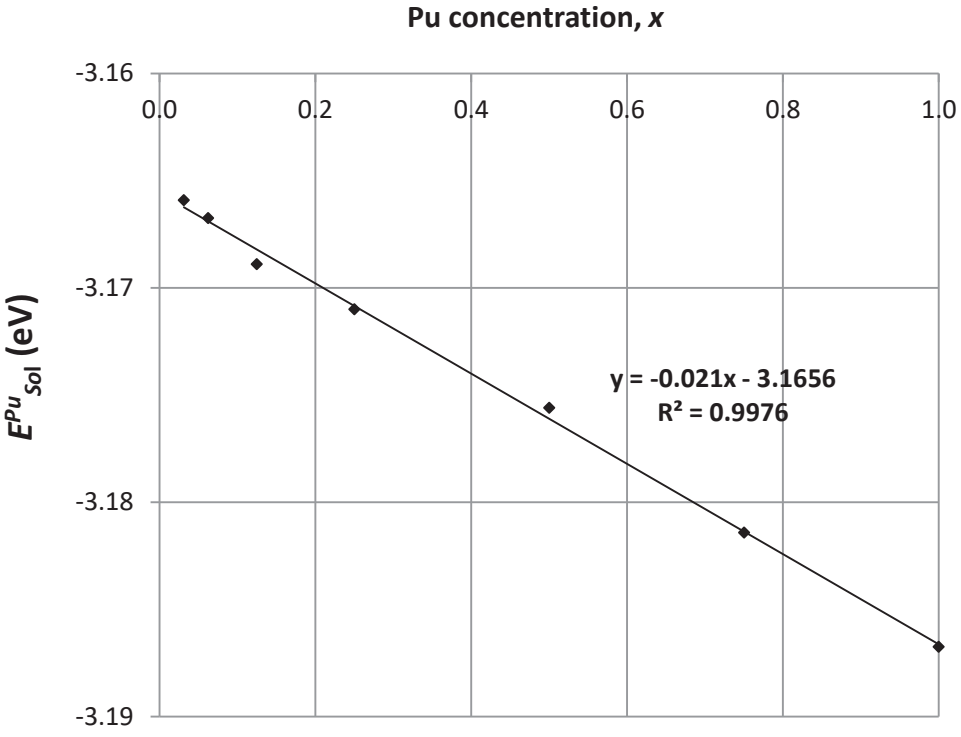


**Figure 8.3: Graph of the Pu solution energy ($E^{Pu}_{Sol}$) in MOX fuel as a function of Pu concentration ($x$).**

## Analysis and Discussion

As shown in Table 8.3, Pu substitution in $UO_2$ is energetically favourable, with exothermic incorporation and solution energies calculated. However, U substitution in $PuO_2$ is energetically unfavourable, with endothermic energies calculated. This is because $Pu^{4+}$ ions in $PuO_2$ have a crystal radius of 1.10 Å, which is 0.04 Å smaller than that of $U^{4+}$ ions in $UO_2$ of 1.14 Å [137]. U doping in $PuO_2$ is energetically unfavourable as there is an energy 'penalty' in substitution of a U ion in a smaller Pu site, due to the slight increase in internal crystal stress.

In contrast, Pu doping in $UO_2$ is energetically favourable with energy released upon substitution of a Pu ion in a larger U site. For Pu substitution in $UO_2$, the defect formation and solution energies depend weakly on the level of Pu

content. The variation in these energies over the full range of $x$ is only ~1%, due to the small differences between $UO_2$ and $PuO_2$. As shown in Figures 8.1 and 8.2, there is a linear dependence of the energies with the Pu concentration.

## 8.4 Structural and Mechanical Properties

Figures 8.4 to 8.7 show the calculated variations in the MOX fuel lattice parameters and bulk and Young's moduli as a function of Pu concentration ($x$). For lattice parameters, Figure 8.3 shows the variation of the MOX fuel supercell lattice constant with Pu content. However, to estimate the crystallographic lattice parameter of the relevant unit cell, only the mean-field method was used as shown in Figure 8.4. For the moduli, both the supercell and mean-field methods were used and their results compared.

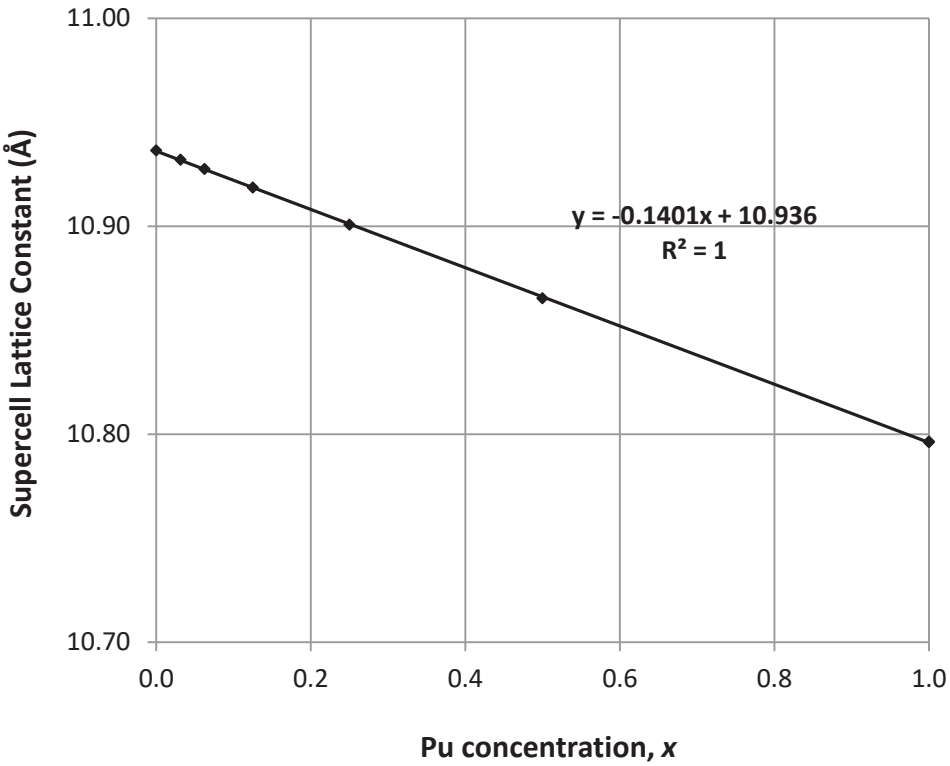


**Figure 8.4: Graph of the MOX fuel supercell lattice constant as a function of Pu concentration ($x$).**

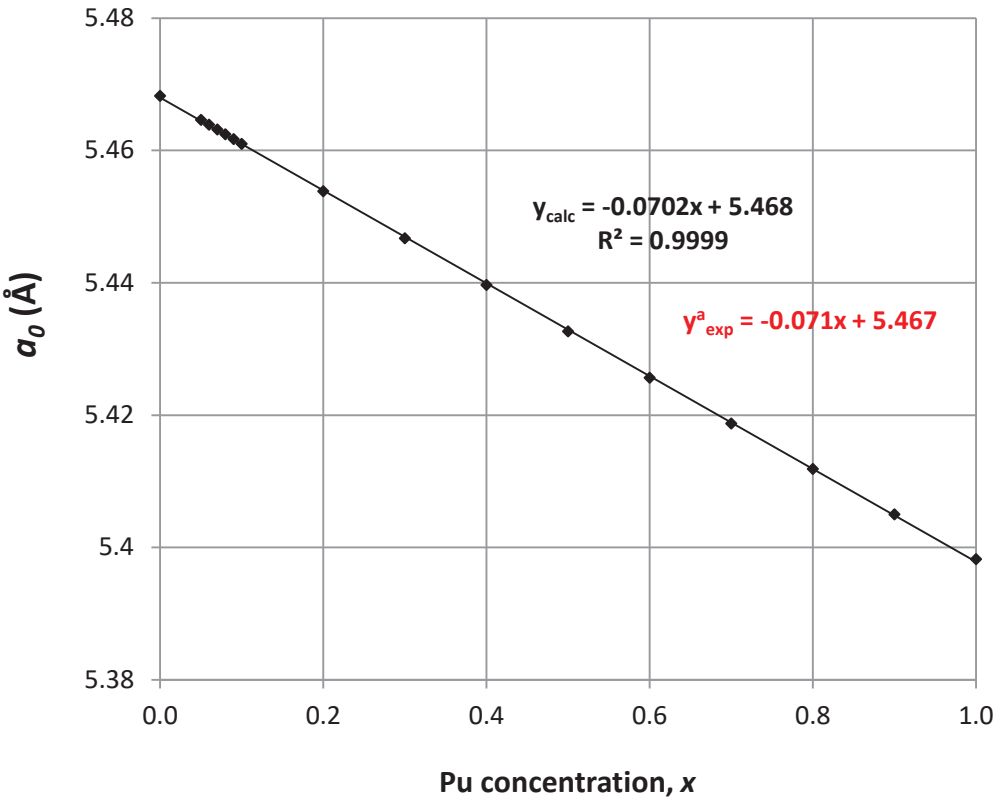


**Figure 8.5: Graph of the unit cell lattice parameter ($a_0$) of MOX fuel as a function of Pu concentration ($x$) using the mean-field method. [a] Arab-Chapelet et al. (2008) [173].**

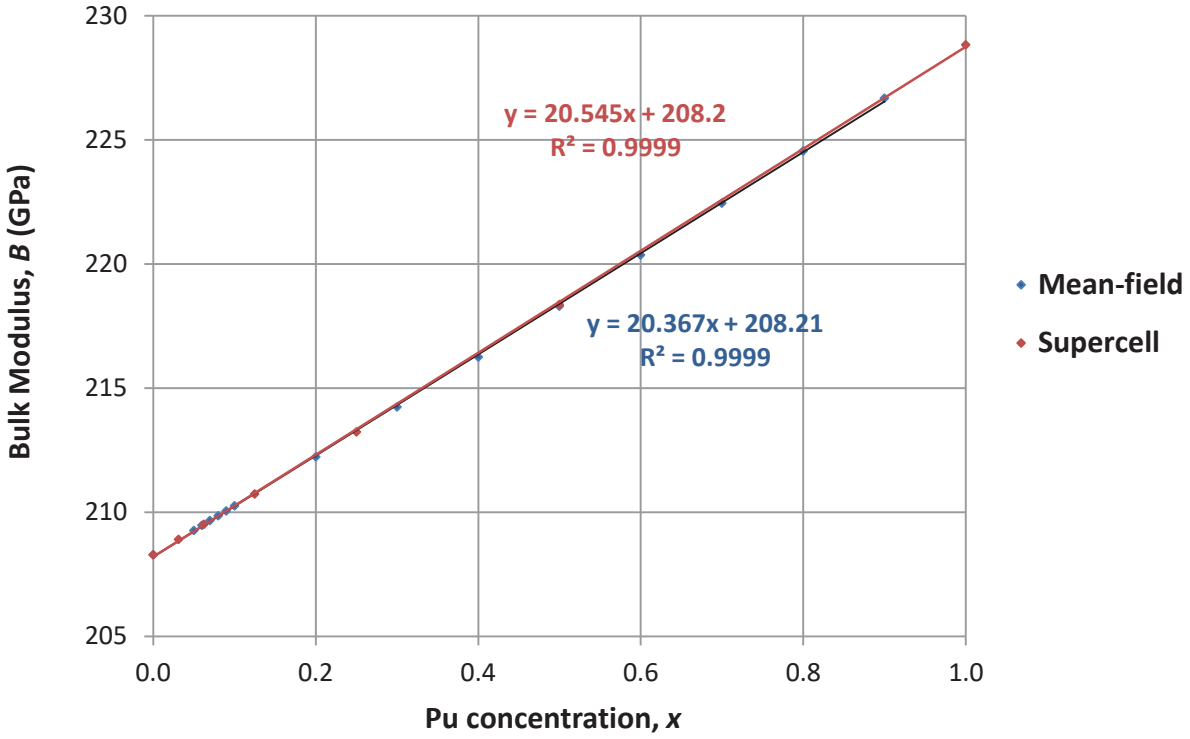


**Figure 8.6: Graph of the bulk modulus ($B$) of MOX fuel as a function of Pu concentration ($x$).**

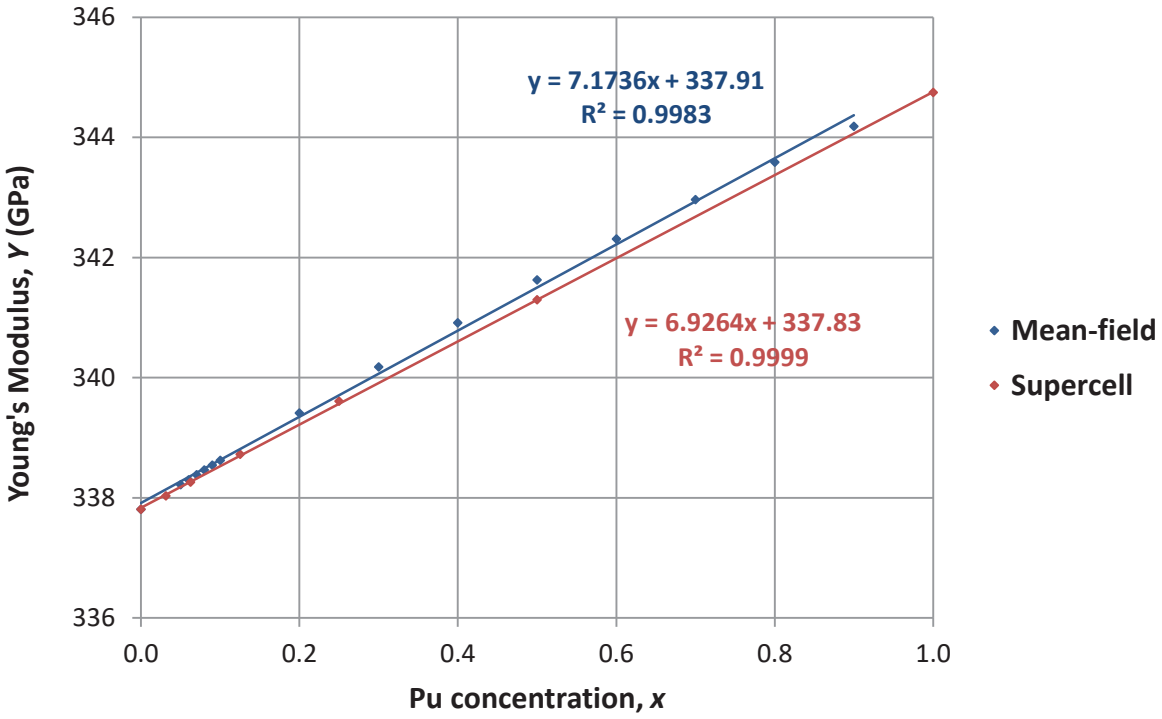


**Figure 8.7: Graph of the Young's modulus ($Y$) of MOX fuel as a function of Pu concentration ($x$).**

## Analysis and Discussion

As shown in the graphs of the properties of MOX fuel, the results using both methods agree. The lattice constant of MOX fuel varies linearly with Pu concentration, confirming MOX fuel is a solid solution, obeying Vegard's Law [167]. The predicted variation in the lattice constant is in very good agreement with experimental data of Arab- Chapelet et al. (2008) [173]. The lattice constant decreases linearly by ~ 0.1 Å from $UO_2$ to $PuO_2$. The mechanical moduli also vary linearly with Pu concentration in MOX fuel. $PuO_2$ and MOX fuel is mechanically stronger than $UO_2$, particularly in response to bulk stress. The bulk modulus of $PuO_2$ is ~9.6% (~20 GPa) greater than that of $UO_2$. The Young's modulus of $PuO_2$ is ~2.1% (~7 GPa) greater than that of $UO_2$. The moduli of MOX fuel lies in between those of $UO_2$ and $PuO_2$, following the linear variation.

## 8.5 Helium Incorporation

Simulations of helium incorporation were performed for pure and defective MOX fuel. The mean-field approach was used to calculate helium incorporation energies as a function of Pu content. In addition, the supercell method was used to model helium trapping in various defects in MOX fuel of 9.26% Pu concentration, which is representative of the average Pu content in commercial MOX fuel. To model helium interactions, the Lennard-Jones potentials of Grimes et al. (1990) [133] were used.

### 8.5.1 Helium in Pure MOX Fuel

Helium was incorporated in pure MOX fuel using the mean-field method and the Pu content varied. A single helium atom was inserted in an octahedral interstitial site (OIS) and the defect formation energy was calculated which is equivalent to the incorporation energy. This performed using the Mott-Littleton method [63] with radii of region 1 and 2a of 14 Å and 28 Å, respectively as used by Read et al.(2010, 2014) for $UO_2$ [30] and $PuO_2$ [64]. Calculated and reported helium incorporation energies in pure $PuO_2$ and $UO_2$ are summarised in Table 8.3. The variation in the helium incorporation energy in MOX fuel with Pu concentration is shown in Figure 8.8.

**Table 8.3: Helium incorporation energies ($E_{He}^{Incorp}$) in an OIS in pure $PuO_2$ and $UO_2$.**

| Compound | Calculated $E_{He}^{Incorp}$ (eV) | Reported $E_{He}^{Incorp}$ (eV) |
|---|---|---|
| $PuO_2$ | -0.07 | 2.73[a], 1.02[b] 0.4[e] |
| $UO_2$ | -0.11 | 0.45[c], -0.1[d], -0.1[e*], 1.3[f], -0.1[g] |

**a-Tian et al. (2013) [126], ab-initio, $PuO_2$, b- Gryaznov et al. (2010) [135], ab-initio, $PuO_2$, c- Yakub et al. (2010) [134], potentials, $UO_{2+x}$, d- Govers et al. (2009) [131], potentials, $UO_2$, e- Freyss et al. (2006) [105], ab-initio, $PuO_2$, e*- Freyss et al. (2006) [105], ab-initio, $UO_2$, f- Crocombette (2002) [127], ab-initio, $UO_2$, g- Grimes et al. (1990) [133], potentials, $UO_2$.**

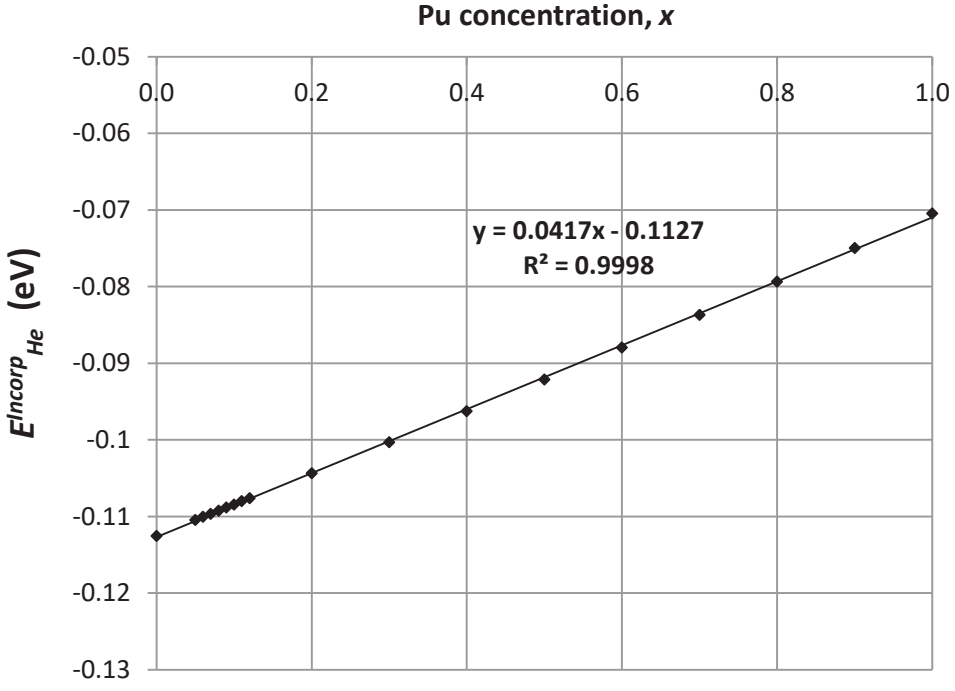


**Fig. 8.8. Graph of the Pu solution energy ($E_{Sol}^{Pu}$) in MOX fuel as a function of Pu concentration ($x$).**

## Analysis and Discussion

The results show that helium incorporation in OISs favourable in MOX fuel over the full range of Pu concentration. There is a linear dependence on the incorporation energy with the Pu content, being ~57% more exothermic for $UO_2$ than for $PuO_2$. This corresponds to a small energy difference of 0.04 eV. For $UO_2$, the calculated incorporation energy is -0.11 eV, in agreement with Govers et al. (2009) [133], Freyss et al. (2006) [105] and Grimes et al. (1990) [133]. The reason for the difference between the two compounds is that $Pu^{4+}$ ions in $PuO_2$ have a crystal radius of 1.10 Å, which is 0.04 Å smaller than that of $U^{4+}$ ions in $UO_2$ of 1.14 Å. Hence, the lattice parameter ($a_0$) of $PuO_2$ is slightly smaller than that of $UO_2$. For $PuO_2$ it is 5.39819 Å [89] and for $UO_2$ it is 5.4682 Å [174]. Therefore, the size of the OISs in the fluorite-structured lattice of $UO_2$ are larger than in $PuO_2$, thus there is a greater free volume available for helium atoms to occupy.

### 8.5.2 Defective 9% Pu MOX Fuel

Simulations of intrinsic defects in MOX fuel of 9.26% Pu content were performed. A 3 × 3 × 3 $UO_2$ supercell (108 U ions, 216 oxygen ions) was doped randomly with Pu by substitution of ten U ions with Pu ions. Point defects, Frenkel pairs and Schottky defects were then created in the supercell, with helium atoms inserted in vacancies. The formation energies of these defects were calculated as the difference in lattice energies of the defective and pure supercells. All defects were positioned near the centre of the supercell to ensure energy convergence. The calculated defect formation and binding energies of the intrinsic defects are listed in Table 8.4.

**Table 8.4: Intrinsic defect formation ($E_D^F$) and binding energies ($E_D^B$) in 9% Pu MOX fuel.**

| Defect | $E_D^F$ (eV) | $E_D^B$ (eV) |
|---|---|---|
| **Oxygen vacancy, $V_O^{\blacksquare\blacksquare}$** | 16.06 | - |
| **Pu vacancy, $V_{Pu}^{////}$** | 78.60 | - |
| **U vacancy, $V_U^{////}$** | 77.06 | - |
| **Oxygen interstitial, $O_i^{//}$** | -11.81 | - |
| **Pu interstitial, $Pu_i^{\blacksquare\blacksquare\blacksquare\blacksquare}$** | -63.68 | - |
| **U interstitial, $U_i^{\blacksquare\blacksquare\blacksquare\blacksquare}$** | -61.73 | - |
| **OFP** | 4.20 | -0.04 |
| **PuFP** | 15.21 | 0.29 |
| **UFP** | 14.91 | -0.41 |
| **Pu type Schottky** | 4.91 | -2.24 |
| **U type Schottky** | 4.99 | -2.20 |

## 8.5.3 Helium in Defective MOX Fuel

In addition to octahedral interstitial sites (OISs), other possible helium trapping sites include oxygen and Pu vacancies and Schottky defects. Using the supercell method, helium incorporation energies ($E_{He}^{Incorp}$) in these trapping sites were calculated as the difference in the supercell lattice energies for the configurations of trapped ($E_{He,trapped}^F$) and untrapped helium ($E_{He,untrapped}^F$), divided by the number of helium atoms ($N_{He}$), given by:

$$E_{He}^{Incorp} = \frac{1}{N_{He}}[E_{He,trapped}^{F} - E_{He,untrapped}^{F}] \quad \textbf{(8.3)}$$

For a single helium atom in an OIS, the defect formation energy is equivalent to the incorporation energy. In the untrapped configuration, the helium atom(s) were positioned in neighbouring OISs to the trapping defect. Calculated helium incorporation energies associated with the different trapping sites in 9.26% Pu doped MOX fuel, $UO_2$ and $PuO_2$ are given in Table 8.5. Calculated and reported helium incorporation energies for $UO_2$ are given in Appendix C.

**Table 8.5: Helium incorporation energies ($E_{He}^{Incorp}$) in 9% Pu MOX fuel, $UO_2$ and $PuO_2$.**

| Helium Trapping Site(s) | $E_{He}^{Incorp}$ (eV) | | |
|---|---|---|---|
| | 9% MOX | $UO_2$ | $PuO_2$ |
| OIS | -0.10 | -0.11 | -0.07 |
| Oxygen vacancy, $V_O^{\blacksquare\blacksquare}$ | -0.20 | -0.08 | -0.55 |
| Pu vacancy, $V_{Pu}^{////}$ | -0.09 | - | -0.24 |
| U vacancy, $V_U^{////}$ | 0.02 | -0.17 | - |
| Pu type Schottky defect | -0.16 | - | -0.17 |
| U type Schottky defect | -0.11 | -0.17 | - |

In addition to calculations of helium incorporation in MOX fuel, the helium migration barrier was calculated. This corresponds to a helium atom positioned between two adjacent oxygen ions in the MOX fuel matrix. The energy barrier was calculated as 2.82 eV, which is 0.69 e V less than that for $PuO_2$ of 3.51 eV, but only 0.11 eV greater than that for $UO_2$ of 2.71 eV, which is due to the modest level of Pu doping.

## Analysis and Discussion

The intrinsic defect energies for MOX fuel are similar to those of $UO_2$ and $PuO_2$, as expected. The most favourable neutral defects are the oxygen Frenkel pairs and Schottky defects, which have formation energies of between ~4 and 5 eV, approximately one third of that of the cation Frenkel pairs. Schottky defects are favourably bound clusters, which have binding energies of ~-2 eV, indicating these would be stable at very high temperatures. Regarding helium trapping in MOX fuel, the incorporation energy in an OIS is 91% of that for $UO_2$, indicating there is a linear dependence on the energy with Pu doping. However, some unexpected deviations form helium trapping in $UO_2$ and $PuO_2$ were predicted.

Helium trapping in an oxygen vacancy is much more exothermic than in $UO_2$, whilst trapping in cation vacancies is (unexpectedly) much less favourable than in $PuO_2$ or $UO_2$. Helium trapping in a Pu vacancy is slightly exothermic but in a U vacancy is endothermic, with incorporation energies of -0.09 eV and 0.02 eV respectively. Helium incorporation in Schottky defects is favourable, having a mean energy of -0.14 eV, slightly more endothermic than the expected -0.17 eV. These deviations could be due to concentration effects in the supercell, and the particular locations of helium atoms within the MOX fuel matrix. For example, helium-trapping locations near Pu ions leads to more $PuO_2$ like behaviour, as for the helium trapping in the oxygen vacancy.

## 8.6 Summary

In summary, the Read et al. and Jackson et al. potentials for $UO_2$ and $PuO_2$ were successfully used to calculate structural, mechanical and defect properties of MOX fuel of formula $Pu_xU_{1-x}O_2$. The Pu concentration ($x$) was varied using both the mean-field and supercell methods. Generally, these methods gave concordant results on the lattice parameter and mechanical moduli of MOX fuel. These results confirmed that MOX fuel is a solid solution, in agreement with the literature. This is because the lattice parameter and mechanical moduli vary linearly as a function of Pu concentration ($x$) over the full range, obeying Vegard's Law.

In addition, the Pu defect formation and solution energies were also calculated based on the supercell method, and were found to vary linearly with the Pu concentration ($x$). Pu incorporation in $UO_2$ is energetically favourable over the full range of Pu concentration for pure MOX fuel. The predicted variation in the energies is very small, ~1%. This is due to the crystal radius of the $Pu^{4+}$ ion being slightly smaller than that of the $U^{4+}$ ion.

Furthermore, helium incorporation and solution energies were calculated for helium atom insertion in an OIS, as a function of Pu content from $UO_2$ to $PuO_2$. Helium incorporation was exothermic over the full range of Pu content. In addition, intrinsic defects and helium trapping was simulated in MOX fuel of 9.26% Pu content. Oxygen Frenkel pairs and Schottky defects were calculated to be the energetically preferred intrinsic defects. Regarding helium trapping, OISs, Schottky defects and oxygen vacancies were the most favourable trapping sites, which could also be effective helium bubble nucleation centres.

# Chapter 9

# Conclusions and Future Work

## 9.1 Overview

In conclusion, the project was successful in achieving the aim to employ atomistic simulations to enhance understanding of the properties and complex ageing behaviour of plutonium dioxide ($PuO_2$). This was achieved through a range of static bulk lattice, surface and molecular dynamics simulations. The foundation of these atomistic simulations was the interatomic potentials used. Appropriate published potentials were used and applied to investigate various aspects of $PuO_2$ and mixed oxide (MOX) fuel. These included bulk lattice properties, intrinsic defects, helium behaviour, surfaces, thermal properties and radiation damage.

Static bulk lattice simulations of $PuO_2$ and MOX fuel predicted bulk lattice properties, intrinsic defects and helium behaviour using the General Utility Lattice Program (GULP) [50,61]. In addition, pure and defective $PuO_2$ surfaces were modelled, using the Minimum Energy Techniques Applied to Dislocations, Interfaces and Surface Energies (METADISE) program [67]. Finally, molecular dynamics simulations were performed on $PuO_2$ to predict thermal properties and to simulate 1keV cascades using the DL_POLY program [150].

## 9.2 Bulk Lattice Simulations

A multitude of static bulk lattice simulations of $PuO_2$ were performed using GULP. Initially, the most suitable $PuO_2$ potentials were chosen from the literature. The published potentials were evaluated by comparison of predicted structural, mechanical and optical properties to reported experimental and computational data. From this, the potentials of Read et al. (2014) [64] and Jackson et al. (1986) [91] (abbreviated Read et al.) were chosen for further static lattice simulations. These potentials are fully ionic, and incorporate the shell model to take into account ionic polarisation. Based on the Born model for ionic solids, the potentials consist of a long-range electrostatic component and a short-range Buckingham potentials. The Mott-Littleton method [63] was used to calculate intrinsic defect formation energies and binding energies of bound defects. The results were comparable to reported data and predicted that oxygen Frenkel pairs and Schottky defects were the preferred forms of intrinsic defects in $PuO_2$.

Static lattice simulations were also performed to model helium behaviour in $PuO_2$. The Lennard-Jones potentials of Grimes et al. (1990) [133] were used to model helium interactions. To predict the energetic favourability of individual atoms in different trapping sites, helium incorporation energies were calculated at octahedral interstitial sites (OISs), individual vacancies and Schottky defects. The results showed helium incorporation is weakly exothermic, with trapping energetically preferred in OISs and Schottky defects in stoichiometric $PuO_2$, which could form effective helium bubble nucleation centres. However, in pure $PuO_2$ helium clustering in a single OIS was predicted to be energetically unfavourable. A thorough study of helium diffusion in defective $PuO_2$ is needed using molecular dynamics to investigate this further.

Mixed oxide (MOX) nuclear fuel was also simulated, which is considered a solid solution of uranium dioxide ($UO_2$) doped with Pu. Static lattice simulations were performed using the Read et al. $UO_2$ [30] and $PuO_2$[64] potentials. Structural and mechanical properties were calculated as a function of Pu content using

mean-field and supercell methods. Pu substitution in $UO_2$ was exothermic due to the slightly smaller ionic radius of $Pu^{4+}$ compared to $U^{4+}$ ions.

The results showed properties varied linearly with Pu content, obeying Vegard's Law [167], confirming MOX fuel is a solid solution. Helium atom insertion in OISs was weakly exothermic (slightly more for $UO_2$) and Schottky defects were the most favourable trapping sites. Simulations of intrinsic defects and helium trapping were performed on MOX fuel of 9.26% Pu content, of relevance to commercial MOX fuel. Schottky defects were the energetically preferred intrinsic defects and amongst the most effective helium trapping sites.

## 9.3 Surface Simulations

The Read et al. $PuO_2$ potentials were transferred to model pure and defective surfaces of $PuO_2$, using the METADISE program. For pure surfaces, the simulations were analogous to those of Williams et al. (2015) [35] for $UO_2$, with the $\{n10\}$, $\{n11\}$ and $\{nn1\}$ pure surfaces modelled for $n$ = 1,2,3. Surface energies and $d$ spacing's were calculated which agreed well with the literature. The (111) was the most stable surface, resulting in an octahedral equilibrium morphology of crystalline $PuO_2$. This is a Tasker type 1 surface that is oxygen terminated, consisting of alternating layers of oxygen and Pu ions. Furthermore, the (221) and (331) surfaces were the other most stable surfaces, which exhibited more complicated facetted terminations.

Simulations of defective (100), (110) and (111) $PuO_2$ surfaces were also performed. Overall, segregation of Schottky defects were shown to be energetically favoured, whilst Frenkel pairs prefer to form within the bulk lattice. Helium incorporation on the (111) surface was also simulated, which revealed helium trapping in individual vacancies and Schottky defects is an order of magnitude more exothermic than in the bulk lattice. Hence, segregation of helium was predicted to

defective surfaces, contributing to helium release. A thorough study of helium diffusion in defective $PuO_2$ is needed using molecular dynamics to investigate this further.

## 9.4 Molecular Dynamics

Molecular dynamics simulations were performed to incorporate temperature and time in the modelling of $PuO_2$, using the DL_POLY program. Thermal properties of $PuO_2$ were calculated and compared to reported experimental and computational data. These included thermal expansion coefficient, constant pressure heat capacity and pair-distribution function data. It was found the Arima et al. (2005) [81] and Inaba et al. (1999) [95] (abbreviated Arima et al.) potentials were more appropriate for molecular dynamics than the Read et al. potentials.

However, this was expected as the Read et al. potentials were fit to properties at room temperature whereas the Arima et al. potentials were fitted to thermal expansion data of cerium dioxide ($CeO_2$). The Arima et al. potentials are partially ionic and rigid ion, and assume the ions have 67.5% of their formal charge and use Buckingham potentials. Using these potentials, thermal properties were calculated as a function of temperature over 298 K to 3000 K. The thermal expansion of $PuO_2$ over this temperature range was only ~4%, and the compound has a relatively large heat capacity, showing it is a thermally resistant material suitable for reactor core conditions.

In addition, 1 keV cascades in $PuO_2$ were simulated using molecular dynamics. ZBL potentials [160] were added to the short-range Arima et al. potentials by splining, making the overall potentials suitable for high-energy ballistic collisions of the ions. A 1 keV Pu ion was projected in the supercell, and the subsequent temperature and defect evolution was predicted. The effect of temperature was modelled using initial temperatures of 298 K and 700 K.

Overall, the simulation results showed that the $PuO_2$ lattice recovered within two pico seconds confirming it is a radiation tolerant material, in agreement with the literature. The system temperature peaked immediately following the initiation of the PKA or cascade, with the excess energy rapidly absorbed by the system increasing the average temperature. Generally, the initial temperatures did not strongly affect the system behaviour, although at the higher temperature, the damage recovery was more efficient. A few Frenkel pairs remained at the end of the simulations at equilibrium, which could affect mechanical properties.

## 9.5 Future Work

Future work relating to the project could consist of a range of additional atomistic simulations of $PuO_2$ and MOX fuel. Clearly, the same areas of research are applicable to both materials and are of general interest e.g. thermo-mechanical properties, radiation damage etc. However, there are specific areas of research of relevance to ageing behaviour in storage scenarios, of importance to the nuclear industry.

In particular, additional molecular dynamics simulations would be useful to model helium diffusion and helium bubbles involving grain boundaries. Regarding Pu, there is the 3+ oxidation state to consider and relates to the sesqui-oxide $Pu_2O_3$, which could be important for stored Pu. In addition, additional surface simulations could investigate surface hydroxylation and the behaviour of impurities. Regarding MOX fuel, the heterogeneous form could be simulated, where there are Pu rich regions that will affect properties. In addition, the behaviour of fission products including xenon and caesium could be modelled to simulate nuclear fission reactions

# Appendices

## Appendix A: Properties of Novel $PuO_2$ Surfaces

Simulation results of a range of novel pure $PuO_2$ surfaces are given in Tables A.1 to A.4. These surfaces include the $\{n10\}$, $\{n11\}$, $\{n10\}$ and $\{nn1\}$ for $n = 4,5,6,7$ and ten other novel surfaces. Tables A.1 and A.2 give the unrelaxed and relaxed energies and the associated surface areas. Tables A.3 and A.4 give the calculated attachment energies and $d$ spacing's of the surfaces.

**Table A.1: Calculated surface energies and associated areas of novel, high index pure $PuO_2$ surfaces.**

| Surface | Area ($Å^2$) | $E_{Surf,Hartman}^{Unrel}$ ($Jm^{-2}$) | $E_{Surf,Gibbs}^{Unrel}$ ($Jm^{-2}$) | $\overline{E}_{Surf}^{Unrel}$ ($Jm^{-2}$) | $E_{Surf}^{Rel}$ ($Jm^{-2}$) | $\%\Delta E_{Surf}$ |
|---|---|---|---|---|---|---|
| **(410)** | 120.15 | 23.47 | 17.47 | 20.47 | 3.28 | -83.99 |
| **(411)** | 123.63 | 15.01 | 11.88 | 13.44 | 2.82 | -79.01 |
| **(441)** | 167.40 | 3.88 | 5.20 | 4.54 | 2.16 | -52.33 |
| **(510)** | 148.59 | 28.60 | 20.21 | 24.40 | 3.24 | -86.74 |
| **(511)** | 151.42 | 18.11 | 13.76 | 15.93 | 2.82 | -82.28 |
| **(551)** | 208.10 | 1.40 | 3.12 | 2.26 | 1.87 | -17.39 |
| **(610)** | 177.25 | 29.37 | 26.22 | 27.80 | 2.64 | -90.51 |
| **(611)** | 179.63 | 18.73 | 17.92 | 18.32 | 2.83 | -84.56 |
| **(661)** | 248.98 | 1.17 | 3.17 | 2.17 | 1.90 | -12.22 |

| | | | | | | |
|---|---|---|---|---|---|---|
| **(710)** | 206.05 | 30.09 | 29.67 | 29.88 | 2.90 | -90.29 |
| **(711)** | 208.10 | 19.27 | 20.29 | 19.78 | 2.85 | -85.60 |
| **(771)** | 289.94 | 1.00 | 3.20 | 2.10 | 1.93 | -8.30 |
| **(810)** | 234.94 | 29.37 | 35.48 | 32.43 | 2.84 | -91.24 |
| **(811)** | 236.74 | 18.94 | 24.31 | 21.63 | 2.89 | -86.65 |
| **(881)** | 330.97 | 1.97 | 4.30 | 3.13 | 2.12 | -32.29 |
| **(910)** | 263.88 | 28.54 | 41.12 | 34.83 | 2.94 | -91.56 |
| **(911)** | 265.48 | 18.73 | 26.96 | 22.85 | 2.75 | -87.96 |
| **(991)** | 372.04 | 0.78 | 3.24 | 2.01 | 1.96 | -2.51 |

**Table A.2: Calculated surface energies and associated areas of novel pure $PuO_2$ surfaces.**

| Surface | Area ($Å^2$) | $E^{Unrel}_{Surf,Hartman}$ ($Jm^{-2}$) | $E^{Unrel}_{Surf,Gibbs}$ ($Jm^{-2}$) | $\overline{E}^{Unrel}_{Surf}$ ($Jm^{-2}$) | $E^{Rel}_{Surf}$ ($Jm^{-2}$) | $\%\Delta E_{Surf}$ |
|---|---|---|---|---|---|---|
| **(320)** | 105.07 | 11.55 | 9.26 | 10.41 | 2.79 | -73.178 |
| **(332)** | 136.68 | 17.15 | 13.69 | 15.42 | 2.00 | -87.036 |
| **(430)** | 145.70 | 7.88 | 8.43 | 8.15 | 2.65 | -67.46 |
| **(433)** | 169.92 | 7.79 | 7.60 | 7.69 | 2.10 | -72.70 |
| **(531)** | 172.40 | 4.46 | 5.74 | 5.10 | 2.20 | -56.86 |
| **(533)** | 191.09 | 5.12 | 5.55 | 5.33 | 2.20 | -58.77 |
| **(540)** | 186.59 | 5.91 | 7.79 | 6.85 | 2.57 | -62.52 |
| **(544)** | 220.01 | 16.15 | 14.39 | 15.27 | 1.95 | -87.25 |

| | | | | | | |
|---|---|---|---|---|---|---|
| **(553)** | 223.83 | 12.71 | 15.46 | 14.09 | 2.15 | -84.76 |
| **(655)** | 270.24 | 24.85 | 29.03 | 26.94 | 2.62 | -90.29 |

**Table A.3: Calculated attachment energies ($E_{Surf}^{Attach}$ per $PuO_2$) and $d$ spacing's of high index pure $PuO_2$ surfaces.**

| Surface | $E_{Surf}^{Attach}$ per $PuO_2$ (eV) | Calculated $d$ Spacing (Å) | Experimental $d$ Spacing [a] (Å) | %Δ ($\times 10^{-2}$) |
|---|---|---|---|---|
| **(410)** | -44.01 | 1.3093 | 1.3087 | 4.23 |
| **(411)** | -28.95 | 1.2724 | 1.2718 | 4.45 |
| **(441)** | -10.13 | 0.9397 | 0.9393 | 4.30 |
| **(510)** | -66.31 | 1.0587 | 1.0582 | 4.46 |
| **(511)** | -42.79 | 1.0389 | 1.0385 | 3.68 |
| **(551)** | -4.54 | 0.7559 | 0.7556 | 3.94 |
| **(610)** | -81.25 | 0.8875 | 0.8871 | 4.02 |
| **(611)** | -52.50 | 0.8757 | 0.8753 | 4.59 |
| **(661)** | -4.54 | 0.6318 | 0.6316 | 3.33 |

| | | | | |
|---|---|---|---|---|
| **(710)** | -96.73 | 0.7634 | 0.7631 | 4.18 |
| **(711)** | -62.56 | 0.7559 | 0.7556 | 3.94 |
| **(771)** | -4.53 | 0.5425 | 0.5423 | 4.40 |
| **(810)** | -107.68 | 0.6696 | 0.6693 | 3.93 |
| **(811)** | -69.97 | 0.6645 | 0.6642 | 4.08 |
| **(881)** | -10.17 | 0.4753 | 0.4751 | 3.88 |
| **(910)** | -117.51 | 0.5961 | 0.5959 | 3.87 |
| **(911)** | -77.60 | 0.5925 | 0.5923 | 3.85 |
| **(991)** | -4.53 | 0.4228 | 0.4226 | 5.18 |

**a- Belin et al. (2004) [89], exp, $PuO_2$.**

**Table A.4: Calculated attachment energies ($E_{Surf}^{Attach}$ per $PuO_2$) and $d$ spacing's of novel, high index pure $PuO_2$ surfaces.**

| Surface | $E_{Surf}^{Attach}$ per $PuO_2$ (eV) | Calculated $d$ Spacing (Å) | Experimental $d$ Spacing [a] (Å) | %Δ ($\times 10^{-2}$) |
|---|---|---|---|---|
| **(320)** | -18.93 | 1.4972 | 1.4966 | 3.93 |
| **(332)** | -36.59 | 1.1509 | 1.1504 | 4.33 |
| **(430)** | -17.92 | 1.0796 | 1.0792 | 4.06 |
| **(433)** | -20.65 | 0.9258 | 0.9254 | 4.13 |
| **(531)** | -12.00 | 0.9125 | 0.9121 | 3.95 |
| **(533)** | -15.26 | 0.8232 | 0.8229 | 3.84 |
| **(540)** | -17.21 | 0.8431 | 0.8427 | 4.22 |
| **(544)** | -55.44 | 0.7150 | 0.7147 | 4.31 |
| **(553)** | -44.40 | 0.7028 | 0.7025 | 4.05 |
| **(655)** | -104.79 | 0.5821 | 0.5819 | 3.47 |

**a- Belin et al. (2004) [89], exp, $PuO_2$.**

# Appendix B: Convergence Testing Data for Modelling Surface Defects

To determine suitable region 1 and 2a Mott-Littleton radii for modelling surface defects, convergence testing was used, by modelling a Schottky defect in the (111) $PuO_2$ surface, at a depth of 0.33 Å. The region 1 and 2a radii were varied, with the region 2a radius a factor of four larger than that of region 1. The region 1 radii used were 7, 8 and 9 Å. Increasing the region 1 radius beyond 9 Å, the defect energy did not change notably, resulting in little accuracy gain. Hence, a region 1 radius of 9 Å was used in the surface defect simulations.

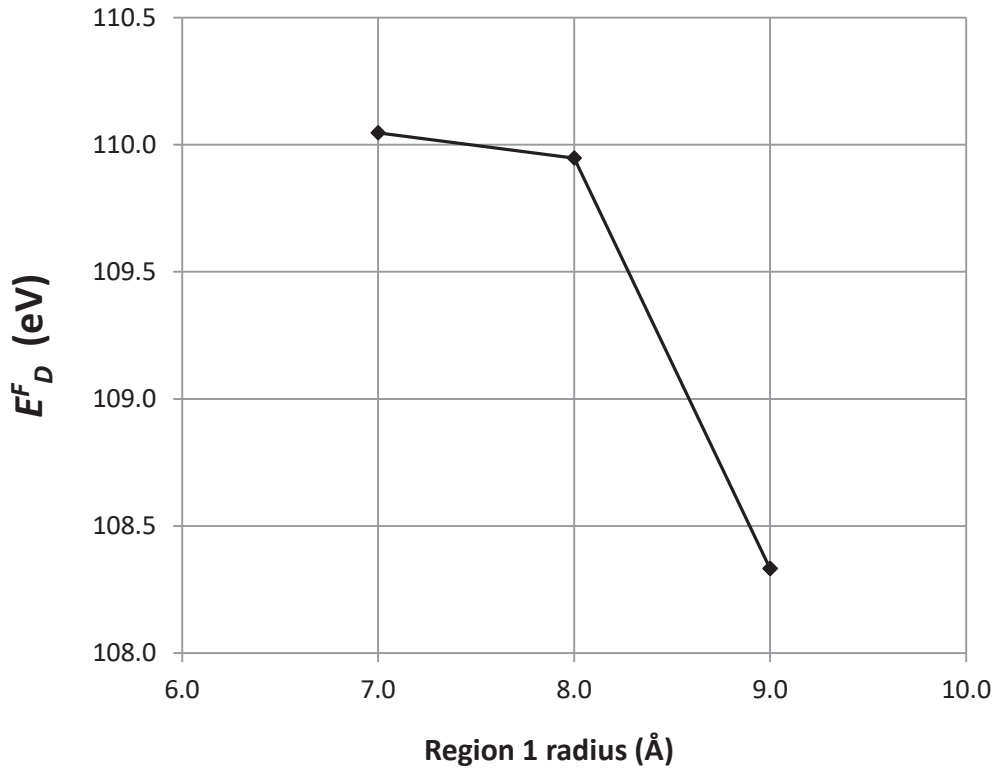


**Figure B.1: Schottky defect formation energy vs. region 1 radius for surface defect calculations.**

# Appendix C: Helium Incorporation Data for $UO_2$

The calculated helium incorporation energies ($E_{He}^{Incorp}$) associated with the different helium trapping sites in $UO_2$ are given in Table C.1. The method of calculation was analogous to that of $PuO_2$.

**Table C.1: Helium incorporation energies ($E_{He}^{Incorp}$) in $UO_2$.**

| Helium Tapping Site(s) | Calculated $E_{He}^{Incorp}$ (eV) | Reported $E_{He}^{Incorp}$ (eV) |
|---|---|---|
| **OIS** | -0.11 | 0.45[a], -0.1[b], -0.1[c], 1.3[d], -0.1[e] |
| **Oxygen vacancy, $V_O^{\blacksquare\blacksquare}$** | -0.08 | -0.19 to -0.09[b], 1.7[d], -0.23[e] |
| **U vacancy, $V_U^{////}$** | -0.17 | -0.2 to 0.18[b], 0.1[d] , -0.2[e] |
| **Schottky defect** | -0.17 | - |

**a- Yakub et al. (2010) [134], potentials, $UO_{2+x}$, b- Govers et al. (2009) [131], potentials, $UO_2$, c- Freyss et al. (2006) [105], ab-initio, $UO_2$, d- Crocombette (2002) [127], ab-initio, $UO_2$, e- Grimes et al. (1990) [133], potentials, $UO_2$.**

# References


1. *Nuclear Power in the World Today*. World Nuclear Association (Online), URL: http://www.world-nuclear.org/information-library/current-and-future-generation/nuclear-power-in-the-world-today.aspx
2. *Nuclear Power in the United Kingdom*. World Nuclear Association (Online), URL: http://www.world-nuclear.org/information-library/country-profiles/countries-t-z/united-kingdom.aspx
3. *Climate Change Act 2008*. UK Government (Online), URL: https://www.legislation.gov.uk/ukpga/2008/27/contents
4. Hinson, S., Sutherland, N, *Nuclear Sector Deal* (July 2018). House of Commons Library (Online), URL: https://researchbriefings.parliament.uk/ResearchBriefing/Summary/CDP-2018-0175#fullreport
5. Hinson, S., *New Nuclear Power* (November 2018). House of Commons Library (Online), URL: https://researchbriefings.parliament.uk/ResearchBriefing/Summary/CBP-8176
6. *Nuclear Fission: Basics*. atomicarchive.com (Online), URL: http://www.atomicarchive.com/Fission/Fission1.shtml
7. *Nuclear Power Plants*. whatisnuclear.com (Online), URL: https://whatisnuclear.com/reactors.html
8. *Plutonium*. World Nuclear Association (Online), URL: http://www.world-nuclear.org/information-library/nuclear-fuel-cycle/fuel-recycling/plutonium.aspx
9. *MOX, Mixed Oxide Fuel*. World Nuclear Association (Online), URL: http://www.world-nuclear.org/information-library/nuclear-fuel-cycle/fuel-recycling/mixed-oxide-fuel-mox.aspx
10. *NuDat 2.7*. National Nuclear Data Center (NNDC), Brookhaven National Laboratory (Online), URL: https://www.nndc.bnl.gov/nudat2/
11. Leafe, M., *End in sight for end for reprocessing nuclear fuel at Sellafield*. UK Government (Online), URL: https://nda.blog.gov.uk/2017/01/24/end-in-sight-for-reprocessing-nuclear-fuel-at-sellafield/
12. *Managing the UK Plutonium Stockpile* (September 2016). The Parliamentary Office of Science and Technology (Online), URL: http://researchbriefings.parliament.uk/ResearchBriefing/Summary/POST-PN-0531#fullreport
13. *Management of the UK's plutonium stocks: consultation response* (December 2011). Department of Energy and Climate Change (DECC) (Online), URL: https://www.gov.uk/government/consultations/managing-our-plutonium-stocks
14. *Enhanced CANDU 6*. SNC- Lavalin (Online), URL: http://www.snclavalin.com/en/enhanced-candu-6-gen-3
15. *GE Hitachi PRISM*. GE Hitachi (Online), URL: http://gehitachiprism.com/
16. *NuScale Power*. NuScale Power (Online), URL: https://www.nuscalepower.com/
17. Takano, Y.*, et al.*, *Journal of the Physical Society of Japan* (2018) **87** (6), 061013
18. Hoffmann, M. J.*, et al.*, *J. Chem. Phys.* (2017) **146** (4), 15
19. Islam, M. S.*, et al.*, *J. Chem. Soc.-Faraday Trans.* (1996) **92** (3), 479
20. Liu, B.-H.*, et al.*, *Applied Physics A* (2016) **122** (4), 465
21. Chroneos, A.*, et al.*, *Acta Chim. Slov.* (2007) **54** (1), 179
22. Baikie, T.*, et al.*, *Journal of Materials Chemistry* (2005) **15** (1), 119
23. Zhang, H. W.*, et al.*, *J. Mater. Chem. A* (2018) **6** (19), 9116
24. Yang, X.*, et al.*, *The Journal of Physical Chemistry C* (2016) **120** (12), 6416
25. Wang, Q. C.*, et al.*, *Solid State Ion.* (2015) **278**, 157

26. Phadke, S.*, et al.*, *Journal of Materials Chemistry* (2012) **22** (48), 25388
27. Chroneos, A.*, et al.*, *Energy Environ. Sci.* (2011) **4** (8), 2774
28. Cooper, M. W. D.*, et al.*, *Journal of Nuclear Materials* (2018) **504**, 251
29. Taller, S. A., and Bai, X.-M., *Journal of Nuclear Materials* (2013) **443** (1–3), 84
30. Read, M. S. D., and Jackson, R. A., *Journal of Nuclear Materials* (2010) **406** (3), 293
31. Park, J.*, et al.*, *Nucl. Eng. Technol.* (2018) **50** (5), 731
32. Balboa, H.*, et al.*, *Journal of Nuclear Materials* (2017) **495**, 67
33. Cooper, M. W. D.*, et al.*, *Journal of Physics: Condensed Matter* (2014) **26** (10), 105401
34. Xiao, H.*, et al.*, *Surface Science* (2016) **649**, 1
35. Williams, N. R.*, et al.*, *Journal of Nuclear Materials* (2015) **458**, 45
36. Behera, R. K., and Deo, C. S., *J. Phys.-Condes. Matter* (2012) **24** (21), 15
37. Wang, Y. F.*, et al.*, *Journal of Materials Science* (2018) **53** (15), 10979
38. Sahi, Q. U. A., and Kim, Y. S., *Eur. Phys. J. B* (2018) **91** (5), 10
39. Rahman, M. J.*, et al.*, *Computational Materials Science* (2018) **154**, 508
40. Zhou, W.*, et al.*, *Journal of Nuclear Materials* (2018) **508**, 540
41. Martin, G.*, et al.*, *Nuclear Instruments and Methods in Physics Research Section B: Beam Interactions with Materials and Atoms* (2015) **352**, 135
42. Jomard, G.*, et al.*, *Journal of Nuclear Materials* (2014) **451** (1–3), 28
43. Rák, Z.*, et al.*, *Surface Science* (2013) **608**, 180
44. Lu, Y.*, et al.*, *Journal of Alloys and Compounds* (2015) **649**, 544
45. Yun, Y.*, et al.*, *Journal of Nuclear Materials* (2009) **385** (2), 364
46. Wang, B.-T.*, et al.*, *Journal of Alloys and Compounds* (2015) **628**, 267
47. Lee, C. W.*, et al.*, *Journal of Nuclear Materials* (2015) **456**, 253
48. Buckingham, R. A., *Proceedings of the Royal Society of London Series a-Mathematical and Physical Sciences* (1938) **168** (A933), 264
49. Rowley, C., CC BY-SA 4.0, original Lennard-Jones graph modified (Online), URL: https://commons.wikimedia.org/w/index.php?curid=42956679,
50. Gale, J. D., and Rohl, A. L., *Molecular Simulation* (2003) **29** (5), 291
51. Dick Jr, B., and Overhauser, A., *Physical Review* (1958) **112** (1), 90
52. Tilley, R. J. D., *Defects in Solids*. John Wiley & Sons, Inc., Hoboken, New Jersey: (2008), Chp. 2.
53. Pauling, L., *The Nature of the Chemical Bond*. 3rd ed.; Cornell University Press: (1960)
54. Ewald, P. P., *Annalen der Physik* (1921) **369** (3), 253
55. Leach, A. R., *Molecular Modelling, Principles and Applications*. 2nd ed.; Pearson Education Limited: (2001), Chp. 6, pp. 303-352.
56. Henao, A., Ph.D. Thesis, *Local Ordering and dynamics of plastic crystals*, Paderborn University: (2016).
57. Parry, D. E., *Surface Science* (1975) **49** (2), 433
58. Wales, D. J., *Energy Landscapes*. Cambridge University Press, Cambridge: (2003), Chp. 4.1, pp. 192-196.
59. Leach, A. R., *Molecular Modelling, Principles and Applications*. 2nd ed.; Pearson Education Limited: (2001), Chp. 5, pp. 253-273.
60. Shanno, D. F., *Mathematics of Computation* (1970) **24**, 647
61. Gale, J. D., *Journal of the Chemical Society, Faraday Transactions* (1997) **93** (4), 629
62. Nye, J. F., *Physical properties of crystals*. Oxford University Press: (1957)
63. Mott, N. F., and Littleton, M. J., *Trans. Faraday Soc.* (1938) **34**, 485
64. Read, M. S. D.*, et al.*, *Journal of Nuclear Materials* (2014) **448** (1–3), 20
65. Tasker, P. W., *Journal of Physics C: Solid State Physics* (1979) **12** (22), 4977
66. Wang, H., and Wu, T., *Journal of Materials Chemistry* (2011) **21** (39), 15095

67. Watson, G. W.*, et al.*, *Journal of the Chemical Society, Faraday Transactions* (1996) **92** (3), 433
68. Hartman, P., *Journal of Crystal Growth* (1989) **96** (3), 667
69. Woensdregt, C. F., *Physics and Chemistry of Minerals* (1992) **19** (1), 52
70. Duffy, D. M., and Tasker, P. W., *A Guide to CHAOS*. Harwell Report, AERE-R11059 (1983)
71. Read, M. S. D., Ph.D. Thesis, *Atomistic Simulation Studies of the Defect and Surface Properties of Pervoskite-based Oxide Catalysts*. University of Surrey: (1999), Chp. 2.
72. Wulff, G., *Z. Kristallogr. Kristallgeom* (1901) **39**, 449
73. Leach, A. R., *Molecular Modelling, Principles and Applications*. 2nd ed.; Pearson Education Limited: (2001), Chp. 7, pp. 353- 360.
74. *Periodic Boundary Conditions*. ISAACS program (Online), URL: http://isaacs.sourceforge.net/phys/pbc.html
75. Swope, W. C.*, et al.*, *J. Chem. Phys.* (1982) **76** (1), 637
76. Mitchell, P. J., and Fincham, D., *J. Phys.-Condes. Matter* (1993) **5** (8), 1031
77. Lindan, P. J. D., and Gillan, M. J., *J. Phys.-Condes. Matter* (1993) **5** (8), 1019
78. Hoover, W. G., *Physical Review A* (1985) **31** (3), 1695
79. *Radial distribution function*. Wikipedia (Online), URL: https://en.wikipedia.org/wiki/Radial_distribution_function
80. Mingjie, W.*, et al.*, *Physica B: Condensed Matter* (2012) **407** (23), 4595
81. Arima, T.*, et al.*, *Journal of Alloys and Compounds* (2005) **400** (1–2), 43
82. Martin, G.*, et al.*, *Nuclear Instruments and Methods in Physics Research Section B: Beam Interactions with Materials and Atoms* (2011) **269** (14), 1727
83. Norgett, M. J.*, et al.*, *Nuclear Engineering and Design* (1975) **33** (1), 50
84. Devanathan, R.*, et al.*, *The Journal of Chemical Physics* (2009) **130** (17), 174502
85. Berlu, L.*, et al.*, *Journal of Nuclear Materials* (2008) **374** (3), 344
86. Jomard, G.*, et al.*, *Journal of Alloys and Compounds* (2007) **444–445**, 310
87. Aidhy, D. S.*, et al.*, *Scripta Materialia* (2011) **65** (10), 867
88. Aidhy, D. S.*, et al.*, *Scripta Materialia* (2015) **98** (Supplement C), 16
89. R. Belin, P. V., M. Reynaud, P. Raison, *J. Appl. Crystallogr.* (2004) **37** (6), 1034
90. Dwivedi, A., and Cormack, A. N., *Philosophical Magazine A* (1990) **61** (1), 1
91. Jackson, R. A.*, et al.*, *Philosophical Magazine A* (1986) **53** (1), 27
92. Meis, C., and Gale, J. D., *Materials Science and Engineering: B* (1998) **57** (1), 52
93. Catlow, C. R. A.*, et al.*, *Journal of Physics C: Solid State Physics* (1977) **10** (10), 1627
94. Uchida, T.*, et al.*, *Journal of Nuclear Materials* (2014) **452** (1–3), 281
95. Inaba, H.*, et al.*, *Solid State Ion.* (1999) **122** (1-4), 95
96. Yamada, K.*, et al.*, *Journal of Alloys and Compounds* (2000) **307** (1–2), 1
97. Kawamura, K., *Springer Series in Solid State Science* (1992) **103**, 88
98. Idiri, M.*, et al.*, *Physical Review B* (2004) **70** (1), 014113
99. Haire, R. G., *American Nuclear Society* (2000)
100. Cooper, M. W. D.*, et al.*, *Proceedings of the Royal Society A: Mathematical, Physical and Engineering Science* (2014) **470** (2171)
101. Bird, R. A., and Read, M. S. D., *Nuclear Instruments and Methods in Physics Research Section B: Beam Interactions with Materials and Atoms* (2017) **393**, 63
102. Kroger, F. A. V., H. J. , *Solid State Physics*. Academic Press: 1956
103. Tilley, R. J. D., *Defects in Solids*. John Wiley & Sons, Inc., Hoboken, New Jersey: (2008), Chp. 1.
104. Terentyev, D., *Computational Materials Science* (2007) **40** (3), 319
105. Freyss, M.*, et al.*, *Journal of Nuclear Materials* (2006) **352** (1–3), 144
106. Murch, G., and Catlow, R. A., *J. Chem. Soc., Faraday Trans. II* (1987) **83** (7), 1157
107. Yu, H. L.*, et al.*, *Journal of Alloys and Compounds* (2016) **654**, 567

108. Yu, H. L.*, et al.*, *Applied Surface Science* (2014) **316**, 625
109. Tan, A. H. H.*, et al.*, *Journal of Nuclear Materials* (2005) **344** (1), 13
110. Sun, B.*, et al.*, *Journal of Nuclear Materials* (2012) **426** (1–3), 139
111. Jomard, G., and Bottin, F., *Physical Review B* (2011) **84** (19), 195469
112. Abramowski, M.*, et al.*, *Journal of Nuclear Materials* (1999) **275** (1), 12
113. Tasker, P. W., *Surface Science* (1979) **87** (2), 315
114. Boyarchenkov, A. S.*, et al.*, *Journal of Nuclear Materials* (2012) **421** (1–3), 1
115. Castell, M. R., *Physical Review B* (2003) **68** (23), 235411
116. Baudin, M.*, et al.*, *Surface Science* (2000) **468** (1-3), 51
117. Conesa, J. C., *Surface Science* (1995) **339** (3), 337
118. Branda, M. M.*, et al.*, *Journal of Physical Chemistry C* (2008) **112** (45), 17643
119. Skorodumova, N. V.*, et al.*, *Physical Review B* (2004) **69** (7), 8
120. Taylor, T. N., and Ellis, W. P., *Surface Science* (1978) **77** (2), 321
121. Quinn, D. (2018), (Online), URL: https://www.drdianaquinn.com/octahedron.
122. Sattonnay, G.*, et al.*, *Journal of Nuclear Materials* (2006) **355** (1), 131
123. Ronchi, C., and Hiernaut, J. P., *Journal of Nuclear Materials* (2004) **325** (1), 1
124. Trocellier, P.*, et al.*, *Nuclear Instruments and Methods in Physics Research Section B: Beam Interactions with Materials and Atoms* (2003) **210** (Supplement C), 507
125. Martin, G.*, et al.*, *Nuclear Instruments and Methods in Physics Research Section B: Beam Interactions with Materials and Atoms* (2012) **273**, 122
126. Tian, X.*, et al.*, *The European Physical Journal B* (2013) **86** (4), 1
127. Crocombette, J. P., *Journal of Nuclear Materials* (2002) **305** (1), 29
128. Matzke, H., *Journal of the Chemical Society, Faraday Transactions 2: Molecular and Chemical Physics* (1987) **83** (7), 1121
129. Lidiard, A. B., *Journal of Nuclear Materials* (1966) **19** (1), 106
130. Dabrowski, L., and Szuta, M., *Journal of Alloys and Compounds* (2014) **615**, 598
131. Govers, K.*, et al.*, *Journal of Nuclear Materials* (2009) **395** (1–3), 131
132. Parfitt, D. C., and Grimes, R. W., *Journal of Nuclear Materials* (2008) **381** (3), 216
133. Grimes, R. W.*, et al.*, *Journal of Nuclear Materials* (1990) **172** (1), 123
134. Yakub, E.*, et al.*, *Journal of Nuclear Materials* (2010) **400** (3), 189
135. Gryaznov, D.*, et al.*, *Nuclear Instruments and Methods in Physics Research Section B: Beam Interactions with Materials and Atoms* (2010) **268** (19), 3090
136. Roudil, D.*, et al.*, *Journal of Nuclear Materials* (2004) **325** (2–3), 148
137. Shannon, R. D., *Acta Crystallographica Section A* (1976) **A32**, 751
138. Talip, Z.*, et al.*, *Journal of Nuclear Materials* (2014) **445** (1), 117
139. Roudil, D.*, et al.*, *Journal of Nuclear Materials* (2008) **378** (1), 70
140. Matsumoto, T.*, et al.*, *Progress in Nuclear Energy* (2015) **85**, 271
141. Kurosaki, K.*, et al.*, *Journal of Nuclear Materials* (2001) **294** (1), 160
142. Dworkin, A. S., and Bredig, M. A., *The Journal of Physical Chemistry* (1968) **72** (4), 1277
143. Cooper, M. W. D.*, et al.*, *Journal of Nuclear Materials* (2015) **461**, 206
144. Kim, Y. E. P., J. W.; Cleveland, J., *Thermophysical properties database of materials for light water reactors and heavy water reactors*. IAEA: (2006);
145. Potashnikov, S. I.*, et al.*, *Journal of Nuclear Materials* (2011) **419** (1–3), 217
146. Tiwary, P.*, et al.*, *Physical Review B* (2011) **83** (9), 094104
147. Ralph, J., *Journal of the Chemical Society, Faraday Transactions 2: Molecular and Chemical Physics* (1987) **83** (7), 1253
148. Clausen, K.*, et al.*, *Physical Review Letters* (1984) **52** (14), 1238
149. De Bruycker, F.*, et al.*, *Materials Today* (2010) **13** (11), 52
150. Todorov, I. T.*, et al.*, *Journal of Materials Chemistry* (2006) **16** (20), 1911
151. Yamashita, T.*, et al.*, *Journal of Nuclear Materials* (1997) **245** (1), 72

152. Taylor, D., *British Ceramic Transactions & Journal* (1984) **83**, 32
153. Touloukian, Y. S.*, et al.*, *Thermophysical Properties of Matter - the TPRC Data Series. Volume 13. Thermal Expansion - Nonmetallic Solids*. Defense Technical Information Center: 1977
154. Marples, J. A. C., Plutonium 1975 and Other Actinides; North Holland, New York, 1976
155. Fahey, J. A.*, et al.*, *Inorganic and Nuclear Chemistry Letters* (1974) **10** (6), 459
156. Oetting, F. L., *Journal of Nuclear Materials* (1982) **105** (2), 257
157. Fink, J. K., *International Journal of Thermophysics* (1982) **3** (2), 165
158. Rance, P. J. W., *A summary of recent work relating to the behaviour of plutonium dioxide in storage*. Nexia Solutions, BNFL: (2005);
159. Garrido, F.*, et al.*, *Nuclear Instruments and Methods in Physics Research Section B: Beam Interactions with Materials and Atoms* (2009) **267** (8), 1451
160. Ziegler, J. F., and Biersack, J. P., *The Stopping and Range of Ions in Matter*. In *Treatise on Heavy-Ion Science: Volume 6: Astrophysics, Chemistry, and Condensed Matter*, Bromley, D. A., (ed.) Springer US, Boston, MA, (1985), p 93
161. Martin, G.*, et al.*, *Nuclear Instruments and Methods in Physics Research Section B: Beam Interactions with Materials and Atoms* (2014) **327**, 108
162. Kinchen, G. H., Pease, R. S., *Reports on Progress in Physics* (1955) **18** (4), 590
163. Tian, X. F.*, et al.*, *Nuclear Instruments and Methods in Physics Research Section B: Beam Interactions with Materials and Atoms* (2011) **269** (15), 1771
164. Ziegler, J. F., and Biersack, J. P., The Stopping and Range of Ions in Matter. In *Treatise on Heavy-Ion Science: Volume 6: Astrophysics, Chemistry, and Condensed Matter*, Bromley, D. A., (ed.) Springer US, Boston, MA, (1985), pp 93
165. Thomé, L.*, et al.*, *Journal of Nuclear Materials* (2009) **389** (2), 297
166. Beauvy, M., *Journal of Nuclear Materials* (1992) **188**, 232
167. Vegard, L., *Zeitschrift für Physik* (1921) **5** (1), 17
168. Kato, M.*, et al.*, *Journal of Nuclear Materials* (2009) **393** (1), 134
169. Nichenko, S., and Staicu, D., *Journal of Nuclear Materials* (2013) **439** (1-3), 93
170. Popov, S., *Thermophysical Properties of MOX and $UO_2$ Fuels Including the Effects of Irradiation.* ONRL: (2000), 2000/351

171. Arima, T.*, et al.*, *Journal of Nuclear Materials* (2008) **376** (2), 139
172. Ma, J.*, et al.*, *Journal of Nuclear Materials* (2014) **452** (1), 230
173. Arab-Chapelet, B.*, et al.*, *Structural characterization of mixed uranium-plutonium co-precipitates and oxides synthesized by oxalic co-conversion route*. Presented at ATALANTE, Montpellier, France, (19-22 May, 2008)
174. Barrett, S. A.*, et al.*, *Acta Crystallographica Section B* (1982) **38**, 2775